INTERFACIAL WATER: A PHYSICAL CHEMISTRY PERSPECTIVE, VOLUME II

EDITED BY: Motomu Tanaka, Yoshihisa Harada, Hideki Seto and Kenichi Yoshikawa

PUBLISHED IN: Frontiers in Chemistry

frontiers Research Topics

frontiers

ISSN 1664-8714
ISBN 978-2-88974-702-3
DOI 10.3389/978-2-88974-702-3

About Frontiers

Frontiers is more than just an open-access publisher of scholarly articles: it is a pioneering approach to the world of academia, radically improving the way scholarly research is managed. The grand vision of Frontiers is a world where all people have an equal opportunity to seek, share and generate knowledge. Frontiers provides immediate and permanent online open access to all its publications, but this alone is not enough to realize our grand goals.

Frontiers Journal Series

The Frontiers Journal Series is a multi-tier and interdisciplinary set of open-access, online journals, promising a paradigm shift from the current review, selection and dissemination processes in academic publishing. All Frontiers journals are driven by researchers for researchers; therefore, they constitute a service to the scholarly community. At the same time, the Frontiers Journal Series operates on a revolutionary invention, the tiered publishing system, initially addressing specific communities of scholars, and gradually climbing up to broader public understanding, thus serving the interests of the lay society, too.

Dedication to Quality

Each Frontiers article is a landmark of the highest quality, thanks to genuinely collaborative interactions between authors and review editors, who include some of the world's best academicians. Research must be certified by peers before entering a stream of knowledge that may eventually reach the public - and shape society; therefore, Frontiers only applies the most rigorous and unbiased reviews.
Frontiers revolutionizes research publishing by freely delivering the most outstanding research, evaluated with no bias from both the academic and social point of view. By applying the most advanced information technologies, Frontiers is catapulting scholarly publishing into a new generation.

What are Frontiers Research Topics?

Frontiers Research Topics are very popular trademarks of the Frontiers Journals Series: they are collections of at least ten articles, all centered on a particular subject. With their unique mix of varied contributions from Original Research to Review Articles, Frontiers Research Topics unify the most influential researchers, the latest key findings and historical advances in a hot research area! Find out more on how to host your own Frontiers Research Topic or contribute to one as an author by contacting the Frontiers Editorial Office: frontiersin.org/about/contact

INTERFACIAL WATER: A PHYSICAL CHEMISTRY PERSPECTIVE, VOLUME II

Topic Editors:
Motomu Tanaka, Heidelberg University, Germany
Yoshihisa Harada, The University of Tokyo, Japan
Hideki Seto, High Energy Accelerator Research Organization, Japan
Kenichi Yoshikawa, Doshisha University, Japan

Topic Editor Harada receives financial support from AGC Research Collaboration System with the title "Research on the control of biocompatibility based on the analysis of substrate surface". The other Topic Editors declare no competing interests

Citation: Tanaka, M., Harada, Y., Seto, H., Yoshikawa, K., eds. (2022). Interfacial Water: A Physical Chemistry Perspective, Volume II. Lausanne: Frontiers Media SA. doi: 10.3389/978-2-88974-702-3

Table of Contents

frontiers | Frontiers in Chemistry

EDITORIAL
published: 23 May 2022
doi: 10.3389/fchem.2022.896586

Editorial: Interfacial Water: A Physical Chemistry Perspective, Volume II

Yoshihisa Harada *

Institute for Solid State Physics, The University of Tokyo, Kashiwa, Japan

Keywords: interfacial water, hydration, aquatic functional materials, surface and interface, hydrogen bonding

Editorial on the Research Topic

Interfacial Water: A Physical Chemistry Perspective, Volume II

Water's properties have always been studied using cutting-edge analytical methods, which is critical because water comprises the earth's surface and our daily lives. However, even the structure of bulk water is being debated, so when it comes to interfacial water, things become much more complicated due to the variety of water networks and interacting materials (Brini et al., 2017). While interfacial water contributes to the diversity of material functions, each phenomenon is so distinct that developing a general concept of interfacial water appears challenging. In the Research Topic on *Interfacial Water: A Physical Chemistry Perspective*, a wide range of viewpoints are used to examine the properties of interfacial water, both from the perspective of water and materials. Because of the success of this Research Topic, Volume II was published, which advances the study of interfacial water by including a broader range of analytical approaches capable of capturing water structure and dynamics. Furthermore, the materials covered are diverse, ranging from solid surfaces to proteins.

In terms of the nature of interfacial water, phospholipid bilayer is a well-studied material. Scollo et al. demonstrated that the degree of hydration and mobility of the interfacial region formed by hydrated lipid headgroups, as well as the composition of the bilayer and headgroups, can be visualized in images using Time-Dependent Fluorescence Shift. They discuss how ions and oxidized phospholipids affect bilayer organization and headgroup packing. Bonini et al. used Small Angle Neutron Scattering and Elastic Neutron Scattering to study the aging of Bio Crude Oils, potential renewable energy sources, and their lignin fractions to better understand aggregate growth and fractal hierarchy. The quantitative discussion of the temporal and spatial changes in molecular activity employs Quasi-Elastic Neutron Scattering to capture the formation and then the dynamics changes.

Lautenbach et al. used sum frequency generation spectroscopy to quantify the polarity and magnitude of the electric field in the hydration shell of a specific model protein adsorbed on a hydrophobic surface, polystyrene (PS). It was discovered that the protein's pH-dependent adsorption behavior on PS correlates with its amino acid composition and degree of hydrophobicity. Meanwhile, Nakagawa et al. investigated the hydration structure and hydrogen bonding states of the protein staphylococcal nuclease at various hydration levels in the crystalline state using all-atom molecular dynamics (MD) simulations. They discovered that the distance and angle of hydrogen bonds in the crystal's hydration water were comparable to those of tetrahedrally-coordinated water molecules in the bulk.

To precisely characterize the character and functional role of water at well-defined surfaces, various interface-sensitive techniques have been used; Li et al. used an external gate potential in conjunction with an electrolyte-insulator-semiconductor junction to control the charge density and charge strength at the silica/water interface. Sum-frequency vibrational spectroscopy was used to successfully observe the alignment of liquid water molecules. Cao et al. reviewed the use of atomic

OPEN ACCESS

Edited and reviewed by:
Malgorzata Biczysko,
Shanghai University, China

***Correspondence:**
Yoshihisa Harada
harada@issp.u-tokyo.ac.jp

Specialty section:
This article was submitted to Physical Chemistry and Chemical Physics, a section of the journal Frontiers in Chemistry

Received: *15 March 2022*
Accepted: *02 May 2022*
Published: *23 May 2022*

Citation:
Harada Y (2022) Editorial: Interfacial Water: A Physical Chemistry Perspective, Volume II. Front. Chem. 10:896586. doi: 10.3389/fchem.2022.896586

force microscopy (AFM) to observe two-dimensional (2D) or three-dimensional (3D) interfacial water at a variety of solid surfaces in order to gain a better understanding of its physicochemical properties. Chang et al. used the AFM to measure surface forces precisely. Antifouling properties of specific zwitterionic amino acid sequences is found to differ significantly, and interfacial water in the vicinity of the specific amino acid sequences may act as a physical barrier to prevent protein and cell adsorption or adhesion. Fujii et al. used Quasielastic Neutron Scattering to observe hydrated poly (methyl methacrylate) (PMMA) and discovered that hydrated water affects the local motion of PMMA and activates local relaxation processes. Akada et al. used soft X-ray emission spectroscopy to observe hydrogen-bonded structure of water in a loop-shaped poly (ethylene glycol) chain in a polyrotaxane and discovered the lack of tetrahedrally-coordinated water in the loop possibly due to entropy loss, suggesting the ability to control the biocompatibility.

It is clear from the preceding investigations that interactions between water and materials alter their respective structures and dynamics, as well as intricately control the function at the interface. Modern analytical methods are being developed on a more microscopic scale, with higher time resolution, or with increased chemical state or interface selectivity, and are expected to shift away from typical interface analysis and toward practical materials analysis in the near future.

AUTHOR CONTRIBUTIONS

The author confirms being the sole contributor of this work and has approved it for publication.

ACKNOWLEDGMENTS

The authors thank Grant-in-Aid for Scientific Research on Innovative Areas No. JP19H05717 (Aquatic Functional Materials).

REFERENCE

Brini, E., Fennell, C. J., Fernandez-Serra, M., Hribar-Lee, B., Lukšič, M., and Dill, K. A. (2017). How Water's Properties Are Encoded in its Molecular Structure and Energies. *Chem. Rev.* 117, 12385–12414. doi:10.1021/acs.chemrev.7b00259

Conflict of Interest: The author declares that the research was conducted in the absence of any commercial or financial relationships that could be construed as a potential conflict of interest.

frontiers in Chemistry

ORIGINAL RESEARCH
published: 26 July 2021
doi: 10.3389/fchem.2021.708633

Mode Bifurcation on Contact Line Dynamics at Oil/Water Interface Depending on the Contact Line Length

Daigo Yamamoto[1]*, *Jumpei Maeno*[1], *Yuki Manabe*[1], *Yasunao Okamoto*[1], *Erika Nawa-Okita*[2] *and Akihisa Shioi*[1]

[1]Department of Chemical Engineering and Materials Science, Doshisha University, Kyoto, Japan, [2]Department of Chemical Engineering, Osaka Prefecture University, Osaka, Japan

The motion of the contact line at the oil/water interface caused by chemical reactions is well known as a typical example of artificial active matter in the field of nonlinear science. When water (containing trimethylstearylammonium chloride) and nitrobenzene (containing iodide anion) phases are in contact, the regulated traveling-wave patterns appear along the inner wall of the glass container. In this study, we demonstrate a new dynamical mode of the contact line, an up-and-down motion, which becomes dominant with the decrease in the size of a glass tube, and the probability of occurrence is extremely high when the diameter of the glass tube is below 1 mm. A physicochemical model of the contact line motion that incorporates the spatiotemporal variation of the surfactant concentration on a glass surface is proposed, and its effect on the wettability of oil/water phases on the walls of the glass tubes is studied. The present model can reproduce the mode bifurcation of the dynamical motion depending on the inner diameter of the glass tubes.

Keywords: contact line, interfacial energy, active matter, bifurcation, traveling-wave motion, up-and-down motion, oil/water interface

OPEN ACCESS

Edited by:
Motomu Tanaka,
Heidelberg University, Germany

Reviewed by:
Jerzy Gorecki,
Institute of Physical Chemistry (PAN), Poland
Nobuhiko J. Suematsu,
Meiji University, Japan

***Correspondence:**
Daigo Yamamoto
dyamamot@mail.doshisha.ac.jp

Specialty section:
This article was submitted to Physical Chemistry and Chemical Physics, a section of the journal Frontiers in Chemistry

Received: *12 May 2021*
Accepted: *13 July 2021*
Published: *26 July 2021*

Citation:
Yamamoto D, Maeno J, Manabe Y, Okamoto Y, Nawa-Okita E and Shioi A (2021) Mode Bifurcation on Contact Line Dynamics at Oil/Water Interface Depending on the Contact Line Length. Front. Chem. 9:708633. doi: 10.3389/fchem.2021.708633

INTRODUCTION

Recently, active matter has become a common topic in mechanical engineering, biology, and nonlinear science (Ramaswamy, 2010; Marchetti et al., 2013; Nakata, 2019; Zhou et al., 2019; Gompper et al., 2020). Active matter exhibits autonomous motion by direct conversion of chemical into kinetic energy in the absence of an external force. It contains not only biological systems (e.g., microorganisms and living cells) but also non-living systems such as camphor boats (Nakata et al., 1997; Suematsu et al., 2010; Kitahata and Koyano, 2020), catalytic particles in solution (Paxton et al., 2004; Yamamoto and Shioi, 2015), and vesicles under a pH gradient (Nawa et al., 2013; Nawa et al., 2015). Since non-living active matter is easier to handle experimentally, a deeper understanding of active matter systems may be gained and used in engineering applications for innovative isothermal high-efficiency energy conversion. For this purpose, a physicochemical model of an artificial active matter system that exhibits biomimetic behavior needs to be constructed, using an experimental setup as simple as possible.

A typical example of an artificial active matter system is the motion of the oil/water interface (nitrobenzene/water) on a glass surface, which was reported in the 1970s (Dupeyrat and Nakache, 1978). Research on the motion of oil/water interfaces has been performed in nonlinear science, which is mainly divided into two types of experimental systems. One type is the motion of an oil droplet on a glass plate placed in the water phase (Sumino et al., 2005a; Sumino et al., 2005b; Sumino and Yoshikawa, 2008). Recently, we reported new applications of such motile oil droplets, such as in

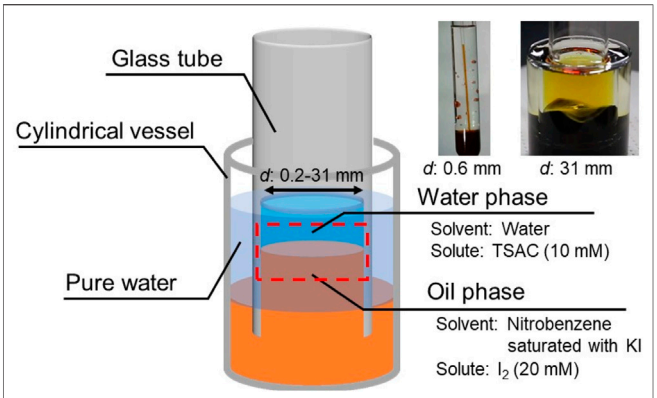

FIGURE 1 | Experimental setup for observation of oil/water contact line motions.

active transport (Goto et al., 2015) and synchronization (Kasai et al., 2020). The other type is the motion of the contact line between the inner wall of a cylindrical glass container and the oil/water interface (Kai et al., 1991; Shioi et al., 2003). The contact line forms a spatiotemporal wave that propagates in the circumferential direction of the container while maintaining its waveform (called traveling-wave motion). These motions are caused by repetitive adsorption/desorption of the surfactant and the consequent change in wettability of the oil/water phases on the glass surface (Shioi et al., 2008a; Shioi et al., 2008b; Sumino and Yoshikawa, 2008).

In this study, we focused on the motion of an oil/water contact line. By devising an experimental setup, we demonstrate a new dynamical mode instead of a traveling-wave motion, that is, an up-and-down motion. Furthermore, we propose a physicochemical model that considers the spatiotemporal variation in the adsorption/desorption process of the surfactants on the glass surface.

EXPERIMENTS

Chemicals

Trimethylstearylammonium chloride (C_{18}TAC, 98.0%) was purchased from Tokyo Chemical Industry Co., Ltd., Iodine (I_2, 99.8%), potassium iodide (KI, 99.5%), and nitrobenzene (99.5%) were purchased from Wako Pure Chemical Industries, Ltd., All chemicals were used without further purification. A C_{18}TAC aqueous solution (10 mM) was prepared as the water phase. Nitrobenzene saturated with KI was used as the oil phase, and 20 mM of I_2 were dissolved in the oil phase.

Observation of the Motion of Oil/Water Contact Line

In this study, we focused on the effect of the contact line length on its dynamical motion. A previous simple experimental setup with a glass container is not available because the volume preservation of the bottom oil phase significantly affects the contact line motion. This effect inhibits the contact line motion if the diameter of the glass container is considerably small. To eliminate the effect of volume preservation on the contact line motion, we used cylindrical glass tubes with open ends (open tube), instead of a glass container, to form a motile oil/water contact line (**Figure 1**).

Open tubes with various inner diameters (d = 0.2–31 mm) were tested. Each open tube was vertically inserted into the reservoir oil contained in a cylindrical vessel. Pure water was then poured into the space between the open tube and the cylindrical vessel to raise the surface level of the oil phase inside the open tube. Then, the water phase was poured into the open tube to form a motile oil/water contact line along the inner wall of the tube (see the red dashed area in **Figure 1**). The contact line motion was monitored using a digital single-lens reflex camera (Canon EOS Kiss X9) at a frame rate of 60 fps. All experiments were performed at room temperature (20–25°C).

EXPERIMENTAL RESULTS AND DISCUSSION

Figures 2A–1 shows the contact line motion in an open tube with an inner diameter of 0.6 mm (= d) (circumferential length L (= πd) = 1.89 mm). The contact line moved up and down periodically for several minutes. (See **Supplementary Video 1** for a smaller tube). **Figures 2A–2** shows a space–time plot of the repetitive up-and-down motion along the red line shown in **Figure 2A**. The average of period T and the height change Δh for the up-and-down motion were estimated to be 2.5 s and 2.3 mm, respectively. The waveform of the space–time plot is asymmetric, which indicates that the rising speed of the contact line is faster than that of the falling contact line. Moreover, the waveform is convex for the rise and concave for the fall of the contact line. Hence, both rising and falling speeds decelerate as the contact line approaches the peak. Such an up-and-down motion was also observed for the glass tubes with intermediate inner diameters (d = 0.6–6.0 mm). However, a tube with a much larger inner diameter [d = 31 mm (L = 97.3 mm)] forms a regulated traveling wave (in this case, Δh is measured to 5.9 mm) (**Figure 2B**), as reported by several researchers including us (Dupeyrat and Nakache, 1978; Kai et al., 1991; Shioi et al., 2003). (See **Supplementary Video 2** for a larger tube) These results demonstrate that the mode bifurcation on the contact line dynamics depends on the contact line length (the inner diameter of the glass tube). To investigate this mode bifurcation between the up-and-down and traveling-wave motions, we evaluated the ratio of each mode of open tubes with various inner diameters. The observed contact line motions are easily classified into the two modes in each experiment as follows. Briefly, when the traveling wave appears, the maximum and minimum of the height of the contact line is observed independent of time. Otherwise, the up-and-down motion keeps the almost same height at whole circumference in one snapshot. The experiments were repeated a minimum of four times for each inner diameter and the results obtained are shown in **Figure 3A**. In the tubes with diameter over 8.0 mm, only the traveling-wave motion was observed, while the up-and-down

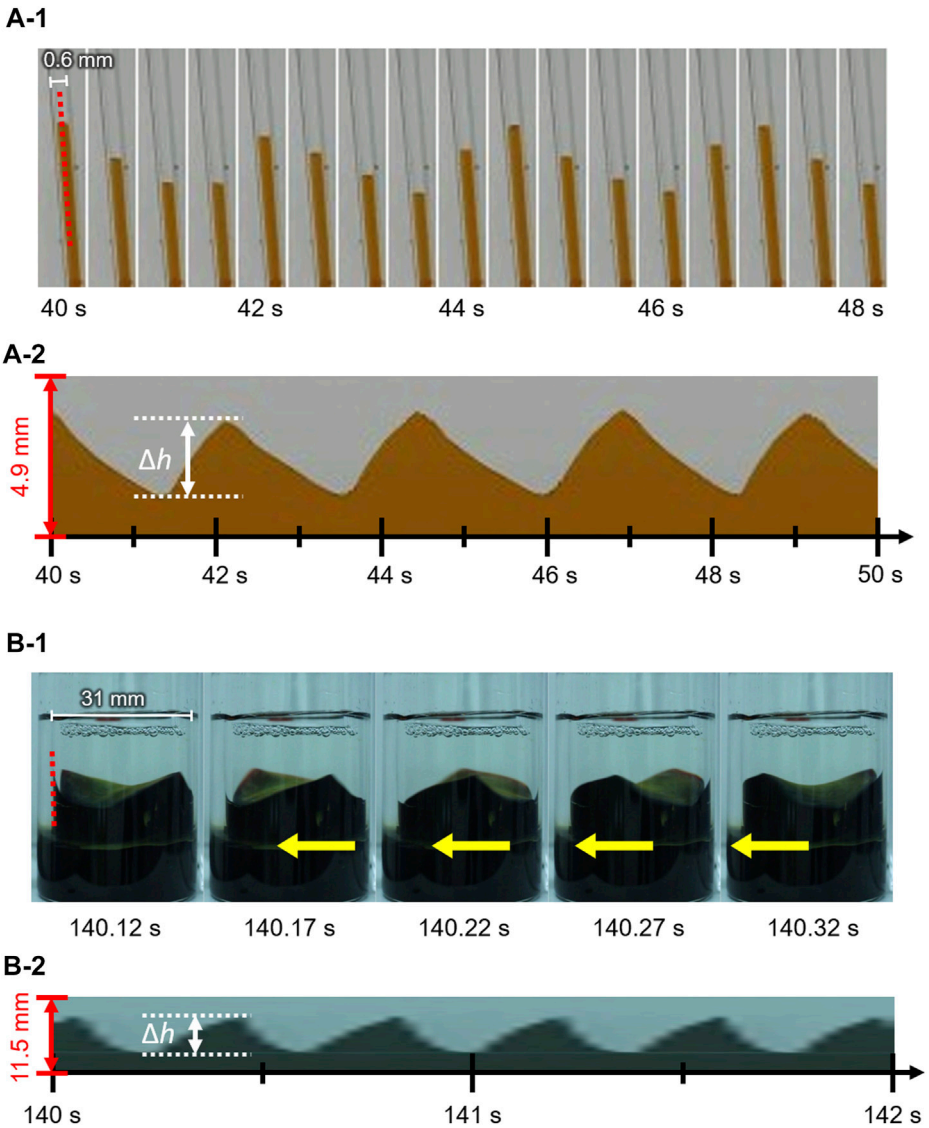

FIGURE 2 | Snapshots and space–time plots of oil/water contact line motions in an open tube with an inner diameter of **(A)** 0.6 mm and **(B)** 31 mm. The contact line of **(A)** and **(B)** exhibits up-and-down motion and traveling-wave motion, respectively.

motion became dominant with a decrease in the diameter. In the tubes with intermediate diameters (d = 1.6–6.0 mm), either mode is observed in each experiment. (See **Supplementary Video 3** for middle tubes). Once one mode appeared, it rarely changed to the other mode during the experiment. Actually, the larger tube tends to cause dynamical modes of longer duration (from several minutes to ten). In addition, the deviations of each Δh is almost zero while the mode remains stable for several tens of cyclic periods. Such a bifurcation may be attributed to an initial fluctuation in the contact line. We confirmed that the two modes switched between each other by stimulating the motile contact line. To investigate the factors causing the bifurcation, the average Δh was measured for each trial (**Figure 3B**). As shown in **Figure 3B**, for the up-and-down motion, Δh decreases with an increase in the inner diameter. A plot of log (Δh) vs. log(d) for up-and-down motion gives a straight line with slope of roughly −1.0, although the distribution of Δh for the same inner diameter is large (probably due to surface condition of each glass tube we used). The slope of −1.0 can be explained by capillary action. When a capillary tube is dipped into liquid, the height h from the liquid interface is given by Jurin's law ($h \propto \gamma \cos\theta / d$), where γ and θ denote the interfacial tension and contact angle on the contact line, respectively. In our experiment, the interfacial tension changed periodically by repetitive adsorption/desorption of surfactants (which corresponds to upward/downward motion of the contact line), while no appreciable change in the contact angle was observed. Assuming that the difference in the interfacial tension $\Delta\gamma_{w/o}$ between the maximum and minimum of the surface level is constant for various diameters, Δh is inversely proportional to the diameter of the

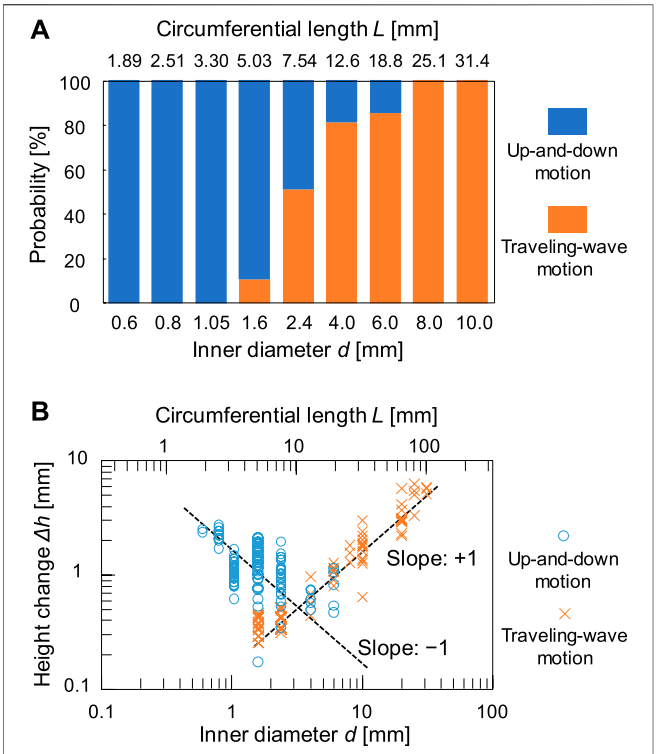

FIGURE 3 | (A) Relationship between probability of occurrence of the two modes and the inner diameter d of tubes and **(B)** double logarithmic plot of height change Δh and d.

tube ($\Delta h \propto \Delta\gamma_{w/o}\cos\theta/d$). On the contrary, a larger inner diameter leads to a larger height change for the traveling-wave motion, as shown in **Figure 3B**. Thus, Δh of the two motions is comparable at the intermediate diameter (d = 2.4–6.0 mm), where both motions appear depending on the initial fluctuation of the contact line. We concluded that bifurcation can be determined by Δh of the two motions.

PHYSICOCHEMICAL MODEL FOR THE BIFURCATION

We have already proposed a mathematical model for traveling-wave motion (Shioi et al., 2008a; Shioi et al., 2008b). However, the previous model hardly considered any concrete physicochemical processes for the adsorption/desorption of surfactants. In this study, we propose a model that incorporates the spatiotemporal variation of the surfactant concentration on a glass surface and its effect on the wettability of oil/water phases on the walls of glass tubes. The equation for the contact line motion is expressed as follows:

$$m\frac{\partial^2 h(t,x)}{\partial t^2} = -\mu\frac{\partial h(t,x)}{\partial t} + \Gamma\frac{\partial^2 h(t,x)}{\partial x^2} - \chi[h(t,x) - h_0] + F(t,x) + \xi(t,x) \tag{1}$$

As shown in **Figure 4A**, $h(t, x)$ denotes the height of the contact line at the coordinate x (the circumferential displacement in our system) at time t. The first term ($-\mu\partial h/\partial t$) on the right-hand side is the dissipation caused by the viscous drag force, where μ is the dumping coefficient. The second term ($\Gamma\partial^2 h/\partial x^2$) works as the vibration control term, leading to a reduction in the roughness of the contact line shape due to interfacial tension (Shioi et al., 2008a). The third term ($\chi[h-h_0]$) is a restoring term owing to the density difference between the oil and water phases, which works as an elastic force that $h(t, x)$ returns to the initial height of the contact line h_0. The term is one of the most significant effects to reproduce the periodic motion. We confirmed in advance that the contact line maintains translation toward one direction when the term is negligible, which mimics our previous experimental results (Kasai et al., 2020). Here, Γ and χ denote proportional constants for each term. The fourth term ($F(t,x)$) is the driving force of the contact line motion caused by the wettability change of oil/water phases on the surface of the glass tube, which results from the repetitive adsorption/desorption of surfactants. The last term ($\xi(t,x)$) (time average: $\xi(t,x) = 0$) is a random noise acting on the oil/water interface for the Marangoni effect. To simplify the model, we assume that the Reynolds number of the contact line is so small that the inertia term on the left-hand side is negligible ($m\partial^2 z/\partial t^2 = 0$) because the viscous force dominates the motion in such a millimeter-sized system.

In the present system, the water and oil phases are placed as layers at the upper and lower positions, respectively. Thus, the driving force caused by the solid–liquid interfacial energy is expressed as follows:

$$F(t,x) = \gamma_{w/s}|_{\Theta(t,x,h)} - \gamma_{o/s}|_{\Theta(t,x,h)} \tag{2}$$

$\gamma_{w/s}|_{\Theta(t,x,h)}$ and $\gamma_{o/s}|_{\Theta(t,x,h)}$ denote the solid–liquid interfacial energies of water/glass and oil/glass around the contact line (at $z = h$), where $\Theta(t, x, z)$ is the adsorption ratio of the surfactant at the vertical displacement z and at the circumferential displacement x of the glass surface ($0 \le \Theta(t,x,z) \le 1$), as shown in **Figure 4B**.

Figure 4B illustrates the adsorption/desorption processes in this model. Most of the $C_{18}TAC$ dissolved in water forms micelles because the initial concentration is much higher than the CMC (critical micelle concentration = 0.3 mM). The resultant micelles were then adsorbed onto the glass surface as a bilayer (Atkin et al., 2003). Assuming that the micelle may be treated as a dimer of the cationic surfactant $C_{18}TA^+$, the absorption onto the site of the glass surface S, is described as follows:

$$\text{Water phase)} \quad (C_{18}TA^+)_2 + S \rightarrow (C_{18}TA^+)_2 \cdot S \tag{3}$$

Here, we ignore the reverse reaction to simplify the model because the concentration of $C_{18}TAC$ is sufficiently high. In the oil phase, the desorption of the surfactant occurs because of the chemical reaction with oil-soluble anions, for example, the polyiodide anion I_n^-.

$$\text{Oil phase)} \quad (C_{18}TA^+)_2 \cdot S + 2I_n^- \rightarrow 2C_{18}TA \cdot I_n + S \tag{4}$$

From the above two equations, the reaction rate for the adsorption ratio can be expressed as:

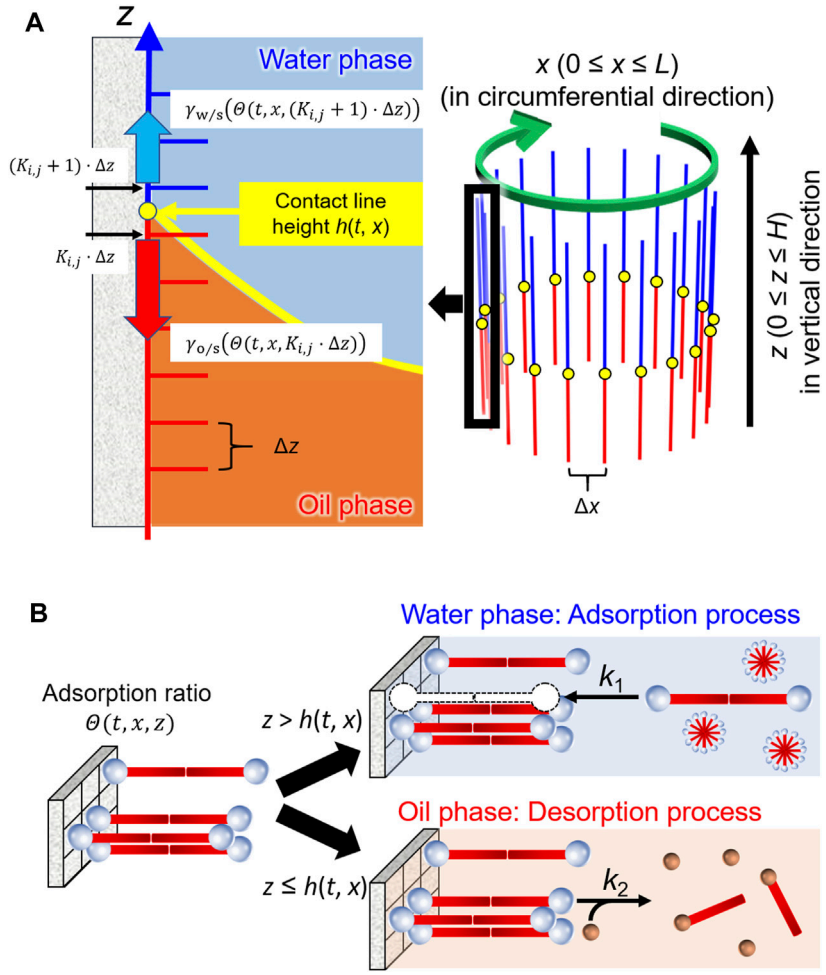

FIGURE 4 | Schematic illustrations of the model for **(A)** the contact line motion along inner wall of a glass tube and **(B)** adsorption/desorption processes of the surfactants in water and oil phases.

Water phase)

$$\frac{d\Theta(t,x,z)}{dt} = k_1\frac{C_{A0}}{2}(1-\Theta(t,x,z))\,(\text{at } h(t,x) < z \le H) \tag{5}$$

Oil phase) $\dfrac{d\Theta(t,x,z)}{dt} = -k_2 C_{I0}^2 \dfrac{C_{A0}}{2}\Theta(t,x,z)\quad (\text{at } 0 \le z \le h(t,x))$ (6)

Here, k_1 and k_2 are the reaction rate constants for adsorption/desorption. C_{A0} is the C_{18}TAC concentration in the water phase, which is divided by two to approximate the bilayer state. C_{I0} is the anion concentration in the oil phase. According to the Cassie model (Cassie, 1948), $\gamma_{w/s}(\Theta(t,x,h))$ and $\gamma_{o/s}(\Theta(t,x,h))$ around the contact line were estimated from the values of $\Theta(t,x,z)$ as follows:

$$\gamma_{w/s}|\Theta(t,x,h) = \Theta(t,x,h)\cdot\gamma_{w/s}(\Theta=1) + (1-\Theta(t,x,h))\cdot\gamma_{w/s}(\Theta=0) \tag{7}$$

$$\gamma_{o/s}|\Theta(t,x,h) = \Theta(t,x,h)\cdot\gamma_{o/s}(\Theta=1) + (1-\Theta(t,x,h))\cdot\gamma_{o/s}(\Theta=0) \tag{8}$$

$\gamma_{w/s}(\Theta=1)$, $\gamma_{w/s}(\Theta=0)$, $\gamma_{o/s}(\Theta=1)$, or $\gamma_{o/s}(\Theta=0)$ are the interfacial tensions of the water/glass or oil/glass phases at $\Theta = 1$ or 0, respectively.

When this series of calculation processes (**Equations 1**, **2**, **5**, **6**, **7**, **8**) is performed for all displacements x in the circumferential direction at time t, the time course of the contact line shape is obtained. Here, we preset the maximum height H for the contact line height (h). For the circumferential length L ($= \pi d$), a periodic boundary condition was applied.

The numerical calculation was performed using the finite-difference method. Δt, Δx, and Δz, step width of t, x, and z, are 0.001, 0.01, and 0.001, respectively. Here, it is difficult to calculate the accurate value of $\Theta(t,x,h)$ at an arbitrary h because z in **Equations 5**, **6** is divided discretely in the numerical calculation. As t, x, and z can take $i\cdot\Delta t$ ($i = 0, 1, 2, \ldots, i_{max}$), $j\cdot\Delta x$ ($j = 0, 1, 2, \ldots, j_{max}$), and $k\cdot\Delta z$ ($k = 0, 1, 2, \ldots, k_{max}$), there exists an integer $K_{i,j}$ that satisfies the following equation:

$$K_{i,j}\cdot\Delta z \le h_{i,j}\left(= h(i\cdot\Delta t, j\cdot\Delta x)\right) < \left(K_{i,j}+1\right)\cdot\Delta z \tag{9}$$

In the calculation, $\gamma_{w/s}(\Theta(t,x,h))$ and $\gamma_{o/s}(\Theta(t,x,h))$ were approximated by $\gamma_{w/s}(\Theta(t,x,(K_{i,j}+1)\cdot\Delta z))$ and $\gamma_{o/s}(\Theta(t,x,K_{i,j}\cdot\Delta z))$, respectively, that is, $\Theta(t,x,h)$ in

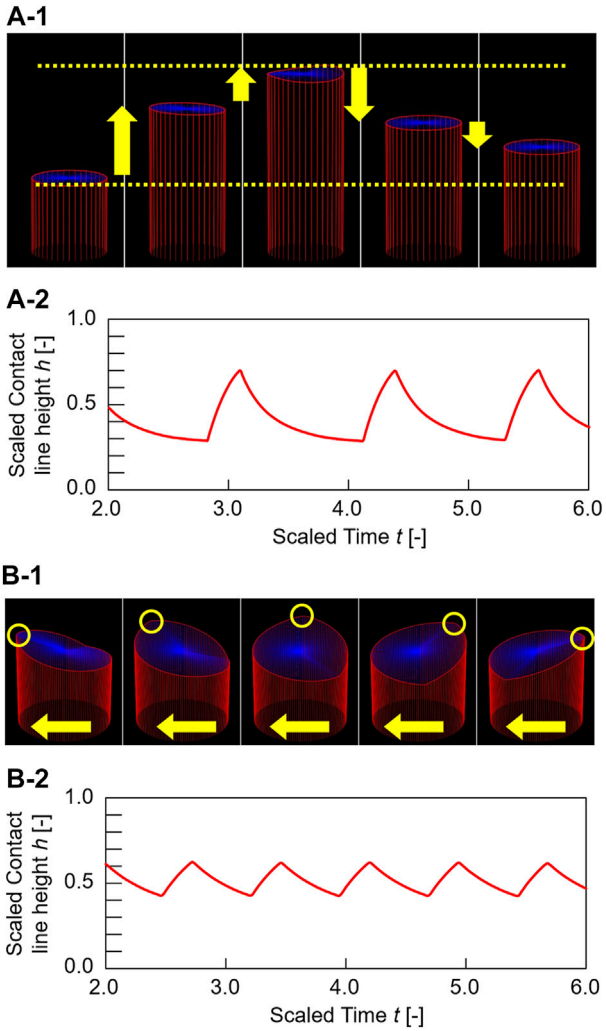

FIGURE 5 | Calculation results. Three-dimensional graphs and time course of contact line height change Δh of the oil/water contact line motions for **(A)** $L = 0.4$ and **(B)** $L = 1.5$. The contact lines of **(A)** and **(B)** exhibit up-and-down motion and traveling-wave motion, respectively. Blue top surfaces in the three-dimensional graphs represent oil/water interfaces. The curved surfaces were drawn by connecting between the oil/water interfacial height at center $h_c(t)$ and the contact line height at arbitrary circumferential displacement. $h_c(t)$ was estimated by calculating the average of the contact line height at each time $< h(t) > (h_c(t) = \int_0^L h(t,x)dx/L)$.

Equations 7, **8** are evaluated at $K_{i,j} \cdot \Delta z$, and $(K_{i,j} + 1) \cdot \Delta z$ in the oil and water phases, respectively. This is shown in **Figure 4A**. **Supplementary Note 1**; **Supplementary Figure 1** show procedure for calculating a physicochemical model of the contact line motion and a flowchart for the numerical solutions of the differential equations for the present model. The parameters used for our model are $\mu = 3.0$, $\Gamma = 0.12$, $\chi = 15$, $\langle|\xi(t,x)|^2\rangle = 0.03$, $k_1 = 22$, $k_2 = 0.3$, $C_{A0} = 10$, $C_{I0} = 20$, $\gamma_{w/s}(\Theta = 1) = 9$, $\gamma_{w/s}(\Theta = 0) = 13$, $\gamma_{o/s}(\Theta = 1) = 2$, $\gamma_{o/s}(\Theta = 0) = 15$, $z_0 = 0.5$, and $H = 1$. At the initial conditions, $\Theta(t, x, z)$ at $t = 0$ is zero, which means that no surfactant is adsorbed on the glass surface. The initial height of the contact line $h(t, x)$ at $t = 0$ is equal to H multiplied by random numbers between 0 and 1. This is because the shape of the initial contact line is complicated by the initial turbulence caused by pouring water on the oil phase. **Figures 5A–1, B–1** show three-dimensional graphs of typical calculation results for $L = 0.4$ and 1.5. The contact lines exhibit up-and-down and traveling-wave motions, respectively, which are similar to the experimental results in **Figures 2A–1, B–1**. **Figures 5A–2, B–2** show the time course of the contact line height $h(t, x)$ at $x = 0$ for **Figures 5A–1, B–1**. The time variation shows an asymmetric pattern similar to the space–time plot in **Figure 2**.

In the calculation, the dynamical mode is changed by the initial condition and the random force term, even in the same conditions (See **Supplementary Video 4** for the simulation results). Once the contact line exhibits one mode, the mode remains stable for several cyclic periods. Therefore, we investigated the probability of the occurrence of the two modes by calculating 1,000 trials for each circumferential length (**Figure 6**). As shown in **Figure 6**, a remarkable mode bifurcation depending on L is observed. The up-and-down motion is dominant for L = 0.1–0.15, while the traveling-wave motion dominates for L = 20.0. In addition, a transition region exists for L = 0.2–10.0, which means that both motions are observed depending on the initial conditions and the random force term. This result reproduces the mode bifurcation qualitatively, similar to that shown in **Figure 3A**. These results demonstrated the validity of our physicochemical mechanism.

Finally, we compare the experimental and calculation results to investigate the bifurcation mechanism. The probability depending on the size is scaled appropriately and superposed in **Supplementary Figure 2**. A plot of probability vs. logarithm of the size in experiments has much larger slope than that in

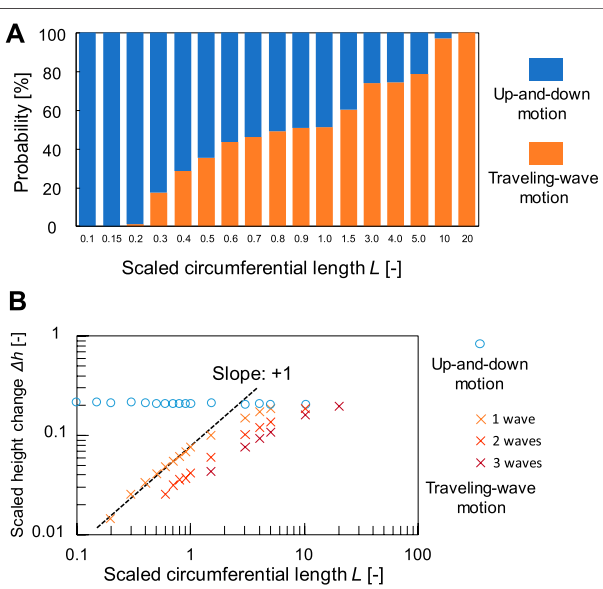

FIGURE 6 | Calculation results. **(A)** Relationship between probability of occurrence of the two modes and scaled circumferential length L and **(B)** double logarithmic plot of height change Δh and L. For the traveling-wave motion, the number of formed waves (n_{TW}) is different for each trial. Thus, the plots of **(B)** are divided into three marks depending on n_{TW} for the traveling-wave motion. The plot for $n_{TW} \geq 4$ was eliminated.

calculation, which means that the actual bifurcation is sharp depending on the inner diameter. This is because our model ignores the long-range effect that the height of the contact line is affected by that at the opposite side. The effect will become dominant for smaller tubes. In order to examine the contribution of the long-range effect, we investigated the height change Δh for each circumferential length L in our model (**Figure 6B**). Because we neglect the interaction with the contact line at opposite side through capillary effect in our model, Δh is almost constant regardless of the circumferential length for the up-and-down motion. The actual sharp bifurcation may be reproduced when the long-range effect is added in our model, whereas the calculation result predicts that the mode bifurcation can appear without the effect (for instance, by using flat plates with a different width).

On the other hand, a plot of $\log(\Delta h)$ vs. $\log(L)$ for the traveling wave motion gives a straight line with slope of +1.0, which agrees with experimental results in **Figure 3B**. The reason why the larger tube gives the higher Δh for the traveling-wave motion may be because the rate of adsorption/deadsorption is comparable to the traveling speed. We confirmed that traveling speed of the wave is almost the same regardless to the circumferential length for both experiment and simulation. Thus, when the same number of waves appears, the larger circumferential length leads to the longer period of the traveling-wave motion. This delay of arrival of the next wave affects time evolution of adsorption/deadsorption, which may result in the larger driving force deriving from the interfacial energy.

In the present stage, the detailed mechanism of the bifurcation is not elucidated completely because there are many parameters in our model. However, we need to note the contribution of elasticity of fringe (Gennes et al., 2010) and driving force, which correspond to second and fourth terms on the right-hand side in **Equation 1**. Both terms are derived from interfacial energy. We think that the balance between the amplitude of the two terms determines the bifurcation point. The physical kinetics of our system may be similar to other chemical systems such as size-depending bifurcation of Belousov–Zhabotinsky (BZ) patterns (Aihara and Yoshikawa, 2001), where the diffusion and growth rate of chemical wave.

CONCLUSION

In this study, we demonstrated that the contact line motion at oil/water on a glass surface has two types of dynamical modes depending on the inner diameters of the glass tubes. That is, smaller inner diameters tend to originate up-and-down motion, while larger diameters tend to result in traveling-wave motion. Furthermore, to investigate the bifurcation mechanism, we proposed a physicochemical model of the contact line motion that considers the spatiotemporal variation of the adsorption/desorption process of the surfactants on the glass surface. The present model can reproduce the dynamics of both motion and mode bifurcation depending on the contact line length. However, our model has several parameters. The quantitative measurement of the reaction rate constants for adsorption/desorption and interfacial tension is desirable.

DATA AVAILABILITY STATEMENT

The original contributions presented in the study are included in the article/**Supplementary Material**, further inquiries can be directed to the corresponding author.

AUTHOR CONTRIBUTIONS

JM and YM performed all experiments and calculations. DY, YO, EO, and AS conceived the study. DY, JM, YM, and AS used a physicochemical model. All authors have discussed this research.

FUNDING

YO and AS acknowledges the financial support from JSPS KAKENHI Grant Number 20K22335 and 16H04189, respectively. DY and AS also acknowledge the MEXT-Supported Program for the Strategic Research Foundation at Private Universities.

ACKNOWLEDGMENTS

We thank Tatsuya Taguchi and Kazuhiro Ogata for carrying out the experiments and simulations.

SUPPLEMENTARY MATERIAL

The Supplementary Material for this article can be found online at: https://www.frontiersin.org/articles/10.3389/fchem.2021.708633/full#supplementary-material

REFERENCES

Aihara, R., and Yoshikawa, K. (2001). Size-Dependent Switching of the Spatiotemporal Structure between a Traveling Wave and Global Rhythm. *J. Phys. Chem. A.* 105, 8445–8448. doi:10.1021/jp010908r

Atkin, R., Craig, V. S. J., Wanless, E. J., and Biggs, S. (2003). Mechanism of Cationic Surfactant Adsorption at the Solid-Aqueous Interface. *Adv. Colloid Interf. Sci.* 103, 219–304. doi:10.1016/s0001-8686(03)00002-2

Cassie, A. B. D. (1948). Contact Angles. *Discuss. Faraday Soc.* 3, 11–16. doi:10.1039/df9480300011

Dupeyrat, M., and Nakache, E. (1978). 205 - Direct Conversion of Chemical Energy into Mechanical Energy at an Oil Water Interface. *Bioelectrochemistry Bioenerg.* 5, 134–141. doi:10.1016/0302-4598(87)87013-7

Gennes, P. G. D., Brochard-Wyart, F., and Quéré, D. (2010). *Capillarity and Wetting Phenomena : Drops, Bubbles, Pearls, Waves.* New York, United States: Springer.

Gompper, G., Winkler, R. G., Speck, T., Solon, A., Nardini, C., Peruani, F., et al. (2020). The 2020 Motile Active Matter Roadmap. *J. Phys. Condens. Matter* 32, 193001. doi:10.1088/1361-648x/ab6348

Goto, Y., Kanda, M., Yamamoto, D., and Shioi, A. (2015). An Abiotic Glass-Bead Collector Exhibiting Active Transport. *Sci. Rep.* 5, 14348. doi:10.1038/srep14348

Kai, S., Muller, S. C., Mori, T., and Miki, M. (1991). Chemically Driven Nonlinear Waves and Oscillations at an Oil-Water Interface. *Physica D: Nonlinear Phenomena* 50, 412–428. doi:10.1016/0167-2789(91)90008-w

Kasai, M., Yamamoto, D., Nawa-Okita, E., and Shioi, A. (2020). Synchronization of Chemo-Mechanical Oscillators. *AIP Adv.* 10, 065007. doi:10.1063/5.0006387

Kitahata, H., and Koyano, Y. (2020). Spontaneous Motion of a Camphor Particle with a Triangular Modification from a Circle. *J. Phys. Soc. Jpn.* 89, 094001. doi:10.7566/jpsj.89.094001

Marchetti, M. C., Joanny, J. F., Ramaswamy, S., Liverpool, T. B., Prost, J., Rao, M., et al. (2013). Hydrodynamics of Soft Active Matter. *Rev. Mod. Phys.* 85, 1143–1189. doi:10.1103/revmodphys.85.1143

Nakata, S., Iguchi, Y., Ose, S., Kuboyama, M., Ishii, T., and Yoshikawa, K. (1997). Self-Rotation of a Camphor Scraping on Water: New Insight into the Old Problem. *Langmuir* 13, 4454–4458. doi:10.1021/la970196p

Nakata, S. (2019). *Self-organized Motion : Physicochemical Design Based on Nonlinear Dynamics*. London: Royal Society of Chemistry.

Nawa, E., Nishigaki, Y., Yamamoto, D., and Shioi, A. (2013). Rhythmic Shape Change of a Vesicle under a pH Gradient. *Soft Matter* 9, 7832–7842. doi:10.1039/c3sm51100f

Nawa, E., Yamamoto, D., and Shioi, A. (2015). Chemotactic Amoeboid-like Shape Change of a Vesicle under a pH Gradient. *Bcsj* 88, 1536–1544. doi:10.1246/bcsj.20150190

Paxton, W. F., Kistler, K. C., Olmeda, C. C., Sen, A., St. Angelo, S. K. S. K., Cao, Y., et al. (2004). Catalytic Nanomotors: Autonomous Movement of Striped Nanorods. *J. Am. Chem. Soc.* 126, 13424–13431. doi:10.1021/ja047697z

Ramaswamy, S. (2010). The Mechanics and Statistics of Active Matter. *Annu. Rev. Condens. Matter Phys.* 1, 323–345. doi:10.1146/annurev-conmatphys-070909-104101

Shioi, A., Ban, T., and Suzuki, S. (2008a). Model of Traveling Wave Formed by Autonomous Motion of Contact Line with Oil/water Interface. *Chem. Phys. Lett.* 467, 210–215. doi:10.1016/j.cplett.2008.11.037

Shioi, A., Ban, T., and Suzuki, S. (2008b). Noise-induced Kinetic Model for Autonomous Motion of the Contact Line in Oil-Water Systems with Chemical Reactions. *Phys. Rev. E* 77, 036208. doi:10.1103/physreve.77.036208

Shioi, A., Katano, K., and Onodera, Y. (2003). Effect of Solid walls on Spontaneous Wave Formation at Water/oil Interfaces. *J. Colloid Interf. Sci.* 266, 415–421. doi:10.1016/s0021-9797(03)00672-6

Suematsu, N. J., Ikura, Y., Nagayama, M., Kitahata, H., Kawagishi, N., Murakami, M., et al. (2010). Mode-Switching of the Self-Motion of a Camphor Boat Depending on the Diffusion Distance of Camphor Molecules. *J. Phys. Chem. C* 114, 9876–9882. doi:10.1021/jp101838h

Sumino, Y., Kitahata, H., Yoshikawa, K., Nagayama, M., Nomura, S.-I. M., Magome, N., et al. (2005a). Chemosensitive Running Droplet. *Phys. Rev. E* 72, 041603. doi:10.1103/physreve.72.041603

Sumino, Y., Magome, N., Hamada, T., and Yoshikawa, K. (2005b). Self-Running Droplet: Emergence of Regular Motion from Nonequilibrium Noise. *Phys. Rev. Lett.* 94, 068301. doi:10.1103/physrevlett.94.068301

Sumino, Y., and Yoshikawa, K. (2008). Self-motion of an Oil Droplet: A Simple Physicochemical Model of Active Brownian Motion. *Chaos* 18, 026106. doi:10.1063/1.2943646

Yamamoto, D., and Shioi, A. (2015). Self-Propelled Nano/Micromotors with a Chemical Reaction: Underlying Physics and Strategies of Motion Control. *Kona* 32, 2–22. doi:10.14356/kona.2015005

Zhou, C., Zhu, P., Tian, Y., Xu, M., and Wang, L. (2019). Engineering Micromotors with Droplet Microfluidics. *ACS Nano* 13, 6319–6329. doi:10.1021/acsnano.9b00731

Conflict of Interest: The authors declare that the research was conducted in the absence of any commercial or financial relationships that could be construed as a potential conflict of interest.

Publisher's Note: All claims expressed in this article are solely those of the authors and do not necessarily represent those of their affiliated organizations, or those of the publisher, the editors and the reviewers. Any product that may be evaluated in this article, or claim that may be made by its manufacturer, is not guaranteed or endorsed by the publisher.

frontiers in Chemistry

ORIGINAL RESEARCH
published: 30 July 2021
doi: 10.3389/fchem.2021.712978

Isoelectric Point of Proteins at Hydrophobic Interfaces

Vanessa Lautenbach†, *Saman Hosseinpour**† *and Wolfgang Peukert**

Institute of Particle Technology (LFG), Friedrich-Alexander Universität Erlangen-Nürnberg (FAU), Erlangen, Germany

Structural and colloidal stability of proteins at different surfaces and interfaces is of great importance in many fields including medical, pharmaceutical, or material science. Due to their flexibility, proteins tend to respond to their environmental conditions and can undergo structural and conformational changes. For instance, alterations in physiological factors such as temperature, ions concentration, or pH as well as the adsorption to an interface can initiate protein aggregation. Therefore, at different surfaces and interfaces the characterization of the structural and colloidal stability of proteins, which is mainly influenced by their electrostatic and hydrophobic interactions, is of fundamental importance. In this study, we utilized sum frequency generation (SFG) spectroscopy to assess the role of solution pH on the polarity and magnitude of the electric field within the hydration shell of selected model proteins adsorbed to a hydrophobic surface. We used polystyrene (PS) as a model hydrophobic surface and determined the isoelectric point (IEP) of four structurally different model proteins. Comparing the measured IEP of proteins at the PS/solution or air/solution interface with that determined in the bulk solution *via* zeta potential measurement, we found significant similarities between the IEP of surface adsorbed proteins and those in the bulk aqueous phase. The pH dependence behavior of proteins was correlated to their amino acid composition and degree of hydrophobicity.

Keywords: proteins, isoelectric point, sum frequency generation spectroscopy, surface hydrophobicity, zeta potential

OPEN ACCESS

Edited by:
Yoshihisa Harada,
University of Tokyo, Japan

Reviewed by:
Rekha Gaba,
DAV University, India
Ramon Castañeda-Priego,
University of Guanajuato, Mexico

****Correspondence:***
Saman Hosseinpour
saman.hosseinpour@fau.de
Wolfgang Peukert
wolfgang.peukert@fau.de

†These authors have contributed equally to this work and share first authorship

Specialty section:
This article was submitted to Physical Chemistry and Chemical Physics, a section of the journal Frontiers in Chemistry

Received: *21 May 2021*
Accepted: *19 July 2021*
Published: *30 July 2021*

Citation:
Lautenbach V, Hosseinpour S and Peukert W (2021) Isoelectric Point of Proteins at Hydrophobic Interfaces. Front. Chem. 9:712978. doi: 10.3389/fchem.2021.712978

INTRODUCTION

Proteins are flexible macromolecules that react sensitively to environmental conditions and external stimulators. For instance, alteration in physiological factors such as temperature, ion concentration, or pH often results in changes in the secondary or tertiary structure of proteins, their solubility, or colloidal stability (Sarkar et al., 2009; Maldonado-Valderrama et al., 2010). Moreover, the adsorption of proteins to different surfaces, e.g., cell membranes and implants in biological systems or pipings during industrial processing, is often accompanied by proteins' structural and conformational alterations (Yano, 2012; FaulónMarruecos et al., 2018; Mitra, 2020). These changes in protein structure not only affect protein functionality but also may trigger their abnormal folding. For instance, the hydrophobicity of cell membranes can initiate protein aggregation, which is assumed to be the cause of severe neuronal diseases such as Alzheimer's or Parkinson's disease (Beyer, 2007; Gonzalez-Garcia et al., 2021; Saghir et al., 2021). Similarly, in downstream processing and adsorption chromatography of proteins irreversible binding of proteins on commercially available hydrophobic adsorbents is accompanied by structural changes in proteins, a process that is influenced by solution pH (Millitzer et al., 2005).

Hence, molecular understanding of the protein behavior at different surfaces and interfaces is of great importance in many fields including biopharmaceutical development, drug targeting, development of implant materials, or biomembrane processing. So far numerous experimental and computational studies have been performed on model proteins such as serum albumin, beta-lactoglobulin, or lysozyme to unravel their specific interactions with different surfaces. Among many parameters that affect protein adsorption, conformation, and stability at different surfaces and interfaces, hydrophobic and electrostatic interactions are considered to be the main factors (van Dulm and Norde, 1983; Norde, 1996; McUmber et al., 2015). Upon interaction with a surface, proteins usually adopt a different conformation than those in the bulk solution, to minimize their free energy. For instance, Roach et al. (2005) showed that increased surface hydrophobicity increases the adsorption affinity of amphiphilic proteins and triggers structural changes. Meanwhile, electrostatic attraction or repulsion not only affect the adsorption of proteins on surfaces but also alters proteins' structural and conformational stability. The magnitude of electrostatic interactions between proteins and surfaces and between protein molecules can be altered either by the ionic content or the pH value of the surrounding medium. At pH values close to the isoelectric point (IEP), proteins possess a net neutral charge whereas at pH values above and below IEP they exhibit net negative and net positive charge, respectively. The IEP of proteins is strongly influenced by the composition of amino acids, their local distribution in protein structure, as well as the structural conformation of proteins. The latter, as was mentioned earlier, is dependent on the surfaces to which proteins adsorb.

In this work, we address the question of whether the adsorption of proteins at a hydrophobic solid surface leads to a change in electrostatic interactions and consequently to a shift in the isoelectric point of proteins. As previously mentioned, the adsorption as well as the structural and conformational stability of proteins are affected by important factors like electrostatic forces, the structure and dynamics of the hydration layer surrounding proteins, and hydrophobic interactions. However, characterization of protein properties at surfaces and interfaces is experimentally challenging and requires surface sensitive analytical tools to differentiate the overwhelming number of molecules in the bulk phase from those at surfaces and interfaces. Over the last decades, sum frequency generation (SFG) spectroscopy has proven to be a powerful tool for this purpose and SFG has been applied to study proteins at interfaces in numerous cases (Dreesen et al., 2004; Vidal and Tadjeddine, 2005; Zhang et al., 2013; Hosseinpour et al., 2020).

In this work, we present the SFG results of four proteins at the hydrophobic polystyrene (PS)/water interface to assess the polarity and magnitude of the electric field within the hydration shell of the adsorbed proteins on a solid hydrophobic surface. Accordingly, the IEP of each protein was precisely determined at the buried PS/solution interface, by analyzing the SFG spectra of each protein as a function of solution pH. Based on the previous studies on the IEP of proteins in the bulk solutions and at the liquid/air interface, in this study we have selected model proteins with very different hydrophobicity indices and bulk isoelectric points, as these parameters are expected to have the most dominant impacts on protein adsorption and restructuring at hydrophobic surfaces and interfaces.

The comparison between the measured IEP of proteins at the buried PS/solution interface and at the air/solution interface (Guckeisen et al., 2019) as well as with the IEP measured in the bulk solution *via* zeta potential showed significant similarities between the IEP of proteins in the bulk aqueous phase and those adsorbed at the air/liquid or solid/liquid interface.

MATERIALS AND METHODS

Protein Sample Preparation

For the determination of the IEP at the solid/liquid interface, four proteins were chosen, which differ in terms of their bulk IEP and hydrophobicity (see **Table 1**). Bovine serum albumin (BSA, A7030), hemoglobin (H7379), and lysozyme (L6876) were purchased from Sigma-Aldrich (St. Louis, Missouri, United States). Antifreeze protein type III (AFP III) was obtained from A/F Protein Inc., Waltham, United States. The proteins were used as received from the manufacturer with no further purification and protein solutions in concentrations of either 0.1 g/L, 1 g/L, or 2 g/L were prepared. The protein concentrations that are used are all below the solubility limit of the corresponding proteins (see **Table 1**). To keep the ionic strength constant, the desired amount of protein lyophilisate was dissolved in 10 mM NaCl (≥99.8%, Carl Roth GmbH, Karlsruhe, Germany) solution. A QUINTIX64-1S analytical lab balance with the measurement accuracy of 0.1 mg from Sartorius AG (Goettingen, Germany) was used. For each protein, different pH values were set between 1.7 and 11.3 by adding HCl (0.1 M Honeywell™ Fluka™, Thermo Fisher Scientific Inc., Schwerte Germany) and NaOH (0.1 M Merck KGaA, Darmstadt, Germany) to the solution. The pH was determined by a inoLab pH7110 pH meter from WTW (Xylem Analytics Germany Sales GmbH and Co. KG, Weilheim, Germany) equipped with an InLab-Micro-Pro-ISM pH electrode from Mettler Toledo GmbH (Greifensee, Switzerland).

Prism Coating with Polystyrene

For the investigation of the proteins on the hydrophobic surface, deuterated polystyrene (dPS, PolymereSource Inc., Dorval, Canada) was spin coated on a CaF_2 dove prism (Ma Teck GmbH, Jülich, Germany), following the procedure used by Wang et al. (2003). Before each coating, the prism was ultrasonically cleaned in toluene (≥99.5% VWR, Darmstadt, Germany), ethanol (≥99.8%, VWR, Darmstadt, Germany), and Alconox® (Alconox Inc., NY, United States) solution for 15 min each and finally rinsed with water. After this procedure, the prism was treated for 5 min in an O_2 plasma oven (Femto, Diener electronic GmbH + Co. KG, Ebhausen, Germany) in order to remove persistent contaminations from the surface. A stock solution of 2 w% dPS in deuterated toluene (≥99.00%, Sigma-Aldrich, St. Louis, Missouri, United States) was used to coat the prism. After fixing the prism on the spin coater (KLM

TABLE 1 | Different Protein properties and comparison of different IEP.

Protein property	BSA	Lysozyme	Hemoglobin	AFP III
UniPort ID	P02769	P00698	P69905/P68871	P12416
Molecular weight/kDa	66.5	14.4	64.5	9.4
α-helix content/%	47	20	56	-
β-sheet content/%	0	10	0	-
Solubility in water/mg ml−1	40[a]	10[a]	20[a]	20[b]
Aromatic amino acid content/%	8.4	9.3	8.4	1.5
Hydrophobicity index[c]	−0.43	−0.15	0.03	0.41
Theoretical IEP[d]	5.59[e]	8.37[e]	7.29	8.94
Bulk IEP (zeta potential)	5.1	10	7.1	6–8
Air/solution IEP (SFG)	5.5	7–9.5	6.5	8
dPS/solution IEP (SFG)[f]	5.5	8.3	7.0	6–8

[a]*Sigma Aldrich data sheets and*
[b]*manufacturers website.*
[c]*Hydrophobicity was calculated with GPMAW lite (Hoejrup).*
[d]*The theoretical IEPs were determined with an isoelectric point calculator (Kozlowski, 2016) from the proteins amino acid sequence given by the listed UniPort accession number.*
[e]*These calculated theoretical IEP values differ from the previously published ones (Guckeisen et al., 2019), because of the usage of different protein amino acid sequences.*
[f]*The uncertainties in the determination of the IEPs of the studied proteins include: the minor inaccuracy in protein concentration in the prepared solutions, the minor changes in the solution pH during data collection, the temporal fluctuations in the intensity of the IR and Vis beams during the SFG measurements, and the contribution of spectral noise in the determination of the minimum signal intensity. Attempts are made to minimize these possible inaccuracies during our measurements.*
The solubility values were obtained by the proteins

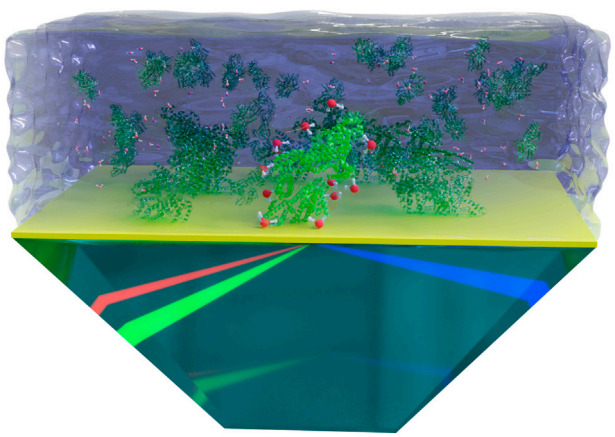

FIGURE 1 | A schematic representation of the SFG measurements in the TIR geometry. The dPS layer is depicted in yellow. Proteins and water molecules are depicted out of scale for better visualization. Note that the preferential adsorption sites and the possible rearrangement of proteins upon adsorption to the hydrophobic surface are not considered in this schematic figure.

Spin-Coater SCC, Schaefer Technologie GmbH, Langen, Germany) using a home built holder, 100 µl of dPS solution was added on the large flat side of the cleaned prism. The prism was rotated at 20 rotations per second for 5 s and the coated prism was dried overnight at room temperature. The cleanliness of the dPS layer was controlled by measuring the SFG response at the dPS-air interface in the C-H stretching spectral region.

Sum Frequency Generation Measurements

For the determination of the proteins' IEP at the interface, SFG spectra were obtained by a broadband SFG spectrometer, which is described in detail elsewhere (Beierlein et al., 2015; Braunschweig et al., 2016). The spatial and temporal overlap of an etalon-narrowed beam in the visible wavelength range [ω_{vis} = 800 nm, full width half maximum (FWHM) ≈ 10 cm^{-1}] and a femtosecond infrared beam (ω_{IR}, FWHM ≈ 200 cm^{-1}) generates an SFG signal ($\omega_{SFG} = \omega_{vis} + \omega_{IR}$). The IR wavelength was tuned in the frequency range of 2,800–3,800 cm^{-1} in five steps with 20 s acquisition time per step and accumulations of five for each spectrum. The SFG spectra of proteins on the surface of the dPS coated prism were collected at the total internal reflection (TIR) geometry (See **Figure 1**), enhancing the signal-to-noise ratio (Zhang et al., 2015). The dPS coated prism was fixed in a home built cell, which allows the change of the height, lateral position, and tilt of the sample surface with high precision. The height of the sample surface was controlled *via* a laser height sensor (LK-H052, Keyence Corporation, Osaka, Japan). For each protein, a set of different pH solutions were placed successively on top of the dPS coated CaF_2 prism. In order to exclude signal deviations due to the possible inhomogeneities in the dPS layer, the series of measurements for one protein were carried out on the same coated prism without changing the spot of the laser irradiation (i.e., without moving the sample). The intensity of the incoming laser beams and the duration of the signal acquisition were adjusted to ensure no laser induced sample damaging occurred during the measurements. All SFG measurements were performed in the SSP (S-polarized SFG signal, S-polarized visible beam, and P-polarized IR beam) polarization combination where S stands for perpendicular and P for parallel to the plane of incidence.

Zeta Potential Measurements

For the determination of the proteins' IEP in the bulk phase, the zeta potential for all protein solutions was measured with a Nano ZS Zetasizer instrument (Malvern Instruments, Herrenberg, Germany), in which a folded-capillary cuvette (Malvern Instruments, Malvern, Grovewood, United Kingdom) was used. The temperature was controlled at 25°C and the initial

equilibration time was set to 120 s. The zeta potential is correlated with the proteins' net surface charge (Keppler et al., 2021), hence, the pH value for which the measured zeta potential value reaches 0 mV was determined as the bulk IEP of the corresponding protein. Each sample was measured three times within one measurement cycle and the results were averaged.

RESULTS AND DISCUSSION

In this study, the IEP of four proteins BSA, lysozyme, AFP III, and hemoglobin were investigated in contact with a hydrophobic layer at the dPS-water interface, using SFG spectroscopy. The dPS layer represents an exemplary hydrophobic surface on which the proteins adsorb and react to the different solution pH values. As presented in **Table 1**, these proteins differ in terms of their IEP in the bulk and their hydrophobicity index, which are the main factors affecting their electrostatic and hydrophobic interactions, respectively. Other important characteristics of the studied proteins such as molecular weights and solubility as well as the content of α-helix and β-sheet in their structures are also provided in **Table 1**.

Based on the SFG spectroscopy selection rules, to obtain an SFG signal, molecules should reside in a non-centrosymmetric environment, must have a certain degree of order, and should contain vibrations that are simultaneously IR and Raman active. These selection rules provide SFG with an inherent surface sensitivity, which allows detecting surface adsorbed molecules without the inclusion of bulk molecules in the signal.

As demonstrated in **Eq. 1** the SFG signal intensity is a function of non-resonant *NR* and resonant *R* parts of the second-order nonlinear electric susceptibility $\chi^{(2)}$ and is proportional to the intensities of the fundamental incoming visible I_{vis} and infrared I_{IR} beams. (Richmond, 2002; Shen and Ostroverkhov, 2006; Zhang et al., 2013).

$$I_{SFG} \propto \left|\chi^{(2)}_{NR} + \chi^{(2)}_{R}\right|^2 . I_{vis}.I_{IR} \propto \left|\chi^{(2)}_{NR} + \sum_n \frac{A_n}{\omega_n - \omega_{IR} + i\Gamma_n}\right|^2 . I_{vis}.I_{IR} \quad (1)$$

The non-resonant portion of the SFG signal is frequency independent and the resonant part can be described as a function of the amplitude A_n, damping factor Γ_n, and the frequencies of the IR (ω_{IR}) and the nth vibrational mode (ω_n).

The mathematical relation between the oscillator strength A_n and the number N of contributing oscillators in **Eq. 2** further shows that the SFG signal intensity also scales with the number of ordered molecules at the surface.

$$A_n = Na_n \quad (2)$$

in which the angular brackets refer to an orientational average over all interfacial molecules and a_n describes the molecules' tensorial mode strength (Shen and Ostroverkhov, 2006). At the electrified surfaces, the interfacial potential ($\Phi(0)$) interacts with both $\chi^{(2)}$ and third-order susceptibility ($\chi^{(3)}$). However, for comparison of the SFG results with those published earlier (Guckeisen et al., 2019), here we make no distinction between the relative contribution of $\chi^{(2)}$ and $\chi^{(3)}$ and use effective $\chi^{(2)}$ for fitting our SFG spectra, as was utilized by Das et al. (Das et al., 2019).

Proteins at pH values above and below their corresponding IEP become negatively or positively charged, respectively. Accordingly, the polar water molecules surrounding proteins adopt a preferential H-up and H-down configuration, with respect to the protein surface. The larger electric field (i.e., proteins with higher net charge) hence aligns a greater number of water molecules with the same orientation resulting in an enhanced SFG signal (see **Eq. 2**).

Figure 2 shows the recorded SFG spectra of the investigated proteins as a function of the solution pH over a wavenumber range from 2,800 cm^{-1} to 3,600 cm^{-1}. Multiple vibrational modes can be recognized in this spectral region. Within the interval from 2,800 cm^{-1} to 3,000 cm^{-1}, the CH vibrations from the proteins side chain amino acids appear, the assignments of which have been provided elsewhere (Chen et al., 2007).

Another peak can be detected at ~3,060 cm^{-1}, which represents the so-called ring mode and originates from vibrations of the aromatic rings in amino acids such as phenylalanine, tryptophan, and tyrosine. This particular peak is expressed clearly for BSA, lysozyme, and hemoglobin, especially in predominantly acidic or basic pH regimes.

With increasing the solution pH, the ring mode peak undergoes a sign change (from a positive to a negative peak) and its amplitude passes zero during this transition. This observation is consistent with previous publications (Engelhardt et al., 2013; Guckeisen et al., 2019; Wang et al., 2002) and is a consequence of the interference between the proteins' ring mode vibration and interfacial water, which can be either constructive or destructive depending on the proteins' net charge (Guckeisen et al., 2019). The transition point of the sign of the ring mode peak is a first approximation for determining the IEP at the interface since the IEP describes the state at which the protein is net uncharged. The measured SFG spectra for AFP III, as demonstrated in **Figure 2**, do not show significant peak intensity of the ring mode over the whole pH range. Referring to **Table 1**, it becomes evident that the negligible ring mode SFG signal in the AFP III spectra correlated well with its relatively low content of aromatic amino acids. It should, nevertheless, be noted that the absolute orientation of the ring mode in the structure of proteins would also affect the intensity of the corresponding peaks in their SFG spectra (Naseri et al., 2018).

In the frequency region of 3,100 cm^{-1} to 3,600 cm^{-1}, broad vibrational modes are observed from the OH stretching vibrations of polar water molecules, which arrange themselves at the buried dPS/solution interface due to the charge state of the protein (Ohshima, 1995; Po and Senozan, 2001; Beierlein et al., 2015). As can be seen in **Figure 2**, the signal intensity in this frequency region is very sensitive to the change of the solution pH. According to **Eqs 1**, **2**, the SFG signal intensity at this frequency region is mainly influenced by the number density of the ordered interfacial molecules, whose extent of order can be triggered by the pH dependent charge of the proteins. In other words, the higher the absolute charge of proteins, the higher the intensity of the OH SFG signal intensity, because more polar water molecules similarly oriented at the buried dPS/solution interface. At extreme

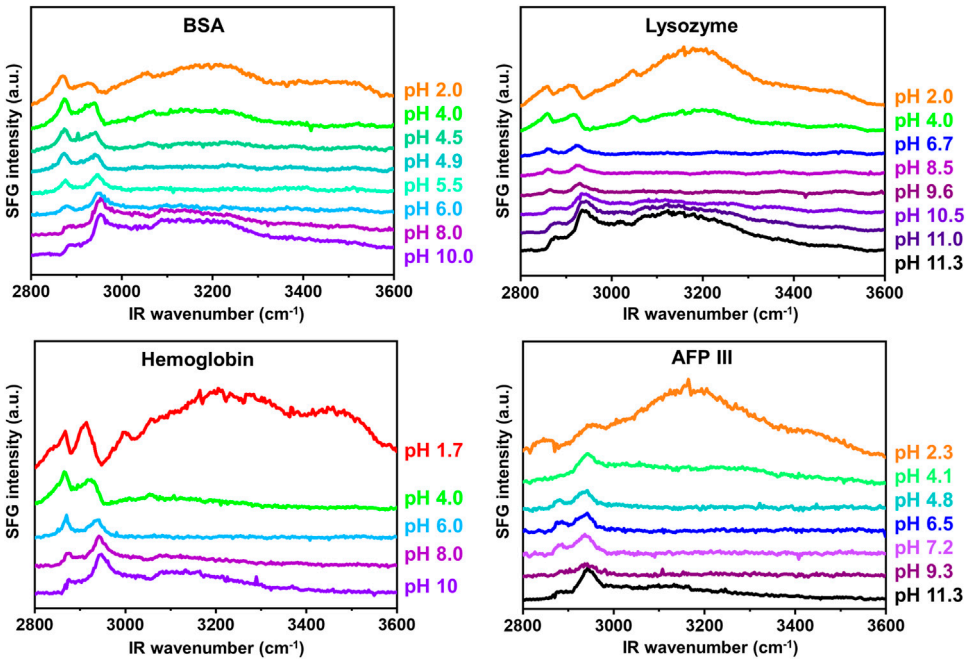

FIGURE 2 | pH dependent SFG spectra measured in ssp polarization combination in the wavenumber range of 2,800cm^{-1} and 3,600 cm^{-1}.

acidic solutions, in which the proteins are predominantly protonated and positively charged, the OH signal intensity reaches a maximum since a large number of water molecules are aligned with oxygen toward the protein at the buried dPS/solution interface. With increasing pH, the OH signal intensity first approaches a minimum and then reaches another maximum at extreme alkaline solutions.

To precisely determine the isoelectric point at the buried dPS/solution interface, the SFG spectra were integrated in the range of 3,100 cm^{-1} and 3,600 cm^{-1} and the results are provided in **Figure 3**. For all proteins, the integrated SFG signal intensity passes through a global minimum, which represents the IEP of the corresponding protein at the buried dPS/solution interface. For comparison, the pH dependent integrated SFG signal intensity of the same proteins at the air/solution interface is also shown in **Figure 3** [red curves, right *Y*-axis, reproduced from Guckeisen et al. (2019)]. As also tabulated in **Table 1**, a very good agreement exists between the measured IEPs of proteins at the dPS/solution interface and those at the air/solution interface. Interestingly, the measured IEPs of the surface adsorbed proteins (at either dPS/solution or the air/solution interfaces) do not differ from the corresponding theoretically calculated or measured IEPs *via* Zeta potential measurements (*vide infra*), which denotes that the electrostatic interactions in the studied proteins are independent of their local environment or the interface to which they adsorb.

Besides the general agreement in the IEPs of the surface adsorbed proteins, there are other similarities and some differences in the observed trends in the integrated SFG signal intensity of the proteins at the dPS/solution and the air/solution

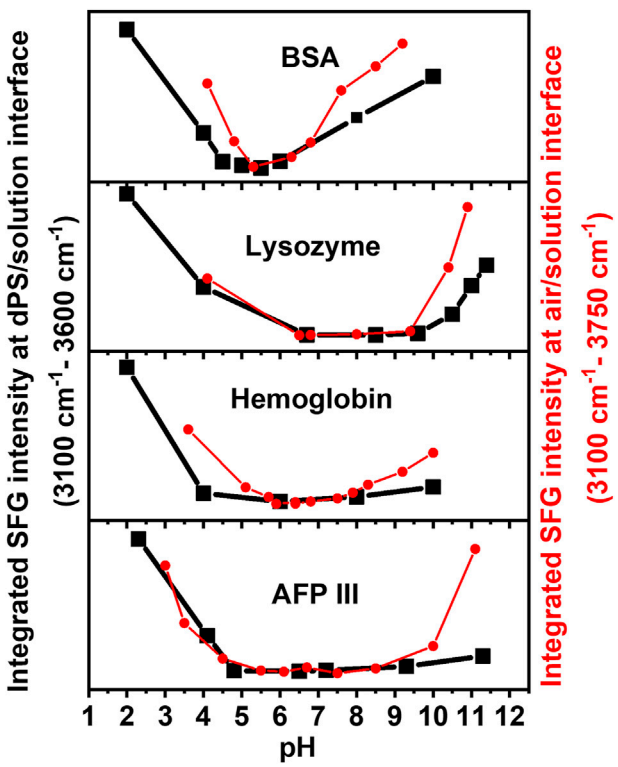

FIGURE 3 | Integrated SFG signal intensity in the range between 3,100 cm^{-1} and 3,600 cm^{-1} (at the buried dPS/solution interface, black) and between 3,100 cm^{-1} and 3750 cm^{-1} (at the air/solution interface, red) for four different proteins. The latter data are reproduced from (Guckeisen et al. (2019)). Adapted with permission from Langmuir 35 (14), 5004–5012. Copyright 2021 American Chemical Society.

interfaces (**Figure 3**, black and red curves). To some extent, the changes in the integrated SFG signal intensity above and below the IEP of the investigated proteins are asymmetrical, to some extent. Furthermore, the broadness of the region corresponding to the minimum integrated SFG signal (hereafter referred to as "minimum region") differs for different proteins; it is narrowest for BSA and broadest for AFP III at both the dPS/solution and the air/solution interfaces. The asymmetry of the curves and width of this "minimum region" in **Figure 3** correlates with the dissociation constant (pK_a) values of the individual ionizable amino acids in the proteins' primary structure and their structural stability. According to Pace et al., glutamate (Glu), aspartate (Asp), cysteine (Cys), tyrosine (Thr), histidine (His), lysine (Lys), and arginine (Arg) are the predominant ionizable amino acids, which with the exception of cysteine, all have a negative hydrophobicity index and thus belong to the polar amino acids. These amino acids are mainly located in the hydrophilic regions of the protein and are most likely to be in contact with the polar water (Pace et al., 2009; Kozlowski, 2016), as will be discussed in the following. Comparing the results in **Table 1** and **Figure 3**, the role of the amino acid composition of proteins and their hydrophobicity in determining the width of the "minimum region" becomes evident. Narrower "minimum regions" are observed for the proteins in which the pK_a of their constituent amino acids are close to each other. Moreover, proteins with a large negative hydrophobicity index (such as BSA) are composed of a higher proportion of polar amino acids and have a more symmetrical and narrower "minimum region." However, it is noticeable that the black curves (i.e., proteins at the buried dPS/solution interface) in **Figure 3** have a slightly flatter "minimum region" compared to the red curves (i.e., proteins at the air/solution interface), a phenomenon which is related to the less hydrophobic nature of air compared to dPS. A possible explanation for this behaviour could be the more pronounced conformational change in the proteins' structure after the adsorption to the dPS/solution interface. Upon adsorption to a surface, proteins tend to undergo structural changes to minimize their free energy (ΔG). For instance, the adsorption free energy of proteins is reduced by the displacement of the water molecules surrounding the nonpolar amino acid residues that interact with the nonpolar solid surfaces (Rabe et al., 2011; Latour, 2020; Mitra, 2020). As described by Rabe et al. (2011) and Rahimi et al. (2021), depending on the electrostatic interactions between the adsorbing proteins and substrate, as well as the density of the surface, different pathways of adsorption (e.g., cooperative or non-cooperative) can be expected. It is also discussed that proteins adsorb more strongly to hydrophobic surfaces than to hydrophilic surfaces.

The difference between the black and red curves in **Figure 3** is more dominant in the basic regime (especially for Lysozyme and AFP III), which is consistent with previous studies showing that proteins at the surface tend to undergo more structural changes in the basic pH regime than in the acidic solutions (Guckeisen et al., 2021).

The similarity between the IEP of the surface adsorbed proteins (either at the dPS/solution or at the air/solution interfaces) and those found in the bulk solution (see **Table 1**) can also be correlated to the role of hydrophobic side chain amino acids in proteins structure. As provided in this table, for each protein a theoretical hydrophobicity index can be calculated from the hydrophobicity of the individual amino acid constituents. Depending on the type and sequence of amino acids in a protein, they contribute with a negative or positive index to the total hydrophobicity index of the proteins. According to Kyte and Doolittle (1982), amino acids such as isoleucine and valine with a hydrophobicity index value of 4.5 and 4.2 have the highest hydrophobicity and arginine and lysine with the hydrophobicity index value −4.5 and −3.9 have the lowest hydrophobicity, respectively. Comparing the amino acid content in the structure of studied proteins, it became evident that BSA and Lysozyme contain a relatively small amount of hydrophobic amino acids, whereas hemoglobin and AFP III consist mainly out of the hydrophobic valine and are more hydrophobic. BSA and Lysozyme include more amino acids with negative hydrophobicity indices, which are preferably located in the hydrophilic part of the protein and therefore are more probable to come in contact with surrounding water molecules. Di Rienzo et al. developed a computational method to predict the hydrophobicity of amino acid side chains in proteins based on the orientation of surrounding water molecules. They defined four groups of amino acids by applying a principal component analysis and distinguish between negatively charged, positively charged, polar, and nonpolar amino acids. Accordingly, comparing the amino acid content of investigated proteins in this study, it is confirmed that hemoglobin and AFP III consists mainly out of hydrophobic amino acids whereas in BSA and Lysozyme most prevalent amino acids belong to the charged group (Di Rienzo et al., 2021).

In the bulk aqueous phase, hydrophobic amino acids of proteins are preferentially localized in the hydrophobic inner part of the protein, away from the surrounding water molecules (Janin, 1979). Similarly, at both dPS/solution interface and air/solution interface, primary interactions take place between the nonpolar parts of the protein and the hydrophobic interface. Therefore, the hydrophobic side chains of the surface adsorbed proteins protrude toward the hydrophobic phase (i.e., dPS or air, respectively), whereas the hydrophilic side chains face toward polar water molecules. Hence, these hydrophilic amino acids contribute the most to the electrostatic interactions with the surrounding medium or with other protein molecules, whereas the shielded hydrophobic amino acids (in the core of bulk proteins, or those protruding to hydrophobic dPS or air) do not come into the direct contact with water and have minor effects on the overall electrostatic interactions in protein systems. Indeed, reorientation of the proteins and the change in their secondary and tertiary structure are also plausible under these conditions to minimize the overall free energy of the system. Using coarse grain protein simulations, Zhao and Cieplak show that proteins are twisted at both air/solution and oil/solution interface and support the explanation for the equality of the IEPs given in this paper (Cieplak et al., 2014; Zhao and Cieplak, 2017).

CONCLUSION

In this study, we utilized an inherently surface sensitive nonlinear spectroscopic tool, sum frequency generation (SFG) spectroscopy, to assess the impact of solution pH on selected model proteins adsorbed at a solid hydrophobic surface. Deuterated polystyrene (dPS) was used as a model hydrophobic surface and the changes in the polarity and magnitude of the induced electric field at the dPS/

solution interface were utilized as a function of the solution pH to determine the IEP of surface adsorbed proteins.

The measured IEPs for proteins adsorbed to the dPS/solution interface were comparable to those at the air/solution interface and IEPs measured for proteins in the bulk solution. The IEP of proteins and the trends in the change of the electrostatic interactions in proteins as a function of solution pH were described based on the amino acid content and hydrophobicity of the studied proteins. Our results indicate that the IEP of proteins is mainly dependent on the polar amino acids in their structure, which are similarly accessible to surrounding water molecules in the bulk solution and at the PS/solution or air/solution interface, despite the possible reorganization of proteins and changes in their secondary structure upon adsorption to hydrophobic interfaces.

DATA AVAILABILITY STATEMENT

The datasets presented in this study can be found in online repositories. The names of the repository/repositories and accession number(s) can be found below: https://www.uniprot.org/, BSA: P02769 Lsyozyme: P00698 Hemoglobin: P69905/P68871 AFP III: P12416.

AUTHOR CONTRIBUTIONS

VL: Investigation, Formal analysis, Writing Original Draft, Visualization. SH: Conceptualization, Writing Original Draft, Review and Editing, Visualization, Supervision. WP: Funding acquisition, Review and Editing, Supervision, Resources.

ACKNOWLEDGMENTS

The authors gratefully thank the financial support provided by the German Research Foundation (DFG) priority program, SPP 1934 "DiSPBiotech–Dispersity, structural, and phase modifications of proteins and biological agglomerates in biotechnological processes" and the Cluster of Excellence Engineering of Advanced Materials–Hierarchical Structure Formation for Functional Devices (EAM).

REFERENCES

Beierlein, F. R., Clark, T., Braunschweig, B., Engelhardt, K., Glas, L., and Peukert, W. (2015). Carboxylate Ion Pairing with Alkali-Metal Ions for β-Lactoglobulin and its Role on Aggregation and Interfacial Adsorption. *J. Phys. Chem. B* 119 (17), 5505–5517. doi:10.1021/acs.jpcb.5b01944

Beyer, K. (2007). Mechanistic Aspects of Parkinson's Disease: α-synuclein and the Biomembrane. *Cell Biochem Biophys* 47 (2), 285–299. doi:10.1007/s12013-007-0014-9

Braunschweig, B., Schulze-Zachau, F., Nagel, E., Engelhardt, K., Stoyanov, S., Gochev, G., et al. (2016). Specific Effects of Ca2+ions and Molecular Structure of β-lactoglobulin Interfacial Layers that Drive Macroscopic Foam Stability. *Soft matter* 12 (27), 5995–6004. doi:10.1039/c6sm00636a

Chen, X., Sagle, L. B., and Cremer, P. S. (2007). Urea Orientation at Protein Surfaces. *J. Am. Chem. Soc.* 129 (49), 15104–15105. doi:10.1021/ja075034m–15105

Cieplak, M., Allan, D. B., Leheny, R. L., and Reich, D. H. (2014). Proteins at Air-Water Interfaces: a Coarse-Grained Model. *Langmuir* 30 (43), 12888–12896. doi:10.1021/la502465m

Das, S., Bonn, M., and Backus, E. H. G. (2019). The surface affinity of cations depends on both the cations and the nature of the surface. *J. Chem. Phys.* 150, 44706. doi:10.1063/1.5065075

Di Rienzo, L., Miotto, M., Bò, L., Ruocco, G., Raimondo, D., and Milanetti, E. (2021). Characterizing Hydropathy of Amino Acid Side Chain in a Protein Environment by Investigating the Structural Changes of Water Molecules Network. *Front. Mol. Biosci.* 8, 626837. doi:10.3389/fmolb.2021.626837

Dreesen, L., Humbert, C., Sartenaer, Y., Caudano, Y., Volcke, C., Mani, A. A., et al. (2004). Electronic and Molecular Properties of an Adsorbed Protein Monolayer Probed by Two-Color Sum-Frequency Generation Spectroscopy. *Langmuir* 20 (17), 7201–7207. doi:10.1021/la0488001

Engelhardt, K., Lexis, M., Gochev, G., Konnerth, C., Miller, R., Willenbacher, N., et al. (2013). pH Effects on the Molecular Structure of β-Lactoglobulin Modified Air-Water Interfaces and its Impact on Foam Rheology. *Langmuir* 29 (37), 11646–11655. doi:10.1021/la402729g

Faulón Marruecos, D., Schwartz, D. K., and Kaar, J. L. (2018). Impact of Surface Interactions on Protein Conformation. *Curr. Opin. Colloid Interf. Sci.* 38, 45–55. doi:10.1016/j.cocis.2018.08.002

Gonzalez-Garcia, M., Fusco, G., and De Simone, A. (2021). Membrane Interactions and Toxicity by Misfolded Protein Oligomers. *Front. Cel Dev. Biol.* 9 (2021), 642623. doi:10.3389/fcell.2021.642623

Guckeisen, T., Hosseinpour, S., and Peukert, W. (2021). Effect of pH and Urea on the Proteins Secondary Structure at the Water/air Interface and in Solution. *J. Colloid Interf. Sci.* 590, 38–49. doi:10.1016/j.jcis.2021.01.015

Guckeisen, T., Hosseinpour, S., and Peukert, W. (2019). Isoelectric Points of Proteins at the Air/Liquid Interface and in Solution. *Langmuir* 35 (14), 5004–5012. doi:10.1021/acs.langmuir.9b00311

Hoejrup, P. GPMAW Lite. Available at: https://www.alphalyse.com/gpmaw-bioinformatics-tool/start-gpmaw-lite/. (Accessed May 21, 2021).

Hosseinpour, S., Roeters, S. J., Bonn, M., Peukert, W., Woutersen, S., and Weidner, T. (2020). Structure and Dynamics of Interfacial Peptides and Proteins from Vibrational Sum-Frequency Generation Spectroscopy. *Chem. Rev.* 120 (7), 3420–3465. doi:10.1021/acs.chemrev.9b00410

Janin, J. (1979). Surface and inside Volumes in Globular Proteins. *Nature* 277 (5696), 491–492. doi:10.1038/277491a0

Keppler, J. K., Heyse, A., Scheidler, E., Uttinger, M. J., Fitzner, L., Jandt, U., et al. (2021). Towards Recombinantly Produced Milk Proteins: Physicochemical and Emulsifying Properties of Engineered Whey Protein Beta-Lactoglobulin Variants. *Food Hydrocolloids* 110 (4), 106132. doi:10.1016/j.foodhyd.2020.106132

Kozlowski, L. P. (2016). IPC - Isoelectric Point Calculator. *Biol. Direct* 11 (1), 55. doi:10.1186/s13062-016-0159-9

Kyte, J., and Doolittle, R. F. (1982). A Simple Method for Displaying the Hydropathic Character of a Protein. *J. Mol. Biol.* 157 (1), 105–132. doi:10.1016/0022-2836(82)90515-0

Latour, R. A. (2020). Fundamental Principles of the Thermodynamics and Kinetics of Protein Adsorption to Material Surfaces. *Colloids Surf. B: Biointerfaces* 191, 110992. doi:10.1016/j.colsurfb.2020.110992

Maldonado-Valderrama, J., Miller, R., Fainerman, V. B., Wilde, P. J., and Morris, V. J. (2010). Effect of Gastric Conditions on β-Lactoglobulin Interfacial Networks: Influence of the Oil Phase on Protein Structure. *Langmuir* 26 (No. 20), 15901–15908. doi:10.1021/la102294u

McUmber, A. C., Randolph, T. W., and Schwartz, D. K. (2015). Electrostatic Interactions Influence Protein Adsorption (But Not Desorption) at the Silica-Aqueous Interface. *J. Phys. Chem. Lett.* 6 (13), 2583–2587. doi:10.1021/acs.jpclett.5b00933

Millitzer, M., Wenzig, E., and Peukert, W. (2005). Adsorption Isotherms and Irreversible Binding of Proteins on Commercially Available Hydrophobic Adsorbents. *Chem. Eng. Technol.* 28 (7), 756–761. doi:10.1002/ceat.200500072

Mitra, Sankar. P. (2020). Protein Adsorption on Biomaterial Surfaces: Subsequent Conformational and Biological Consequences -A Review. *J. Surf. Sci. Technol.* 36, 7–38. doi:10.18311/jsst/2020/23282

Naseri, E., Hajisafari, M., Kosari, A., Talari, M., Hosseinpour, S., and Davoodi, A. (2018). Inhibitive Effect of Clopidogrel as a green Corrosion Inhibitor for Mild Steel; Statistical Modeling and Quantum Monte Carlo Simulation Studies. *J. Mol. Liquids* 269 (4), 193–202. doi:10.1016/j.molliq.2018.08.050

Norde, W. (1996). Driving Forces for Protein Adsorption at Solid Surfaces. *Macromolecular Symposia* 103 (1), 5–18. doi:10.1002/masy.19961030104

Ohshima, H. (1995). Electrophopretic Mobility of Soft Particles. *Electrophoresis* 16 (8), 1360–1363. doi:10.1002/elps.11501601224

Pace, C. N., Grimsley, G. R., and Scholtz, J. M. (2009). Protein Ionizable Groups: pK Values and Their Contribution to Protein Stability and Solubility. *J. Biol. Chem.* 284 (20), 13285–13289. doi:10.1074/jbc.R800080200

Po, H. N., and Senozan, N. M. (2001). The Henderson-Hasselbalch Equation: Its History and Limitations. *J. Chem. Educ.* 78 (11), 1499. doi:10.1021/ed078p1499

Rabe, M., Verdes, D., and Seeger, S. (2011). Understanding Protein Adsorption Phenomena at Solid Surfaces. *Adv. Colloid Interf. Sci.* 162 (1-2), 87–106. doi:10.1016/j.cis.2010.12.007

Rahimi, E., Offoiach, R., Hosseinpour, S., Davoodi, A., Baert, K., Lutz, A., et al. (2021). Effect of Hydrogen Peroxide on Bovine Serum Albumin Adsorption on Ti6Al4V alloy: A Scanning Kelvin Probe Force Microscopy Study. *Appl. Surf. Sci.* 563 (1), 150364. doi:10.1016/j.apsusc.2021.150364

Richmond, G. L. (2002). Molecular Bonding and Interactions at Aqueous Surfaces as Probed by Vibrational Sum Frequency Spectroscopy. *Chem. Rev.* 102 (8), 2693–2724. doi:10.1021/cr0006876

Roach, P., Farrar, D., and Perry, C. C. (2005). Interpretation of Protein Adsorption: Surface-Induced Conformational Changes. *J. Am. Chem. Soc.* 127 (22), 8168–8173. doi:10.1021/ja042898o

Saghir, A. E., Farrugia, G., and Vassallo, N. (2021). The Human Islet Amyloid Polypeptide in Protein Misfolding Disorders: Mechanisms of Aggregation and Interaction with Biomembranes. *Chem. Phys. Lipids* 234 (2021), 105010. doi:10.1016/j.chemphyslip.2020.105010

Sarkar, A., Goh, K. K. T., and Singh, H. (2009). Colloidal Stability and Interactions of Milk-Protein-Stabilized Emulsions in an Artificial Saliva. *Food Hydrocolloids* 23 (No. 5), 1270–1278. doi:10.1016/j.foodhyd.2008.09.008

Shen, Y. R., and Ostroverkhov, V. (2006). Sum-frequency Vibrational Spectroscopy on Water Interfaces: Polar Orientation of Water Molecules at Interfaces. *Chem. Rev.* 106 (4), 1140–1154. doi:10.1021/cr040377d

van Dulm, P., and Norde, W. (1983). The Adsorption of Human Plasma Albumin on Solid Surfaces, with Special Attention to the Kinetic Aspects. *J. Colloid Interf. Sci.* 91 (1), 248–255. doi:10.1016/0021-9797(83)90329-6

Vidal, F., and Tadjeddine, A. (2005). Sum-frequency Generation Spectroscopy of Interfaces. *Rep. Prog. Phys.* 68 (5), 1095–1127. doi:10.1088/0034-4885/68/5/R03

Wang, J., Buck, S. M., and Chen, Z. (2002). Sum Frequency Generation Vibrational Spectroscopy Studies on Protein Adsorption. *J. Phys. Chem. B* 106 (44), 11666–11672. doi:10.1021/jp021363j

Wang, J., Even, M. A., Chen, X., Schmaier, A. H., Waite, J. H., and Chen, Z. (2003). Detection of Amide I Signals of Interfacial Proteins *In Situ* Using SFG. *J. Am. Chem. Soc.* 125 (33), 9914–9915. doi:10.1021/ja036373s

Yano, Y. F. (2012). Kinetics of Protein Unfolding at Interfaces. *J. Phys. Condens. Matter* 24 (50), 503101. doi:10.1088/0953-8984/24/50/503101

Zhang, C., Jasensky, J., and Chen, Z. (2015). Multireflection Sum Frequency Generation Vibrational Spectroscopy. *Anal. Chem.* 87 (16), 8157–8164. doi:10.1021/acs.analchem.5b00641

Zhang, C., Myers, J. N., and Chen, Z. (2013). Elucidation of Molecular Structures at Buried Polymer Interfaces and Biological Interfaces Using Sum Frequency Generation Vibrational Spectroscopy. *Soft matter* 9, 4738–4761. doi:10.1039/C3SM27710K

Zhao, Y., and Cieplak, M. (2017). Proteins at Air-Water and Oil-Water Interfaces in an All-Atom Model. *Phys. Chem. Chem. Phys.* 19 (36), 25197–25206. doi:10.1039/c7cp03829a

Conflict of Interest: The authors declare that the research was conducted in the absence of any commercial or financial relationships that could be construed as a potential conflict of interest.

Publisher's Note: All claims expressed in this article are solely those of the authors and do not necessarily represent those of their affiliated organizations, or those of the publisher, the editors and the reviewers. Any product that may be evaluated in this article, or claim that may be made by its manufacturer, is not guaranteed or endorsed by the publisher.

frontiers in Chemistry

ORIGINAL RESEARCH
published: 17 August 2021
doi: 10.3389/fchem.2021.717167

Gate Alignment of Liquid Water Molecules in Electric Double Layer

*Xiaoqun Li, Xin Lin, Ying Li and Wei-Tao Liu**

Physics Department, State Key Laboratory of Surface Physics, Key Laboratory of Micro and Nano Photonic Structures [Ministry of Education (MOE)], Fudan University, Shanghai, China

The behavior of liquid water molecules near an electrified interface is important to many disciplines of science and engineering. In this study, we applied an external gate potential to the silica/water interface via an electrolyte-insulator-semiconductor (EIS) junction to control the surface charging state. Without varying the ionic composition in water, the electrical gating allowed an efficient tuning of the interfacial charge density and field. Using the sum-frequency vibrational spectroscopy, we found a drastic enhancement of interfacial OH vibrational signals at high potential in weakly acidic water, which exceeded that from conventional bulk-silica/water interfaces even in strong basic solutions. Analysis of the spectra indicated that it was due to the alignment of liquid water molecules through the electric double layer, where the screening was weak because of the low ion density. Such a combination of strong field and weak screening demonstrates the unique tuning capability of the EIS scheme, and would allow us to investigate a wealth of phenomena at charged oxide/water interfaces.

Keywords: oxide interface, water interface, electric double layer, electrochemical gating, sum frequency vibrational spectroscopy, field alignment of water

OPEN ACCESS

Edited by:
Hideki Seto,
High Energy Accelerator Research Organization, Japan

Reviewed by:
Satoshi Nihonyanagi,
RIKEN, Japan
Yuka Ikemoto,
Japan Synchrotron Radiation Research Institute, Japan

****Correspondence:***
Wei-Tao Liu
wtliu@fudan.edu.cn

Specialty section:
This article was submitted to Physical Chemistry and Chemical Physics, a section of the journal Frontiers in Chemistry

Received: *30 May 2021*
Accepted: *02 August 2021*
Published: *17 August 2021*

Citation:
Li X, Lin X, Li Y and Liu W-T (2021) Gate Alignment of Liquid Water Molecules in Electric Double Layer. Front. Chem. 9:717167. doi: 10.3389/fchem.2021.717167

INTRODUCTION

The oxides/water interfaces are ubiquitous in nature, and are important to an enormous range of fields including environmental science, geoscience, catalysis, etc (Putnis, 2014; Covert and Hore, 2016; Schaefer et al., 2018). At these interfaces, oxide surface lattices react with vicinal water molecules, forming charged surface groups that may only be stable in aqueous environments, and lead to the formation of electric double layers (EDL) (Brown, 2001; Gaigeot et al., 2012; Sulpizi et al., 2012; Brown et al., 2016; Boily et al., 2019). The rich phenomena and functionalities of oxide/water interfaces are largely based on their interfacial charging states and properties of EDLs (Brown, 2001; Putnis, 2014; Covert and Hore, 2016; Ohno et al., 2016; Schaefer et al., 2018). For example, the water electric dipole moment can be aligned by the electrostatic field in EDL and affect the interfacial chemistry (Brown, 2001; Nihonyanagi et al., 2004; Aragones et al., 2011; Saitta et al., 2012; Brown et al., 2016; Montenegro et al., 2021). In the case of ice, such field alignment could give rise to a ferroelectric state of highly oriented water molecules, which was readily probed using the surface-sensitive sum-frequency vibrational spectroscopy (SFVS) (Miranda et al., 1998; Verdaguer et al., 2006; Anim-Danso et al., 2016). Whether similar states exist or not in the liquid phase has remained unclear. One problem is that, to achieve a strong polar ordering of water in EDLs, it requires a large electrostatic field thus a high surface charge density on the solid surface. Meanwhile, the surface charge density was usually tuned through protonation/deprotonation of surface lattices by varying the water pH value (Brown et al., 2016). Unfortunately, many oxide/water interfaces have their point-zero-charge (pzc) near neutral pH (Kosmulski, 2002; Backus et al., 2020), hence cannot reach very

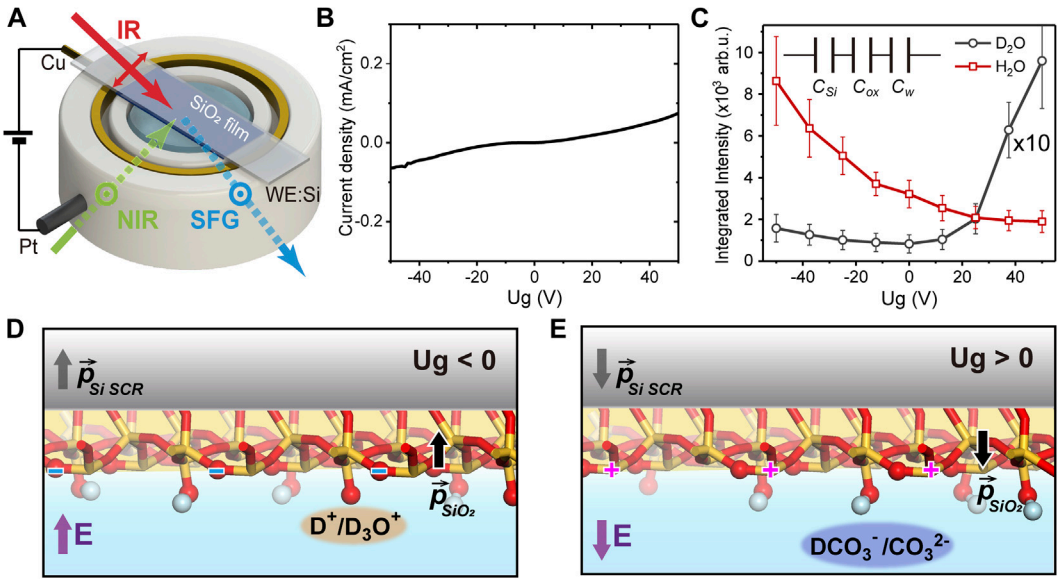

FIGURE 1 | (A) Sketch of the experimental geometry. **(B)** The leak current versus the gate potential (U_g). **(C)** The gate-dependent spectrally-integrated SFVS signal in D_2O (black, magnified by 10 times) and H_2O (red). Inset: the capacitor-in-series model of the junction. Sketches of the interfacial structure in D_2O experiments at **(D)** $U_g < 0$ and **(E)** $U_g > 0$.

high surface charge density. The amorphous silicon dioxide (SiO_2, silica) in water has a low pzc value of around pH 2~3, thus can reach a high density of negative charges in strong basic solutions. However, the ion concentration in water is then inevitably large, which screens the surface field and reduces the EDL thickness (Jena et al., 2011; DeWalt-Kerian et al., 2017). In our previous study (Wang et al., 2019), we demonstrated a new scheme to control the oxide surface charging state utilizing an electrolyte-insulator-semiconductor (EIS) junction (Waleed Shinwari et al., 2007). The scheme allowed us to tune the surface charge and field without varying the electrolyte ionic composition, which provided a new dimension to control the charged solid/liquid interfaces. Nonetheless, the native oxide used before withstood only small gate potential and exhibited large leak current due to defects, which limited its tunability of the surface charging state.

In the present work, we utilized a much thicker SiO_2 film of ~100 nm that allowed the application of +/−50 V of gate potential, in contrast to the +/−1 V in the previous case. The thicker film also had a much smaller capacitance, leading to a much greater potential drop and stronger electric polarization across the film, as well as a higher net surface charge density. We used SFVS to investigate OH stretching vibrational spectra from the SiO_2 interface in neutral water (exposed to the atmosphere). From zero potential to −50 V on the silicon electrode, we observed a drastic enhancement of the interfacial OH signal, which even exceeded that observed at the bulk-silica/water interfaces in strong basic solutions (Ostroverkhov et al., 2004, 2005; DeWalt-Kerian et al., 2017). The silica/water interface can be strongly negatively charged at high pH, which supposedly would induce a highly ordered interfacial water structure (Ostroverkhov et al., 2004; 2005). The greater OH intensity in our case suggested that external gating can lead to an even higher degree of polar ordering in the OH structure. Toward more positive gate potential, the OH signal dropped asymmetrically, exhibiting similar spectral profiles to those from bulk-silica/water interfaces at low pH values. Combined with fitting results, we attributed the observation to an effective field alignment of water molecules inside the diffuse layer. Because the ion density remained low in our case, the electrostatic screening of the surface field was poor, and the long-range alignment of water molecules could be readily detected. Basically, our study demonstrated the unique tuning capability of aqueous oxide interfaces by externally gating the EIS junction, and allowed us to achieve an overall greater polar alignment of interfacial water molecules compared to that achievable *via* conventional means.

MATERIALS AND METHODS

Sample and Chemicals

The experimental and sample geometries were sketched in **Figure 1A**. The silicon (Si) substrate was in contact with a copper ring as the gate electrode, and a platinum wire in water serving as the ground (GND). A silicon dioxide (SiO_2) thin film of about ~100 nm-thick was deposited through magnetron sputtering procedure (DE500 Sputter) on the silicon wafer (0.5 mm-thick Si (100), n-doped, resistivity: 1–10 Ω cm). A source meter (Keithley 2400) was used to control the gate potential (U_g) and measure the leak current between the two electrodes. **Figure 1B** shows the leak current versus U_g from a test sample. Within U_g of −50 ~ +50 V, the leak current was small and almost increased linearly with U_g, without

any sudden jump indicating breakdown of the oxide film. We thus limited U_g between −50 and +50 V in the present study.

Prior to all SF measurements, the thin-film sample was calcinated in UV ozone (BZS250GF-TC) for ~1 h, then soaked in nonchromix/H_2SO_4 mixture (4 g nonchromix/100 ml H_2SO_4) for ~0.5 h and rinsed thoroughly with deionized water (18.2 MΩ cm, Thermo Scientific Barnstead MicroPure UV). Besides, the Teflon cell was ultrasonicated successively in acetone, ethanol, and deionized water. Ultrapure deionized water and deuterated water (Sigma Aldrich, 99.9 atom % D) were used in the experiment.

Laser and Optical System

A regenerative amplifier (Spitfire, Spectra-Physics) seeded by a Ti: sapphire oscillator (MaiTai SP, Spectra-Physics) was used to produce about 7 W of 800 nm, 35 fs pulses at a 2 kHz repetition rate. Around 40% output beam was used to generate a broadband IR beam (~500 cm^{-1}) centered at about 3,300 cm^{-1} by pumping an TOPAS-C/DFG system (Spectra-Physics), while the rest of the output beam was used to generate a narrowband beam (NIR) of ~3 nm bandwidth by passing through an interference filter (LL01-808-25, Semrock). The NIR and IR beams were then focused and overlapped at the silica/water interface with incident angles of 45° and 60° (in air), respectively. The generated SFG signal was detected by a spectrograph (Acton SP300i, Princeton Instruments) and CCD camera (PyLoN: 400BR eXcelon, Princeton Instruments). All SF experiments were conducted in the atmosphere and room temperature. The beam polarization combination used was SSP (S for the SF beam, S for NIR, and P for IR).

Electrical System

The operation principle of the electrolyte-insulator-semiconductor junction was described elsewhere (Waleed Shinwari et al., 2007; Wang et al., 2019). In a simplified representation, the Si/SiO_2/water EIS junction can be modelled as three capacitors in series [C_{Si}, C_{ox} and C_w (water), see insert of **Figure 1C**], with the respective capacitances per unit area being $C_i \sim \varepsilon_0\varepsilon_{ri}/d_i$ (i = *Si, ox, w*). ε_0 is the vacuum permittivity, ε_{ri} and d_i are the dielectric constant and effective thickness of the ith layer, respectively. The charge density on each plate of the capacitors can be estimated *via* $\sigma \sim U_g C_{\text{tot}} = \Delta\phi_i C_i$, from which the potential drop on the ith layer ($\Delta\phi_i$) could be obtained. The electrostatic field across each layer is then $E_i \sim \Delta\phi_i/d_i$. Compared to our previous study (Wang et al., 2019), the SiO_2 film in this case was much thicker, leading to a much smaller C_{ox}. The potential drop was then mostly on the oxide film (~64%) instead of mostly on Si (Wang et al., 2019), which caused the electrostatic field as well as the dielectric polarization in the oxide layer to be much greater. The large polarization further led to a high surface density of bound charges that distributed on both oxygen and silicon sites (Jackson, 1999). This is also different from the previous case, where all surface charges were assumed to result from the protonation/deprotonation reactions (Wang et al., 2019). With $C_{Si} \sim 0.065\,\mu F/cm^2$, $C_w \sim 12\,\mu F/cm^2$ [effective capacitances deduced from (Wang et al., 2019)], and d_{ox} = 100 nm, $\varepsilon_{rSi} \sim 12$, $\varepsilon_{rox} = 3.9$, and $\varepsilon_{rw} \sim 80$, we estimated that at $U_g \sim 50$ V, the total surface charge density on oxide is ~0.07 e/nm^2 (e refers to the elementary charge), and the electrostatic field within the interfacial water layer is about 4–16 mV/nm (between the two extreme cases when all charges are assumed to be reactive or bounded). Both were much greater than those achieved before, thus allowed us to investigate a much broader range of phenomena.

Basics of SFVS

The basic principle of SFG was described elsewhere (Tian and Shen, 2014). As in a typical SFVS experiment, an infrared (IR) and a near infrared (NIR) beam are overlapped at the interface and generate a sum-frequency (SF) signal with a frequency of $\omega_{SF} = \omega_{NIR} + \omega_{IR}$. The total SF signal intensity is:

$$I_{SF} \propto \left| \overleftrightarrow{\chi}^{(2)}_{eff} : \vec{E}(\omega_{NIR})\,\vec{E}(\omega_{IR}) \right|^2 \tag{1}$$

where $\overleftrightarrow{\chi}^{(2)}_{eff}$ is the effective second-order nonlinear susceptibility tensor of the system, and $\vec{E}$'s are the electric field vectors at the corresponding frequency. In our measurements in the OH stretching vibrational frequency range, the $\chi^{(2)}_{eff}$ was contributed from both the resonant part from interfacial OH bonds, as well as the non-resonant (NR) part from Si SCR and elsewhere in the Si/SiO_2/water junction (Liu et al., 2019; Wang et al., 2019), which could be expressed as

$$\chi^{(2)}_{eff} = \chi^{(2)}_R + \chi^{(2)}_{NR}, \chi^{(2)}_R = \sum_q \frac{A_q}{\omega - \omega_q + i\Gamma_q} \tag{2}$$

with A_q, ω_q, Γ_q corresponding to the amplitude, frequency and the damping coefficient of the qth resonance mode, respectively.

RESULTS AND DISCUSSION

SFVS in D_2O as References

As mentioned above, the total SF response consisted of both non-resonant and resonant contributions. For references, we first filled the cell with D_2O and took SF spectra in the OH stretching vibrational range. Since D_2O yields negligible signal within this range (Nihonyanagi et al., 2011; Myalitsin et al., 2016), we could therefore single out the non-resonant response (Wang et al., 2019). **Figure 1C** presented the gate-dependent, spectrally-integrated SF signal with D_2O. In the previous study, for U_g between −1 and +1 V, the integrated non-resonant signal exhibited a quadratic dependence on U_g as expected for the electric-field-induced response from Si SCR (Lüpke, 1999; Wang et al., 2019), which almost vanished near the flat-band potential, and grew symmetrically around it (Wang et al., 2019). Yet here, within a much greater potential range between −50 and +50 V, the non-resonant SF signal was no longer quadratic, nor symmetric, with respect to U_g (**Figure 1C**) (Bian et al., 2018). The minimum still appeared near $U_g \sim 0$, but the signal grew faster toward positive U_g compared to negative U_g. This obvious deviation from a pure electric-field-induced behavior indicated that the non-resonant signal from other parts of the junction must be taken into accounts. Since the polarization of the SiO_2

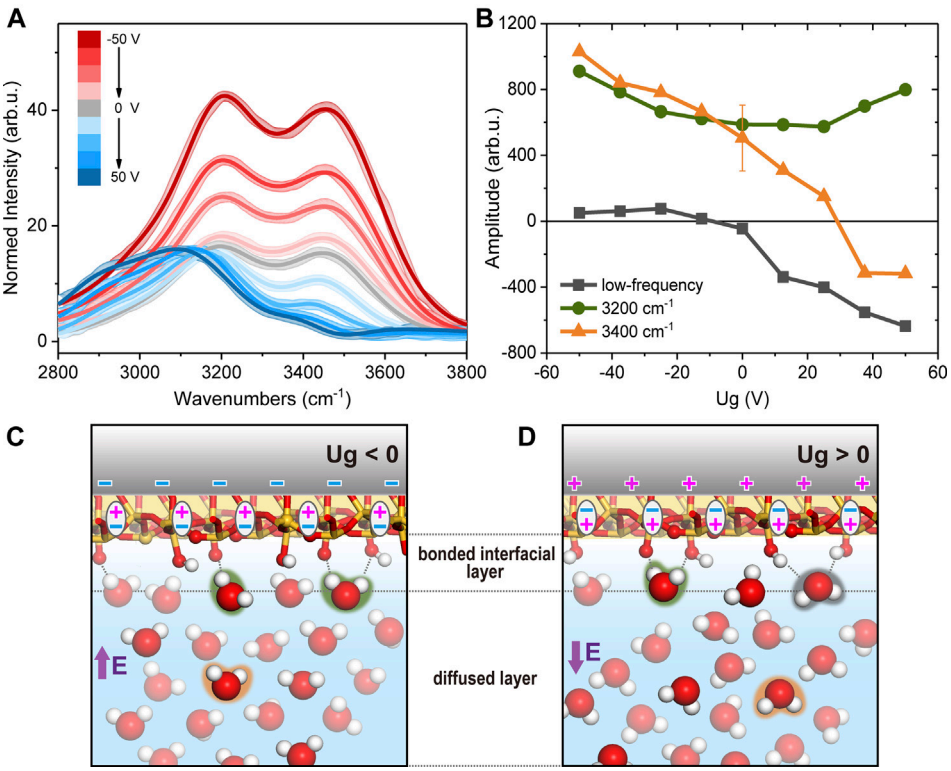

FIGURE 2 | (A) Normalized SFVS spectra in H_2O. Solid curves are fits. **(B)** Fitted amplitudes of the low frequency mode (black square), 3,200 cm^{-1} (green circle) and 3,400 cm^{-1} (orange triangle) modes. Sketches of the interfacial structures in H_2O when **(C)** $U_g < 0$ and **(D)** $U_g > 0$.

film and the charge density at SiO_2/water interface are both much greater than those in the previous study, they can also contribute to the overall non-resonant response. We then attribute the deviation from quadratic response to the asymmetric interaction between the SiO_2 surface and ionic species in the electrolyte at positive/negative U_g. The water solution we used is weakly acidic (pH 5.8) due to the atmospheric carbon dioxide, so the major ionic species reacting with SiO_2 are the positively charged hydroniums (H_3O^+/D_3O^+) or protons (H^+/D^+). At $U_g < 0$, the Si SCR, SiO_2 film, and the SiO_2/D_2O interface were all polarized along the "upward" direction (defined to be pointing water to oxide) (**Figure 1D**). This led to a negative net charge density, including bound charges on bridging oxygen sites and SiO^- moieties. The latter could be protonated by above cations accumulating at the interface, thus partly compensated the overall polarization and the non-resonant signal strength. While at $U_g > 0$, the polarization of the SiO_2 film was "downward" (**Figure 1E**), which resulted in a positive density of bound charges, most likely on silicon sites. The major anions (HCO_3^-/DCO_3^- or CO_3^{2-}) attracted to the surface could not react with such silicon sites, and could not compensate for the surface charges as cations did. Combined this could cause the non-resonant signal to be weaker at $U_g < 0$, and stronger at $U_g > 0$.

SFVS in H_2O

We then filled the cell with H_2O and took OH spectra, which are presented in **Figure 2A** with varying U_g. To correct for the variation in the infrared input energy, spectra were normalized to the intensity profile of non-resonant SiO_2/D_2O spectra. And since the non-resonant spectra profiles were not sensitive to the potential, we use the averaged spectra at all potentials for normalization to increase the signal-noise-ratio. In the previous study for U_g between −1 and +1 V, the non-resonant signal from Si SCR was comparable to the OH resonances from H_2O, and spectra were from the interference between the two components (Wang et al., 2019). Here with a much thicker film, and at much greater U_g, the spectra became dominated by OH resonances (**Figures 1C**, **2A**). We first discuss the overall intensity variation of OH spectra versus potential. The integrated spectral intensity was the lowest at the most positive potential, grew slowly as approaching the neutral potential, but started to increase rapidly toward more negative potential (**Figure 1C**). Since the ionic composition remained unchanged in our case, so did the Debye length and beam coherence length, change in the spectral intensity directly reflected the degree of polar orientation of contributing OH moieties. From the features mentioned above, we concluded that the OH bonds were less (more) ordered when the surface was covered by positive (negative) bound charges. The overall trend agreed with that observed for the bulk-SiO_2/H_2O interfaces, that OH intensity is greater at higher pH value (Ostroverkhov et al., 2004; 2005; DeWalt-Kerian et al., 2017), as well as at lower ion concentrations (Jena and Hore, 2009; Yang et al., 2009; Jena

et al., 2011; Li et al., 2015; Hore and Tyrode, 2019). Without extra buffer ions, the highest OH peak intensity recorded was near pH 11.5, and was roughly twice of that at pH 5.8 at the SiO_2/H_2O interface (Ostroverkhov et al., 2004; 2005; DeWalt-Kerian et al., 2017). While in our case, the peak intensity at U_g = −50 V was over three times greater than that at U_g = 0 V. The zero potential spectrum corresponded to the usual pH 5.8 spectrum for a bulk-SiO_2/H_2O interface (Wang et al., 2019). That means we achieved an even higher degree of polar orientation of interfacial OH bonds than that achievable at the bulk-SiO_2/H_2O interface. At pH 11.5, the SiO_2 surface is often regarded as highly deprotonated with a surface charge density being ~ −1.4 e/nm^2; meanwhile, the Debye length is about 5.3 nm (without additional buffer ions), and the SF signal in the OH range is considered mostly from the topmost layer of water molecules directly adsorbed to the interface, or equivalently, in the bonded interfacial layer (**Figures 2C,D**) or topmost EDL layer (Urashima et al., 2018). In our system, at pH 5.8 and U_g = −50 V, the net charge density was lower than that at pH 11.5, but the Debye length is as long as 240 nm due to the low ion concentration (the beam coherence length was 50–60 nm). Therefore, the strong SF signal at negative U_g could contain a large contribution from water molecules in the diffuse layer (**Figures 2C,D**). According to the classical dynamic simulation, an electrostatic field as strong as 10^1 mV/nm was needed to appreciably reorient the interfacial water molecules (Wang et al., 2019). The gating field in our case is strong enough to make the above scenario possible.

Before we go on with detailed analysis of OH spectra, we would like to emphasize again that in the present study with a thick silica film, a large portion of the surface charges was due to the polarization of oxide film. As we mentioned above, the distribution of bound charges is not necessarily the same with that from surface chemistry. For example, when pH is low, the positive charge centers are on $SiOH_2^+$ moieties at the bulk-silica/water interface due to protonation of SiOH species; while upon gating, positive surface charges could be simply due to the polarization of Si-O bonds. With only interfacial OH spectra, we could not distinguish between the two cases at this stage, thus only qualitative interpretations would be provided as follows. Here we discuss the overall variation in the spectral profile. Like those from bulk-SiO_2/H_2O interfaces, our spectra exhibited two major resonance features (Ostroverkhov et al., 2004; 2005; Myalitsin et al., 2016): the one at ~3,200 cm^{-1} and another at ~3,400 cm^{-1}. The exact origin of the two peaks is still being investigated (Sovago et al., 2008; Myalitsin et al., 2016), but it is generally agreed that the lower the OH stretching frequency is, the stronger, and/or more ordered, H-bonding environment the corresponding moieties sense. On the bulk-SiO_2/H_2O interfaces, the 3,200 cm^{-1} mode (assigned to the topmost water layer (Urashima et al., 2018)) was found to grow more rapidly than the 3,400 cm^{-1} one (H-bonded to bulk-like water molecules (Montenegro et al., 2021)) at increasing pH, which suggested a more ordered water structure near the more negatively charged surface. In contrast, in our case, when the SiO_2 surface bound charge evolved from positive to negative, the 3,400 cm^{-1} mode appeared to increase more rapidly. This agreed with our discussion above, that the polar ordered OH signal detected at strongly negative U_g had a large contribution from the diffuse layer composed of bulk liquid water, and thus exhibited a greater 3,400 cm^{-1} contribution.

Since there was no direct information about the spectral phase and exact field distribution in the EDL, we could not separate the double layer contributions as in Refs (Tian and Shen, 2014; Urashima et al., 2018). Therefore, we tentatively fitted the spectra in the conventional means by using **Equations (1)** and **(2)** (**Figures 2A,B**), which yielded reasonable results for qualitative understanding (Ostroverkhov et al., 2004; Myalitsin et al., 2016). Fitting parameters are also tabulated in **Table 1**. The fitting involved a low frequency mode ~2,800–3,000 cm^{-1} besides the 3,200 cm^{-1} and 3,400 cm^{-1} modes, as in previous studies (Ostroverkhov et al., 2004; 2005; Nihonyanagi et al., 2011; Pezzotti et al., 2019; Wang et al., 2019; Rehl and Gibbs, 2021). When the surface charge varied from negative to positive, the 3,400 cm^{-1} mode changed from a large positive amplitude to a negative one. This corresponds to our discussion above, that water molecules inside diffuse layer made a major contribution to the 3,400 cm^{-1} peak and reoriented at varying U_g. This also defined that the positive amplitude from fitting corresponded to an "upward" polarization. For the lowest frequency mode, it had a negligible amplitude at negative U_g, and increased negatively toward more positive potential. This agreed with previous observations on neutral or positively charged SiO_2 surfaces, and the mode could be attributed to "downward" OH groups accepting H-bonds with SiOH species (highlighted in black color in **Figure 2D**). The 3,200 cm^{-1} mode did not exhibit as much amplitude change as the other two modes, and remained positive in the whole potential range. We attributed this mode to "upward" OH groups donating H-bonds to the SiO_2 surface (highlighted in green in **Figures 2C,D**), similarly to the findings in Refs (Urashima et al., 2018; Rehl and Gibbs, 2021). Combining the fitting results and discussions above, we summarized the microscopic pictures of the interface. At negative U_g (**Figure 2C**), the SiO_2 film was polarized "upward", and the surface held negative bound charges centered at oxygen sites. These sites could accept H-bonds from vicinal water molecules and caused an upward OH dipole orientation. Meanwhile, the gating field penetrating into the bulk water also rendered water molecules in diffuse layer to be aligned "upward". The two polarizations superimposed constructively, leading to an enhancement of SF intensity at negative U_g. And due to the long Debye length in our case, the SF intensity was even stronger than that achieved at pH 11.5 for a bulk-SiO_2/H_2O interface. At positive U_g, the SiO_2 film was polarized "downward", and the surface held positive bound charges, presumably centered at silicon sites. Meanwhile, it was still the surface SiOH groups that form H-bonds with vicinal water molecules. As SiOH can be both H-bond donors and acceptors, they led to both upward

TABLE 1 | The fitting parameters of the normalized SFVS spectra in H_2O.

U_g (V)	Low-frequency			3,200 cm^{-1}			3,400 cm^{-1}			$\chi^{(2)}_{NR}$	
	ω_1 (cm^{-1})	A_1 (a. u.)	Γ_1 (cm^{-1})	ω_2 (cm^{-1})	A_2 (a. u.)	Γ_2 (cm^{-1})	ω_3 (cm^{-1})	A_3 (a. u.)	Γ_3 (cm^{-1})	Re[a] (a. u.)	Im[b] (a. u.)
−50	3,008	51	107	3,187	911	155	3,477	1,030	225	−0.17	0.07
−37.5	2,999	61	106	3,176	785	150	3,492	840	204	−0.07	0.22
−25	3,012	76	116	3,174	665	144	3,489	783	206	−0.02	0.26
−12.5	2,983	15	116	3,180	622	158	3,464	666	223	−0.04	0.06
0	2,861	−45	111	3,186	587	161	3,459	505	209	−0.01	−0.25
12.5	2,862	−338	158	3,181	586	145	3,442	310	169	0.40	−0.22
25	2,877	−400	138	3,166	575	140	3,415	151	155	0.46	−0.28
37.5	2,890	−553	143	3,158	699	152	3,419	−314	151	0.68	−0.15
50	2,865	−636	136	3,125	799	179	3,398	−318	141	0.78	−0.35

[a]*Re: the real part of the non-resonant background.*
[b]*Im: the imaginary part of the non-resonant background.*

(highlighted in green) and downward (highlighted in black) alignments of water OH groups as shown in **Figure 2D**. The former conflicted with the preferred downward field induced alignment (highlighted in orange) in diffuse layer (**Figure 2D**), and therefore the overall polar orientation was not as strong as that observed at negative U_g.

CONCLUSION

To conclude, by applying an electrostatic gate potential to a silica thin film in neutral water, we observed a prominent enhancement of interfacial OH sum-frequency vibrational signals, with even greater relative intensity than that achieved at bulk-silica/water interfaces in strong basic solution. By fitting and analyzing the spectra, we attributed this observation to an effective field alignment of water molecules throughout the diffuse layer, which was resultant from the small number of ions and weak screening in our case. This demonstrates the unique tuning capability of the EIS structure as we previously reported (Wang et al., 2019). On the other hand, as we mentioned above, we could not distinguish between bound charges and surface charges from protonation/deprotonation reactions at this stage, and only qualitative interpretations were provided based on assumptions on the SiO_2 surface structures. Further studies on the SiO_2 side, for example the *in situ* detection of its surface phonon spectra in water, would be essential for us to fully understand the phenomenon and the entire aqueous interface at the molecular level.

DATA AVAILABILITY STATEMENT

The original contributions presented in the study are included in the article/supplementary material, further inquiries can be directed to the corresponding author.

AUTHOR CONTRIBUTIONS

WL conceived the project and supervised the lab works. XqL, XL, and YL conducted the experiments. WL and XqL did the data analysis, and drafted the manuscript. All authors agreed to this manuscript.

FUNDING

National Key Research and Development Program of China and National Natural Science Foundation of China (2019YFA0308404, 11991062); Science and Technology Commission of Shanghai Municipality (Grant No. 20JC1415900); National Program for Support of Top-Notch Young Professionals (W03070062); Shu Guang Project by Shanghai Education Development Foundation (18SG02).

ACKNOWLEDGMENTS

The part of sample fabrication was conducted at Fudan Nano-fabrication Lab.

REFERENCES

Anim-Danso, E., Zhang, Y., and Dhinojwala, A. (2016). Surface Charge Affects the Structure of Interfacial Ice. *J. Phys. Chem. C* 120 (7), 3741–3748. doi:10.1021/acs.jpcc.5b08371

Aragones, J. L., MacDowell, L. G., Siepmann, J. I., and Vega, C. (2011). Phase Diagram of Water Under an Applied Electric Field. *Phys. Rev. Lett.* 107 (15), 155702. doi:10.1103/PhysRevLett.107.155702

Backus, E. H. G., Schaefer, J., and Bonn, M. (2020). Probing the Mineral-Water Interface with Nonlinear Optical Spectroscopy. *Angew. Chem. Int. Ed.* 60, 10482–10501. doi:10.1002/anie.202003085

Bian, H.-T., Guo, Y., and Wang, H.-F. (2018). Non-Parabolic Potential Dependence of Optical Second Harmonic Generation from the Si(111) Electrode/Electrolyte Interface. *Phys. Chem. Chem. Phys.* 20 (46), 29539–29548. doi:10.1039/C8CP05621H

Boily, J.-F., Fu, L., Tuladhar, A., Lu, Z., Legg, B. A., Wang, Z. M., et al. (2019). Hydrogen Bonding and Molecular Orientations across Thin Water Films on Sapphire. *J. Colloid Interf. Sci.* 555, 810–817. doi:10.1016/j.jcis.2019.08.028

Brown, G. E., Jr. (2001). Surface Science: How Minerals React with Water. *Science* 294 (5540), 67–69. doi:10.1126/science.1063544

Brown, M. A., Goel, A., and Abbas, Z. (2016). Effect of Electrolyte Concentration on the Stern Layer Thickness at a Charged Interface. *Angew. Chem. Int. Ed.* 55 (11), 3790–3794. doi:10.1002/anie.201512025

Covert, P. A., and Hore, D. K. (2016). Geochemical Insight from Nonlinear Optical Studies of Mineral-Water Interfaces. *Annu. Rev. Phys. Chem.* 67 (1), 233–257. doi:10.1146/annurev-physchem-040215-112300

DeWalt-Kerian, E. L., Kim, S., Azam, M. S., Zeng, H., Liu, Q., and Gibbs, J. M. (2017). pH-Dependent Inversion of Hofmeister Trends in the Water Structure of the Electrical Double Layer. *J. Phys. Chem. Lett.* 8 (13), 2855–2861. doi:10.1021/acs.jpclett.7b01005

Gaigeot, M.-P., Sprik, M., and Sulpizi, M. (2012). Oxide/water Interfaces: How the Surface Chemistry Modifies Interfacial Water Properties. *J. Phys. Condens. Matter* 24 (12), 124106. doi:10.1088/0953-8984/24/12/124106

Hore, D. K., and Tyrode, E. (2019). Probing Charged Aqueous Interfaces Near Critical Angles: Effect of Varying Coherence Length. *J. Phys. Chem. C* 123 (27), 16911–16920. doi:10.1021/acs.jpcc.9b05256

Jackson, J. D. (1999). *Classical Electrodynamics*. New York: Wiley Press.

Jena, K. C., Covert, P. A., and Hore, D. K. (2011). The Effect of Salt on the Water Structure at a Charged Solid Surface: Differentiating Second- and Third-Order Nonlinear Contributions. *J. Phys. Chem. Lett.* 2 (9), 1056–1061. doi:10.1021/jz200251h

Jena, K. C., and Hore, D. K. (2009). Variation of Ionic Strength Reveals the Interfacial Water Structure at a Charged Mineral Surface. *J. Phys. Chem. C* 113 (34), 15364–15372. doi:10.1021/jp905475m

Kosmulski, M. (2002). The pH-Dependent Surface Charging and the Points of Zero Charge. *J. Colloid Interf. Sci.* 253 (1), 77–87. doi:10.1006/jcis.2002.8490

Li, X., Feng, R.-J., Wang, J.-J., Zhang, Z., Lu, Z., and Guo, Y. (2015). Role of Refractive index in Sum Frequency Generation Intensity of Salt Solution Interfaces. *Chin. Chem. Lett.* 26 (12), 1542–1546. doi:10.1016/j.cclet.2015.10.020

Liu, X., Yang, D., Li, Y., Gao, Y., and Liu, W.-T. (2019). Anisotropic Adsorption of 2-Phenylethyl Alcohol on a Rutile (110) Surface. *J. Phys. Chem. C* 123 (49), 29759–29764. doi:10.1021/acs.jpcc.9b09209

Lüpke, G. (1999). Characterization of Semiconductor Interfaces by Second-Harmonic Generation. *Surf. Sci. Rep.* 35 (3), 75–161. doi:10.1016/S0167-5729(99)00007-2

Miranda, P. B., Xu, L., Shen, Y. R., and Salmeron, M. (1998). Icelike Water Monolayer Adsorbed on Mica at Room Temperature. *Phys. Rev. Lett.* 81 (26), 5876–5879. doi:10.1103/PhysRevLett.81.5876

Montenegro, A., Dutta, C., Mammetkuliev, M., Shi, H., Hou, B., Bhattacharyya, D., et al. (2021). Asymmetric Response of Interfacial Water to Applied Electric fields. *Nature* 594 (7861), 62–65. doi:10.1038/s41586-021-03504-4

Myalitsin, A., Urashima, S.-H., Nihonyanagi, S., Yamaguchi, S., and Tahara, T. (2016). Water Structure at the Buried Silica/Aqueous Interface Studied by Heterodyne-Detected Vibrational Sum-Frequency Generation. *J. Phys. Chem. C* 120 (17), 9357–9363. doi:10.1021/acs.jpcc.6b03275

Nihonyanagi, S., Ishiyama, T., Lee, T.-K., Yamaguchi, S., Bonn, M., Morita, A., et al. (2011). Unified Molecular View of the Air/Water Interface Based on Experimental and Theoretical χ(2)Spectra of an Isotopically Diluted Water Surface. *J. Am. Chem. Soc.* 133 (42), 16875–16880. doi:10.1021/ja2053754

Nihonyanagi, S., Ye, S., Uosaki, K., Dreesen, L., Humbert, C., Thiry, P., et al. (2004). Potential-Dependent Structure of the Interfacial Water on the Gold Electrode. *Surf. Sci.* 573 (1), 11–16. doi:10.1016/j.susc.2004.04.059

Ohno, P. E., Saslow, S. A., Wang, H.-F., Geiger, F. M., and Eisenthal, K. B. (2016). Phase-Referenced Nonlinear Spectroscopy of the α-Quartz/Water Interface. *Nat. Commun.* 7 (1), 13587. doi:10.1038/ncomms13587

Ostroverkhov, V., Waychunas, G. A., and Shen, Y. R. (2005). New Information on Water Interfacial Structure Revealed by Phase-Sensitive Surface Spectroscopy. *Phys. Rev. Lett.* 94 (4), 46101–46102. doi:10.1103/PhysRevLett.94.046102

Ostroverkhov, V., Waychunas, G. A., and Shen, Y. R. (2004). Vibrational Spectra of Water at Water/α-Quartz (0001) Interface. *Chem. Phys. Lett.* 386 (1-3), 144–148. doi:10.1016/j.cplett.2004.01.047

Pezzotti, S., Galimberti, D. R., and Gaigeot, M.-P. (2019). Deconvolution of BIL-SFG and DL-SFG Spectroscopic Signals Reveals Order/Disorder of Water at the Elusive Aqueous Silica Interface. *Phys. Chem. Chem. Phys.* 21 (40), 22188–22202. doi:10.1039/c9cp02766a

Putnis, A. (2014). Why mineral Interfaces Matter. *Science* 343 (6178), 1441–1442. doi:10.1126/science.1250884

Rehl, B., and Gibbs, J. M. (2021). Role of Ions on the Surface-Bound Water Structure at the Silica/water Interface: Identifying the Spectral Signature of Stability. *J. Phys. Chem. Lett.* 12 (11), 2854–2864. doi:10.1021/acs.jpclett.0c03565

Saitta, A. M., Saija, F., and Giaquinta, P. V. (2012). Ab InitioMolecular Dynamics Study of Dissociation of Water Under an Electric Field. *Phys. Rev. Lett.* 108 (20), 207801. doi:10.1103/PhysRevLett.108.207801

Schaefer, J., Backus, E. H. G., and Bonn, M. (2018). Evidence for Auto-Catalytic Mineral Dissolution from Surface-Specific Vibrational Spectroscopy. *Nat. Commun.* 9 (1), 3316. doi:10.1038/s41467-018-05762-9

Sovago, M., Campen, R. K., Wurpel, G. W. H., Müller, M., Bakker, H. J., and Bonn, M. (2008). Vibrational Response of Hydrogen-Bonded Interfacial Water Is Dominated by Intramolecular Coupling. *Phys. Rev. Lett.* 100 (17), 173901. doi:10.1103/PhysRevLett.100.173901

Sulpizi, M., Gaigeot, M.-P., and Sprik, M. (2012). The Silica-Water Interface: How the Silanols Determine the Surface Acidity and Modulate the Water Properties. *J. Chem. Theor. Comput.* 8 (3), 1037–1047. doi:10.1021/ct2007154

Tian, C. S., and Shen, Y. R. (2014). Recent Progress on Sum-Frequency Spectroscopy. *Surf. Sci. Rep.* 69 (2-3), 105–131. doi:10.1016/j.surfrep.2014.05.001

Urashima, S.-h., Myalitsin, A., Nihonyanagi, S., and Tahara, T. (2018). The Topmost Water Structure at a Charged Silica/aqueous Interface Revealed by Heterodyne-Detected Vibrational Sum Frequency Generation Spectroscopy. *J. Phys. Chem. Lett.* 9 (14), 4109–4114. doi:10.1021/acs.jpclett.8b01650

Verdaguer, A., Sacha, G. M., Bluhm, H., and Salmeron, M. (2006). Molecular Structure of Water at Interfaces: Wetting at the Nanometer Scale. *Chem. Rev.* 106 (4), 1478–1510. doi:10.1021/cr040376l

Waleed Shinwari, M., Jamal Deen, M., and Landheer, D. (2007). Study of the Electrolyte-Insulator-Semiconductor Field-Effect Transistor (EISFET) with Applications in Biosensor Design. *Microelectronics Reliability* 47 (12), 2025–2057. doi:10.1016/j.microrel.2006.10.003

Wang, H., Xu, Q., Liu, Z., Tang, Y., Wei, G., Shen, Y. R., et al. (2019). Gate-Controlled Sum-Frequency Vibrational Spectroscopy for Probing Charged Oxide/Water Interfaces. *J. Phys. Chem. Lett.* 10 (19), 5943–5948. doi:10.1021/acs.jpclett.9b01908

Yang, Z., Li, Q., and Chou, K. C. (2009). Structures of Water Molecules at the Interfaces of Aqueous Salt Solutions and Silica: Cation Effects. *J. Phys. Chem. C* 113 (19), 8201–8205. doi:10.1021/jp811517p

Conflict of Interest: The authors declare that the research was conducted in the absence of any commercial or financial relationships that could be construed as a potential conflict of interest.

frontiers in Chemistry

PERSPECTIVE
published: 22 September 2021
doi: 10.3389/fchem.2021.745446

Advances in Atomic Force Microscopy: Imaging of Two- and Three-Dimensional Interfacial Water

Duanyun Cao[1]†, Yizhi Song[2†], BinZe Tang[2] and Limei Xu[2,3,4]**

[1]Beijing Key Laboratory of Environmental Science and Engineering, School of Materials Science and Engineering, Beijing Institute of Technology, Beijing, China, [2]International Center for Quantum Materials, School of Physics, Peking University, Beijing, China, [3]Collaborative Innovation Center of Quantum Matter, Beijing, China, [4]Interdisciplinary Institute of Light-Element Quantum Materials and Research Center for Light-Element Advanced Materials, Peking University, Beijing, China

Interfacial water is closely related to many core scientific and technological issues, covering a broad range of fields, such as material science, geochemistry, electrochemistry and biology. The understanding of the structure and dynamics of interfacial water is the basis of dealing with a series of issues in science and technology. In recent years, atomic force microscopy (AFM) with ultrahigh resolution has become a very powerful option for the understanding of the complex structural and dynamic properties of interfacial water on solid surfaces. In this perspective, we provide an overview of the application of AFM in the study of two dimensional (2D) or three dimensional (3D) interfacial water, and present the prospect and challenges of the AFM-related techniques in experiments and simulations, in order to gain a better understanding of the physicochemical properties of interfacial water.

Keywords: interfacial water, atomic force microscopy, structure and dynamics, liquid/solid interface, machine learning

OPEN ACCESS

Edited by:
Kenichi Yoshikawa,
Doshisha University, Japan

Reviewed by:
Akitoshi Shiotari,
Fritz-Haber-Institut, Germany
Runze Ma,
Pacific Northwest National Laboratory (DOE), United States

****Correspondence:***
Duanyun Cao
dycao@bit.edu.cn
Limei Xu
limei.xu@pku.edu.cn

†DC and YS have contributed equally to this work and share first authorship

Specialty section:
This article was submitted to Physical Chemistry and Chemical Physics, a section of the journal Frontiers in Chemistry

Received: *22 July 2021*
Accepted: *10 September 2021*
Published: *22 September 2021*

Citation:
Cao D, Song Y, Tang B and Xu L (2021) Advances in Atomic Force Microscopy: Imaging of Two- and Three-Dimensional Interfacial Water. Front. Chem. 9:745446. doi: 10.3389/fchem.2021.745446

INTRODUCTION

Interfacial water is ubiquitous in nature and closely related to various issues both in fundamental research and technological applications, such as the dissolution of salts (Wandelt and Thurgate, 2002), desalination of seawater (Somorjai and Li, 2010), biological reactions (Tanaka et al., 2002), nanoconfined amorphous water (Manni et al., 2019) and lubricant systems (Urbakh et al., 2004). To gain a deep understanding of these important processes, the investigation of the structure and dynamic process like the rearrangement and growth mechanism of interfacial water on heterogeneous surfaces should be conducted. The symmetry of interfacial water is complex, for it shares boundaries with other substances. Therefore, it is more difficult to investigate interfacial water compared with bulk water which is well known to have 20 kinds of crystalline polymorph (ice Ih, ice Ic, ice II ~ XIX) (Gasser et al., 2021). Particularly, the investigation of the growth process of interfacial water is extremely challenging, which requires non-invasive high resolution imaging, as the metastable or intermediate edge structures involved are rather fragile. With high sensitivity to the local environment and short range forces, AFM is very useful to detect the structure and dynamics of water molecules on a diversity of substrates, from insulating to metal substrate (Peng et al., 2018a). Until now, AFM imaging, together with *ab initio* calculation, classical molecular dynamics (MD) calculation and AFM simulation, has been applied to the investigation of the interfacial water on a wide variety of substrates, such as minerals (Putnis, 2014), biomolecules (Maver et al., 2016; Dufrene et al., 2017), and organic films (Verma and Sharma, 2010). Previously, we introduced the development of AFM technique both in experiments and simulations, as well as their

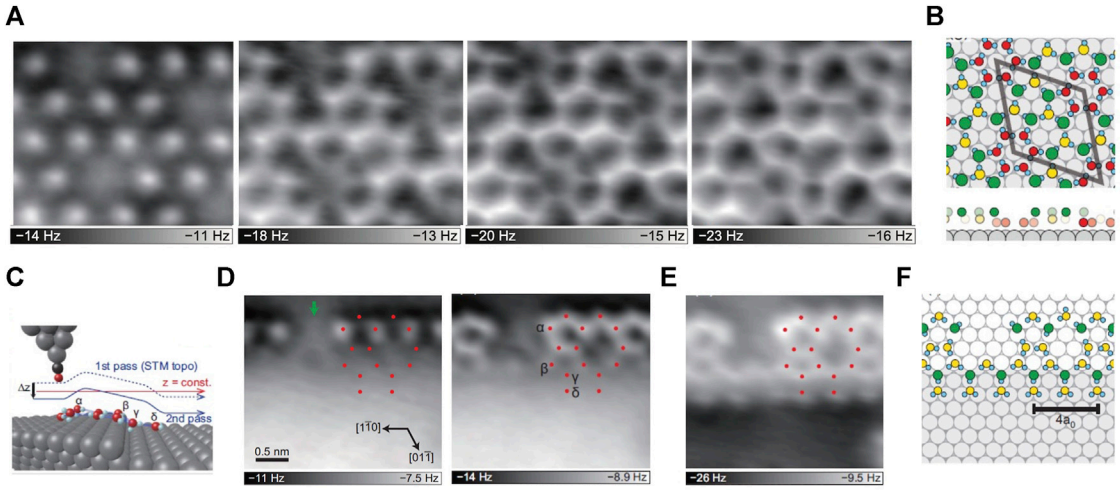

FIGURE 1 | 2D water networks on Ni(111) **(A)** AFM images of the 2D water networks of the same area on the terraces, the tip height decreases from left to right **(B)** The proposed structure of the water monolayer based on the AFM images. The gray, cyan, green, yellow and red spheres represent Ni, H, topmost O, middle O and bottommost O atoms, respectively; the unit cell of ($\sqrt{28} \times \sqrt{28}$) R19 is represented by the gray rhombus; the bottom panels are the side-view of the above structures, without H atoms for clarity **(C)** The schematic diagram of the tip and step. The gray, cyan, black and red spheres represent Ni, H, C and O atoms, respectively **(D)** Constant-height AFM images of the water network at the step edge, the tip height decreases from left to right **(E)** AFM image of the same region in **(D),** but the tip trajectory is consistent with that of the STM image, as the solid blue line in **(C)**. The red dots in **(D–E)** represent the O-atom positions **(F)** The water network structure at the step edge proposed based on the AFM images. Adapted with permission from Shiotari, et al., 2019. *Physical Review Materials* 3(9): 093,001 (Shiotari et al., 2019).

applications in the study of interfacial water, with particular emphasis on the detection of the nanoclusters and one-dimensional chains (Cao et al., 2019). As a continuation, this perspective reviews the latest progresses in the utilization of AFM imaging in 2D and 3D interfacial water, including adsorbed water networks and electrolytes, as well as their growth processes. An outlook of future AFM study and a brief summary are presented in the end.

THE ULTRAHIGH-RESOLUTION IMAGING OF INTERFACIAL WATER ON VARIOUS SUBSTRATES

Interfacial water molecules on solid surfaces could form various structures, which depends not only on the lattice spacing and symmetry, but also on the substrate chemical reactivity and water-substrate interaction (Hodgson and Haq, 2009). With the consideration of the lattice matching with bulk water, the close-packed surfaces of Ni, Pt, Ru and Au are ideal substrates for studying water adsorption (Thurmer and Nie, 2013; Shiotari et al., 2019; Ma et al., 2020). Besides, the structures and properties of interfacial water in ionic hydration systems, which are susceptible to the influences of ions in the environment, are of particular importance to tackle many scientific and technical issues (Strmcnik et al., 2009), for instance, the kinetics of hydrogen evolution and oxidation reactions. In the following, we discuss the recent advances in the structural and dynamic properties of interfacial water and electrolytes on various substrates with the application of AFM.

Characterization of 2D Ice on Various Substrates

1) Characterization of 2D Water Networks on Ni(111)

Ni commonly used in alloys and cell electrodes, direct observations of water adsorptions on Ni-based materials are helpful to understand various surface phenomena, such as corrosion, wetting, electrochemical reactions and the water-related heterogeneous catalysis (Michaelides et al., 2004). Recently, with low-temperature AFM, the structures of 2D water networks on the terraces and at the step edges of Ni(111) were observed (Shiotari et al., 2019). It was found that at 78K, water molecules are assembled in disorder, while at 140–145K, they rearrange the structure and form small clusters with a central cyclic $(H_2O)_6$, which are possibly the nucleus of the initial growth of H-bonding networks (Nakamura and Ito, 2004). Such small clusters then disappear after annealed at 150K, homogeneous huge islands of the ($\sqrt{28} \times \sqrt{28}$)R19° superstructure starting to dominate on the terraces, which are composed of pentagonal, hexagonal and heptagonal rings (**Figures 1A,B**). Meanwhile, at the monoatomic step edge of Ni(111), another water network is formed, containing pentagonal and octagonal rings along the step direction with a periodicity of four times Ni interatomic distance ($4a_0$) (**Figures 1C–F**). Such a periodic 1D pentagonal-octagonal network closely resembles the domain boundaries of H_2O/Ru (0001) (Maier et al., 2016), the water islands on stepped Cu(551) surface (Lin et al., 2018), and the defect rows in the second water layer on SnPt (111) (Gerrard et al., 2019). This indicates that the 1D pentagonal-octagonal network structure is a representative defect existing in the

interfacial water layers on metal surfaces. Moreover, 2D water networks on metal surfaces, such as Pt (111) (Nie et al., 2010) and Ru (0001) (Maier et al., 2014), have also been studied by AFM. Variations in water networks on different surfaces have been reported, ranging from close-packed metal surfaces to the insulating surfaces. These studies revealed the adsorption structures of water on different metals, which is important for a deep understanding of the catalytic reactivity and the wettability on terraces and at step edges.

2) Determination of Intrinsic Reconstruction of Ice-I Surfaces on Rh (111) and Pt (111)

Compared with non-contact AFM using quartz tuning fork sensors (Thurmer and Nie, 2013), AFM with a silicon cantilever and optical interferometer possesses a higher sensitivity in interatomic force detection (Kaiser et al., 2007). Based on this technique, Kawakami et al. studied the atomic structures of ice-I surfaces on Rh (111) and Pt (111), and found that the AFM images of the terraces of ice on both Rh (111) and Pt (111) have rather similar characteristics, e.g., random distribution, number reduction and (2 × 2) order of dangling H atoms, and (2 × 2) order distortion of O lattice (Kawakami et al., 2020). However, only one crystalline phase of ice (ice-Ih) is observed on Rh (111), while the crystalline phase of ice on Pt (111) varies with the thickness of the ice film, e.g., the number of ice layers (Thurmer and Nie, 2013). That is to say, it is ice-Ic at medium thickness (10–50 BLs) and ice-Ih in a dominant state at other thicknesses. Although the crystalline phase of ice on Pt substrate differs at different ice thickness, their densities of the dangling H atoms are the same, and their AFM images are quite similar with a (2 × 2) order. This reveals that the changes in the H-atom orientation and the interface effects of ice Ih and ice Ic have a negligible influence on the surface reconstruction. Moreover, it is found that the (2 × 2) order reconstruction of ice-I surfaces, including the sparse distribution of the residual dangling H atoms and the removal of dangling H atoms, is caused by the electrostatic repulsion between the dangling H atoms. The above findings about the molecular reconstruction are crucial to understand chemical and physical phenomena, such as the growth and melting of ice, and chemical reactions (Kawakami et al., 2020).

3) Atomic Imaging of Edge Structure and Growth of a 2D Hexagonal Ice

Although the structure of 2D water network on surface has been widely studied (Nie et al., 2010; Kiselev et al., 2017), it is rather challenging to capture the atomic details of metastable or intermediate edge structures during ice growth. This is due to the fact that the fragileness and the short life span of intermediate edge structures call for fast and non-invasive detection (Lupi et al., 2014). Recently, Ma et al. achieved a high resolution imaging of the edge structures of a 2D bilayer hexagonal ice on Au (111) by weakly perturbative AFM with a CO-functionalized tip (Ma et al., 2020). Combining experiments with theoretical calculations, the orientation of each water molecule, namely the O-H directionality in the 2D bilayer ice, was revealed. Moreover, a new type of edge, which coexists with the zigzag edge in 2D hexagonal ice and along the armchair direction but is reconstructed into a complex periodical structure consisting of 5756-membered rings, was also found. Ma et al. also achieved the freeze and imaging of various intermediate structures at the two types of edges, and rebuilt distinct ice growth mechanisms (**Figures 2A,B**). Combined with *ab initio* calculations and classical MD simulations, the growth at the zigzag edge was found to follow a collective bridging mechanism facilitated by a periodic array of pentagons, in contrast to a local seeding growth mode with a manifestation of the 5756–5656 interconversion at the armchair edge (**Figures 2C,D**). Furthermore, not only the distance between water molecules but also the commensurability between ice lattice and the substrate was found to have a negligible effect on the relative stability of the two types of edges, demonstrating the generality of observed growth behavior. Such new growth pattern is in sharp contrast to the conventional growth mode of bilayer hexagonal ices and 2D hexagonal material, shedding light on the physical mechanism of ice growth on hydrophobic substrates or under hydrophobic confinement.

Probing the Adsorption of Electrolytes at Liquid/Kaolinite Interfaces

The above mentioned works were all performed in a vacuum at low temperature using *non-contact* AFM (nc-AFM) to guarantee that the sample would not be disturbed and the tip would not be contaminated. However, in case of structure probing of the solid/liquid interface at room temperature, nonnegligible disturbance and tip contamination becomes unavoidable. As a result, nc-AFM imaging under such conditions becomes very difficult. Therefore, the contact mode AFM, whose tip contacts the measured sample during imaging, is more appropriate here due to its higher stability in such cases. With the contact mode AFM, surface structures in liquids could be characterized.

Adsorption of electrolytes (ions) at liquid/solid interfaces plays a critical role in nanomaterial processing to gain desired structures and morphology, since it can alter physicochemical nature of materials (Nelson and Schwartz, 2013; DeWalt-Kerian et al., 2017). Various electrical double layer (EDL) models have been used to describe the ion adsorption on charged surfaces in liquids, but the model-dependent approaches lead to inaccurate predictions of ion adsorption due to inevitable assumptions, for example, whether the diffusion and thermal motion of ions are taken into account for molecular modeling (Modi and Fuerstenau, 1957; Ardizzone et al., 1982). Without any approximation or assumption, Chang et al. studied the electrolytes adsorption at liquid/kaolinite interfaces using an *in situ* AFM (Chang et al., 2021). They directly visualized the ions located in the EDL and adsorbed on the anisotropic kaolinite, and detected the changes of surface structure of kaolinite during the adsorption of mono- and divalent metal cations.

As a result, it was found that the adsorption of K^+ and Cl^- in solution cannot change the lattice structure of kaolinite surfaces. Unlike monovalent ions, the adsorption of calcium ions can lead

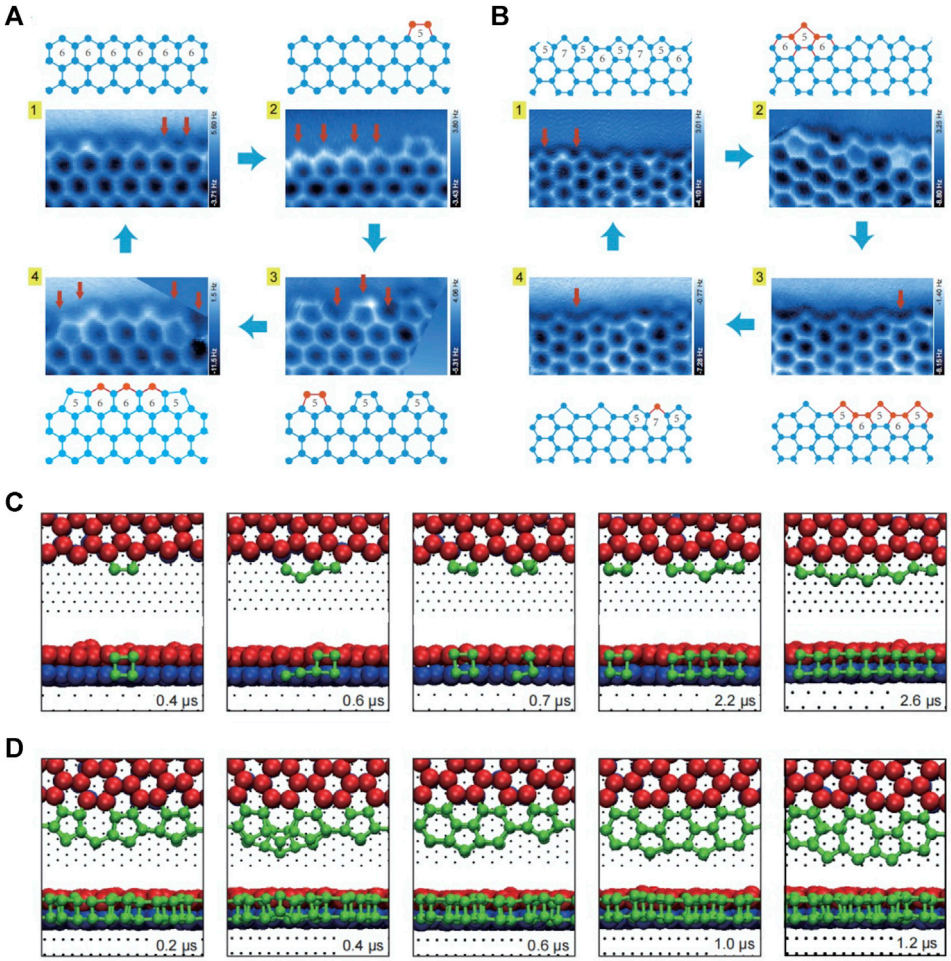

FIGURE 2 | The growth process of zigzag and armchair edges of the 2D bilayer hexagonal ice formed on Au(111) **(A–B)** Constant-height AFM images and corresponding models of the steady state (1) and metastable states (2–4) of the zigzag **(A)** and armchair edges **(B) (C–D)** Time-elapsed snapshots during the growth of zigzag **(C)** and armchair edges **(D)** obtained by MD simulation. In **(A–B)**, the proposed growing process (from one to 4) is indicated by blue arrows; the addition of one bilayer water pair is labeled by a red arrow in AFM images; the red balls and sticks in ball-stick models represent the newly added bilayer water pairs, while the blue ones represent the existing structures. In **(C–D)**, the simulation times are shown on bottom right of each snapshot, the bottom- and top-layer water molecules of the preexistent bilayer ice are denoted by the blue and red spheres, respectively; the newly deposited water molecules are denoted by the green spheres. Adapted with permission from Ma, et al. 2020. *Nature* 577(7788): 60–63 (Ma et al., 2020).

to the changes of the surface morphology at high pH, presenting in a specific adsorption mode. This suggests the strong and direct binding between cations and substrates. Moreover, it was first found that the specific adsorption caused by the hydrolysis of Ca^{2+} can weaken the electrostatic interaction and decrease the ionic charge. To conclude, AFM is a very useful imaging tool to disclose ion adsorption at the liquid/kaolinite interface and it can be extended to other interfaces.

PERSPECTIVE

Identification of Multiple Chemical Species in 2D H-Bonding Networks

Identification of multiple chemical species such as OH^- or H_3O^+ solvated in 2D and 3D H-bonding water networks is significant for deepening our knowledge about electrochemical reactions, such as hydrogen or oxygen evolution reaction. Previous studies of the systems like partially dissociated water networks or hydrated protons solvated in H-bonding networks, have been mainly investigated by vibrational spectroscopy such as X-ray photoelectron spectroscopy, infrared and Raman spectroscopies, which can determine the extent of partial dissociation (Meier et al., 2018), or the molecular structures of hydrated protons in water clusters (Fournier et al., 2015). However, these techniques suffer from the difficulty of spectral assignment and the limited spatial resolution (Shen and Ostroverkhov, 2006). In contrast, nc-AFM with a CO-terminated tip which can be operated in a vacuum at low temperatures, shows the ability to imaging the water molecule with sub-molecular resolution in a nearly non-invasive manner (Peng et al., 2018a; Peng et al., 2018b). In this way, partially dissociated water networks on various substrates,

like Fe_3O_4(001) (Meier et al., 2018) and Cu(110) (Shiotari and Sugimoto, 2017) have been studied. However, the identification of chemical species related to water just based on the AFM images is difficult due to the fact that AFM is not very sensitive to H atom, which is small and interacts weakly with the tip. Fortunately, this difficulty can be overcome by the aid of DFT calculation and AFM image simulations (Hapala et al., 2014). Nevertheless, due to the high similarity of H_3O^+ to H_2O, the imaging and identification of H_3O^+ in the H-bonding network of water is much more challenging, and the related AFM-based studies have not been reported yet. It is believed that by further improving the resolution and sensitivity of qPlus-AFM, this will soon no longer be an issue.

3D Atomic Force Microscopy

Interfacial aqueous layer plays an intermediate or significant role in many aspects, such as corrosion, nanopatterning and adhesion in material science (Garcia et al., 2014), protein folding, inactivation and molecular identification in molecular biology (Laage et al., 2017), the dissolution and growth of ore in geology (Laanait et al., 2015). To fully understand such phenomena and reveal the detailed interactions of liquid water on different solid interface, the detailed 3D structure of hydration layer needs to be established. While nc-AFM is usually affected by the motion of liquid molecules, 3D-AFM with an authentic 3D depth and a high spatial resolution of 1–3 Å is the newest and most successful attempt to achieve this goal, making an accurate imaging of the atom position. In fact, it has already been applied to uncover the nature of a few liquid/solid interfaces, achieving high resolution imaging of water layers at the flat liquid/mica interface (Fukuma et al., 2010) and on non-flat surfaces, such as lipid membranes (Kobayashi et al., 2013), proteins (Herruzo et al., 2013), or DNA (Kuchuk and Sivan, 2018).

The achievements of 3D-AFM made in the investigation of interfacial water on stiff crystalline surfaces and in soft biomolecules (Fukuma and Garcia, 2018) highlight its widely potential applications in catalysis, electrochemistry, cell and molecular biology. Nevertheless, there are still some scientific and instrumental challenges for the promotion of 3D-AFM. For instance, the 3D-AFM-based z-depth imaging, with a maximum of 10 nm (Martin-Jimenez et al., 2016) and a common value of 1 nm, is ideal for the exploration of the adsorption of ions and solvent molecules on flat substrates (Jariwala et al., 2017), but it is rather small for detecting the hydration structures on non-flat systems, such as isolated proteins, nanostructured surfaces and cells (Fukuma and Garcia, 2018). Thus, it is of great significance to improve the sensitivity, resolution and scanning speed of 3D-AFM for its broader applications, e.g., the study of 3D distribution of flexible surface structures, such as chain polymers or lipid headgroups on a biological membrane surface, and *in-situ* observation.

Multifunctional AFM Techniques for Aqueous Battery Characterization

Being capable of performing under realistic *in-situ* conditions, multifunctional AFM is conductive to revealing the detailed mechanisms of scientific phenomena and technological processes, the extremely important evolution of liquid/solid interface in battery, for instance. At present, different kinds of multifunctional AFMs have been used in the research of lithium-ion batteries with organic solvents as electrolytes (Yoon et al., 2016), among which electrochemical AFM (EC-AFM) was more widely utilized than others. It can characterize the morphology evolution on anodes (Jeong et al., 2001) and cathodes (Wu et al., 2017), the formation of Li-dendrite (Shen et al., 2018) and the kinetic process of solid electrolyte interface (Novak et al., 2001). Electro-chemical strain microscopy is a very useful tool to measure the volumetric strain driven by potential pulse, and to detect the microscopic details of electronic or ionic transport processes (Yang et al., 2015). Meanwhile, the ability to detect the surface potential between the tip and the sample measured, allows Kelvin probe force microscopy to investigate the relationship between ion distributions and battery performance, as well as the impact of surface charges on ionic intercalation (Luchkin et al., 2014). Moreover, combined with infrared or Raman spectroscopy and mass spectrometry, AFM can effectively overcome the shortcoming of being unable to distinguish the composition of the detected substances, greatly expanding its application in energy fields.

Aqueous battery with water as the electrolyte solvent is the most potential technology for large-scale energy storage systems of wind and solar photovoltaic power generation (Wang et al., 2018). This is due to its superiority of low cost, environmental friendliness, high safety and theoretical capacity (Glatz et al., 2019), while the application of lithium-ion batteries is hindered by its high cost, low safety and environmental issues. However, studies of aqueous batteries are still at the early stage, and further investigations need to be carried out, including in-depth structures and dynamic properties of aqueous battery, as well as their changes in the electro-chemical processes (Zhou et al., 2020). Despite their powerfulness in nanoscale characterization, all types of multifunctional AFMs have limitations in spatial and temporal resolution. For example, EC-AFM has limited scanning rate, thus some fast interface reactions cannot be monitored in real time. In addition, drift during scanning make it difficult to obtain reliable surface characteristics (Chen et al., 2020). These limitations are expected to be overcome in the near future by developing low-noise cantilever deflection sensor (Fukuma et al., 2005) and drift-compensated data acquisition schemes (Abe et al., 2007). Besides, optimal tip preparation is often a key issue in AFM-based techniques such as tip enhanced Raman spectroscopy to ensure high enhancement and good reproducibility (Toca-Herrera, 2019).

Machine Learning to Enhance AFM Interpretation

The interpretation of AFM signals, especially the 3D features appearing in the submolecular-resolution 3D-AFM images, has been achieved by introducing MD simulations. In 2015, with the comparison between the result of 3D-AFM experiment and MD simulation, it was found that the activities between the uppermost surface atoms and tip apex predominantly affected the tip-sample

interaction (Fukuma et al., 2015). This finding provides a qualitative answer to the question on the imaging mechanism: why the intrinsic 3D hydration structure (without the AFM tip) is similar to the sub-nanometer resolution contrast appearing in 3D-AFM images.

However, MD simulation has been mainly applied to study the pure water on uniform and rigid surfaces (Miyazawa et al., 2016; Vilhena et al., 2016). It is impractical to utilize MD to analyze 3D-AFM features in many complex problems, owing to its high computational costs. Currently, there is still a large gap between the AFM simulation and experiments. Many issues under more complicated conditions remain to be tackled theoretically, such as the treatment of ions, the influence of ions on force contrast, and the appropriate construction of tip model. In recent years, with the emergence of more and more powerful, effective and efficient algorithms for object detection, classification, image segmentation and quality enhancement, machine learning (ML) has been gradually employed in many physical (Karniadakis et al., 2021) and chemical (Mater and Coote, 2019) investigations, including the applications in solving related questions about AFM.

Using convolutional neural networks, Gordon et al. discerned several spatially correlated patterns of self-organized nanoparticles based on the mixed, highly varied experimental AFM images (Gordon et al., 2020). What's more, Alldritt et al. developed a deep learning framework that enables a unique molecular structure descriptor to match a suit of AFM images, allowing direct structure determination of organic molecules based on AFM images (Alldritt et al., 2020). Going even further, applying ML to identify configurations and structural evolution of larger and more complex systems, like liquid and ionic hydration layer, requires a great deal of effective, high quality training data obtained from simulation or experiment. As a result, it will lead to the need for a delicate balance between accuracy increasing and resource consuming. Nevertheless, ML is still a promising tool for the in-depth study of all kinds of complex water-related systems, where traditional interpretation means have been a failure or cannot even be attempted. In other words, it could save researchers from tedious and time-consuming repetitive work, and uncover hidden patterns or properties that are invisible to the human eye. Therefore, the development of ML technique will play a crucial role in prompting AFM at the forefront of the characterization technologies.

CONCLUSION

This perspective presents recent applications of AFM in the study of 2D and 3D interfacial water on solid interfaces, including structures of water networks, ice reconstructions, edge structures and growth mechanism of 2D hexagonal ice as well as the adsorption of electrolytes. The prospect of AFM is to study the more intricate and subsistent interfacial water-related systems, which needs to employ 3D- and multifunction AFM. Furthermore, the interpretation of AFM images of the intricate liquid/solid interface, especially the evolution of 3D-AFM features in AFM image, is extremely challenging due to the fact that AFM signals can be affected by environmental factors. Thus, it urgently requires a further development of effective interpretation approaches of AFM. ML is the most likely solution for the related questions about AFM imaging in complex systems associated with water, when traditional interpretation methods fail or cannot even be attempted. It is reasonable to predict that, with the improvement of AFM imaging and ML techniques, there will be a rapid increase in the atomic-scale investigations of the structural and dynamic properties of liquid/solid interfaces in the foreseeable future.

DATA AVAILABILITY STATEMENT

The original contributions presented in the study are included in the article/Supplementary Material, further inquiries can be directed to the corresponding authors.

AUTHOR CONTRIBUTIONS

All authors listed have made a substantial, direct, and intellectual contribution to the work and approved it for publication.

FUNDING

We are thankful for the financial support from the National Natural Science Foundation of China under Grant No. 11935002, the National Key R&D Program under Grant No. 2016YFA0300901, the National Postdoctoral Program for Innovative Talents under Grant No. BX2021040 and the China Postdoctoral Science Foundation under Grant No. 2021M690408.

REFERENCES

Abe, M., Sugimoto, Y., Namikawa, T., Morita, K., Oyabu, N., and Morita, S. (2007). Drift-compensated Data Acquisition Performed at Room Temperature with Frequency Modulation Atomic Force Microscopy. *Appl. Phys. Lett.* 90 (20), 203103. doi:10.1063/1.2739410

Alldritt, B., Hapala, P., Oinonen, N., Urtev, F., Krejci, O., Federici Canova, F., et al. (2020). Automated Structure Discovery in Atomic Force Microscopy. *Sci. Adv.* 6 (9), eaay6913. ARTN. doi:10.1126/sciadv.aay6913

Ardizzone, S., Formaro, L., and Lyklema, J. (1982). Adsorption from Mixtures Containing Mono- and Bivalent Cations on Insoluble Oxides and a Revision of the Interpretation of Points of Zero Charge Obtained by Titration. *J. Electroanalytical Chem. Interfacial Electrochemistry* 133 (1), 147–156. doi:10.1016/0022-0728(82)87013-7

Cao, D., Song, Y., Peng, J., Ma, R., Guo, J., Chen, J., et al. (2019). Advances in Atomic Force Microscopy: Weakly Perturbative Imaging of the Interfacial Water. *Front. Chem.* 7, 626. doi:10.3389/fchem.2019.00626

Chang, J., Liu, B., Grundy, J. S., Shao, H., Manica, R., Li, Z., et al. (2021). Probing Specific Adsorption of Electrolytes at Kaolinite-Aqueous Interfaces by Atomic Force Microscopy. *J. Phys. Chem. Lett.* 12 (9), 2406–2412. doi:10.1021/acs.jpclett.0c03521

Chen, H., Qin, Z., He, M., Liu, Y., and Wu, Z. (2020). Application of Electrochemical Atomic Force Microscopy (EC-AFM) in the Corrosion Study of Metallic Materials. *Materials* 13 (3), 668. doi:10.3390/ma13030668

DeWalt-Kerian, E. L., Kim, S., Azam, M. S., Zeng, H., Liu, Q., and Gibbs, J. M. (2017). pH-Dependent Inversion of Hofmeister Trends in the Water Structure of the Electrical Double Layer. *J. Phys. Chem. Lett.* 8 (13), 2855–2861. doi:10.1021/acs.jpclett.7b01005

Dufrêne, Y. F., Ando, T., Garcia, R., Alsteens, D., Martinez-Martin, D., Engel, A., et al. (2017). Imaging Modes of Atomic Force Microscopy for Application in Molecular and Cell Biology. *Nat. Nanotech* 12 (4), 295–307. doi:10.1038/Nnano.2017.45

Fournier, J. A., Wolke, C. T., Johnson, M. A., Odbadrakh, T. T., Jordan, K. D., Kathmann, S. M., et al. (2015). Snapshots of Proton Accommodation at a Microscopic Water Surface: Understanding the Vibrational Spectral Signatures of the Charge Defect in Cryogenically Cooled H+(H2O)n=2-28 Clusters. *J. Phys. Chem. A.* 119 (36), 9425–9440. doi:10.1021/acs.jpca.5b04355

Fukuma, T., Ueda, Y., Yoshioka, S., and Asakawa, H. (2010). Atomic-Scale Distribution of Water Molecules at the Mica-Water Interface Visualized by Three-Dimensional Scanning Force Microscopy. *Phys. Rev. Lett.* 104 (1), 016101. doi:10.1103/PhysRevLett.104.016101

Fukuma, T., and Garcia, R. (2018). Atomic- and Molecular-Resolution Mapping of Solid-Liquid Interfaces by 3D Atomic Force Microscopy. *ACS Nano* 12 (12), 11785–11797. doi:10.1021/acsnano.8b07216

Fukuma, T., Kimura, M., Kobayashi, K., Matsushige, K., and Yamada, H. (2005). Development of Low Noise Cantilever Deflection Sensor for Multienvironment Frequency-Modulation Atomic Force Microscopy. *Rev. Scientific Instr.* 76 (5), 053704. doi:10.1063/1.1896938

Fukuma, T., Reischl, B., Kobayashi, N., Spijker, P., Canova, F. F., Miyazawa, K., et al. (2015). Mechanism of Atomic Force Microscopy Imaging of Three-Dimensional Hydration Structures at a Solid-Liquid Interface. *Phys. Rev. B* 92 (15), 155412. ARTN 15541210. doi:10.1103/physrevb.92.155412

Garcia, R., Knoll, A. W., and Riedo, E. (2014). Advanced Scanning Probe Lithography. *Nat. Nanotech* 9 (8), 577–587. doi:10.1038/Nnano.2014.157

Gasser, T. M., Thoeny, A. V., Fortes, A. D., and Loerting, T. (2021). Structural Characterization of Ice XIX as the Second Polymorph Related to Ice VI. *Nat. Commun.* 12 (1), 1128. ARTN. doi:10.1038/s41467-021-21161-z

Gerrard, N., Gattinoni, C., McBride, F., Michaelides, A., and Hodgson, A. (2019). Strain Relief during Ice Growth on a Hexagonal Template. *J. Am. Chem. Soc.* 141 (21), 8599–8607. doi:10.1021/jacs.9b03311

Glatz, H., Lizundia, E., Pacifico, F., and Kundu, D. (2019). An Organic Cathode Based Dual-Ion Aqueous Zinc Battery Enabled by a Cellulose Membrane. *ACS Appl. Energ. Mater.* 2 (2), 1288–1294. doi:10.1021/acsaem.8b01851

Gordon, O. M., Hodgkinson, J. E. A., Farley, S. M., Hunsicker, E. L., and Moriarty, P. J. (2020). Automated Searching and Identification of Self-Organized Nanostructures. *Nano Lett.* 20 (10), 7688–7693. doi:10.1021/acs.nanolett.0c03213

Gross, L., Mohn, F., Moll, N., Liljeroth, P., and Meyer, G. (2009). The Chemical Structure of a Molecule Resolved by Atomic Force Microscopy. *Science* 325 (5944), 1110–1114. doi:10.1126/science.1176210

Hapala, P., Kichin, G., Wagner, C., Tautz, F. S., Temirov, R., and Jelinek, P. (2014). Mechanism of High-Resolution STM/AFM Imaging with Functionalized Tips. *Phys. Rev. B* 90 (8), 085421. doi:10.1103/PhysRevB.90.085421

Herruzo, E. T., Asakawa, H., Fukuma, T., and Garcia, R. (2013). Three-dimensional Quantitative Force Maps in Liquid with 10 Piconewton, Angstrom and Sub-minute Resolutions. *Nanoscale* 5 (7), 2678–2685. doi:10.1039/c2nr33051b

Hodgson, A., and Haq, S. (2009). Water Adsorption and the Wetting of Metal Surfaces. *Surf. Sci. Rep.* 64 (9), 381–451. doi:10.1016/j.surfrep.2009.07.001

Inami, E., and Sugimoto, Y. (2015). Accurate Extraction of Electrostatic Force by a Voltage-Pulse Force Spectroscopy. *Phys. Rev. Lett.* 114 (24), 246102. ARTN 24610210. doi:10.1103/physrevlett.114.246102

Jariwala, D., Marks, T. J., and Hersam, M. C. (2017). Mixed-dimensional van der Waals heterostructures. *Nat. Mater* 16 (2), 170–181. doi:10.1038/Nmat4703

Jeong, S.-K., Inaba, M., Mogi, R., Iriyama, Y., Abe, T., and Ogumi, Z. (2001). Surface Film Formation on a Graphite Negative Electrode in Lithium-Ion Batteries: Atomic Force Microscopy Study on the Effects of Film-Forming Additives in Propylene Carbonate Solutions. *Langmuir* 17 (26), 8281–8286. doi:10.1021/la015553h

Jesse, S., Balke, N., Eliseev, E., Tselev, A., Dudney, N. J., Morozovska, A. N., et al. (2011). Direct Mapping of Ionic Transport in a Si Anode on the Nanoscale: Time Domain Electrochemical Strain Spectroscopy Study. *Acs Nano* 5 (12), 9682–9695. doi:10.1021/nn203141g

Kaiser, U., Schwarz, A., and Wiesendanger, R. (2007). Magnetic Exchange Force Microscopy with Atomic Resolution. *Nature* 446 (7135), 522–525. doi:10.1038/nature05617

Karniadakis, G. E., Kevrekidis, I. G., Lu, L., Perdikaris, P., Wang, S., and Yang, L. (2021). Physics-informed Machine Learning. *Nat. Rev. Phys.* 3 (6), 422–440. doi:10.1038/s42254-021-00314-5

Kawakami, N., Iwata, K., Shiotari, A., and Sugimoto, Y. (2020). Intrinsic Reconstruction of Ice-I Surfaces. *Sci. Adv.* 6 (37), eabb7986. doi:10.1126/sciadv.abb7986

Kiselev, A., Bachmann, F., Pedevilla, P., Cox, S. J., Michaelides, A., Gerthsen, D., et al. (2017). Active Sites in Heterogeneous Ice Nucleation-The Example of K-Rich Feldspars. *Science* 355 (6323), 367–371. doi:10.1126/science.aai8034

Kobayashi, K., Oyabu, N., Kimura, K., Ido, S., Suzuki, K., Imai, T., et al. (2013). Visualization of Hydration Layers on Muscovite Mica in Aqueous Solution by Frequency-Modulation Atomic Force Microscopy. *J. Chem. Phys.* 138 (18), 184704. doi:10.1063/1.4803742

Kuchuk, K., and Sivan, U. (2018). Hydration Structure of a Single DNA Molecule Revealed by Frequency-Modulation Atomic Force Microscopy. *Nano Lett.* 18 (4), 2733–2737. doi:10.1021/acs.nanolett.8b00854

Laage, D., Elsaesser, T., and Hynes, J. T. (2017). Water Dynamics in the Hydration Shells of Biomolecules. *Chem. Rev.* 117 (16), 10694–10725. doi:10.1021/acs.chemrev.6b00765

Laanait, N., Callagon, E. B. R., Zhang, Z., Sturchio, N. C., Lee, S. S., and Fenter, P. (2015). X-ray-driven Reaction Front Dynamics at Calcite-Water Interfaces. *Science* 349 (6254), 1330–1334. doi:10.1126/science.aab3272

Lin, C., Avidor, N., Corem, G., Godsi, O., Alexandrowicz, G., Darling, G. R., et al. (2018). Two-Dimensional Wetting of a Stepped Copper Surface. *Phys. Rev. Lett.* 120 (7), 076101. doi:10.1103/PhysRevLett.120.076101

Luchkin, S. Y., Amanieu, H.-Y., Rosato, D., and Kholkin, A. L. (2014). Li Distribution in Graphite Anodes: A Kelvin Probe Force Microscopy Approach. *J. Power Sourc.* 268, 887–894. doi:10.1016/j.jpowsour.2014.06.143

Lupi, L., Kastelowitz, N., and Molinero, V. (2014). Vapor Deposition of Water on Graphitic Surfaces: Formation of Amorphous Ice, Bilayer Ice, Ice I, and Liquid Water. *J. Chem. Phys.* 141 (18), 18C508. Artn 18c50810. doi:10.1063/1.4895543

Ma, R., Cao, D., Zhu, C., Tian, Y., Peng, J., Guo, J., et al. (2020). Atomic Imaging of the Edge Structure and Growth of a Two-Dimensional Hexagonal Ice. *Nature* 577 (7788), 60–63. doi:10.1038/s41586-019-1853-4

Maier, S., Lechner, B. A. J., Somorjai, G. A., and Salmeron, M. (2016). Growth and Structure of the First Layers of Ice on Ru(0001) and Pt(111). *J. Am. Chem. Soc.* 138 (9), 3145–3151. doi:10.1021/jacs.5b13133

Maier, S., Stass, I., Cerdá, J. I., and Salmeron, M. (2014). Unveiling the Mechanism of Water Partial Dissociation on Ru(0001). *Phys. Rev. Lett.* 112 (12), 126101. doi:10.1103/physrevlett.112.126101

Martin-Jimenez, D., Chacon, E., Tarazona, P., and Garcia, R. (2016). Atomically Resolved Three-Dimensional Structures of Electrolyte Aqueous Solutions Near a Solid Surface. *Nat. Commun.* 7, 12164. doi:10.1038/ncomms12164

Mater, A. C., and Coote, M. L. (2019). Deep Learning in Chemistry. *J. Chem. Inf. Model.* 59 (6), 2545–2559. doi:10.1021/acs.jcim.9b00266

Maver, U., Velnar, T., Gaberšček, M., Planinšek, O., and Finšgar, M. (2016). Recent Progressive Use of Atomic Force Microscopy in Biomedical Applications. *Trac Trends Anal. Chem.* 80, 96–111. doi:10.1016/j.trac.2016.03.014

Meier, M., Hulva, J., Jakub, Z., Pavelec, J., Setvin, M., Bliem, R., et al. (2018). Water Agglomerates on Fe3O4(001). *Proc. Natl. Acad. Sci. USA* 115 (25), E5642–E5650. doi:10.1073/pnas.1801661115

Michaelides, A., Alavi, A., and King, D. A. (2004). Insight into H2O-Ice Adsorption and Dissociation on Metal Surfaces from First-Principles Simulations. *Phys. Rev. B* 69 (11), 113404. doi:10.1103/PhysRevB.69.113404

Miyazawa, K., Kobayashi, N., Watkins, M., Shluger, A. L., Amano, K.-i., and Fukuma, T. (2016). A Relationship between Three-Dimensional Surface Hydration Structures and Force Distribution Measured by Atomic Force Microscopy. *Nanoscale* 8 (13), 7334–7342. doi:10.1039/c5nr08092d

Modi, H. J., and Fuerstenau, D. W. (1957). Streaming Potential Studies on Corundum in Aqueous Solutions of Inorganic Electrolytes. *J. Phys. Chem.* 61(5), 640–643. doi:10.1021/j150551a029

Nakamura, M., and Ito, M. (2004). Ring Hexamer like Cluster Molecules of Water Formed on a Ni(111) Surface. *Chem. Phys. Lett.* 384 (4-6), 256–261. doi:10.1016/j.cplett.2003.11.110

Nelson, N., and Schwartz, D. K. (2013). Specific Ion (Hofmeister) Effects on Adsorption, Desorption, and Diffusion at the Solid-Aqueous Interface. *J. Phys. Chem. Lett.* 4 (23), 4064–4068. doi:10.1021/jz402265y

Nie, S., Feibelman, P. J., Bartelt, N. C., and Thürmer, K. (2010). Pentagons and Heptagons in the First Water Layer on Pt(111). *Phys. Rev. Lett.* 105 (2), 026102. doi:10.1103/PhysRevLett.105.026102

Novák, P., Joho, F., Lanz, M., Rykart, B., Panitz, J.-C., Alliata, D., et al. (2001). The Complex Electrochemistry of Graphite Electrodes in Lithium-Ion Batteries. *J. Power Sourc.* 97-98, 39–46. doi:10.1016/s0378-7753(01)00586-9

Peng, J., Cao, D., He, Z., Guo, J., Hapala, P., Ma, R., et al. (2018a). The Effect of Hydration Number on the Interfacial Transport of Sodium Ions. *Nature* 557 (7707), 701–705. doi:10.1038/s41586-018-0122-2

Peng, J., Guo, J., Hapala, P., Cao, D., Ma, R., Cheng, B., et al. (2018b). Weakly Perturbative Imaging of Interfacial Water with Submolecular Resolution by Atomic Force Microscopy. *Nat. Commun.* 9, 122. doi:10.1038/s41467-017-02635-5

Putnis, A. (2014). Why Mineral Interfaces Matter. *Science* 343 (6178), 1441–1442. doi:10.1126/science.1250884

Salvati Manni, L., Assenza, S., Duss, M., Vallooran, J. J., Juranyi, F., Jurt, S., et al. (2019). Soft Biomimetic Nanoconfinement Promotes Amorphous Water over Ice. *Nat. Nanotechnol.* 14 (6), 609–615. doi:10.1038/s41565-019-0415-0

Shen, C., Hu, G., Cheong, L. Z., Huang, S., Zhang, J. G., and Wang, D. (2018). Direct Observation of the Growth of Lithium Dendrites on Graphite Anodes by Operando EC-AFM. *Small Methods*, 2, 1700298. doi:10.1002/smtd.201700298

Shen, Y. R., and Ostroverkhov, V. (2006). Sum-Frequency Vibrational Spectroscopy on Water Interfaces: Polar Orientation of Water Molecules at Interfaces. *Chem. Rev.* 106 (4), 1140–1154. doi:10.1021/cr040377d

Shiotari, A., Sugimoto, Y., and Kamio, H. (2019). Characterization of Two- and One-Dimensional Water Networks on Ni(111) via Atomic Force Microscopy. *Phys. Rev. Mater.* 3 (9), 093001. doi:10.1103/PhysRevMaterials.3.093001

Shiotari, A., and Sugimoto, Y. (2017). Ultrahigh-resolution Imaging of Water Networks by Atomic Force Microscopy. *Nat. Commun.* 8, 14313. ARTN 1431310. doi:10.1038/ncomms14313

Somorjai, G. A., and Li, Y. (2010). *Introduction to Surface Chemistry and Catalysis*. Hoboken, NY: John Wiley & Sons.

Strmcnik, D., Kodama, K., van der Vliet, D., Greeley, J., Stamenkovic, V. R., and Marković, N. M. (2009). The Role of Non-covalent Interactions in Electrocatalytic Fuel-Cell Reactions on Platinum. *Nat. Chem* 1 (6), 466–472. doi:10.1038/Nchem.330

Tanaka, M., Mochizuki, A., Ishii, N., Motomura, T., and Hatakeyama, T. (2002). Study of Blood Compatibility with Poly(2-Methoxyethyl Acrylate). Relationship between Water Structure and Platelet Compatibility in Poly(2-Methoxyethylacrylate-Co-2-Hydroxyethylmethacrylate). *Biomacromolecules* 3 (1), 36–41. doi:10.1021/bm010072y

Thürmer, K., Nie, S., Feibelman, P. J., and Bartelt, N. C. (2014). Clusters, Molecular Layers, and 3D Crystals of Water on Ni(111). *J. Chem. Phys.* 141 (18), 18C520. doi:10.1063/1.4896300

Thurmer, K., and Nie, S. (2013). Formation of Hexagonal and Cubic Ice during Low-Temperature Growth. *Proc. Natl. Acad. Sci.* 110 (29), 11757–11762. doi:10.1073/pnas.1303001110

Urbakh, M., Klafter, J., Gourdon, D., and Israelachvili, J. (2004). The Nonlinear Nature of Friction. *Nature* 430 (6999), 525–528. doi:10.1038/nature02750

Verma, A., and Sharma, A. (2010). Enhanced Self-Organized Dewetting of Ultrathin Polymer Films under Water-Organic Solutions: Fabrication of Sub-micrometer Spherical Lens Arrays. *Adv. Mater.* 22 (46), 5306–5309. doi:10.1002/adma.201002768

Vilhena, J. G., Pimentel, C., Pedraz, P., Luo, F., Serena, P. A., Pina, C. M., et al. (2016). Atomic-Scale Sliding Friction on Graphene in Water. *Acs Nano* 10 (4), 4288–4293. doi:10.1021/acsnano.5b07825

Wandelt, K., and Thurgate, S. (2002). *Solid-Liquid Interfaces: Macroscopic Phenomena—Microscopic Understanding*. Heidelberg, Berlin: Springer Science & Business Media.

Wang, F., Borodin, O., Gao, T., Fan, X., Sun, W., Han, F., et al. (2018). Highly Reversible Zinc Metal Anode for Aqueous Batteries. *Nat. Mater* 17 (6), 543–549. doi:10.1038/s41563-018-0063-z

Wu, J., Yang, S., Cai, W., Bi, Z., Shang, G., and Yao, J. (2017). Multi-characterization of LiCoO2 Cathode Films Using Advanced AFM-Based Techniques with High Resolution. *Sci. Rep.* 7, 11164. ARTN 1116410. doi:10.1038/s41598-017-11623-0

Yang, S., Yan, B., Li, T., Zhu, J., Lu, L., and Zeng, K. (2015). *In Situ* studies of Lithium-Ion Diffusion in a Lithium-Rich Thin Film Cathode by Scanning Probe Microscopy Techniques. *Phys. Chem. Chem. Phys.* 17 (34), 22235–22242. doi:10.1039/c5cp01999k

Yoon, I., Abraham, D. P., Lucht, B. L., Bower, A. F., and Guduru, P. R. (2016). *In Situ* Measurement of Solid Electrolyte Interphase Evolution on Silicon Anodes Using Atomic Force Microscopy. *Adv. Energ. Mater.* 6 (12), 1600099. ARTN. doi:10.1002/aenm.201600099

Zhou, X., Lu, Y., Zhang, Q., Miao, L., Zhang, K., Yan, Z., et al. (2020). Exploring the Interfacial Chemistry between Zinc Anodes and Aqueous Electrolytes via an *In Situ* Visualized Characterization System. *ACS Appl. Mater. Inter.* 12 (49), 55476–55482. doi:10.1021/acsami.0c17023

Zhu, J., Zeng, K., and Lu, L. (2012). *In-situ* Nanoscale Mapping of Surface Potential in All-Solid-State Thin Film Li-Ion Battery Using Kelvin Probe Force Microscopy. *J. Appl. Phys.* 111 (6), 063723. doi:10.1063/1.3699214

Conflict of Interest: The authors declare that the research was conducted in the absence of any commercial or financial relationships that could be construed as a potential conflict of interest.

The reviewer (RM) declared a past co-authorship with the authors (DC, LX) to the handling Editor.

Publisher's Note: All claims expressed in this article are solely those of the authors and do not necessarily represent those of their affiliated organizations, or those of the publisher, the editors and the reviewers. Any product that may be evaluated in this article, or claim that may be made by its manufacturer, is not guaranteed or endorsed by the publisher.

frontiers in Chemistry

ORIGINAL RESEARCH
published: 06 October 2021
doi: 10.3389/fchem.2021.748017

Protein- and Cell-Resistance of Zwitterionic Peptide-Based Self-Assembled Monolayers: Anti-Biofouling Tests and Surface Force Analysis

*Ryongsok Chang[1], Evan Angelo Quimada Mondarte[1], Debabrata Palai[1], Taito Sekine[1], Aki Kashiwazaki[2], Daiki Murakami[2], Masaru Tanaka[2,3] and Tomohiro Hayashi[1,4,5]**

[1]Department of Material Science and Engineering, School of Materials and Chemical Technology, Tokyo Institute of Technology, Yokohama, Japan, [2]Institute for Materials Chemistry and Engineering, Kyushu University, Fukuoka, Japan, [3]Department of Applied Chemistry, Graduate School of Engineering, Kyushu University, Fukuoka, Japan, [4]JST-PRESTO, Saitama, Japan, [5]The Institute for Solid State Physics, the University of Tokyo, Chiba, Japan

OPEN ACCESS

Edited by:
Min-Cherl JUNG,
University of Tsukuba, Japan

Reviewed by:
Ravindra Pandey,
Indian Institute of Technology Roorkee, India
Apurba Das,
Indian Institute of Technology Indore, India

***Correspondence:**
Tomohiro Hayashi
tomo@mac.titech.ac.jp

Specialty section:
This article was submitted to Physical Chemistry and Chemical Physics, a section of the journal Frontiers in Chemistry

Received: 27 July 2021
Accepted: 15 September 2021
Published: 06 October 2021

Citation:
Chang R, Quimada Mondarte EA, Palai D, Sekine T, Kashiwazaki A, Murakami D, Tanaka M and Hayashi T (2021) Protein- and Cell-Resistance of Zwitterionic Peptide-Based Self-Assembled Monolayers: Anti-Biofouling Tests and Surface Force Analysis. Front. Chem. 9:748017. doi: 10.3389/fchem.2021.748017

Peptide-based self-assembled monolayers (peptide-SAMs) with specific zwitterionic amino acid sequences express an anti-biofouling property. In this work, we performed protein adsorption and cell adhesion tests using peptide-SAMs with repeating units of various zwitterionic pairs of amino acids (EK, DK, ER, and DR). The SAMs with the repeating units of EK and DK (EK and DK SAMs) manifested excellent bioinertness, whereas the SAMs with the repeating units of ER and DR (ER and DR SAMs) adhered proteins and cells. We also performed surface force measurements using atomic force microscopy to elucidate the mechanism underlying the difference in the anti-biofouling property. Our measurements revealed that water-induced repulsion with a range of about 8 nm acts between EK SAMs (immobilized on both probe and substrate) and DK SAMs, whereas such repulsion was not observed for ER and DR SAMs. The strength of the repulsion exhibited a clear correlation with the protein- and cell-resistance of the SAMs, indicating that the interfacial water in the vicinity of EK and DK SAMs is considered as a physical barrier to deter protein and cells from their adsorption or adhesion. The range of the repulsion observed for EK and DK SAMs is longer than 8 nm, indicating that the hydrogen bonding state of the interfacial water with a thickness of 4 nm is modified by EK and DK SAMs, resulting in the expression of the anti-biofouling property.

Keywords: anti-biofouling behavior, surface force analysis, self-assembled monolayers, blood compatibility, zwitterionic peptide, biocompatibility, atomic force microcopy, quartz crystal microbalance

INTRODUCTION

Biomolecules including proteins, lipids, DNA, and polysaccharides smartly interact or react with each other, and then our bodies can maintain the homeostasis of our lives. The biomolecules are responsible for many biomolecular processes such as signal processing, enzymatic reaction, self-assembly, replication. These processes occur in crowding conditions, in which the biomolecules coexist at high concentrations (approximately 200–320 mg/ml in cells) (Cayley et al., 1991).

Therefore, biomolecules are endowed with the capability of forming specific bonds with their target molecules and of rejecting other non-target molecules.

To elucidate the mechanism underlying the rejection of non-specific interaction in the molecular recognition of proteins, White *et al.* investigated the composition of amino acid residues at the protein surfaces, which are loca for the biomolecular processes. Their most significant finding was that glutamic acid (E) and lysine (K) are the most and second abundant amino acids (they investigated 1,162 proteins constituting a human body). Moreover, the authors also reported that the zwitterionic pair of E and K is the most frequently found pair on the protein surfaces, followed by DK (D stands for aspartic acid) (White et al., 2012).

Based on these findings, Jiang *et al.* constructed peptide-based self-assembled monolayers (peptide-SAMs) with various repeating zwitterionic pairs of amino acids (Chen et al., 2009; Nowinski et al., 2012; White et al., 2012; White et al., 2013). They found out that self-assembled monolayers (SAMs) containing the repeating units of EK and DK (denoted as EK and DK SAMs hereafter) exhibited excellent anti-biofouling properties, whereas SAMs containing the repeating units of ER and DR (denoted as ER and DR SAMs hereafter) did not. They explained that the difference in the anti-biofouling behavior originates in the different hydration states of the peptide molecules. Unfortunately, the mechanism underlying the sharp contrast in the anti-biofouling properties and the difference in the interfacial interaction have not been clarified experimentally.

This work aims to clarify the interfacial interaction responsible for the protein- and cell-(peptide-SAM) interactions. For this, we first characterize the fundamental physicochemical properties (molecular packing density, thickness, and water contact angle) of the peptide-SAMs and evaluate their anti-biofouling properties by protein-adsorption and cell-adhesion tests. In addition, we performed surface force measurements to elucidate the interfacial interaction responsible for the anti-biofouling property of the peptide-SAMs.

MATERIALS AND METHODS

Fabrication of Peptide-Self-Assembled Monolayers

We used a p-type silicon wafer [Si(100), Thickness and diameter of the wafers are 525 ± 25 μm and 100.0 ± 0.5 mm, respectively, Furuuchi Chemical Co., Japan] cut into pieces with a size of 10 × 10 mm^2 as the substrates. The silicon substrates were washed by ultrasonic cleaning in acetone, ethanol, and pure water, followed by a nitrogen gas blow.

Colloidal probes were prepared by attaching a washed silica bead (diameter: 18 μm, Duke Sci. Corp., CA, United States) to the end of a tipless cantilever (NP-OW, Bruker, MA, United States) using epoxy glue (Araldite, Huntsman Corp., UT, United States). The nominal spring constant of the cantilevers was 0.06 N m^{-1}. After attaching the silica bead, the probes were kept for 12 h at room temperature to fix the bead at the cantilever. Then, the colloidal probes and the silicon substrates were cleaned with a UV-O_3 cleaner (UV-300, SUMCO, Japan) for 15 min. First, the colloidal probes and substrates were coated with a wetting layer (adhesion promoter) of germanium (99.999%, Nilaco Corp., Japan) with a thickness of 5 nm by thermal evaporation under vacuum (base pressure 1.0 × 10^{-5} Pa) at 350 K. Then, the germanium-coated probes and substrates were coated with gold (99.999%, Furuuchi Chemical Co., Japan) with a thickness of 100 nm at 350 K (Logeeswaran VJ et al., 2009). The deposition rates for germanium and gold were 0.01 and 0.1 nm s^{-1}, respectively.

The gold-coated probes and substrates were immersed in a phosphate-buffered saline (PBS) solution (pH 7.4 and ionic strength 167 mM) containing 0.14 mM peptide for 24 h to form covalent bonds between the thiol groups and gold. After the immersion, the probes and substrates were rinsed with pure water to remove excess adsorbed molecules. The peptide-SAMs were prepared for static water contact angle measurement, platelet adhesion test, and surface force measurement. The amino acid sequences of the peptide were summarized in **Table 1**.

TABLE 1 | List of peptides used in this work.

Abbreviation	Amino acid sequence
EK	EKEKEKE-PPPPC-Am[a]
DK	DKDKDKD-PPPPC-Am
ER	ERERERE-PPPPC-Am
DR	DRDRDRD-PPPPC-Am

[a]*Am stands for amide bond group ($CONH_2$).*

X-Ray Photoelectron Spectroscopy

X-ray photoelectron (XP) spectra in C1s and S2p were measured with a commercial XPS system (Theta Probe, Thermo Electron, United Kingdom). Al Kα radiation (photon energy of 1,486.6 eV and spot size of 400 μm) was used for the X-ray. All XP spectra were acquired at a take-off angle of 48° from the surface normal. The numbers of scans of the C1s and S2p spectra were 40 and 1,000, respectively.

Static Water Contact Angle Measurement

Static water contact angles (WCA) were measured by the sessile drop method at room temperature (Model G-1-1,000, ERMA, Tokyo, Japan). 2 μl of the water droplet was placed on a peptide SAM, and the WCAs were recorded after 30 s. The measurement was carried out at five different points per substrate using three substrates for one peptide SAM and averaged (n = 15).

Fibrinogen Adsorption Test

We employed quartz crystal microbalance with an energy dissipation system (QCM-D) (D300, Q-Sense, Sweden) to measure the amounts and viscoelasticity of fibrinogen adsorbed onto the peptide-SAMs. Firstly, gold-coated QCM sensors were cleaned with a UV-O_3 cleaner for 10 min, then immersed into a 1:1:5 solution of hydrogen peroxide (30%), ammonia (25%), and pure water heated to a temperature of

75 C for 5 min. Immediately rinse with pure water and blow of nitrogen gas. Then the gold-coated QCM sensors were cleaned with UV-O_3 cleaner for 10 min. The peptide-SAMs were prepared in the same manner for the gold-coated substrates. We used human fibrinogen (Biogenesis Ltd., United Kingdom) dissolved in PBS at a concentration of 1 mg mL^{-1}. In the QCM measurements, a measurement chamber was first filled with PBS. Then, the fibrinogen solution was injected into the chamber. After the sensor's resonant frequency became constant, the PBS solution was injected into the chamber again for rinsing. The amount of the adsorbed fibrinogen was defined as the difference in weights before the injection and after rinsing. The conversion from resonant frequency to weight was based on the Sauerbrey equation shown as **Eq. 1**,

$$\Delta m = -\frac{C \cdot \Delta f}{n} \tag{1}$$

where C = 17.7 ng cm^{-2} Hz^{-1}, Δf is the change in the resonant frequency due to protein adsorption, and the n is the overtone number [(n = 3) in this work]. All data were collected at the n = 3 overtone. The energy dissipation factor D was measured by switching off the driving power and monitoring the amplitude decay profile. The amplitude decays as an exponentially damped sinusoidal function with a characteristic decay time (τ_0). The decay time is related to the energy dissipation factor (D) shown as **Eq. 2**,

$$D = \frac{1}{\pi f \tau_0} \tag{2}$$

where f is the resonant frequency of the sensor. The viscoelasticity of the protein layer was compared with the value of Δd (change in energy dissipation)/Δf (change in resonant frequency). In this approach, a rigid layer yields a small value of $\Delta d/\Delta f$.

TABLE 2 | The number of carbon atoms in the peptide molecules and relative packing density with respect to peptides. The packing densities were calculated by C1s intensity and divided by the number of carbon atoms in the molecules.

Peptide-SAMs	Number of carbon atoms in the peptide molecules	C1s intensity/the number of carbon atoms in the molecules
EK SAMs	61	32.0
DK SAMs	57	35.5
ER SAMs	61	31.6
DR SAMs	57	36.3

Platelet Adhesion Test

Blood was drawn from healthy volunteers and mixed with a 1/9 volume of acid citrate dextrose (ACD). Platelet-rich plasma (PRP) and platelet-poor plasma (PPP) were obtained by centrifugation of the blood at 1,500 rpm for 5 min and at 4,000 rpm for 10 min, respectively. The platelet suspension plasma containing 2 × 10^5 cells μl^{-1} of platelet was prepared by mixing the PRP with PPP. The platelet concentration was determined with a cell-counting hemato-cytometer (Neubauer chamber). Then, 200 µl of the plasma was placed on the peptide-SAMs and incubated for 60 min at 37 C. After the peptide-SAMs were washed with PBS solution twice, the peptide-SAMs were immersed in 1% glutaraldehyde in PBS solution overnight at 4 C to fix the adhered platelets. The fixed samples were immersed in PBS for 10 min, in a 1:1 mixture of PBS and pure water for 8 min, and in pure water for 8 min twice and dried in air overnight. Then the samples were sputter-coated using gold (JFC-1200, JEOL) prior to observation by scanning electron microscopy (VE-9800, KEYENCE, Japan). The number of adhered platelet cells was counted in five positions in the SEM images (100 × 80 μm^2) using nine substrates for one peptide-SAM and averaged (n = 45).

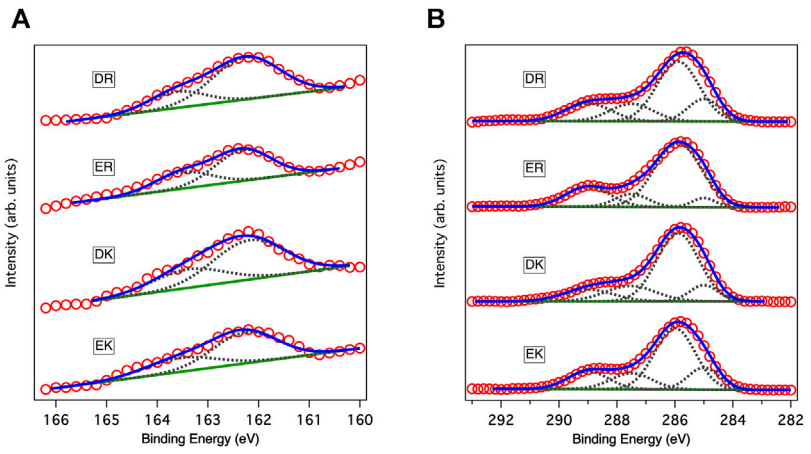

FIGURE 1 | XP spectra of peptide-SAMs in **(A)** C1s and **(B)** S2p regions. Red circles, solid blue lines, solid green lines, and gray dotted lines show data points in the spectra, fitting results, backgrounds, and deconvoluted spectra, respectively. In fitting the spectra in the S2p region, the ratio between the two states and the splitting gap were kept at 2:1 and 1.2 eV, respectively.

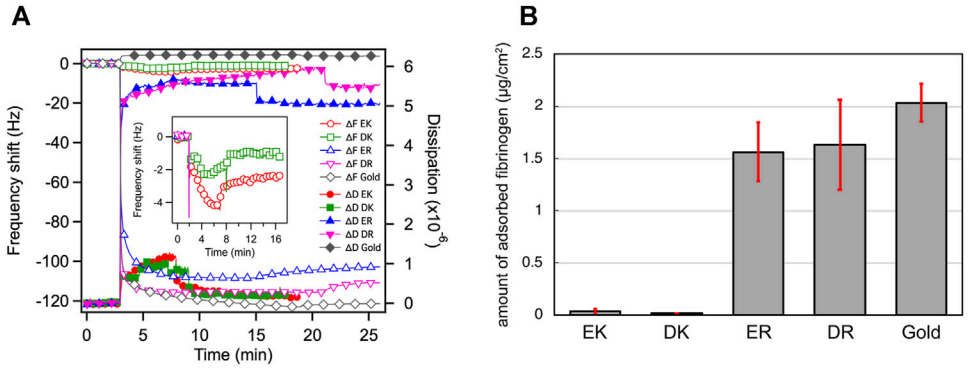

FIGURE 2 | (A) QCM chart (frequency and dissipation) observed for adsorption of fibrinogen onto the peptide-SAMs. Rinsing with PBS were performed at 8, 9, 15, 21, 17 min for EK, DK, ER, DR, and bare gold, respectively. **(B)** The amount of adsorbed fibrinogen on peptide-SAMs in the PBS solution measured by QCM-D. Error bars denote standard deviation (n = 3).

TABLE 3 | $\Delta d/\Delta f$ of fibrinogen on the peptide-SAMs in the PBS solution measured by QCM-D after the rinsing. Numbers in parenthesis are standard deviations (n = 3).

Peptide-SAMs	$\Delta d/\Delta f$ (10^{-6})
EK SAMs	0.25 (0.078)
DK SAMs	0.13 (0.046)
ER SAMs	0.04 (0.006)
DR SAMs	0.04 (0.005)

Surface Force Measurement

All force curve measurements were performed with a commercial AFM system equipped with a liquid cell (MFP-3D, Oxford Instruments, United Kingdom). Spring constants of the colloidal probes were determined by monitoring the thermal fluctuations of the probes (Hutter and Bechhoefer, 1993). Velocity on approach and retraction of the probe was fixed at 200 nm s^{-1}. All force measurements were performed in PBS solution and 1 mM PB (pH 7.4 and ionic strength 2.32 mM) at room temperature. In this study, we simply defined a distance of zero as where linearity in the constant compliance region started in the force-distance curve. We measured 50 times force curves and averaged them.

RESULTS AND DISCUSSION

Characterization of Peptide-Self-Assembled Monolayers

Figure 1A shows the XP spectra in an S2p region. The spectra in the S2p region for all peptide-SAMs were deconvoluted into two peaks with an area ratio of 2:1 due to the spin-orbit coupling. The peaks at 162 eV and its satellite peak at 163.2 eV are assigned to the bound state of the sulfur (sulfur is covalently attached to the gold substrate) (Ishida et al., 1999). We did not observe any peaks assigned to the unbound state (usually observed at 163–164 eV), indicating that the peptide molecules are immobilized on gold substrates via a covalent bond and repeating units of the zwitterionic peptides face to the solution phase.

Figure 1B displays the XP spectra of the peptide-SAMs in the C1s region. The spectra are deconvoluted into four peaks. Peaks at about 284, 286, 287, and 289 eV can be assigned to C-(C, H), C-O, C-O next to O=C-O (carbonyl group), and carbonyl group, respectively (Pourcelle et al., 2007). Next, we compared the total peak area divided by the number of carbon atoms in the peptide molecules (**Table 2**). The results suggest that the peptide molecules are accumulated on the substrate and that the packing densities of DK and DR SAMs are higher than those of EK and ER SAMs. The difference may be attributed to the difference in the steric structure of the amino acid residues in the peptide molecules.

We also performed force-distance curve measurements using a probe with a sharp tip (tip radius is about 8 nm) (**Supplementary Figure S1**). The results showed that the thicknesses of the peptide-SAMs were around 2 nm, which corresponds to the Cα-to-Cα end-to-end distance of the EK (White et al., 2012). Taken together, the peptide molecules form a monolayer on gold substrates via covalent gold-sulfur bonds with directing the zwitterionic parts toward the solution phase.

Fibrinogen Adsorption Test

Figure 2A shows the change in the resonant frequency and energy dissipation measured in the QCM measurements. ER and DR SAMs adsorbed fibrinogen with a significant increase in the dissipation rapidly after the injection of the protein solution, whereas we did not observe the adsorption for EK and DK SAMs without a drastic change in the energy dissipation. **Figure 2B** compares the amount of the adsorbed fibrinogen after rinsing, displaying the clear contrast in the degree of protein resistance, in good agreement with the report by Chen et al. (2009). In particular, the protein-resistance of EK and DK SAMs are comparable to that of the SAMs comprised of oligo (ethylene glycol)- or sulfobetaine-terminated alkanethiols, which are often widely used for the suppression of non-specific adsorption in biosensing (Hayashi et al., 2012; Tanaka et al., 2013; Sekine et al., 2015; Chang et al., 2018; Kwaria et al., 2020; Hayashi, 2021; Tanaka et al., 2021).

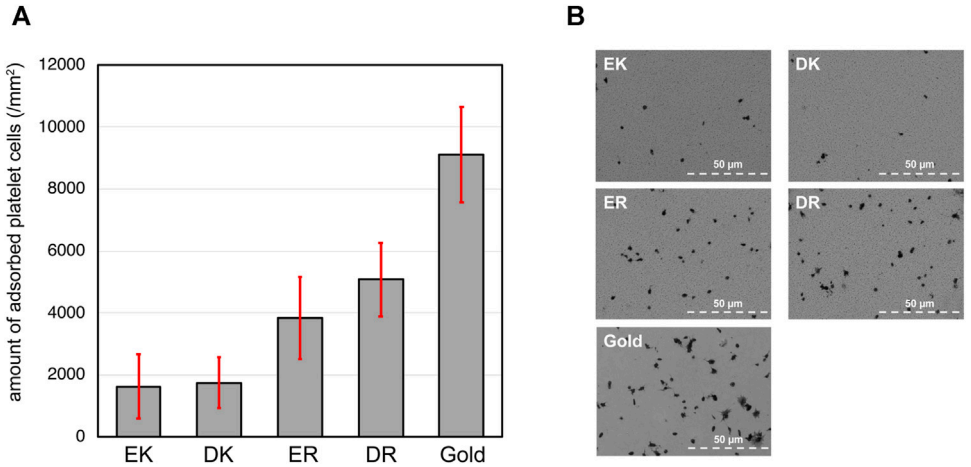

FIGURE 3 | (A) The density of adhered platelet cells on peptide-SAMs and gold surface. Error bars denote standard deviation (n = 45). **(B)** Representative SEM images of the adhered platelet cells on the peptide-SAMs and the gold surface. Note that the particles smaller than the platelets are gold clusters formed after the deposition of gold to enhance the conductivity for SEM imaging.

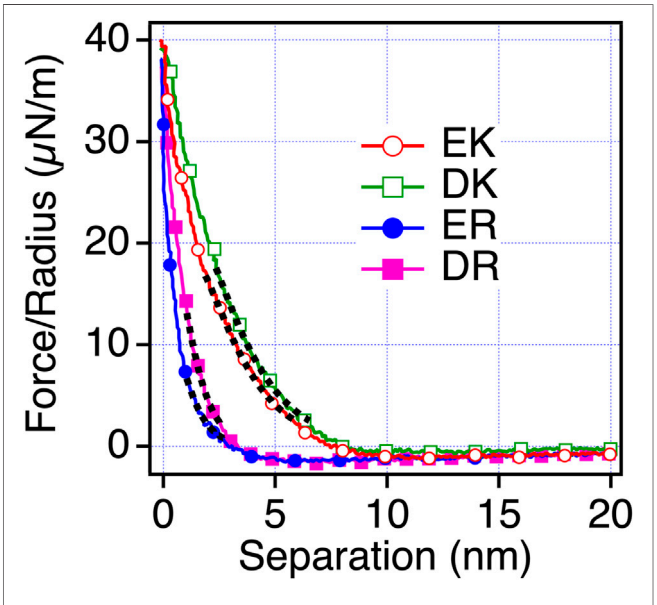

FIGURE 4 | Force-separation curves recorded on an approach for the symmetric system of the peptide-SAMs (the same SAMs formed on both probe and substrate) in PBS solution. The fitting results are shown with black dotted lines.

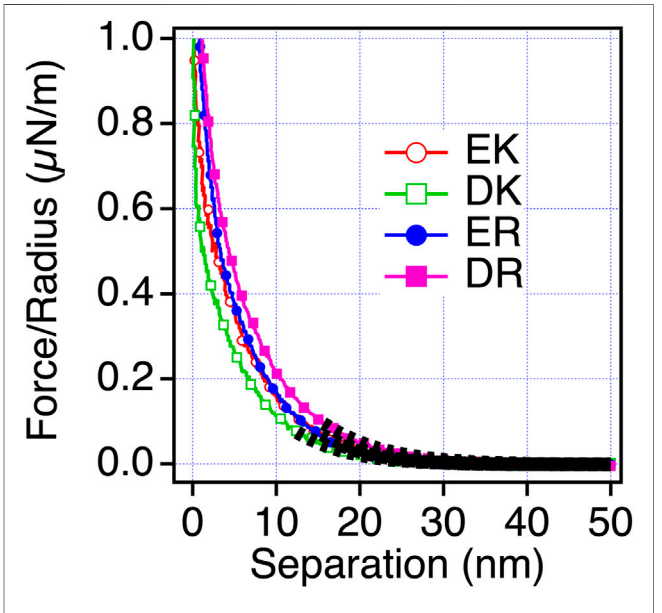

FIGURE 5 | Force-separation curves recorded on an approach for the symmetric system of the peptide-SAMs (the same SAMs prepared for both the probe and substrate) in a 1 mM PB solution. The fitting results are shown in a black dotted line.

TABLE 4 | Static water contact angles (WCA).

Peptide-SAMs	Static water contact angle[a]
EK SAMs	34 (11)
DK SAMs	27 (9.2)
ER SAMs	29 (8.1)
DR SAMs	34 (11)

[a]*Values in parentheses are standard deviation (n = 15).*

The $\Delta d/\Delta f$ values also provide insight into the mechanical properties of the protein layer formed on the peptide-SAMs (**Table 3**). The $\Delta d/\Delta f$ values for protein-resistant EK and DK are higher than those for protein-adsorbing ER and DR SAMs (**Table 3**). These results indicate that the interaction of fibrinogen with ER and DR SAMs is stronger than that with EK and DK SAMs and/or the formed protein layer is highly viscoelastic because of the denaturation of the protein molecules after adsorption.

TABLE 5 | Decay lengths of the repulsion acting between the peptide-SAMs in PBS.

Peptide-SAMs	Decay length in PBS (nm)
EK SAMs	1.76
DK SAMs	1.86
ER SAMs	0.698
DR SAMs	0.746

Platelet Adhesion Test

The density of adhered platelet cells on the peptide-SAMs and the representative SEM images of the substrates are summarized in **Figures 3A,B**. Compared with the bare gold substrates, the adhesion and activation of platelets were suppressed on the peptide-SAMs. However, there was a distinct difference in their anti-platelet adhesion properties. Apparently, we can conclude that the platelet compatibility of EK and DK SAMs is higher compared with ER and DR SAMs.

In our platelet adhesion test, plasma proteins first accumulate on the peptide-SAMs and form a layer. Then, the protein layer interfaces the peptide-SAMs and platelet cells. The proteins' composition, orientation, and conformation significantly affect the adhesion and activation of platelet cells (Hylton et al., 2005). There have been many works reporting a clear correlation between protein adsorption and platelet adhesion. In particular, adsorption tests of fibrinogen correlate well with platelet cells' adhesion (Tanaka et al., 2000). Our results here are in good agreement with previous findings. The analysis of the protein composition by mass spectroscopy is underway (Hirohara et al., 2019).

Static Water Contact Angle Measurements

Water contact angles (WCA) have often been an indicator of protein- and cell resistance for monolayer and polymer systems, although there are apparent exceptions (Alexander and Williams, 2017; Kwaria et al., 2020). We also investigated the surface wettability of peptide-SAMs by WCA on the peptide-SAMs (**Table 4**). The WCA showed that all peptide-SAMs are hydrophilic in terms of macroscopic wettability, indicating that strong interaction of fibrinogen with ER and DR SAMs is due not to hydrophobic interaction but to electrostatic interaction.

The main finding here is that the bioinertness of the zwitterionic peptide-SAMs cannot be explained with the macroscopic wettability of the peptide-SAMs. This has also been found for the SAMs of oligo (ethylene glycol)-terminated and several blood compatible polymers, including relatively hydrophobic poly (2-methoxyethyl acrylate) (PMEA) and hydrophilic poly (2-methacryloyloxyethyl phosphorylcholine) (PMPC) (Hayashi et al., 2007; Tanaka et al., 2013; Hayashi, 2021; Tanaka et al., 2021).

Surface Force Measurements

To understand the mechanism underlying the anti-biofouling property of EK and DK SAMs and the difference in the protein and cell resistance among the peptide-SAMs, we investigated the surface force induced by the peptide-SAMs. To clarify the physical origin of the surface forces, we performed surface force measurements in PBS solution, which is the solution condition used in protein adsorption and cell adhesion tests (**Figure 4**). The repulsive force was observed for all the peptide-SAMs, although the ranges of the repulsive force are different. As for ER and DR SAMs, the onset of the repulsion is at 4–5 nm of the separation. In contrast, the working distance of the repulsion for EK and DK SAMs is at around 8–9 nm. The repulsion's decay lengths obtained by fitting the curves with a single exponential function are summarized in **Table 5**. The interaction in water is described as a sum of DLVO (electrostatic and van der Waals interaction) and non-DLVO (hydration force, steric repulsion, etc.) interactions. Among them, possible origins of the repulsive force are electrostatic double-layer force (DLVO), hydration force, and steric repulsion due to the deformation of the SAM after the physical contact of the peptide-SAMs (non-DLVO). Considering that the thicknesses of all the peptide-SAMs are about 2 nm (**Supplementary Figure S1**), the steric repulsion is not the origin of the difference in the repulsion observed in the force measurements.

Next, we examined the possibility of the electric double layer force for the difference in the repulsion by changing the ion concentration of the solution. We performed the measurements in phosphate buffer (PB) (1 mM) solution, whose Debye length is compared with PBS solution (**Figure 5**). With this solution condition, we observed the repulsion for all the peptide-SAMs, and the force curves can be fitted with the DLVO theory shown as **Eq. 3**,

$$F(D) = -\frac{H_s R}{6D^2} + \frac{4\pi R \epsilon \epsilon_0 \psi^2}{\lambda_D}\left[exp\left(\frac{-D}{\lambda_D}\right) - exp\left(\frac{-2D}{\lambda_D}\right)\right] \quad (3)$$

where H_s, D, R, ε, ε_0, ψ, and λ_D are the Hamaker constant for the interaction of peptide-SAMs across the water, the separation between the probe and surface, probe radius, relative dielectric constant, dielectric constant of vacuum, the surface potential of the surface and probe (peptide-SAMs), and the Debye length,

TABLE 6 | Estimated surface potential and Hamaker constant from force-separation curves between peptide SAMs in 1 mM PB.

Peptide-SAMs	Debye length (nm)	Surface potential (mV)	Hamaker constant (J)
EK SAMs	6.2	8.5	1.2×10^{-21}
DK SAMs	5.8	7.4	1.0×10^{-21}
ER SAMs	5.4	9.2	1.2×10^{-21}
DR SAMs	6.7	9.7	2.4×10^{-21}

respectively (Butt et al., 2005). The results of the fitting are shown in **Figure 5** and **Table 6**.

The fitting results show that the calculated Debye lengths range between 5.4 and 6.7 nm. Compared with the decay length observed in PBS, the decay lengths of the repulsion are much longer compared with those in PBS (theoretical Debye length of PBS is 0.745 nm) and are in agreement with the theoretical value (6.32 nm). Therefore, we concluded that electrostatic double-layer force is dominant in PB solution. Unfortunately, we cannot determine the signs of the surface potentials because the same SAMs were formed on both probe and surface (**Eq. (3)**). By considering the strong basic character of arginine (R) (Fitch et al., 2015), we speculate that ER and DR SAMs are more positively charged than EK and DK SAMs.

The trend in the strength of the repulsion depending on the sequences in PB is different from that in PBS. Therefore, we consider that the repulsion observed for EK and DK SAMs is not electrostatic double-layer force. The decay lengths of the repulsion observed for EK and DK SAMs are far beyond the theoretical Debye length of PBS (0.745 nm) and cannot be explained by the electrostatic double-layer force. Combining the above discussions, the only possible origin for the repulsion is water-induced force.

To confirm that the origin of the repulsive force observed for EK and DK in PBS is water-induced force, we measured the interaction force in mixtures of PBS and ethanol. When water is mixed with ethanol, water and ethanol molecules are phase-separated at a low concentration of ethanol. When the concentration of ethanol increases, ethanol molecules are mixed with water molecules with disrupting three-dimensional networks of hydrogen bonding of water. At the ethanol's molar ratio of 0.23, water and ethanol completely mix together (Matsumoto et al., 1995). As seen in **Figure 6**, The short-range repulsion in PBS disappeared in ethanol and PBS solution. The results indicated that water molecules near EK and DK possess the hydration barrier with a thickness of 3–4 nm (half of the working distance of the repulsion force) and prevent the approaches of protein molecules and cells, whereas ER and DR possess the hydration barrier with a thickness less than 2 nm and allowed their approaches.

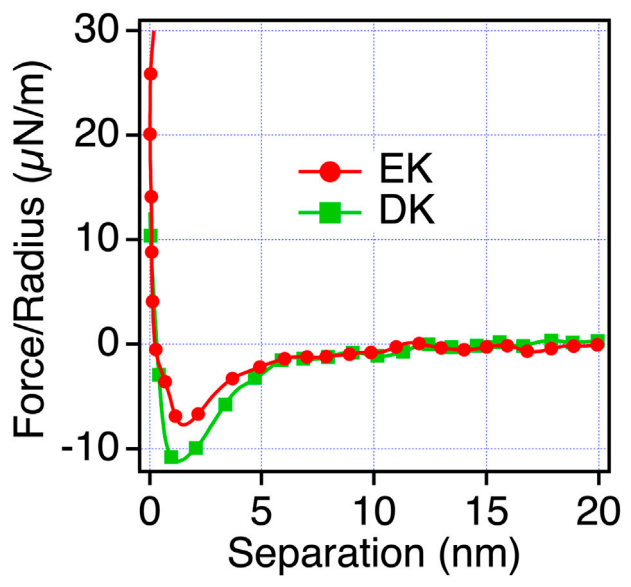

FIGURE 6 | Force-separation curves recorded on an approach for the symmetric system of the EK and DK SAMs (the same SAMs prepared for both the probe and substrate) in ethanol and PBS solution [0.23 mol (ethanol)/mol (water)].

CONCLUSION AND PERSPECTIVES

In this work, we attempted to unveil the mechanism underlying the anti-biofouling properties of zwitterionic peptide-SAMs reported by Chen et al. (2009) and White et al. (2012). First, we investigated the adsorption states of the peptide molecules by XPS and measured the thicknesses of the peptide layers by AFM, confirming that the molecules form monolayers immobilized via covalent Au-S bonds on gold. Second, we verified that EK and DK SAMs exhibited excellent protein- and platelet resistance, whereas ER and DR did not, leading to the conclusion that the difference in the anti-biofouling property cannot be explained by their macroscopic surface wettability.

To evaluate the interfacial interaction responsible for the anti-biofouling property, we performed surface force measurements to assess the interaction between the peptide-SAMs. Water-induced repulsion with a range more extended than 8 nm was observed for EK and DK SAMs, whereas only weak and short-ranged (<4 nm) repulsion was observed. Furthermore, there was a clear correlation of protein- and platelet-resistance with the water-induced repulsion. Therefore, we concluded that the water-induced repulsion induced by the EK and DK SAMs is responsible for their anti-biofouling property.

Our previous surface force measurements revealed a similar water barrier for SAMs of oligo (ethylene glycol)-terminated alkanethiols (OEG-SAMs) and DNA-based SAMs (Hayashi et al., 2012; Sekine et al., 2015; Kanayama et al., 2016; Sekine et al., 2017; Sekine et al., 2018). As for the OEG-SAMs, the strength and acting range of the water-induced repulsion are very sensitive to the number of the EG units in the molecule and molecular packing density. In DNA-based SAMs, the strength and acting range critically depend on the complementarity of terminal base pairs of the DNA molecules. These facts suggest that the local arrangement of functional groups with respect to water modulates, and the resulting hydrogen bonding network of the interfacial water determines anti-biofouling potential.

There have been many works on the hydration of zwitterionic functional groups, including carboxy or sulfobetaine, phosphatidylcholine, zwitterionic peptides. Many of them stated the importance of the strongly trapped water molecules to the charged groups in their anti-biofouling property. Also, some works suggested that the guanidinium group in R is one of the weakly hydrated cations and this may be a weak protein resistance of ER and DR SAMs (Mason et al., 2003; White et al., 2013). However, our surface force analysis revealed that the water barrier extends up to 4 nm, suggesting that the water-peptide (EK and DK) interaction

modulates the hydrogen bonding states of the vicinal water molecules, resulting in the formation of the physical barrier to prevent the approach of protein molecules and cells.

In this work, we clarified the correlation among the amino acid sequence of the peptide constituting the SAMs, anti-biofouling property, and water-induced interfacial forces. However, unfortunately, we have not elucidated the molecular processes inducing water-mediated repulsion responsible for the anti-biofouling property. Currently, we are performing surface vibrational spectroscopy measurements and theoretical calculations to understand the hydrogen bonding states of the interfacial water. These results will be published elsewhere.

DATA AVAILABILITY STATEMENT

The original contributions presented in the study are included in the article/**Supplementary Files,** further inquiries can be directed to the corresponding author.

AUTHOR CONTRIBUTIONS

RC and TH designed experiments and performed XP measurements. RC performed WCA and Surface force measurements and analyzed WCA. RC, EM, and DP performed fibrinogen adsorption test. RC, AK, DM, and MT performed platelet adhesion test and analyzed the data. TS and TH performed the initial investigation of this project. TH supervised this project.

FUNDING

This work was supported by the JSPS KAKENHI grant (Grant NOs JP21H05511, JP20H05210, JP 19H02565 and JP19H05720) and Cooperative Research Program "Dynamic Alliance for Open Innovation Bridging Human, Environment, and Materials.

ACKNOWLEDGMENTS

We thank Kazue Taki for the administration of this project.

SUPPLEMENTARY MATERIAL

The Supplementary Material for this article can be found online at: https://www.frontiersin.org/articles/10.3389/fchem.2021.748017/full#supplementary-material

REFERENCES

Alexander, M. R., and Williams, P. (2017). Water Contact Angle Is Not a Good Predictor of Biological Responses to Materials. *Biointerphases* 12, 02C201. doi:10.1116/1.4989843

Butt, H.-J., Cappella, B., and Kappl, M. (2005). Force Measurements with the Atomic Force Microscope: Technique, Interpretation and Applications. *Surf. Sci. Rep.* 59, 1–152. doi:10.1016/j.surfrep.2005.08.003

Cayley, S., Lewis, B. A., Guttman, H. J., and Record, M. T. (1991). Characterization of the Cytoplasm of *Escherichia coli* K-12 as a Function of External Osmolarity. *J. Mol. Biol.* 222, 281–300. doi:10.1016/0022-2836(91)90212-o

Chang, R., Asatyas, S., Lkhamsuren, G., Hirohara, M., Mondarte, E. A. Q., Suthiwanich, K., et al. (2018). Water Near Bioinert Self-Assembled Monolayers. *Polym. J.* 50, 563–571. doi:10.1038/s41428-018-0075-1

Chen, S., Cao, Z., and Jiang, S. (2009). Ultra-low Fouling Peptide Surfaces Derived from Natural Amino Acids. *Biomaterials* 30, 5892–5896. doi:10.1016/j.biomaterials.2009.07.001

Fitch, C. A., Platzer, G., Okon, M., Garcia-Moreno E., B., and McIntosh, L. P. (2015). Arginine: Its pKavalue Revisited. *Protein Sci.* 24, 752–761. doi:10.1002/pro.2647

Hayashi, T., Tanaka, M., Yamamoto, S., Shimomura, M., and Hara, M. (2007). Direct Observation of Interaction between Proteins and Blood-Compatible Polymer Surfaces. *Biointerphases* 2, 119–125. doi:10.1116/1.2794712

Hayashi, T., Tanaka, Y., Koide, Y., Tanaka, M., and Hara, M. (2012). Mechanism Underlying Bioinertness of Self-Assembled Monolayers of Oligo(ethyleneglycol)-Terminated Alkanethiols on Gold: Protein Adsorption, Platelet Adhesion, and Surface Forces. *Phys. Chem. Chem. Phys.* 14, 10196–10206. doi:10.1039/c2cp41236e

Hayashi, T. (2021). Water at Interfaces: Its Behavior and Roles in Interfacial Phenomena. *Chem. Lett.* 50, 1173–1180. doi:10.1246/cl.210049

Hirohara, M., Maekawa, T., Mondarte, E. A. Q., Nyu, T., Mizushita, Y., and Hayashi, T. (2019). Proteomic Analysis of Biomaterial Surfaces after Contacting with Body Fluids by MALDI-ToF Mass Spectroscopy. *Coatings* 10, 12. doi:10.3390/coatings10010012

Hutter, J. L., and Bechhoefer, J. (1993). Calibration of Atomic-force Microscope Tips. *Rev. Scientific Instr.* 64, 1868–1873. doi:10.1063/1.1143970

Hylton, D. M., Shalaby, S. W., and Latour, R. A., Jr (2005). Direct Correlation between Adsorption-Induced Changes in Protein Structure and Platelet Adhesion. *J. Biomed. Mater. Res.* 73A, 349–358. doi:10.1002/jbm.a.30295

Ishida, T., Choi, N., Mizutani, W., Tokumoto, H., Kojima, I., Azehara, H., et al. (1999). High-resolution X-ray Photoelectron Spectra of Organosulfur Monolayers on Au(111): S(2p) Spectral Dependence on Molecular Species. *Langmuir* 15, 6799–6806. doi:10.1021/la9810307

Kanayama, N., Sekine, T., Ozasa, K., Kishi, S., Nyu, T., Hayashi, T., et al. (2016). Terminal-Specific Interaction between Double-Stranded DNA Layers: Colloidal Dispersion Behavior and Surface Force. *Langmuir* 32, 13296–13304. doi:10.1021/acs.langmuir.6b03470

Kwaria, R. J., Mondarte, E. A. Q., Tahara, H., Chang, R., and Hayashi, T. (2020). Data-Driven Prediction of Protein Adsorption on Self-Assembled Monolayers toward Material Screening and Design. *ACS Biomater. Sci. Eng.* 6, 4949–4956. doi:10.1021/acsbiomaterials.0c01008

Logeeswaran Vj, V., Kobayashi, N. P., Islam, M. S., Wu, W., Chaturvedi, P., Fang, N. X., et al. (2009). Ultrasmooth Silver Thin Films Deposited with a Germanium Nucleation Layer. *Nano Lett.* 9, 178–182. doi:10.1021/nl8027476

Mason, P. E., Neilson, G. W., Dempsey, C. E., Barnes, A. C., and Cruickshank, J. M. (2003). The Hydration Structure of Guanidinium and Thiocyanate Ions: Implications for Protein Stability in Aqueous Solution. *Proc. Natl. Acad. Sci.* 100, 4557–4561. doi:10.1073/pnas.0735920100

Matsumoto, M., Nishi, N., Furusawa, T., Saita, M., Takamuku, T., Yamagami, M., et al. (1995). Structure of Clusters in Ethanol-Water Binary Solutions Studied by Mass Spectrometry and X-Ray Diffraction. *Bcsj* 68, 1775–1783. doi:10.1246/bcsj.68.1775

Nowinski, A. K., Sun, F., White, A. D., Keefe, A. J., and Jiang, S. (2012). Sequence, Structure, and Function of Peptide Self-Assembled Monolayers. *J. Am. Chem. Soc.* 134, 6000–6005. doi:10.1021/ja3006868

Pourcelle, V., Devouge, S., Garinot, M., Préat, V., and Marchand-Brynaert, J. (2007). PCL–PEG-Based Nanoparticles Grafted with GRGDS Peptide: Preparation and Surface Analysis by XPS. *Biomacromolecules* 8, 3977–3983. doi:10.1021/bm700841y

Sekine, T., Asatyas, S., Sato, C., Morita, S., Tanaka, M., and Hayashi, T. (2017). Surface Force and Vibrational Spectroscopic Analyses of Interfacial Water Molecules in the Vicinity of Methoxy-Tri(ethylene Glycol)-Terminated Monolayers: Mechanisms Underlying the Effect of Lateral Packing Density on Bioinertness. *J. Biomater. Sci. Polym. Edition* 28, 1231–1243. doi:10.1080/09205063.2017.1303120

Sekine, T., Kanayama, N., Ozasa, K., Nyu, T., Hayashi, T., and Maeda, M. (2018). Stochastic Binding Process of Blunt-End Stacking of DNA Molecules Observed by Atomic Force Microscopy. *Langmuir* 34, 15078–15083. doi:10.1021/acs.langmuir.8b02224

Sekine, T., Tanaka, Y., Sato, C., Tanaka, M., and Hayashi, T. (2015). Evaluation of Factors to Determine Platelet Compatibility by Using Self-Assembled Monolayers with a Chemical Gradient. *Langmuir* 31, 7100–7105. doi:10.1021/acs.langmuir.5b01216

Tanaka, M., Hayashi, T., and Morita, S. (2013). The Roles of Water Molecules at the Biointerface of Medical Polymers. *Polym. J.* 45, 701–710. doi:10.1038/pj.2012.229

Tanaka, M., Morita, S., and Hayashi, T. (2021). Role of Interfacial Water in Determining the Interactions of Proteins and Cells with Hydrated Materials. *Colloids Surf. B: Biointerfaces* 198, 111449. doi:10.1016/j.colsurfb.2020.111449

Tanaka, M., Motomura, T., Kawada, M., Anzai, T., Yuu Kasori, Y., Shiroya, T., et al. (2000). Blood Compatible Aspects of Poly(2-Methoxyethylacrylate) (PMEA)-relationship between Protein Adsorption and Platelet Adhesion on PMEA Surface. *Biomaterials* 21, 1471–1481. doi:10.1016/s0142-9612(00)00031-4

White, A. D., Keefe, A. J., Ella-Menye, J.-R., Nowinski, A. K., Shao, Q., Pfaendtner, J., et al. (2013). Free Energy of Solvated Salt Bridges: a Simulation and Experimental Study. *J. Phys. Chem. B* 117, 7254–7259. doi:10.1021/jp4024469

White, A. D., Nowinski, A. K., Huang, W., Keefe, A. J., Sun, F., and Jiang, S. (2012). Decoding Nonspecific Interactions from Nature. *Chem. Sci.* 3, 3488–3494. doi:10.1039/c2sc21135a

Conflict of Interest: The authors declare that the research was conducted in the absence of any commercial or financial relationships that could be construed as a potential conflict of interest.

Publisher's Note: All claims expressed in this article are solely those of the authors and do not necessarily represent those of their affiliated organizations, or those of the publisher, the editors and the reviewers. Any product that may be evaluated in this article, or claim that may be made by its manufacturer, is not guaranteed or endorsed by the publisher.

frontiers in Chemistry

ORIGINAL RESEARCH
published: 18 October 2021
doi: 10.3389/fchem.2021.738077

Hydration and its Hydrogen Bonding State on a Protein Surface in the Crystalline State as Revealed by Molecular Dynamics Simulation

Hiroshi Nakagawa[1,2]* *and Taro Tamada*[3]

[1]Materials Science Research Center, Japan Atomic Energy Agency, Ibaraki, Japan, [2]J-PARC Center, Japan Atomic Energy Agency, Ibaraki, Japan, [3]Institute for Quantum Life Science, National Institutes for Quantum Science and Technology, Ibaraki, Japan

Protein hydration is crucial for the stability and molecular recognition of a protein. Water molecules form a hydration water network on a protein surface via hydrogen bonds. This study examined the hydration structure and hydrogen bonding state of a protein, staphylococcal nuclease, at various hydration levels in its crystalline state by all-atom molecular dynamics (MD) simulation. Hydrophilic residues were more hydrated than hydrophobic residues. As the water content increases, both types of residues were uniformly more hydrated. The number of hydrogen bonds per single water asymptotically approaches 4, the same as bulk water. The distances and angles of hydrogen bonds in hydration water in the protein crystal were almost the same as those in the tetrahedral structure of bulk water regardless of the hydration level. The hydrogen bond structure of hydration water observed by MD simulations of the protein crystalline state was compared to the Hydrogen and Hydration Database for Biomolecule from experimental protein crystals.

Keywords: protein hydration, hydrogen bond, protein crystal, molecular dynamics simulation, neutron crystallography

OPEN ACCESS

Edited by:
Hideki Seto,
High Energy Accelerator Research Organization, Japan

Reviewed by:
David Antony Morton-Blake,
Trinity College Dublin, Ireland
Ayori Mitsutake,
Meiji University, Japan

***Correspondence:**
Hiroshi Nakagawa
nakagawa.hiroshi@jaea.go.jp

Specialty section:
This article was submitted to Physical Chemistry and Chemical Physics, a section of the journal Frontiers in Chemistry

Received: *08 July 2021*
Accepted: *29 September 2021*
Published: *18 October 2021*

Citation:
Nakagawa H and Tamada T (2021) Hydration and its Hydrogen Bonding State on a Protein Surface in the Crystalline State as Revealed by Molecular Dynamics Simulation. Front. Chem. 9:738077. doi: 10.3389/fchem.2021.738077

INTRODUCTION

In an aqueous environment, there is hydration water on a protein surface (Nakasako et al., 2004; Niimura et al., 2006; Gnesi et al., 2017). Hydration water plays an important role in the structural dynamics, stability, and functional expression of a protein (Rupley et al., 1983; Careri et al., 1998). Hydration water not only forms hydrogen bonds with amino acid residues in proteins but also between water molecules in the hydration layers. As a result, a hydration water network is formed on the protein surface (Nakasako et al., 2004). The protein hydration structure has been studied by crystallography. Many hydration water molecules are observed at cryogenic temperatures by X-ray crystallography (Nakasako et al., 1999). Hydration structures are efficiently observed at room temperature by neutron crystallography (Niimura et al., 2006). The structure and dynamics of hydration water are examined in protein crystals (Podjarny et al., 1997). Based on crystal structures, including hydrogen atoms in the Protein Data Bank (PDB), the Hydrogen and Hydration Database for Biomolecules (HHDB © National Institutes for Quantum and Radiological Science and Technology (QST) licensed under CC BY-SA4.0 International; doi: 10.18908/lsdba.nbdc00495-000.V002) has been constructed (Niimura et al., 2006). In this database, hydration structures and hydrogen bonding states observed in the crystal structure analysis of biological macromolecules are summarized.

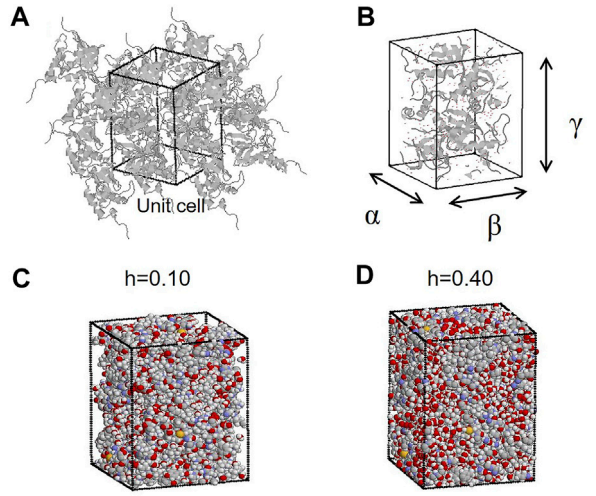

FIGURE 1 | (A) MD simulation system of protein crystals (with periodic boundary condition) of SNase. The rectangular box indicates the unit cell. **(B)** Lengths of the three sides of a rectangular unit cell (lattice constants) are denoted by α, β, and γ. **(C** and **D)** Proteins and water molecules in the unit cell at hydration levels of h = 0.10 (g water/g protein) and h = 0.40 (g water/g protein). In this figure, all the atoms outside the unit cell are put inside the unit cell according to the periodic boundary condition.

Protein hydration has also been analyzed by molecular dynamics (MD) simulations (Higo et al., 2002). In this MD simulation in solution, the solvent density and solvent dipole on the protein surface were in good agreement with the hydration structure observed by crystal structure analysis, indicating that the combination of computational and experimental analysis is effective in protein hydration studies. Most MD simulations of proteins are performed in solution, but the protein's conformation, dynamics, and function are changed in the crystalline state from in a solution (Li et al., 2017; Srivastava et al., 2018; Konold et al., 2020). Because the limitation of crystallography in not analyzing the protein dynamics is discussed (Srivastava et al., 2018), MD simulations in a protein crystalline state should be useful to compare them to experimental protein crystallography. Many MD simulations of protein crystalline states have been performed (Meinhold et al., 2005; Hu et al., 2008; Joti et al., 2008; Janowski et al., 2016; Cerutti et al., 2018). It should be also effective to quantitatively compare the experimental and calculated protein and hydration structures in crystals to evaluate the validity of MD simulations. In some experiments on protein dynamics, such as inelastic and quasi-elastic neutron scatterings, dielectric relaxation, and terahertz spectroscopy, hydrated powder proteins are used as samples (Nakagawa et al., 2010; Yamamoto et al., 2021). MD simulations of protein dynamics in the crystalline state have been shown to quantitatively reproduce neutron quasi-elastic scattering spectra of hydration water as well as protein (Tarek et al., 1999; Tarek et al., 2000). The structure and dynamics of biomolecules and hydration water in the crystalline state will also provide useful information for various spectroscopic experiments.

Enzyme activity decreases with the decrease in hydration level (Careri et al., 1998). With decreasing water content, the molecular mobility of both protein and hydration water decreases, and proteins become vitrified. Minimum hydration is necessary for enzymatic activity (Careri et al., 1998), and its threshold hydration level is correlated to percolation transisiton of hydration water (Careri et al., 1998; Nakagawa et al., 2010). Protein crystallography and MD simulations have been performed under varying humidity conditions to investigate the protein conformation and hydration states at atomic resolution (Kodandapani et al., 1990; Hu et al., 2008; Takayama et al., 2011; Trampari et al., 2018; Salinas-Garcia et al., 2019).

In this study, MD simulations of staphylococcal nuclease (SNase) in the crystalline state were performed at various hydration levels. The hydration level-dependent hydration structure and hydrogen bonding states were analyzed. As the water content increased, amino acid residues on a protein surface were uniformly more hydrated, and the number of hydrogen bonds per single water asymptotically approached 4, the same as bulk water. The distances and angles of hydrogen bonds in hydration water in the protein crystal were almost identical to those in the tetrahedral structure of bulk water regardless of water content. The hydrogen bond structure of hydration water observed by MD simulations of the protein crystalline state was compared to the HHDB from the experimental protein crystal.

MATERIALS AND METHODS

MD Simulation of Protein Crystal and Analysis of the Trajectories

The crystal structure of SNase (PDB code: 1EY0) was used as the initial simulation structure. The simulated system was constructed to reproduce the crystal unit cell, having a space group symmetry of $P4_1$ (**Figures 1A,B**). Missing residues 1 to 5 and 142 to 149 in 1EY0 were modeled based on the nuclear magnetic resonance structures (PDB code: 1JOR). The system contained four protein molecules, including crystal water registered in 1EY0. In addition, water molecules were added randomly distributed in the empty space in each system (**Figures 1C,D**) to construct the protein crystal with different hydration levels (h) from 0.10 to 0.55 (g water/g protein). The number of water molecules and atoms in the simulation system are summarized in **Supplementary Table S1**. To neutralize the system, 32 chloride ions were randomly placed in the system. Apart from MD simulations of crystalline proteins, MD simulations of bulk water were also performed. For the simulation of bulk water, 440 water molecules were set in a rectangular box. The periodic boundary condition was imposed, and the particle mesh Ewald method was used with a cutoff of 10 Å. The AMBER *ff14SB* force field and the TIP3P water model were employed. After energy minimization (2000 steps), 2 ns MDs were performed to equilibrate the systems at 300 K and 1 atm, which were maintained following the Berendsen method (relaxation time of 1 ps for both) using the program AMBER (Case et al., 2015). For equilibration MD, the ensemble is NPT. Successive 4 ns trajectories in the NPT ensemble were obtained for the analyses. For hydrogen bond analysis, pairs of water

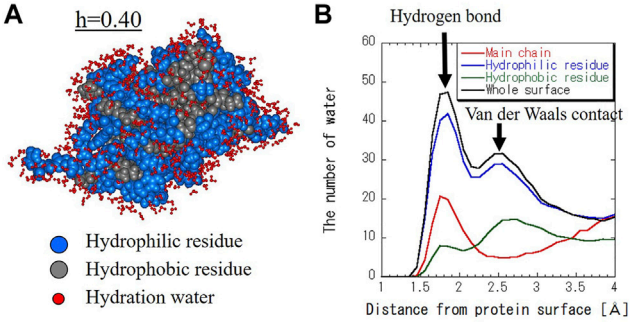

FIGURE 2 | (A) Structure of hydrated SNase at h = 0.40 (g water/g protein). Hydrophilic and hydrophobic residues are blue and gray balls, respectively. Hydration water molecules whose oxygen atom is within 4 Å from the protein surface are shown in red. **(B)** The number of hydration water as a function of distance from the protein surface for the main chain, hydrophilic and hydrophobic residues, and whole surface. The distance between the protein surface and the water molecules was calculated as the distance between the atoms that make up the protein and the oxygen atoms of the water molecules.

molecules were selected as hydrogen-bonded only if their interoxygen distance was <3.5 Å and simultaneously the O–H. . .O angle was > from 120° to 180°. To check the reproducibility of the simulation results, several simulations from different initial atomic velocities from a Boltzmann distribution were performed. The analytical results did not depend on the trajectories of different times and initial states. The thermal equilibration of the simulation was checked through total energy in the system and the temperature. **Supplementary Figure S1** shows the lattice constants and simulation boxes as a function of the hydration level. As the hydration level increases, these parameters increase to keep a constant pressure in the system. As for the distance between proteins in an unit cell, the contact maps between proteins were calculated (Joti et al., 2008). At low water content, there is more protein-protein contact, and at high water content, hydration water enters the gaps between the proteins, resulting in less protein-protein contact.

RESULTS AND DISCUSSION

Hydration Structure and Distribution of Water Molecules on the Protein Surface

Figure 2A shows the molecular structure and hydration water of SNase with the hydration level of h = 0.40 as a snapshot of the MD trajectory. Hydration water spreads not only on the hydrophilic surface but also on the hydrophobic surface. **Figure 2B** shows the number of hydration water around hydrophilic residues,

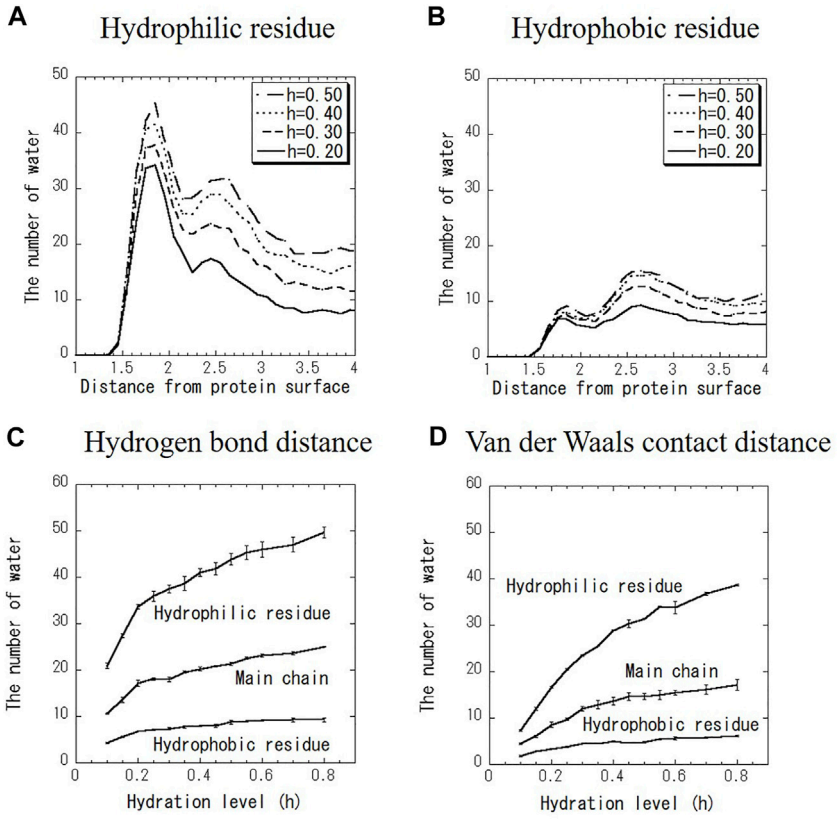

FIGURE 3 | Distribution of the number of water molecules on (A) hydrophilic residue and (B) hydrophobic residue. Hydration level dependence of the number of water molecules at (C) hydrogen bond distance (1.8 Å) and (D) VDW contact distance (2.5 Å) for hydrophilic and hydrophobic residues and the main chain.

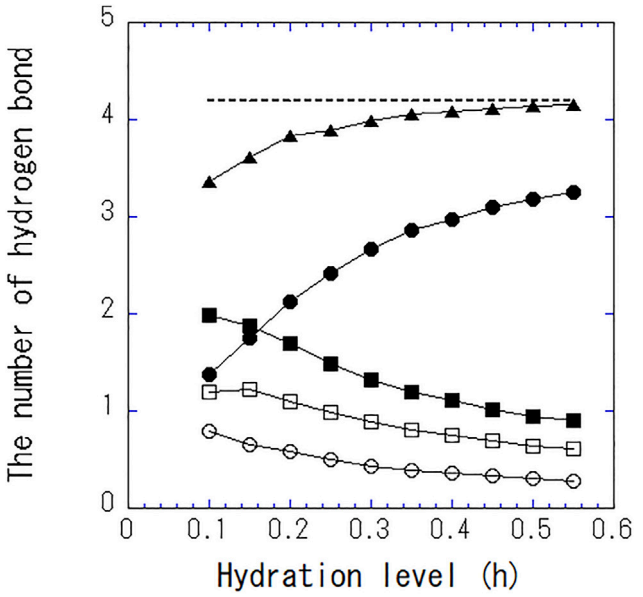

FIGURE 4 | The number of total hydrogen bonds per single water (▲), between water and water (●), between water and protein (■), between water and the side chain of the amino acid (□), and between water and the main chain of the amino acid (○). The dashed line indicates the number of hydrogen bond per single water in bulk water.

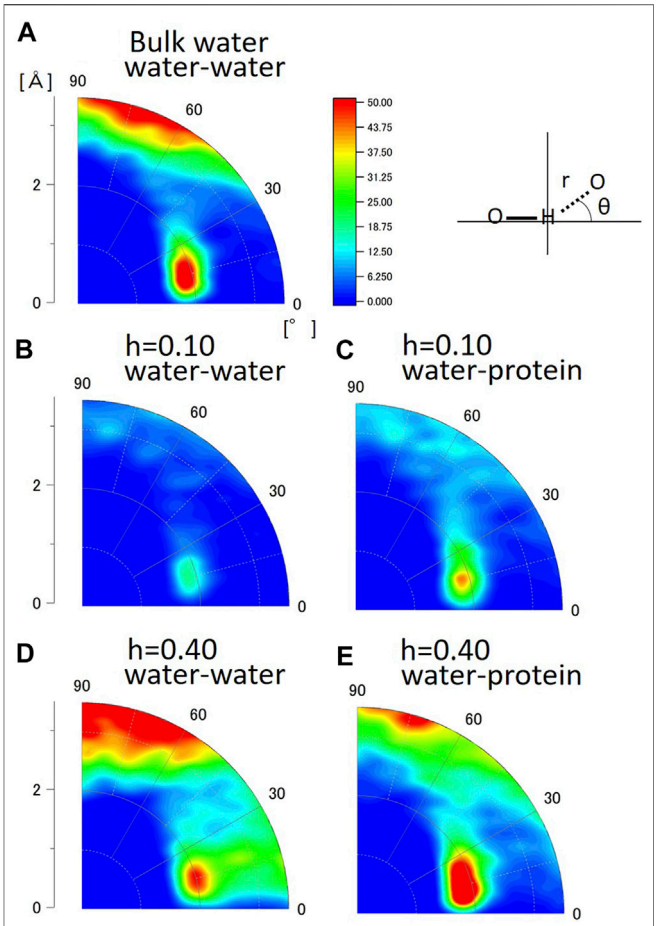

FIGURE 5 | Geometrical distribution of O-H. . .O calculated from MD simulation **(A)** between water and water in bulk water, **(B)** water and water at h = 0.10 (g water/g protein), **(C)** water and protein at h = 0.10 (g water/g protein), **(D)** water and water at h = 0.40 (g water/g protein), and **(E)** water and protein at h = 0.40 (g water/g protein).

hydrophobic residues, and the main chain per protein as a function of the distance from the protein surface. Hydration water around the main chain is mainly present at the hydrogen bond distance (Kumar et al., 2009). This indicates the water molecules that are hydrogen-bonded to the peptide bonds. For hydrophilic residues, the first major peak is at the hydrogen bond distance and the second peak is at the van der Waals (VDW) distance. For hydrophobic residues, there is more hydration at the VDW distance than the hydrogen bond distance. This is a reasonable result because hydrophobic surfaces have fewer donors and acceptors for hydrogen bonding.

Figures 3A,B shows the distribution of the number of water molecules on the hydrophilic and hydrophobic residues at various hydration levels. Data at every hydration level are shown in **Supplementary Figure S2**. As shown in **Figures 3A,B**, the number of hydration water on hydrophilic and hydrophobic surfaces has the one peak at the hydrogen bond distance and another peak at the VDW distance at every hydration level. The former peak is more intense for hydrophilic surface, and vice versa for hydrophobic one. For example, hydration water molecules around hydrophilic residues are hydrogen-bonded to carboxyl groups and amino groups of amino acid side chains. On the hydrophobic surface, hydrated water with pentagonal (five-membered) ring structures were observed (See **Supplementary Figure S3**). Such characteristic hydration structures have been previously confirmed by crystal structure analysis and MD calculations (Teeter et al., 1984; Lounnas et al., 1994; Nakasako et al., 2004). The shapes of the distributions in **Figures 3A,B** change similarly to hydration level. **Figures 3C,D** shows the number of hydration water at the two peaks of the hydrogen bond distance and VDW distance around hydrophilic residue, hydrophobic one and the main chain as a function of hydration level. The magnitudes of both peaks increase with the increase in hydration level. With increasing hydration levels, the number of hydration water does not increase preferentially around hydrophilic residues but increases uniformly around hydrophobic residues as well. This result suggests that hydration water is spread evenly over the entire protein surface rather than aggregating on the hydrophilic protein surface.

Figure 4 shows the number of hydrogen bonds per one water molecule at different hydration levels. As hydration level increases, the number of hydrogen bonds between water and water increases, whereas that between water and protein decreases. The total number of hydrogen bonds per single water asymptotically approaches 4, the same as bulk water. The hydrogen bonding with protein is replaced with that with water. At high hydration levels, approximately one of the four hydrogen bonds in a single water is bound to the protein and three are bound between water molecules.

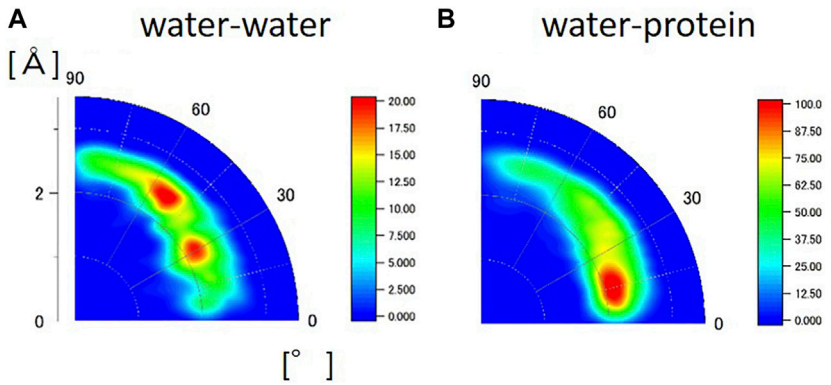

FIGURE 6 | Geometrical distribution of O-H. . .O calculated from HHDB **(A)** between water and water and **(B)** water and protein from the HHDB. Neutron data above 2.0 Å resolution are used for the analysis.

Geometry of the Hydrogen Bond in Hydration Water

Next, the hydrogen bond structures of water molecules were analyzed in a two-dimensional map of distance and angle. **Figure 5** shows the geometrical distribution of O-H. . .O between water and water in bulk water, between water and water, and between water and protein in the hydrated crystalline protein at h = 0.10 and h = 0.40. The distribution data for all hydration levels from h = 0.10 to h = 0.55 are shown in **Supplementary Figure S4**. The angle of O-H. . .O is 180°-θ (see the sketch in **Figure 5**). The peak in the distribution of O-H. . .O between water and water in bulk water is located at r = 2.0Å and θ = 15°. This geometrical feature suggests the tetrahedral hydrogen bond structure of water, as shown in **Supplementary Figure S5**. Crystallographic studies of proteins at low temperatures have also shown the presence of similar hydration water-formed hydrogen-bonded tetrahedral structures, suggesting their contribution to protein stability and folding (Nakasako, 2004). The present analysis shows that the tetrahedral structure of hydration water on the protein surface is independent of hydration level. The distribution of r > 3.0 Å at 60° < θ < 90° in bulk water indicates the presence of water molecules in proximity, but they do not form hydrogen bonds at this geometric location. The peak in the distributions were also observed for the geometrical distribution of O-H. . .H of between water and water (**Figures 5B,D**) and between water and protein (**Figures 5C,E**) in the hydrated protein crystal. These results suggest that the hydrogen bond structure of hydration water is similar to that of bulk water, and that the O-H. . .O positional relationship between water molecules in the hydration layers and protein is also similar to that of bulk water. The hydrogen bonds of water molecules maintain their tetrahedral structure regardless of their interaction with proteins or in a dry environment.

Hydrogen and Hydration in Biomolecules

The HHDB is a database of hydrogen atom positions in biological macromolecules, such as protein and DNA, and hydration water molecules, based on the selected PDB data (neutron crystallography and high-resolution X-ray crystallography). **Figure 6** shows the geometrical distribution of O-H. . .O between water and water and between water and protein from the HHDB. Neutron data above 2.0 Å resolution are used for the analysis. In **Figure 6A**, the two peaks are observed in the geometrical distribution of O-H. . .O between water and water at the distance of around 2.0 Å and the angle of around 30° and 55°. The distance is equal to the distance obtained by MD simulation (**Figures 5A,B,D**). The angle of the peak position around 30° should correspond to that around 15° in the hydrated crystalline protein by MD simulations. Although the reason for the difference is unclear, it could be ascribed to the hydrogen bond in the tetrahedral geometry. The second peak around 55° is not observed in the hydrated crystalline protein (**Figures 5B,D**) or bulk water (**Figure 5A**) in the MD simulation. A typical case of the relative geometry of two water molecules observed at r = 2.5 Å and θ = 55° is shown in **Supplementary Figure S6**; (Tamada et al., 2009). In this geometry, a hydrogen bond can be formed. This arrangement may indicate some kind of hydration water cluster, although they do not necessarily form a tetrahedral structure. The water molecules registered in the HHDB may be water molecules that form hydrogen bonds in some cases; in other cases, water may be registered against the observed electron density or nuclear density regardless of hydrogen bond formation. This difference may lead to the discrepancy between HDDB and MD calculations. In the geometrical distribution of O-H. . .O between water and protein, as shown in **Figure 6B**, the peak in the distribution is located at r = 2.0 Å and θ = 15°. This is in good agreement with that in the hydrated protein crystalline state in MD simulation (**Figures 5C,E**). The geometrical relationship between water and protein in the HHDB is thought to maintain the tetrahedron of water molecules, consistent with low-temperature crystal structure analysis.

CONCLUSIONS

MD simulations shows that, on the surface of hydrophilic residues, hydration water was abundant at the hydrogen bond distance from the protein surface. In contrast, on hydrophobic residues, hydration water was more abundant at the VDW distance than at the hydrogen bond distance. With increasing hydration levels, both types of

residues were uniformly more hydrated, and the number of hydrogen bonds per single water asymptotically approached 4, the same as bulk water. The hydrogen bond structure of protein hydration water was shown to be independent of hydration level and adopt a tetrahedral structure like bulk water. The hydrogen bond between water and protein observed in the protein crystalline state in MD simulations is consistent with the hydrogen bond structure of hydrated water observed in neutron crystallography presented in the HHDB. In contrast, the hydrogen bonds between water and water are slightly different from each other. The difference could be the arbitrary nature of hydrogen bonds in water molecules registered in the HHDB. MD simulations of proteins in crystalline states should be useful for the combined analysis of protein hydration by crystallography, especially neutron crystallography, an effective tool for analyzing hydrogen and hydration structures.

DATA AVAILABILITY STATEMENT

The original contributions presented in the study are included in the article/**Supplementary Material**, further inquiries can be directed to the corresponding author.

AUTHOR CONTRIBUTIONS

HN designed the research and performed the MD simulation and analysis. TT analyzed the HHDB. HN and TT discussed the data together. HN wrote the first manuscript. HN and TT improved the manuscript together.

FUNDING

This work was partly supported by the JSPS KAKENHI Grant Numbers JP20H02944, JP20K03878, JP18H05229, and JP18K18828, the Shimazu Science Foundation, and the Toray Science Foundation.

SUPPLEMENTARY MATERIAL

The Supplementary Material for this article can be found online at: https://www.frontiersin.org/articles/10.3389/fchem.2021.738077/full#supplementary-material

REFERENCES

Careri, G. (1998). Cooperative Charge Fluctuations by Migrating Protons in Globular Proteins. *Prog. Biophys. Mol. Biol.* 70, 223–249. doi:10.1016/S0079-6107(98)00030-3

Case, D. A., Berryman, J. T., Betz, R. M., Cerutti, D. S., Cheatham, T. E. I., Darden, T. A., et al. (2015). *AMBER 2015*. San Francisco: University of California.

Cerutti, D. S., and Case, D. A. (2018). Molecular Dynamics Simulations of Macromolecular Crystals. *Wires Comput. Mol. Sci.* 9, e1402. doi:10.1002/wcms.1402

Gnesi, M., and Carugo, O. (2017). How Many Water Molecules Are Detected in X-ray Protein crystal Structures? *J. Appl. Cryst.* 50, 96–101. doi:10.1107/S1600576716018719

Higo, J., and Nakasako, M. (2002). Hydration Structure of Human Lysozyme Investigated by Molecular Dynamics Simulation and Cryogenic X-ray Crystal Structure Analyses: On the Correlation between Crystal Water Sites, Solvent Density, and Solvent Dipole. *J. Comput. Chem.* 23, 1323–1336. doi:10.1002/jcc.10100

Hu, Z., and Jiang, J. (2008). Molecular Dynamics Simulations for Water and Ions in Protein Crystals. *Langmuir* 24, 4215–4223. doi:10.1021/la703591e

Janowski, P. A., Liu, C., Deckman, J., and Case, D. A. (2016). Molecular Dynamics Simulation of Triclinic Lysozyme in a Crystal Lattice. *Protein Sci.* 25, 87–102. doi:10.1002/pro.2713

Joti, Y., Nakagawa, H., Kataoka, M., and Kitao, A. (2008). Hydration-Dependent Protein Dynamics Revealed by Molecular Dynamics Simulation of Crystalline Staphylococcal Nuclease. *J. Phys. Chem. B* 112, 3522–3528. doi:10.1021/jp710039p

Kodandapani, R., Suresh, C. G., and Vijayan, M. (1990). Crystal Structure of Low Humidity Tetragonal Lysozyme at 2.1-A Resolution. Variability in Hydration Shell and its Structural Consequences. *J. Biol. Chem.* 265, 16126–16131. doi:10.1016/S0021-9258(17)46197-7

Konold, P. E., Arik, E., Weißenborn, J., Arents, J. C., Hellingwerf, K. J., van Stokkum, I. H. M., et al. (2020). Confinement in crystal Lattice Alters Entire Photocycle Pathway of the Photoactive Yellow Protein. *Nat. Commun.* 11, 4248. doi:10.1038/s41467-020-18065-9

Kumar, P. P., Kalinichev, A. G., and Kirkpatrick, R. J. (2009). Hydrogen-Bonding Structure and Dynamics of Aqueous Carbonate Species from Car–Parrinello Molecular Dynamics Simulations. *J. Phys. Chem. B* 113, 794–802. doi:10.1021/jp809069g

Li, J., Hu, Z., Beuerman, R., and Verma, C. (2017). Molecular Environment Modulates Conformational Differences between Crystal and Solution States of Human β-Defensin 2. *J. Phys. Chem. B* 121, 2739–2747. doi:10.1021/acs.jpcb.7b00083

Lounnas, V., and Pettitt, B. M. (1994). A Connected-Cluster of Hydration Around Myoglobin: Correlation between Molecular Dynamics Simulations and experiment. *Proteins* 18, 133–147. doi:10.1002/prot.340180206

Meinhold, L., and Smith, J. C. (2005). Fluctuations and Correlations in Crystalline Protein Dynamics: a Simulation Analysis of Staphylococcal Nuclease. *Biophysical J.* 88, 2554–2563. doi:10.1529/biophysj.104.056101

Nakagawa, H., and Kataoka, M. (2010). Percolation of Hydration Water as a Control of Protein Dynamics. *J. Phys. Soc. Jpn.* 79, 083801. doi:10.1143/JPSJ.79.083801

Nakasako, M. (1999). Large-Scale Networks of Hydration Water Molecules Around Bovine β-Trypsin Revealed by Cryogenic X-ray crystal Structure Analysis. *J. Mol. Biol.* 289, 547–564. doi:10.1006/jmbi.1999.2795

Nakasako, M. (2004). Water-Protein Interactions from High-Resolution Protein Crystallography. *Phil. Trans. R. Soc. Lond. B* 359, 1191–1206. doi:10.1098/rstb.2004.1498

Niimura, N., Arai, S., Kurihara, K., Chatake, T., Tanaka, I., and Bau, R. (2006). Recent Results on Hydrogen and Hydration in Biology Studied by Neutron Macromolecular Crystallography. *Cell. Mol. Life Sci.* 63, 285–300. doi:10.1007/s00018-005-5418-3

Podjarny, A. D., Howard, E. I., Urzhumtsev, A., and Grigera, J. R. (1997). A Multicopy Modeling of the Water Distribution in Macromolecular Crystals. *Proteins* 28, 303–312. doi:10.1002/(sici)1097-0134(199707)28:3<303::aid-prot1>3.0.co;2-d

Rupley, J. A., Gratton, E., and Careri, G. (1983). Water and Globular Proteins. *Trends Biochem. Sci.* 8, 18–22. doi:10.1016/0968-0004(83)90063-4

Salinas-Garcia, M. C., Plaza-Garrido, M., Alba-Elena, D., and Camara-Artigas, A. (2019). Major Conformational Changes in the Structure of Lysozyme Obtained from a crystal with a Very Low Solvent Content. *Acta Cryst. Sect F* 75, 687–696. doi:10.1107/S2053230X19013189

Srivastava, A., Nagai, T., Srivastava, A., Miyashita, O., and Tama, F. (2018). Role of Computational Methods in Going beyond X-ray Crystallography to Explore Protein Structure and Dynamics. *Int. J. Mol. Sci.* 19, 3401. doi:10.3390/ijms19113401

Takayama, Y., and Nakasako, M. (2011). A Few Low-Frequency normal Modes Predominantly Contribute to Conformational Responses of Hen Egg white Lysozyme in the Tetragonal crystal to Variations of Molecular Packing

Controlled by Environmental Humidity. *Biophysical Chem.* 159, 237–246. doi:10.1016/j.bpc.2011.07.001

Tamada, T., Kinoshita, T., Kurihara, K., Adachi, M., Ohhara, T., Imai, K., et al. (2009). Combined High-Resolution Neutron and X-ray Analysis of Inhibited Elastase Confirms the Active-Site Oxyanion Hole but Rules against a Low-Barrier Hydrogen Bond. *J. Am. Chem. Soc.* 131, 11033–11040. doi:10.1021/ja9028846

Tarek, M., and Tobias, D. J. (1999). Environmental Dependence of the Dynamics of Protein Hydration Water. *J. Am. Chem. Soc.* 121, 9740–9741. doi:10.1021/ja990643i

Tarek, M., and Tobias, D. J. (2000). The Dynamics of Protein Hydration Water: A Quantitative Comparison of Molecular Dynamics Simulations and Neutron-Scattering Experiments. *Biophysical J.* 79, 3244–3257. doi:10.1016/S0006-3495(00)76557-X

Teeter, M. M. (1984). Water Structure of a Hydrophobic Protein at Atomic Resolution: Pentagon Rings of Water Molecules in Crystals of Crambin. *Proc. Natl. Acad. Sci.* 81, 6014–6018. doi:10.1073/pnas.81.19.6014

Trampari, S., Valmas, A., Logotheti, S., Saslis, S., Fili, S., Spiliopoulou, M., et al. (2018). *In Situ* detection of a Novel Lysozyme Monoclinic crystal Form upon Controlled Relative Humidity Variation. *J. Appl. Cryst.* 51, 1671–1683. doi:10.1107/S1600576718013936

Yamamoto, N., Kofu, M., Nakajima, K., Nakagawa, H., and Shibayama, N. (2021). Freezable and Unfreezable Hydration Water: Distinct Contributions to Protein Dynamics Revealed by Neutron Scattering. *J. Phys. Chem. Lett.* 12, 2172–2176. doi:10.1021/acs.jpclett.0c03786

Conflict of Interest: The authors declare that the research was conducted in the absence of any commercial or financial relationships that could be construed as a potential conflict of interest.

Publisher's Note: All claims expressed in this article are solely those of the authors and do not necessarily represent those of their affiliated organizations, or those of the publisher, the editors and the reviewers. Any product that may be evaluated in this article, or claim that may be made by its manufacturer, is not guaranteed or endorsed by the publisher.

frontiers in Chemistry

ORIGINAL RESEARCH
published: 18 October 2021
doi: 10.3389/fchem.2021.743255

Hydrogen-Bonded Structure of Water in the Loop of Anchored Polyrotaxane Chain Controlled by Anchoring Density

Keishi Akada[1]†, Kosuke Yamazoe[1†], Jun Miyawaki[1,2,3†], Rina Maeda[2], Kohzo Ito[2] and Yoshihisa Harada[1,2,3]**

[1]Institute for Solid State Physics (ISSP), The University of Tokyo, Chiba, Japan, [2]Department of Advanced Materials Science, Graduate School of Frontier Sciences, The University of Tokyo, Chiba, Japan, [3]Synchrotron Radiation Research Organization, The University of Tokyo, Chiba, Japan

Hydrogen-bonded network of water surrounding polymers is expected to be one of the most relevant factors affecting biocompatibility, while the specific hydrogen-bonded structure of water responsible for biocompatibility is still under debate. Here we study the hydrogen-bonded structure of water in a loop-shaped poly(ethylene glycol) chain in a polyrotaxane using synchrotron soft X-ray emission spectroscopy. By changing the density of anchoring molecules, hydrogen-bonded structure of water confined in the poly(ethylene glycol) loop was identified. The XES profile of the confined water indicates the absence of the low energy lone-pair peak, probably because the limited space of the polymer loop entropically inhibits the formation of tetrahedrally coordinated water. The volume of the confined water can be changed by the anchoring density, which implies the ability to control the biocompatibility of loop-shaped polymers.

Keywords: polyrotaxane, PEG, polymer loop, biocompatibility, soft X-ray emission

OPEN ACCESS

Edited by:
Javier Carrasco,
CIC energigune, Spain

Reviewed by:
Manabu Inutsuka,
National Institute of Advanced Industrial Science and Technology (AIST), Japan
Takahiro Seki,
Nagoya University, Japan

***Correspondence:**
Keishi Akada
akada.keishi.fw@u.tsukuba.ac.jp
Yoshihisa Harada
harada@issp.u-tokyo.ac.jp

†Present address:
Keishi Akada,
Institute of Applied Physics, Graduate School of Pure and Applied Sciences, University of Tsukuba, Tsukuba, Japan;
Kosuke Yamazoe,
Japan Synchrotron Radiation Research Institute, Sayo, Japan;
Jun Miyawaki,
National Institutes for Quantum and Radiological Science and Technology (QST), Sayo, Japan

Specialty section:
This article was submitted to Physical Chemistry and Chemical Physics, a section of the journal Frontiers in Chemistry

Received: *18 July 2021*
Accepted: *27 September 2021*
Published: *18 October 2021*

Citation:
Akada K, Yamazoe K, Miyawaki J, Maeda R, Ito K and Harada Y (2021) Hydrogen-Bonded Structure of Water in the Loop of Anchored Polyrotaxane Chain Controlled by Anchoring Density. Front. Chem. 9:743255. doi: 10.3389/fchem.2021.743255

INTRODUCTION

Water is well known to play an important role in most biological processes by mediating specific functions, such as biocompatibility of biomaterials (Bag and Valenzuela, 2017; Laage et al., 2017). When a biomolecule approaches the surface of a biomaterial, a few layers of water molecules surrounding both interacting media, called hydration shells, directly interact with each other and regulate the adsorption or desorption property. Many researchers have proposed various models for the hydrogen-bonded structure of the hydration shell of biomaterials (Kitano et al., 2000; Asay and Kim, 2005; Morita et al., 2007). However, much debate still exists on the structure of water that provides biocompatibility and how to design biomaterials to improve this function (Jena and Hore, 2010; Tanaka and Mochizuki, 2010; Bag and Valenzuela, 2017; Laage et al., 2017). Indeed, biocompatibility can also be improved by the morphology of the polymer in addition to its constituents. For example, an excellent anti-fouling property [hereafter referred to as biocompatibility because this is often linked to nonbiofouling (Schlenoff, 2014)] has been reported for looped polymers (Yamada et al., 2012; Kang et al., 2016; Benetti et al., 2017). Articular joints of mammalians are coated with a lubricating protein, which adopts the looped conformation, has also exhibited outstanding biocompatibility (Greene et al., 2015). The looped shape is more rigid and provides stronger resistance against compression than a linear one. The higher resistance of the looped chains towards external compression translated into an excellent biocompatibility, a protein repellent behavior (Yamada et al., 2012; Benetti et al., 2017). The looped shape also accommodates water molecules inside loops having a size of a few nanometers (Ostaci

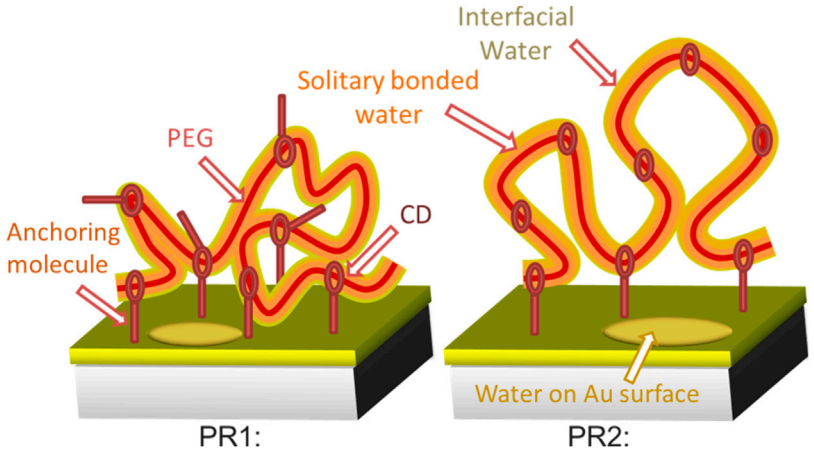

SCHEME 1 | Schematic images of the surface morphology of polyrotaxane and incorporated water at RH 50%. A thin single bonded water layer (orange) surrounds the hydrophilic PEG (red string) surface. Interfacial water is present in the outer region of the incorporated water (yellow). Water molecules also present on the exposed Au surface.

et al., 2011). Water encapsulated within such a small space, e.g., in mesoporous silica, has changed freezing and melting points much lower than those of bulk water (Kittaka et al., 2006). This property is called cold crystallization, which is commonly observed in biocompatible materials like poly (methoxyethyl acrylate) (PMEA), one of the most practical biocompatible polymer materials (Tanaka and Mochizuki, 2010).

In this study, due to its superb biocompatible properties and simple molecular structure, we investigated a looped poly (ethylene glycol) (PEG) to identify the hydrogen-bonded structure of water responsible for the biocompatibility (Bag and Valenzuela, 2017). Among various polymer materials, PEG is one of the most widely used polymers for biocompatible applications (Lowe et al., 2015; Bag and Valenzuela, 2017). To investigate the effect of looped morphology, we controlled the loop size by introducing multiple fixing points in a PEG chain using a polyrotaxane consisting of α-cyclodextrin (CD) and PEG chains (**Scheme 1**). The PEG chain can be fixed by the reaction between the dithiol end of an anchoring molecule connected to the topological ring of a CD molecule and Au substrate (Liu et al., 1999). By changing the density of the anchoring molecules and the number of fixing points in the main chain, we expected to control the size of confined spaces in the polymer loops and the amount of confined water in it. Indeed, a larger density of the fixing points reduced the volume expansion by water uptake (Kato et al., 2015).

The hydrogen-bond network of water surrounded by the looped PEG chains was investigated by monitoring the electronic structure of water using oxygen K-edge X-ray emission spectroscopy (XES), which is very sensitive to the hydrogen-bonded network of water (Tokushima et al., 2008; Yamazoe et al., 2017). By gradually increasing the humidity and monitoring O 1s XES spectra for looped PEG chains having different anchoring densities, we have successfully elucidated the structure of water inside the looped PEG and proposed the actual role of the confined water on biocompatibility.

MATERIALS AND METHODS

Synthesis and Preparation of Anchored Polyrotaxane Samples

A hydroxypropyl-modified polyrotaxane consisting of CD and PEG (M_w = 350,000) end-capped with adamantane was purchased from Advanced Softmaterials Inc (Tokyo, Japan). Each polyrotaxane molecule had a structure with 100 CD molecules. All other chemicals and solvents were purchased from Sigma-Aldrich (Tokyo, Japan) or Wako Pure Chemical Industries, Ltd (Osaka, Japan) and used without further purification. Here is an example of preparation of lipoic-acid-introduced polyroaxane (LAPR). 325 mg of dried polyrotaxane was dissolved in 5 ml of dried *N*, *N*-dimethylformamide (DMF). 89 mg of (±)-α lipoic acid, 124 mg of 1-ethyl-3-(3-dimethylaminopropyl) carbodiimide hydrochloride, and 75 mg of *N*-hydroxysuccinimide were added in the solution. The solution was stirred at room temperature under an Ar atmosphere for 12 h. After the reaction, the solution was poured into an excess amount of acetone to reprecipitate LAPR. After drying in vacuum at room temperature, 130 mg of LAPR was obtained. We prepared two kinds of LAPRs with different density of anchoring molecules of sulfo groups per CD: high density (LAPR1) and low density (LAPR2). Each polyrotaxane was dissolved in dehydrated dimethyl sulfoxide (0.2 mg/L). Au-coated membranes were immersed in the solutions and mixed together to initiate a reaction of Au and dithiol. After overnight mixing at room temperature under an Ar atmosphere, the LAPR was anchored to an Au-coated membrane surface. Measured samples with different anchoring densities (PR1 and PR2) were obtained from solution of LAPR1 and LAPR2, respectively.

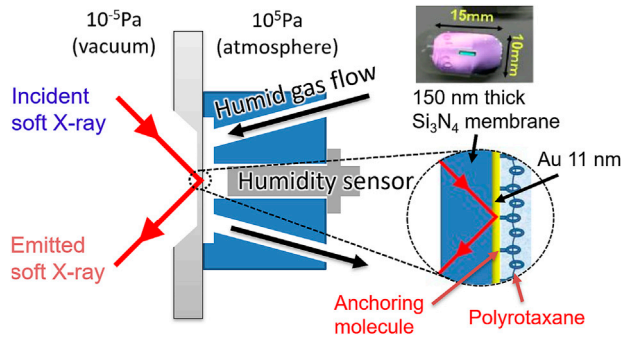

FIGURE 1 | Schematic image of a sample cell for soft X-ray absorption and emission spectroscopy. Polyrotaxane polymers were fixed onto an Au/Ti-coated 150 nm thick Si_3N_4 membrane using an anchoring molecule and exposed to N_2 gas flow with precisely controlled humidity.

XES Measurement of Humidity Controlled Looped PEG

We used the HORNET XES station (Harada et al., 2012) installed at the University of Tokyo Synchrotron Radiation Outstation beamline BL07LSU (Yamamoto et al., 2014) in SPring-8. In this system, an originally developed liquid cell separates a sample in ambient condition and the high vacuum using a 150-nm-thick Si_3N_4 membrane coated with 3-nm Ti and 11-nm Au layers (NTT-AT, **Figure 1**).

In this cell, the flow path is designed so that the humidified gas flows along the membrane, in front of which a humidity sensor was attached. By flowing a gas with precisely controlled humidity in step-wise increments, we can detect water being gradually adsorbed on the sample surface without accumulating huge background of bulk liquid water on the flow path of the humidified gas. Thus the hydrated water on the polymer can be detected without being buried in the signal from the bulk water. In the XES experiment, the analytical depth is c.a. 350 nm estimated by using an online software package at CXRO (Henke). Since the adsorbed water is only distributed in the polymer region, which is approx. 35 nm as discussed in Results and Discussion and much shallower than the detection depth, the signal detection efficiency does not vary significantly between those closer to the substrate and those in the deeper region. Roughly estimated by using the same software, the detection efficiency at the 35 nm region is about 90% of the substrate region, thus the signal near the substrate is not enhanced compared to the deeper region.

During the experiment, the temperature inside the cell was kept at 30°C, and the gas flow tube was heated at 40°C to avoid dew condensation of the humidified gas in the tube. The relative humidity (RH) of the humidified gas at the sample was precisely controlled within ±1.5% measurement error by a steam generator (HUM-1, Rigaku Corp.) that mixed vapor with dry nitrogen. Ultrapure water (Direct-Q, Millipore Inc.) was used as the steam source. When we took measurements under dry condition, dry nitrogen directly flowed into the cell to keep the relative humidity below 10%. This dry gas effectively prevents water adsorption on the sample and enables us to obtain only signals from oxygens in the polyrotaxane polymer film and in the Si_3N_4 membrane.

All O 1s XES measurements were performed at an ionization condition with an incident energy of 550 eV and total energy resolution of 0.15 eV. At each humidity condition, three or four XES spectra were obtained and summed after a consistency check, where the exposure time for each spectrum was 30 min, while for those with higher H_2O signal intensity from pure water and at RH 95% in PR1 and PR2, only one 30 min spectrum was obtained. The obtained XES spectrum at dry condition (<RH 10%) was subtracted from the spectrum at each humidity condition. Raw XES spectra are shown in **Supplementary Figure S1**. To estimate background contributions from water adsorbed on the substrate 11-nm Au layers, an XES spectrum of water adsorbed on the same Si_3N_4 membrane without PR1 and PR2 samples was also obtained.

RESULTS AND DISCUSSION

Figure 2 shows the XES spectra of water in the polyrotaxane polymer film at RH 50% (orange plots). They are subtracted by the corresponding RH 10% (dry condition: red plots) spectra showing oxygen signals from the polyrotaxane and Si_3N_4 membrane. For comparison, the XES spectrum of bulk liquid water multiplied by 0.1 (black line) and vapor gas (blue line) (Weinhardt et al., 2012) are also added. The bulk water spectrum is an integration of signals from a probing depth of 300 nm, and is multiplied by 0.1 because it is much more intense than adsorbed water, from a few tens of nm on the substrate surface. The bulk liquid water spectrum showed two sharp $1b_1$-derived peaks, which correspond to tetrahedrally coordinated ($1b_1'$) and distorted ($1b_1''$) hydrogen-bonds (Tokushima et al., 2008). The XES spectra of water in the polyrotaxane polymer films have a very different profile around the $1b_1$ peaks from the bulk liquid water spectrum, indicating that incorporated water molecules in the films have hydrogen-bonded configuration totally different from that of bulk liquid water.

The PR samples all have a 527.0 eV peak, which is higher than the $1b_1''$ peak of bulk liquid water (526.6 eV), and very close to the $1b_1$ peak of water vapor reported as 527.1 eV (Weinhardt et al., 2012). However, the peak around 527.0 eV often appears in monolayer water molecules directly bonded to metal surfaces, where the water molecules are aligned with direct O bonding or H-down bonding to the metal surface (Schiros et al., 2010). At present, there are two possibilities for the 527.0 eV peak. One is water molecules directly bonded to the PEG chain rotating to point their H atoms to the O atoms in the PEG units (Zhao et al., 2005). The other is water adsorbed on the exposed Au surface not covered by PR1 and PR2 molecules. For the latter contribution the XES spectrum for water adsorbed on the Au surface is also plotted in **Figure 2** as black solid line on the RH 50% spectra for PR1 and PR2. The intensity is normalized not to exceed the PR1 and PR2 spectra at all energies. Approximately 80% of water adsorbed at RH 50% may be ascribed to water on the Au surface, which corresponds to the relative amount of 0.667 and 1.256 for PR1 and PR2, respectively (see **Supplementary Table S1** in the Supporting Information). The remaining water molecules should be

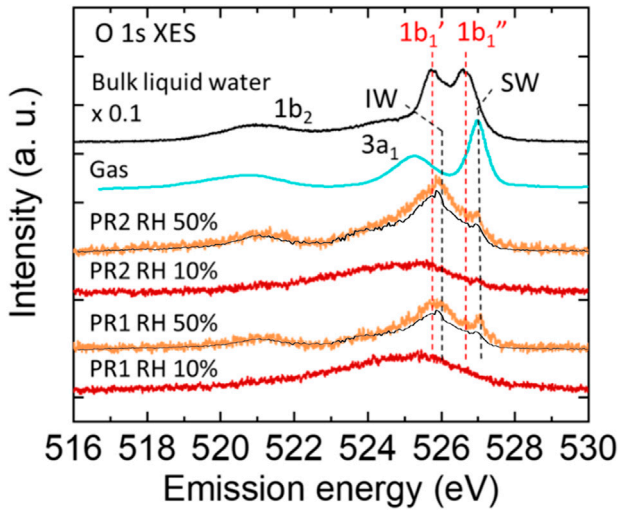

FIGURE 2 | O 1s XES spectra of water in the polyrotaxane polymer film at RH 50% (orange) obtained by subtracting the corresponding polyrotaxane spectra at a dry (<RH 10%) condition (red). The intensity of the bulk liquid water spectrum (black) is multiplied by 0.1. The gas phase spectra (blue) is obtained from other report (Weinhardt et al., 2012). The background XES contribution from water adsorbed on the Au surface is also plotted (black line) on each RH 50% spectrum.

adsorbed on ether O atoms in the PEG units, which was reported to be monomeric (singly bonded) at RH 50% by using infrared spectroscopy (Kitano et al., 2001). Accordingly, we denote the peak at 527 eV a single bonded water (SW) peak, as shown in **Figure 2**.

The PR samples have a primal peak at 525.9 eV which is higher energy than the $1b_1'$ peak of bulk liquid water (525.7 eV) and the $1b_1$ peak of the ice phase reported as 525.6 eV (Gilberg et al., 1982). Similar peak close to the $1b_1'$ peak has been observed in a humidified polyelectrolyte brush (Yamazoe et al., 2017), where absorbed water is surrounded by crowded polyelectrolytes and had a distorted tetrahedrally coordinated (ice-like) hydrogen-bond structure even at room temperature. In previous reports ice-like structures were also observed on PEG self-assembled monolayer (SAM) (Anderson and Ashurst, 2009) and UV/ozone-treated SiO (Asay and Kim, 2005) by using attenuated total reflection infrared spectroscopy (ATR-IR), where water molecules were aligned on the functional groups and formed a few water layers with a tetrahedral network. Kitano et al. (2001) have analyzed ATR-IR results with an ab initio molecular orbital (MO) calculation method and hybrid density functional method. They reported a part of water adsorbed on the ether oxygen forms a dimer structure with other water molecule or bridges other PEG chain to form a hydrogen bonded network of water molecules at 50% RH. Daley and Kubarych found by calculation that water molecules form hexagonally arranged water structures connecting to adjacent PEG oxygen atoms (Daley and Kubarych, 2017). This hexagonal motif is the primitive building block of an ice I_h structure, although water molecules surrounding the PEG chain clearly lack the long-range ordering due to the twisted conformation of the underlying polymer. They also mentioned the tight integration of the PEG/water interface results in a highly "structured" hydration layer. Our obtained peak at 525.9 eV may indicate that the adsorbed water molecules form highly structured hydrogen bonds with other water molecules and/or polymer chains to form a tetrahedrally coordinated network. We call such tetrahedrally coordinated water as "interfacial water" (IW) and denoted the $1b_1$ peak at 525.9 eV as the IW peak.

PR1 and PR2 showed different IW peak intensities at RH 50%. Polyrotaxane molecules with a larger number of anchoring molecules (= PR1) should have a less volume and decreased water content [17]. Accordingly, PR1 shows weaker intensity of the IW peak than that of PR2, as shown in **Scheme 1**.

Figures 3A,B show O 1s XES spectra of PR1 and PR2 under relative humidities of 50, 80, 90, and 95%. They are all subtracted by the corresponding RH 10% (dry condition) spectra. To extract the character of deposited water at each humidity step, difference spectra between the XES spectra of neighboring humidity conditions for PR1 and PR2 are shown in **Figures 3C,D**.

Assuming that the contribution from water on the Au surface may be proportional to the humidity, the amount of water adsorbed on the PR1 and PR2 samples can be estimated by subtracting those contributions from water on the Au surface (shown in the bottom two columns in **Supplementary Table S1**). It is expected that almost all the oxygen moieties of PR1 and PR2 are covered by water molecules above RH 90% as indicated by the value greater than unity. Since the anchoring molecules are hydrophobic, the adsorbed water covering the polyrotaxane chain mainly exists on the hydrophilic PEG and CD surface under humid conditions. Here, the CD ring can slide on the PEG chain, but we do not take care of the sliding effect on the adsorbed water molecules on the PEG chains since those adsorbed water molecules are dynamically adsorbed and desorbed typically in the time scale of 10 ps (Ensing et al., 2019), while the time scale of the sliding of α-CDs along the PEG chains is on the order of 0.1^{-1} ms (Zhao et al., 2005). Therefore, we consider that the motion of α-CDs does not affect the adsorption dynamics of water on the PEG chains. At higher relative humidity than 90%, additional water layer grows. PR2 polymer absorbs more water than PR1 in the swollen structure as shown in bold fonts in **Supplementary Table S1**. Since the density of PEG chains should be almost identical between PR1 and PR2, the increase in the water uptake in PR2 at higher humidity is surely coming from water molecules confined in the polymer loop as discussed in the following.

As already discussed above, for both PR1 and PR2, the RH 50% spectra showed an increase of the IW and SW peaks after humidification. From RH 50–80%, the XES spectrum showed only a slight increase. Upon the humidification process on a hydrophilic Si-OH surface, Asay and Kim (2005) reported that water molecules form bulk-liquid like water layers on the tetrahedrally coordinated hydrogen-bonded layers. In the present case, the spectral difference between RH 50 and 80% would show a small increase of water having a variety of hydrogen-bonded structures on the tetrahedral interfacial water layer. At RH 80% at room temperature, the vapor pressure of water is 3.1 kPa, which is comparable to the osmotic pressure of PEG solution with 3,000 molecular

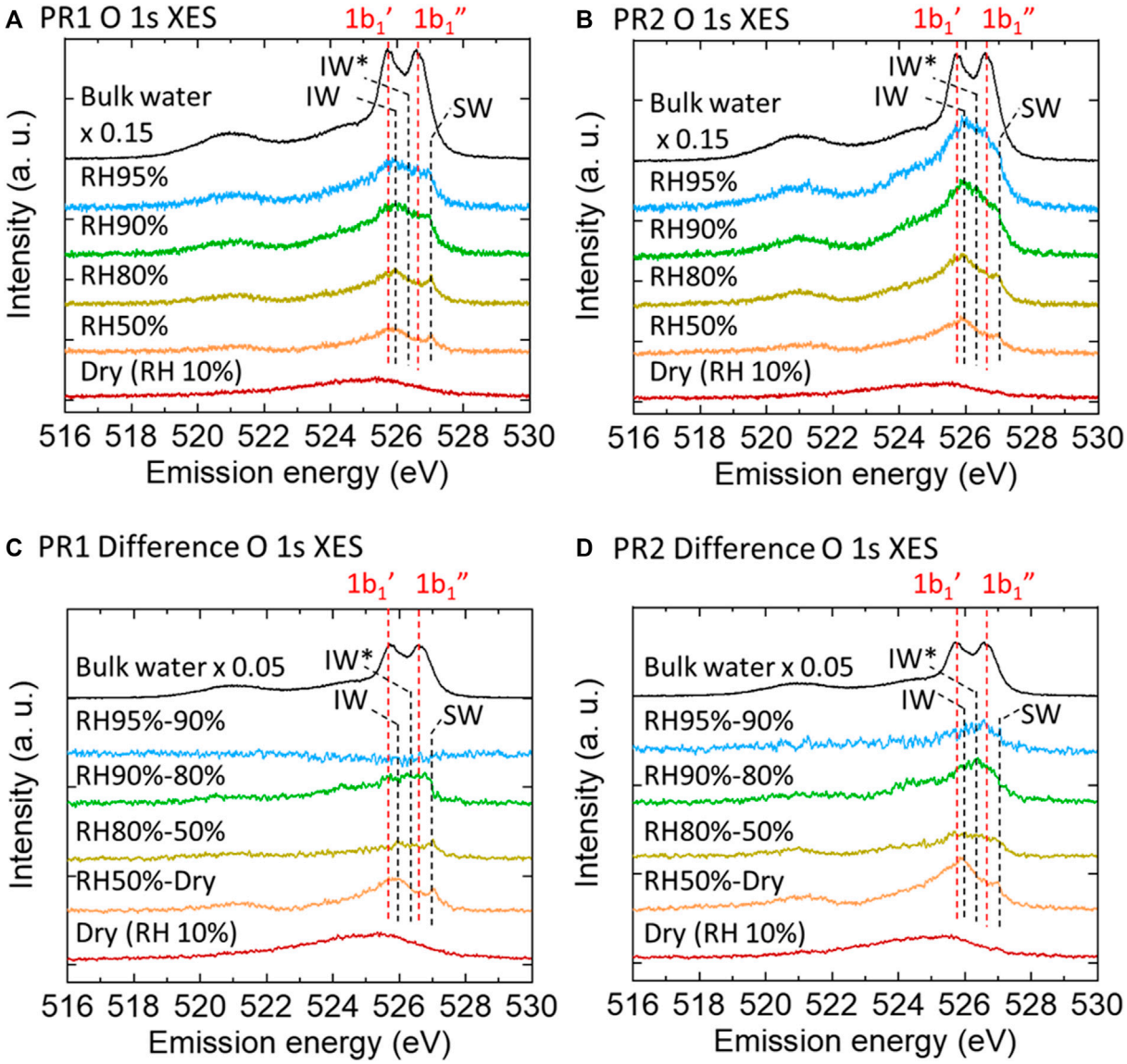

FIGURE 3 | O 1s XES spectra of PR1 **(A)** and PR2 **(B)** polyrotaxane polymer films at various humidities obtained by subtracting the dry polymer spectra. Dry (RH 10%) and pure water spectra are the raw data. Each difference spectrum **(C,D)** was obtained by subtracting the neighboring lower-humidity spectrum.

weights when the PEG/water ratio is 1:2 (Money, 1989). The average chain length between adjacent CDs in our polyrotaxane is 3,000 molecular weights, which is roughly consistent with our XES results in terms of the correlation between the molecular weight and the water content. PEG is well known as a crystalline polymer and generally has a helical conformation in the film state (Gemmei-Ide et al., 2006; Oparaji et al., 2016). The crystallinity of the PEG film was evaluated to be around 70% irrespective of its molecular weight (Kitano et al., 2001), and the other region has amorphous form. Water molecules in the crystalline phase of the PEG film might be localized in the amorphous region of the PEG chain because gaseous water diffuses mostly to the amorphous region in solid PEG polymers (Gemmei-Ide et al., 2006). Oparaji et al. (2016) reported that crystallinity of PEG was almost constant up to around RH80%, and this high ratio of crystallinity could explain the limited water absorption.

In contrast, at RH 90%, the intensity of the difference spectrum in the $1b_1$ region rapidly increases again. The degree of PEG crystallinity decreases with increasing humidity, especially from around 80%RH. Operaji et al. (2016) have demonstrated that the polyethylene oxide (PEO)-water interactions become more favorable with increasing humidity. Even though the PEO was of high molecular weight with highly entangled chains, it became a soft gel with no mechanical strength at high relative humidity. Our sharp upturn in sorption above RH 80% suggests that PEO/water interactions overcome crystallite restraints and lead to dissolution. These spectra show a broad peak centered at around 526.3 eV, which is higher energy than the

TABLE 1 | Detailed peak assignments of the $1b_1$ peak corresponding to each combination of energy and water structure.

Peak	$1b_1'$	IW	IW*	$1b_1''$	SW
Emission energy (eV)	525.7	525.9	526.3	526.6	527.0
Water structure	Bulk-liquid Tetrahedrally coordinated	Interfacial	Loosely bound	Bulk-liquid Distorted	Single bonded

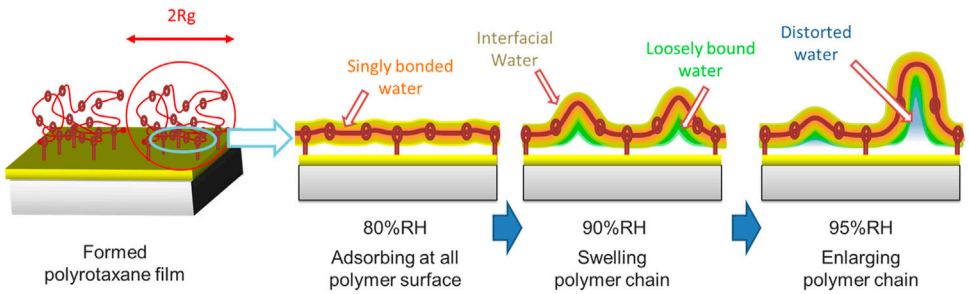

SCHEME 2 | Schematic images of the morphology changes of polyrotaxane and water. A thin directly bonded water layer (light blue) and interfacial water surround the hydrophilic PEG surface. Loosely bound water (green) and distorted water (orange) are located inside the large interfacial water region.

IW peak at 525.9 eV. This is explained by an increase in the number of dangling bond defects in the hydrogen-bonded network (Zhovtobriukh et al., 2018). Such dangling bond defects are observed in a PEG solution; water molecules surrounded by the PEG pseudo-network have distorted hydrogen-bonded structure, which has 1.0 less hydrogen-bonds per monomer unit of a polymer (Kitano et al., 2000). Accordingly, we consider that the absorbed water during the increase from RH 80% to RH 90% is a loosely bound water which has a hydrogen-bonded structure distorted by the nearby polymer chains as in the PEG solution. We call this $1b_1$ peak at 526.3 eV the IW* peak. The corresponding $1b_1$ peaks are tabulated in **Table 1**. The intensity of the difference spectrum in PR2 is larger than that in PR1. When polyrotaxane absorbs a large amount of water, the polymer chain swells to a large volume (Bin Imran et al., 2014) and the size of the PEG loop develops due to the sliding CD rings. Therefore, above RH 90%, slack in the polymer chain would be enlarged and further increase the amount of absorbed water (**Scheme 2**).

At RH 95%, the PR1 $1b_1$ peak does not increase because of the limited space for water absorption, while the PR2 $1b_1$ peak continued to increase, suggesting that additional water molecules can be stored in the large slack of the polymer loop. The PR2 $1b_1$ peak has a peak at 526.6 eV, which is commonly observed in bulk-liquid water as a $1b_1''$ peak. Many researchers have argued that bulk-liquid water contains two types of hydrogen-bonded structure: tetrahedrally coordinated and distorted. The former would correspond to the $1b1'$ peak and the latter to the $1b1''$ peak (Gallo et al., 2016). The 526.6 eV peak in PR2 suggests that the absorbed water has distorted hydrogen-bonded structure close to the $1b_1''$ component in bulk-liquid water. However, the $1b1'$ was not increased. The $1b_1'$ peak originates from water in tetrahedral-like patches with a dimension of 1–1.4 nm in dynamic equilibrium (Huang et al., 2009). The absence of the $1b_1'$ peak is possibly due to the limited space in polyrotaxane chains. In fact, the radius of gyration (Rg) of the PEG samples are estimated to be ~35 nm from the equation Rg (in nm unit) = 0.0215 $M_w^{0.58}$ (Devanand and Selser, 1991) in a solution, where M_w is the molecular weight of PEG. Because the PEG chain is flexible and bendable and some water molecules are bridging neighboring polymer chains, the spaces in some polymer loops might be decreased to less than 2 nm. Therefore, our presumption that water is confined within a space of a few nanometers seems reasonable. This is analogous to the case for mesoporous silica where differential scanning calorimetry measurements showed no freezing and melting point when the pore size of the mesoporous silica was less than 2.1 nm (Kittaka et al., 2006). This is explained that the pore diameter is less than the critical point of the nucleation diameter of 2.2 nm. We expect that the hydrogen-bonded structure of water will be significantly modulated when confined in a polymer loop.

Using various techniques the structure of hydrating water around biocompatible polymers has long been studied. Morita et al. (2007) conducted time-resolved ATR-IR on PMEA, and found that the freezing-bound water, which has hydrogen-bonding to the polymer with an intermediate strength between ice and bulk-liquid water, is likely to function as a biocompatible interface. If their discussion can be applied also to PEG, interfacial water or loosely bound water might be the origin of biocompatibility. Kittaka et al. (2006) found that water confined in a small space shows a cold crystallization property, which is also observed in biocompatible polymers (Tanaka and Mochizuki, 2010). Ide et al. (2003) estimated an extinction coefficient of the OH stretching band of absorbed water on a PMEA biocompatible polymer with ATR-IR measurement, and concluded that a cold crystallization of water is generated by caging water molecules in small spaces formed by the polymer chains. These previous studies indicated that water molecules confined in a narrow space surrounded by polymers could have a relation to the biocompatibility. Indeed, Yamada et al. (2012) reported that a polyrotaxane with looped PEG chains exhibited better biocompatibility than that with a linear one. We expect that the amount of water incorporated into the looped PEG, which may

contribute to biocompatibility, could be controlled by changing the loop size according to the anchoring density.

CONCLUSION

Specific hydrogen-bonded structure of incorporated water into polyrotaxane polymer films was investigated by O 1s X-ray emission spectroscopy. By changing the density of anchoring molecules that determine the number of fixing points in the main chain of the polyrotaxane polymer, we controlled the size of the confined space in the large slack of the polymer loop and the amount of absorbed water in it. The XES spectra showed that at low humidity, water molecules directly bonded to the polymer formed a tetrahedrally coordinated hydrogen-bond, while increasing the humidity, loosely bound and distorted hydrogen-bonded water dominated. In particular, at high humidity above RH 90%, uptake of water having distorted hydrogen-bonded structure with the peak around $1b_1''$ was observed. Intriguingly, the XES spectrum of the incorporated water completely lacks the tetrahedral $1b_1'$ peak, suggesting that the incorporated water is confined in the polymer loop where tetrahedral-like patches could not exist. Because confined water in a similar space in biocompatible polymers shows cold crystallization, the incorporated water in the polymer loop seems to be one of the origins of the superior biocompatibility of the looped polyrotaxane. Our study demonstrated that the amount of the confined water which would contribute to biocompatibility can be controlled by changing the anchoring density of polyrotaxane.

DATA AVAILABILITY STATEMENT

The original contributions presented in the study are included in the article/**Supplementary Material**, further inquiries can be directed to the corresponding authors.

AUTHOR CONTRIBUTIONS

YH and KI conceived, designed and coordinated the study. RM and KI prepared the samples. All authors conducted the synchrotron X-ray experiments. KA and YH analyzed the data. All authors discussed the results. KA and YH wrote the draft. YH reviewed and edited the manuscript. YH and KI supervised the work. YH and KY acquired the funding for this study.

FUNDING

This work was supported by JSPS KAKENHI Grant Numbers JP19H05717 (Grant-in-Aid for Scientific Research on Innovative Area: Aquatic Functional Materials) and 19K22195 (Grant-in-Aid for Challenging Research (Exploratory)).

ACKNOWLEDGMENTS

This work was carried out by joint research by the Synchrotron Radiation Research Organization and the Institute for Solid State Physics, The University of Tokyo (Proposal Numbers 2018A7401, 2018B7401 and 2020A7488). We thank H. Washizu and Y. Ishii for their fruitful discussion about interpretation of hydrogen-bonded configuration of interfacial water surrounding the PEG chains.

SUPPLEMENTARY MATERIAL

The Supplementary Material for this article can be found online at: https://www.frontiersin.org/articles/10.3389/fchem.2021.743255/full#supplementary-material

REFERENCES

Anderson, A., and Ashurst, W. R. (2009). Interfacial Water Structure on a Highly Hydroxylated Silica Film. *Langmuir* 25, 11549–11554. doi:10.1021/la901459b

Asay, D. B., and Kim, S. H. (2005). Evolution of the Adsorbed Water Layer Structure on Silicon Oxide at Room Temperature. *J. Phys. Chem. B* 109, 16760–16763. doi:10.1021/jp053042o

Bag, M., and Valenzuela, L. (2017). Impact of the Hydration States of Polymers on Their Hemocompatibility for Medical Applications: A Review. *Ijms* 18, 1422. doi:10.3390/ijms18081422

Benetti, E. M., Divandari, M., Ramakrishna, S. N., Morgese, G., Yan, W., and Trachsel, L. (2017). Loops and Cycles at Surfaces: The Unique Properties of Topological Polymer Brushes. *Chem. Eur. J.* 23, 12433–12442. doi:10.1002/chem.201701940

Bin Imran, A., Esaki, K., Gotoh, H., Seki, T., Ito, K., Sakai, Y., et al. (2014). Extremely Stretchable Thermosensitive Hydrogels by Introducing Slide-Ring Polyrotaxane Cross-Linkers and Ionic Groups into the Polymer Network. *Nat. Commun.* 5, 5124. doi:10.1038/ncomms6124

Daley, K. R., and Kubarych, K. J. (2017). An "Iceberg" Coating Preserves Bulk Hydration Dynamics in Aqueous PEG Solutions. *J. Phys. Chem. B* 121, 10574–10582. doi:10.1021/acs.jpcb.7b08030

Devanand, K., and Selser, J. C. (1991). Asymptotic Behavior and Long-Range Interactions in Aqueous Solutions of Poly(ethylene Oxide). *Macromolecules* 24, 5943–5947. doi:10.1021/ma00022a008

Ensing, B., Tiwari, A., Tros, M., Hunger, J., Domingos, S. R., Pérez, C., et al. (2019). On the Origin of the Extremely Different Solubilities of Polyethers in Water. *Nat. Commun.* 10, 2893. doi:10.1038/s41467-019-10783-z

Gallo, P., Amann-Winkel, K., Angell, C. A., Anisimov, M. A., Caupin, F., Chakravarty, C., et al. (2016). Water: A Tale of Two Liquids. *Chem. Rev.* 116, 7463–7500. doi:10.1021/acs.chemrev.5b00750

Gemmei-Ide, M., Motonaga, T., and Kitano, H. (2006). State of Irremovable Water in Solid Polymer Films Examined by Fourier Transform Infrared Spectroscopy I: Poly(Ethylene Glycol) Dimethyl Ether. *Langmuir* 22, 2422–2425. doi:10.1021/la053117f

Gilberg, E., Hanus, M. J., and Foltz, B. (1982). Investigation of the Electronic Structure of Ice by High Resolution X-ray Spectroscopy. *J. Chem. Phys.* 76, 5093–5097. doi:10.1063/1.442858

Greene, G. W., Martin, L. L., Tabor, R. F., Michalczyk, A., Ackland, L. M., and Horn, R. (2015). Lubricin: A Versatile, Biological Anti-adhesive with Properties Comparable to Polyethylene Glycol. *Biomaterials* 53, 127–136. doi:10.1016/j.biomaterials.2015.02.086

Harada, Y., Kobayashi, M., Niwa, H., Senba, Y., Ohashi, H., Tokushima, T., et al. (2012). Ultrahigh Resolution Soft X-ray Emission Spectrometer at BL07LSU in SPring-8. *Rev. Scientific Instr.* 83, 013116. doi:10.1063/1.3680559

Henke X-Ray Interactions with Matter. Available at: https://henke.lbl.gov/optical_constants/.

Huang, C., Wikfeldt, K. T., Tokushima, T., Nordlund, D., Harada, Y., Bergmann, U., et al. (2009). The Inhomogeneous Structure of Water at Ambient Conditions. *Proc. Natl. Acad. Sci.* 106, 15214–15218. doi:10.1073/pnas.0904743106

Ide, M., Mori, T., Ichikawa, K., Kitano, H., Tanaka, M., Mochizuki, A., et al. (2003). Structure of Water Sorbed into Poly(MEA-Co-HEMA) Films as Examined by ATR–IR Spectroscopy. *Langmuir* 19, 429–435. doi:10.1021/la020617p

Jena, K. C., and Hore, D. K. (2010). Water Structure at Solid Surfaces and its Implications for Biomolecule Adsorption. *Phys. Chem. Chem. Phys.* 12, 14383. doi:10.1039/C0CP00260G

Kang, T., Banquy, X., Heo, J., Lim, C., Lynd, N. A., Lundberg, P., et al. (2016). Mussel-Inspired Anchoring of Polymer Loops that Provide Superior Surface Lubrication and Antifouling Properties. *ACS Nano* 10, 930–937. doi:10.1021/Acsnano.5B06066

Kato, K., Karube, K., Nakamura, N., and Ito, K. (2015). The Effect of Ring Size on the Mechanical Relaxation Dynamics of Polyrotaxane Gels. *Polym. Chem.* 6, 2241–2248. doi:10.1039/C4PY01644K

Kitano, H., Ichikawa, K., Ide, M., Fukuda, M., and Mizuno, W. (2001). Fourier Transform Infrared Study on the State of Water Sorbed to Poly(ethylene Glycol) Films. *Langmuir* 17, 1889–1895. doi:10.1021/la0008986

Kitano, H., Sudo, K., Ichikawa, K., Ide, M., and Ishihara, K. (2000). Raman Spectroscopic Study on the Structure of Water in Aqueous Polyelectrolyte Solutions. *J. Phys. Chem. B* 104, 11425–11429. doi:10.1021/jp000429c

Kittaka, S., Ishimaru, S., Kuranishi, M., Matsuda, T., and Yamaguchi, T. (2006). Enthalpy and Interfacial Free Energy Changes of Water Capillary Condensed in Mesoporous Silica, MCM-41 and SBA-15. *Phys. Chem. Chem. Phys.* 8, 3223. doi:10.1039/b518365k

Laage, D., Elsaesser, T., and Hynes, J. T. (2017). Water Dynamics in the Hydration Shells of Biomolecules. *Chem. Rev.* 117, 10694–10725. doi:10.1021/acs.chemrev.6b00765

Liu, H., Liu, S., and Echegoyen, L. (1999). Remarkably Stable Self-Assembled Monolayers of New crown-ether Annelated Tetrathiafulvalene Derivatives and Their Cation Recognition Properties†. *Chem. Commun.* 1999, 1493–1494. doi:10.1039/A904249K

Lowe, S., O'Brien-Simpson, N. M., and Connal, L. A. (2015). Antibiofouling Polymer Interfaces: Poly(ethylene Glycol) and Other Promising Candidates. *Polym. Chem.* 6, 198–212. doi:10.1039/C4PY01356E

Money, N. P. (1989). Osmotic Pressure of Aqueous Polyethylene Glycols. *Plant Physiol.* 91, 766–769. doi:10.1104/pp.91.2.766

Morita, S., Tanaka, M., and Ozaki, Y. (2007). Time-Resolved *In Situ* ATR-IR Observations of the Process of Sorption of Water into a Poly(2-Methoxyethyl Acrylate) Film. *Langmuir* 23, 3750–3761. doi:10.1021/la0625998

Oparaji, O., Zuo, X., and Hallinan, D. T., Jr. (2016). Crystallite Dissolution in PEO-Based Polymers Induced by Water Sorption. *Polymer* 100, 206–218. doi:10.1016/j.polymer.2016.08.026

Ostaci, R.-V., Damiron, D., Al Akhrass, S., Grohens, Y., and Drockenmuller, E. (2011). Poly(ethylene Glycol) Brushes Grafted to Silicon Substrates by Click Chemistry: Influence of PEG Chain Length, Concentration in the Grafting Solution and Reaction Time. *Polym. Chem.* 2, 348–354. doi:10.1039/C0PY00251H

Schiros, T., Andersson, K. J., Pettersson, L. G. M., Nilsson, A., and Ogasawara, H. (2010). Chemical Bonding of Water to Metal Surfaces Studied with Core-Level Spectroscopies. *J. Electron Spectrosc. Relat. Phenomena* 177, 85–98. doi:10.1016/j.elspec.2009.09.009

Schlenoff, J. B. (2014). Zwitteration: Coating Surfaces with Zwitterionic Functionality to Reduce Nonspecific Adsorption. *Langmuir* 30, 9625–9636. doi:10.1021/la500057j

Tanaka, M., and Mochizuki, A. (2010). Clarification of the Blood Compatibility Mechanism by Controlling the Water Structure at the Blood-Poly(meth) acrylate Interface. *J. Biomater. Sci. Polym. Edition* 21, 1849–1863. doi:10.1163/092050610X517220

Tokushima, T., Harada, Y., Takahashi, O., Senba, Y., Ohashi, H., Pettersson, L. G. M., et al. (2008). High Resolution X-ray Emission Spectroscopy of Liquid Water: The Observation of Two Structural Motifs. *Chem. Phys. Lett.* 460, 387–400. doi:10.1016/j.cplett.2008.04.077

Weinhardt, L., Benkert, A., Meyer, F., Blum, M., Wilks, R. G., Yang, W., et al. (2012). Nuclear Dynamics and Spectator Effects in Resonant Inelastic Soft X-ray Scattering of Gas-phase Water Molecules. *J. Chem. Phys.* 136, 144311. doi:10.1063/1.3702644

Yamada, K., Katoono, R., and Yui, N. (2012). Controlled Loop and Graft Formations of Water-Soluble Polymers on SAMs for the Design of Biomaterials Surfaces. *Polym. J.* 44, 286–293. doi:10.1038/pj.2011.130

Yamamoto, S., Senba, Y., Tanaka, T., Ohashi, H., Hirono, T., Kimura, H., et al. (2014). New Soft X-ray Beamline BL07LSU at SPring-8. *J. Synchrotron Radiat.* 21, 352–365. doi:10.1107/S1600577513034796

Yamazoe, K., Higaki, Y., Inutsuka, Y., Miyawaki, J., Cui, Y.-T., Takahara, A., et al. (2017). Enhancement of the Hydrogen-Bonding Network of Water Confined in a Polyelectrolyte Brush. *Langmuir* 33, 3954–3959. doi:10.1021/acs.langmuir.7b00243

Zhao, C., Domon, Y., Okumura, Y., Okabe, S., Shibayama, M., and Ito, K. (2005). Sliding Mode of Cyclodextrin in Polyrotaxane and Slide-Ring Gel. *J. Phys. Condens. Matter* 17, S2841–S2846. doi:10.1088/0953-8984/17/31/009

Zhovtobriukh, I., Besley, N. A., Fransson, T., Nilsson, A., and Pettersson, L. G. M. (2018). Relationship between X-ray Emission and Absorption Spectroscopy and the Local H-Bond Environment in Water. *J. Chem. Phys.* 148, 144507. doi:10.1063/1.5009457

Conflict of Interest: The authors declare that the research was conducted in the absence of any commercial or financial relationships that could be construed as a potential conflict of interest.

Publisher's Note: All claims expressed in this article are solely those of the authors and do not necessarily represent those of their affiliated organizations, or those of the publisher, the editors and the reviewers. Any product that may be evaluated in this article, or claim that may be made by its manufacturer, is not guaranteed or endorsed by the publisher.

frontiers in Chemistry

REVIEW
published: 29 October 2021
doi: 10.3389/fchem.2021.738350

What Does Time-Dependent Fluorescence Shift (TDFS) in Biomembranes (and Proteins) Report on?

*Federica Scollo, Hüseyin Evci, Mariana Amaro, Piotr Jurkiewicz, Jan Sykora and Martin Hof**

J. Heyrovský Institute of Physical Chemistry of the CAS, Prague, Czechia

The organization of biomolecules and bioassemblies is highly governed by the nature and extent of their interactions with water. These interactions are of high intricacy and a broad range of methods based on various principles have been introduced to characterize them. As these methods view the hydration phenomena differently (e.g., in terms of time and length scales), a detailed insight in each particular technique is to promote the overall understanding of the stunning "hydration world." In this prospective mini-review we therefore critically examine time-dependent fluorescence shift (TDFS)—an experimental method with a high potential for studying the hydration in the biological systems. We demonstrate that TDFS is very useful especially for phospholipid bilayers for mapping the interfacial region formed by the hydrated lipid headgroups. TDFS, when properly applied, reports on the degree of hydration and mobility of the hydrated phospholipid segments in the close vicinity of the fluorophore embedded in the bilayer. Here, the interpretation of the recorded TDFS parameters are thoroughly discussed, also in the context of the findings obtained by other experimental techniques addressing the hydration phenomena (e.g., molecular dynamics simulations, NMR spectroscopy, scattering techniques, etc.). The differences in the interpretations of TDFS outputs between phospholipid biomembranes and proteins are also addressed. Additionally, prerequisites for the successful TDFS application are presented (i.e., the proper choice of fluorescence dye for TDFS studies, and TDFS instrumentation). Finally, the effects of ions and oxidized phospholipids on the bilayer organization and headgroup packing viewed from TDFS perspective are presented as application examples.

Keywords: hydration, time-dependent fluorescence shift, biomembranes, calcium, oxidized phosholipids, cholesterol, membrane dynamics, lipid headgroups

OPEN ACCESS

Edited by:
Motomu Tanaka,
Heidelberg University, Germany

Reviewed by:
Oh-Hoon Kwon,
Ulsan National Institute of Science and Technology, South Korea
Sadafara Anand Pillai,
P P Savani University, India

****Correspondence:***
Martin Hof
martin.hof@jh-inst.cas.cz

Specialty section:
This article was submitted to Physical Chemistry and Chemical Physics, a section of the journal Frontiers in Chemistry

Received: *08 July 2021*
Accepted: *21 September 2021*
Published: *29 October 2021*

Citation:
Scollo F, Evci H, Amaro M, Jurkiewicz P, Sykora J and Hof M (2021) What Does Time-Dependent Fluorescence Shift (TDFS) in Biomembranes (and Proteins) Report on?. Front. Chem. 9:738350. doi: 10.3389/fchem.2021.738350

INTRODUCTION

The role of the hydration in maintaining the biological function of biomolecules and biomolecular aggregates is unquestionable (Disalvo, 2015; Biedermannová and Schneider, 2016). Water molecules affect their structure, dynamics and mutual interactions. Although water is a relatively simple molecule being built only from three atoms, its capability to form four hydrogen bonds makes its spatial arrangements in solution extremely complex (Kühne and Khaliullin, 2013). This applies also for the water molecules solvating the biomolecules and biomolecular self-assemblies (Martelli et al.,

2020). Huge variety of the achievable hydration motifs bestow the biological entities unique and anomalous properties, which are often supportive for their role and function (Ball, 2008).

In the case of proteins, water interacts with a heterogeneous partner (Levy and Onuchic, 2006). Water molecules can be buried inside the core of proteins employing long residence times which makes them an integral component of protein structure. Such water molecules can be located in confined regions such as internal cavities and active sites being trapped also on a substantially longer time scales than water molecules interacting with the surface of a protein (Russo et al., 2004). Interfacial water molecules are affected by the complex protein topography dynamically interacting with amino acid residues of various chemical compositions and physical properties. This all makes the protein hydration complex and its characterization rather challenging.

Lipid bilayers (core of biomembranes) represent a biomolecular self-assembly essential for the existence of living organisms. Lipid bilayers also show a complex hydration patterns (Disalvo, 2015; Tristram-Nagle, 2015), even when composed of a single lipid species only. In comparison to proteins, such bilayers offer water molecules very limited number of different polar groups for the formation of hydrogen bonds. Biomembranes are self-assembled thanks to the interaction of the amphiphilic lipids with water molecules that stabilize the bilayer structures. Although water presence is an urge for the bilayer existence, its role has often been underestimated in the past when elucidating the membrane structure and function. The complex lipid bilayer was oversimplified and viewed as the rigid nonpolar entity sandwiched by bulk water molecules. Advances in both theoretical and experimental techniques have been gradually revealing the full complexity of water—lipid interactions, putting the bilayer hydration on the merited pedestal. Water not only stabilizes biomembranes *via* hydrophobic effect but also serve as plasticising spacer within the lipid headgroups balancing the free volume in the hydrocarbon chains, which enables the formation of liquid phases. Moreover, hydration enhances the configurational space for additional water and lipid populations which assist for instance the peptide binding (Ge and Freed, 2003).

The closer look on the water distribution along the bilayer normal reveals that majority of water molecules can be found in the interfacial headgroup region (Nagle and Tristram-Nagle, 2000). Three basic types of the interfacial hydration modes have been suggested: evidently free water resembling the bulk; water molecules directly interacting with lipids (Tristram-Nagle, 2015), but also less defined "perturbed" water (Sparr and Wennerström, 2001), whose properties are supposed to be affected by the presence of lipid membranes. Please note, that although the interfacial properties of biomembranes are mostly affected by the headgroup structure and its local hydration and orientation, hydrophobic interactions within the hydrocarbon region considerably modulate the interfacial dynamics as well.

In order to track the degree and nature of the hydration of biomolecules and bioassemblies, manifold of the experimental approaches have been introduced. Each of these methods is unique from the perspective of the length-scale and time-scale of the followed parameters (Biedermannová and Schneider, 2016). Inevitably, the apparent inconsistency among the conclusions based on different approaches may arise, and in fact frequently springs out. To minimize these discrepancies, a critical and explaining reviews are necessary to converge to a consistent picture of the interfacial hydration of the biological molecules and assemblies.

The main topic of this contribution is Time-Dependent Fluorescence Shift (TDFS) (Horng et al., 1995; Jurkiewicz et al., 2012a). TDFS (denoted also as solvent relaxation (SR) or time-dependent Stokes shift (TDSS)) characterize both the dynamics of the hydrated segments of proteins and membranes as well as the level of hydration in the site-specific manner. We would like to point out that there is an extensive literature on the characterization of TDFS in proteins (Pal et al., 2002; Pal and Zewail, 2004; Bagchi, 2005; Li et al., 2007; Bhattacharyya, 2008; Chang et al., 2010; Zhong et al., 2011). Quite a number of these studies were focused on the characterization of the nature of the local water in the hydration shells of proteins by TDFS, including the concept of "biological water." As explained in the following section that concept based on the suggestion of long-range modification of the structure and dynamics of water around proteins appears nowadays questionable. We believe the discussion of these contributions using TFDS in proteins would need the confrontation with the newer literature on the water shell of proteins, which could be the subject of an independent review. In this mini review, we will focus on the applicability of this technique to study biological systems and on the interpretation of its results, with a strong emphasis on model lipid membranes.

Below, we start with a short overview of the current knowledge about the hydration of biological systems. Further, we shortly describe the theoretical background of TDFS method. Then, we cover the interpretation of the relaxation probed in lipid membranes. We address the applicability of the method and clearly point out its limitations. Description of the TDFS instrumentation as well as the choice of the fluorescent probes is also given.

WHAT DOES ONE UNDERSTAND AS THE "WATER SHELL" OF A LIPID BILAYER; CONCLUSIONS FROM LABEL-FREE TECHNIQUES

Before focusing on the principles and applications of the TDFS technique for the investigation of lipid bilayers, it is helpful to discuss the current knowledge on the hydration shell of biomolecules obtained by label free techniques. It is essential to acknowledge that within the last decade advances in molecular dynamics simulations as well as in ultrafast vibrational spectroscopy led to a much clearer picture about how one has to understand the water shell of lipid bilayer. The conclusions drawn were summarized in a seminal review by Laage et al. (2017). We take here the liberty to quote directly from this review: "Starting from the interfacial water layer, the hydration shell

assumes the structure of bulk-like water within a few layers, typically less than five layers. Claims of a significant long-range modification of the structure and dynamics of water around biomolecules lack theoretical and experimental evidence." This finding clarifies what are those three basic types of the interfacial hydration modes mentioned in the introduction: 1) bulk water, 2) water molecules directly interacting with lipids which are imbedded in 3) adjacent water layers. Importantly, these water layers are only a few, typically less than five layers.

Despite that relatively low number of interfacial water molecules, it is undoubtedly accepted that the structure and function of the biological membranes are strongly affected by the dynamic properties of the hydration water layer. Indeed, it plays a pivotal role in transport and signalling functions, mediating membrane-membrane interactions, as well as the ones with ions, DNA or proteins (Disalvo and Bakás, 1986; Hamley, 2000; Berkowitz et al., 2006). This is supported by evidences showing that the number of molecules in the hydration shell influences the properties of the lipid bilayer, such as thickness, area per lipid, melting temperature (Ladbrooke et al., 1968; Gawrisch et al., 1990). Even though above a clear definition of the hydration shell is given, one has to acknowledge an intrinsic variability found in the literature which is dependent on the method used (Laage et al., 2017). Different methods might probe different aspects or concepts of the same issue.

The hydration shell in lipid bilayers is highly oriented, due to the tendency of the water molecules to reach the lowest number of hydrogen bonding configuration as well as electric field created by the oppositely charged choline and phosphate groups (Gawrisch et al., 1990). ATR-FTIR studies have detected perturbation of water through several layers beyond the first one (Arsov, 2015). By using computational approaches, an average value of the hydration shell thickness has been estimated to be around 3.5 Å. The value can be determined as the distance to the first minimum in the radial distribution function (Stirnemann et al., 2013; Duboué-Dijon and Laage, 2014; Fogarty and Laage, 2014; Duboué-Dijon et al., 2016). All-atom simulations have shown that bound water might play an essential role in stabilizing the phospholipid self-assembly, by establishing strong hydrogen bonds and bridging between lipids (Calero and Franzese, 2019).

NMR allows to probe the dynamics of water molecules (Laage et al., 2017). Moreover, it gives information about the water molecular reorientation by monitoring the longitudinal spin relaxation rates of water hydrogen or oxygen isotopes or by measuring the quadrupolar splitting, proportional to water orientation order parameters (Abragam, 1961; König et al., 1994; Ulrich and Watts, 1994; Volke et al., 1994; Wassall, 1996; Berkowitz et al., 2006). Historically, NMR significantly contributed to the current knowledge about the hydration layers, e.g., for PE, PG and PC lipids purified from *E. Coli*, two distinct regions could be distinguished in the relaxation time profile obtained by 2H-NMR. A minimum of 11–16 molecules was found to be part of the first hydration shell, corresponding to a correlation time of 90 ms. Furthermore, an exchange with water molecules not strictly belonging to the first layer has been observed (Borle and Seelig, 1983).

Other representative experimental methods to evaluate water molecules lipid membranes are X-ray and neutron diffraction spectroscopies, specifically the combination of LAXS and neutron scattering from isotropic unilamellar vesicles has been proved to give precise information (Tristram-Nagle and Nagle, 2004; Kučerka et al., 2008). SAXS and SANS are nowadays regularly applied to determine molecular structure at the nanometer scale (Svergun et al., 1998; Merzel and Smith, 2002; Koch et al., 2003; Foglia et al., 2010). Briefly, the combined methods allow to calculate structural features, such as bilayer thickness and area per lipid, which are needed, together with other parameters obtained by specific fitting procedures, to gain information about the number of water molecules. By correcting the equation, insights on the steric number of water molecules, namely headgroup structural water, can be obtained (Tristram-Nagle, 2015). By using the above-described approach, this value was estimated to be between 7 and 8 bound water molecules for phosphatidycholine headgroup (Nagle and Tristram-Nagle, 2000). However, a more comprehensive summary and a related comparison with other experimental techniques can be found elsewhere (Tristram-Nagle, 2015).

QENS and THz TDS are other powerful techniques to study the dynamics of water molecules in the hydration shell, strongly bound to lipid membranes (Swenson et al., 2008; Hishida and Tanaka, 2011; Yamada and Seto, 2020). While QENS probes the hydrogen motions over different length scale by varying the wavenumber, the THz TDS monitors the collective hydrogen-bond distortion by measuring the absorbance in the far infrared frequency range (Laage et al., 2017). Taking advantage of their lower scattering section, hydrogen atoms can be replaced by deuterium ones. The latter renders QENS sensitivity to the specific hydrogen atoms, for instance the water ones and not those belonging to the biomolecules (Laage et al., 2017). THz TDS can measure the dynamics of water molecules around 10^{-13} s (1 THz = 0.16 ps) (Rønne et al., 1999; Yada et al., 2008). NMR and inelastic neutron scattering can investigate time scales up to 10^{-9}–10^{-11} s (Swenson et al., 2008; Amann-Winkel et al., 2016), but the rotational relaxation time of bulk water is around 10^{-13} s (Hishida and Tanaka, 2011). As such, NMR and inelastic neutron scattering methods are capable of investigating the water molecules in the first hydration shell, without accessing the dynamics of the long-range water molecules in the hydration shell. By THz TDS in DOPC bilayers 1–4 "irrotational" water molecules per lipid have been identified (Tielrooij et al., 2009). Whereas employing QENS the number of bound water molecule was found to be around five in DMPC bilayers decreasing with temperature, the sum of tight and loose water molecules around 10, and constant within the studied temperature range (Yamada et al., 2017).

Further insights could be gained by using a combination of different techniques, e.g., NMR and neutron diffraction study have showed that water molecules in the hydration shells actually interact with the headgroup of DOPE lipids, specifically with the ammonium group (Rhys et al., 2019). Moreover, combining THz

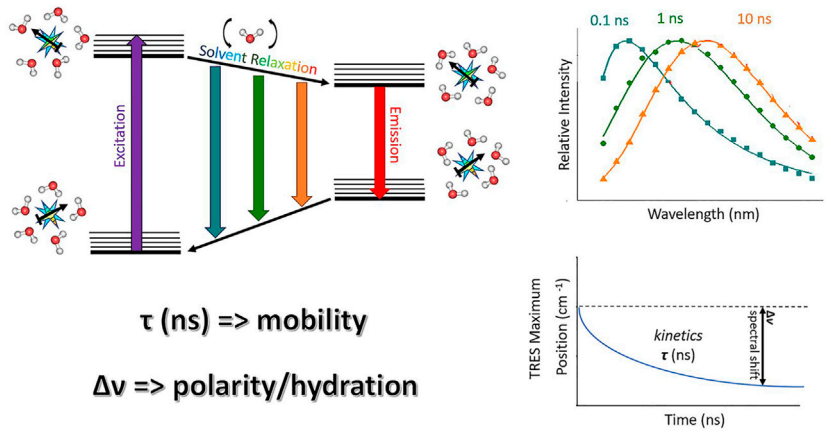

FIGURE 1 | A schematic drawing illustrating TDFS method: On the left, a simplified Jablonski diagram is depicted. A fluorescence probe represented by a light blue star bearing certain dipole moment (black arrow) is solvated by water molecules. These are oriented in the energetically lowest conformation in the ground state. Upon the excitation, a dipole of the dye changes rapidly, organization of the solvation shell thus becomes energetically unfavorable. Consequently, the solvent molecules start to reorient which decreases the energy of the system. This continuous decrease can be accessed by recording TRES which shows red-shift in time (upper right figure). The TRES maxima are then analyzed yielding overall dynamic Stokes shift Δν and characteristic relaxation time τ (lower right figure). Δν and τ reflect the extent of energy relaxation caused by hydration and mobility of the hydrated lipid segments in the probe microenvironment, respectively.

TDS with SAXS, it has been concluded that the thickness of hydration shell in the DMPC membranes is approximately 1 nm and there are around 28 water molecules belonging to this hydration shell (Hishida and Tanaka, 2011). Some of these studies aimed to shed light on the localization of the water molecules composing the hydration layer. It has been shown that the phosphatidylcholine headgroup is strongly associated with water, more specifically, phosphate and carboxyl groups are oversaturated in the number of hydrogen bonding, when compared to the bulk water (Foglia et al., 2010).

It should be highlighted that the here given information on the water shell of lipid bilayers are simply selected examples from a large variety of techniques and does not represent a fully comprehensive overview of the literature. The exact definitions of bound water and the obtained results vary for those techniques. Nevertheless, from those selected examples a rather clear picture of the water shell arises, which we would like to summarize here for a phosphatidylcholine bilayer. A phosphatidylcholine headgroup contains, beside of the three glycerol oxygen atoms and two carbonyls, a positively charged choline and a negatively charged phosphate group. Thus, the phosphatidylcholine offers eight oxygen atoms for establishing hydrogen bonds. Interestingly, the experimentally determined numbers of bound water molecules per lipid molecule are found to be in the same order of magnitude. Further the experimental data suggest the water layers adjacent to those bound water molecules to be thinner than 1 nm and formed by about 20 water molecules or less. Beyond that layers water molecules behave as in the bulk.

While these examples are based on label-free techniques, TDFS requires an introduction of low concentrations of aromatic chromophores to the lipid bilayer, which can disturb the studied system. However, as shown in the next paragraph, TDFS can give distinct information on the changes in hydration and mobility at defined positions within the phospholipid headgroup, with the advantage to the label free techniques of being experimentally simple and inexpensive.

BASIC PRINCIPLES OF TIME-DEPENDENT FLUORESCENCE SHIFT

TDFS was originally applied for studying solvation dynamics in neat solvents, e.g., proving water relaxation to occur on the sub-picosecond time scale. It is based on the perturbation of the solvation shell of the fluorophore caused by its rapid electronic excitation accompanied by the change in its charge distribution. Surrounding molecules, when bearing dipole moment, start to reorient in order to adapt to the abrupt change caused by the solute excitation. The solvent molecules keep on rearranging till the energetically favorable state is reached. This continuous relaxation process leading to the dynamic decrease in the energy of the system is known as solvent relaxation. It is projected as the transient red-shift of the recorded time-resolved emission spectra (TRES) being the core of TDFS technique (**Figure 1**). The TDFS analysis comprise the difference between the energies of initial non-equilibrium Franck-Condon state and fully relaxed excited state, denoted as $\Delta\nu$, which correlates with polarity of the solvent (Horng et al., 1995). Moreover, the kinetics of the TDFS was found to reflect solvent viscosity (Ito et al., 2004). This is the straightforward interpretation that is applicable in the case of neat solvents. However, the situation gets more complex in the presence of biological molecules and biointerfaces, due to their heterogeneous nature. The most striking difference is the retardation of the TDFS timescales occurring universally for the vast majority of biomolecules and biointerfaces. Specifically, significantly slower components (subnano- and nanoseconds) appear in TDFS

kinetics. The explanation for this slow-down implies that the slow TDFS does not originate from the motions of individual water molecules, but is governed by the movements of the hydrated segments of biomolecules. Naturally, the contribution of the segmental movements to TDFS response is highly dependent on the type of biomolecule/bioassembly. Therefore, the analysis and interpretation of TDFS results require profound knowledge of the investigated system. In the following section, we will illustrate this approach on mapping the organization of the lipid bilayers by TDFS, taking into consideration broader atomistic context.

TIME-DEPENDENT FLUORESCENCE SHIFT IN MODEL LIPID MEMBRANES

The Origin of the Solvent Relaxation in Lipid Membranes

The molecules of water hydrating lipid bilayer are the major source of polarity sensed by TDFS. The mobility of those water molecules is, however, strongly restricted. Compared to bulk aqueous solutions the timescale of relaxation probed by TDFS slows down from hundreds of femtoseconds to nanoseconds on the distance of 1–2 nm (Sýkora et al., 2002a). Here we focus on the origin of the relaxation process in lipid membranes. In pure water, the relaxation starts with fast librational motions, after which rotations and translations of water molecules establish a new transiently equilibrated molecular arrangement (Horng et al., 1995). Of course, this new order lasts only till the fluorescent emission of the probe occurs. Relaxation in bulk water is affected by the structural properties of the bulk water with its complex, but dynamic, hydrogen bonding network. Spectroscopic data, as well as computer simulations, clearly demonstrate that solutes can affect only the structure of water within a distance of about the size of two to five water molecules and that the disturbance disappears within picoseconds when its source is removed (Zhong et al., 2011; Laage et al., 2017). This is why the structural properties of water are insufficient to explain the three-orders of magnitude slow-down of the relaxation process in lipid bilayers. The frequent exchanges between the molecules of bulk water and those bound to lipids do not contribute considerably to the relaxation process. It is because the arrangement of the newly arrived water molecules is the same as the one being replaced. It is still defined by the arrangement of the molecules of lipids (Horng et al., 1995). Effectively, all water molecules that are entrapped at phospholipid bilayer are bound to lipids and to each other creating a rather well-defined network. In order to dipolarly relax, this network requires movement of the hydrated lipid molecules or their parts. Of course, the method is sensitive only to the molecular motion relative to the fluorophore. This is an important consideration since the molecule of the fluorescent probe can be equally mobile as the molecules of lipids in its surrounding. Because of the above presented arguments, the slow relaxation components observed in a lipid bilayer should be attributed to the movement of the molecules of lipids and fluorophore, rather than the individual movement of the molecules of water (Sýkora et al., 2002a).

Interpretation of Time-Dependent Fluorescence Shift Results

The polarity sensed by TDFS in lipid bilayer is usually determined by the average number of water molecules within the microenvironments of the fluorescent probes. This is the foundation of TDFS sensitivity to membrane hydration. Not only TDFS provides a quantitative measure of membrane hydration (i.e., the extent of energy relaxation caused by hydration), but it also measures it locally (at certain depth within the membrane). This increases the specificity of the obtained information about membrane hydration and allows assessment of the complete hydration profiles of lipid membranes (an example can be found in **Figure 2A**).

The fact that the nanosecond relaxation probed by TDFS reflects the mobility of hydrated phospholipids is the source of the unique sensitivity of this method to the changes in lipid dynamics. These changes can be easily measured in free standing, fully-hydrated lipid membranes, which is uncommon for other methods including label-free techniques. TDFS allows to study even the subtle effects caused by heavy water (Beranová et al., 2012), specific salt ions (Jurkiewicz et al., 2012b) or lipid and sterol oxidation (Kulig et al., 2015b), to name just a few. As in the case of hydration also the mobility of hydrated lipid moieties is assessed locally. E.g., Patman, which is located at the level of lipid carbonyls, was shown to probe the hydration and mobility of the *sn*-1 lipid carbonyls (Olżyńska et al., 2007). With sensitivity and specificity of TDFS comes the need for the great care when designing and interpreting the results of the experiments.

Limitations of the Method

TDFS interpretation provided above is strictly valid for deeper locations of polarity probes in lipid bilayer, i.e., when fluorophores are positioned around the level of phospholipid glycerol backbone and deeper. Probes located more outside are to some extend influenced by the fast bulk-water relaxation. This contribution becomes a dominant source of the whole relaxation process for the case the probe is located in the outer part of the headgroup region or further away (Horng et al., 1995). Also, in the case of very deep locations of the fluorophores, proper recording of the whole relaxation process might be impossible (Volinsky et al., 2011). It is due to limited probe lifetime (usually a few nanoseconds) and low polarity caused by only sparse presence of water in this region.

Limited fluorescence lifetime of a probe is also the reason, why TDFS is fully applicable only to lamellar liquid-crystalline lipid phases. Heavily immobilized lipids, e.g., in their gel-phase (S_o), do not provide sufficient rearrangement during the lifetime of a probe (Amaro et al., 2014). Fortunately, the most physiologically-relevant are the membranes in their liquid phases. The method is applicable not only to liquid disordered (L_d) phase, but also to the so-called liquid ordered membranes (L_o). In L_o phase the mobility of the molecules is limited by the presence of sterol that fills the gaps between the phospholipids. Nonetheless, for some cases with high content of cholesterol or at low temperatures, limitations of the technique can be also reached in L_o membranes (Kulig et al., 2015a).

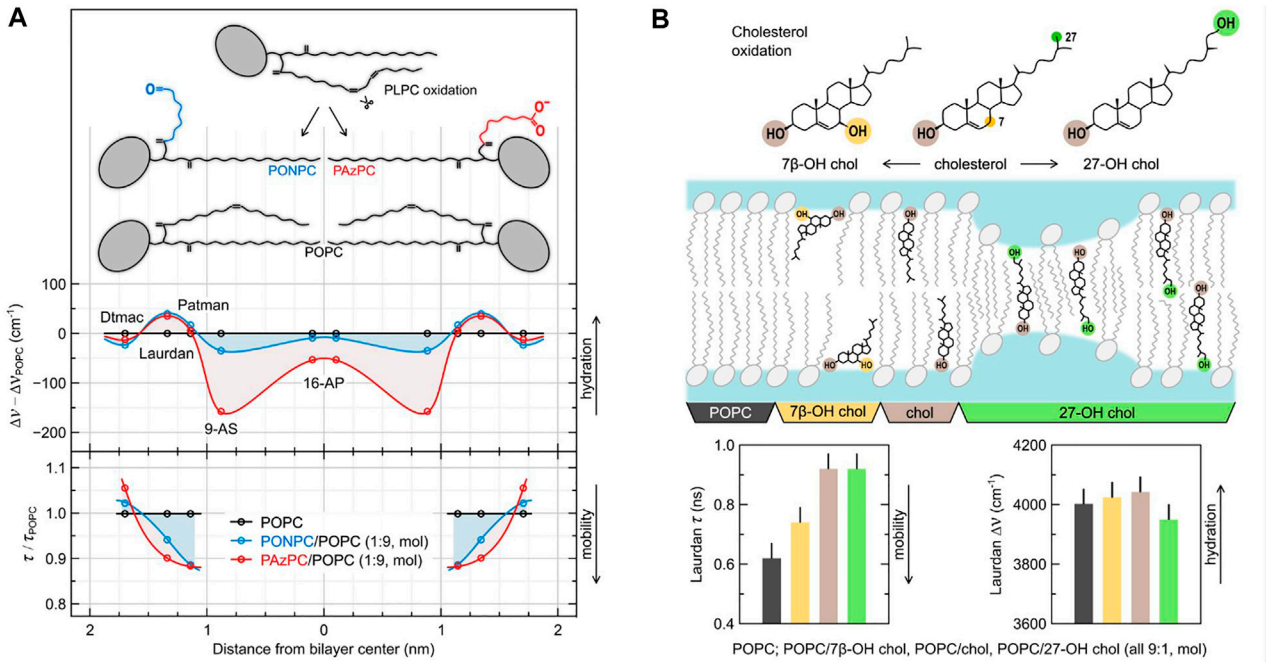

FIGURE 2 | The effects of oxidation of model lipid membranes on local hydration and mobility probed using TDFS. **(A)** depicts the influence of the addition of 10 mol% of truncated oxidized phospholipids (oxPLs) into POPC liposomes. The relative changes in hydration and mobility profiles across the membrane are obtained by comparing TDFS parameters measured in the absence and in the presence of oxPLs. They are presented based on the known or estimated locations of the used fluorophores (Dtmac, Laurdan, Patman, 9-AS, and 16-AP). The schematic structures of the lipid molecules are presented in scale. **(B)** depicts the influence of the addition of 10 mol% of cholesterol and two of its oxidation products into POPC liposomes. Position of the sterol molecules within the bilayer are schematically portrayed based on molecular dynamics simulations, but the effects are exaggerated for the illustrative purposes. The TDFS result shown in the bar graphs are color coded. Experimental details can be found in the original publications the figure was adopted from (Volinsky et al., 2011; Kulig et al., 2015b).

Fortunately, TDFS methodology provides suitable tools to recognize the problematic situations described above. Careful examination of the full-width at half-maxima (FWHM) of TRES and the time-zero spectrum estimation allow for identification of the number of problems and for evaluation of the completeness of the recorded relaxation process. The basics and applicability of these tools was described in detail in our previous work (Jurkiewicz et al., 2005).

The contribution of lipid molecules to the polarity measured by TDFS is usually limited when compared to that of water molecules. Nevertheless, possible contribution of the system components (including lipids) to the measured polarity, as well as possibility of their specific interactions with fluorescent probe should be evaluated in each case. After the issues related to probe relocation (discussed in section "Choice of the suitable dyes for membrane and protein studies"), the specific influence of the studied molecules on the fluorescent probe are the major source of complicacy in TDFS analysis.

Steady-State Alternatives for Time-Dependent Fluorescence Shift

The polarity probes utilized in TDFS can be useful even when time-resolved instrumentation is not available. The most common steady-state methods that utilize fluorescent polarity probes and can be applied to characterize lipid membranes include red-edge excitation shift (REES) (Lakowicz and Keating-Nakamoto, 1984; Demchenko, 2002) and generalized polarization (GP) (Parasassi et al., 1990; Bagatolli, 2012). Lower cost of instrumentation, often simplified analysis and faster measurements, but also compatibility of some of them with fluorescence microscopy are advantages that should not be overlooked. In the case of rigorous evaluation of the lipid membrane properties their major drawback is the lack of the kinetic data. Lipid hydration and mobility, the two parameters, that are readily available from TDFS analysis, remain inevitably coupled in steady-state methods, and additional information is needed in order to separate their contributions to the measured steady-state parameters. The absence of such information might lead to certain misinterpretations, e.g., when the changes of a single parameter, like GP, are interpreted exclusively in terms of either hydration/polarity or mobility/fluidity of lipid bilayer, without considering that they may change together and sometimes even compensate for each other (see, e.g., Amaro et al., 2014). A wise compromise between TDFS and the simplified approaches is sometimes possible. For example, the time-resolved version of GP, proposed already by Parasassi et al. (1986), was recently adapted to confocal microscopy allowing successful GP-FLIM analysis of living cells in a manner assuring both sufficient precision and speed needed for live-cell imaging (Ma et al., 2018).

INTERPRETATION OF TIME-DEPENDENT FLUORESCENCE SHIFT IN COMPLEX BIOMEMBRANES AND PROTEINS

As illustrated above, TDFS possesses a great potential to map hydration and packing effects in monophasic model lipid membranes providing interpretable outputs. The homogeneous membranes present an anisotropic system along the membrane normal, yet staying isotropic in the lateral directions. Although the lipid and probe fluctuations along the z-axis cannot be excluded (Nagle and Tristram-Nagle, 2000), the averaging of the TDFS response over the distribution of locations provides a reasonable estimate on the membrane organization at the bilayer region corresponding to the time-averaged position of the probe. The problem arises at the situations with the multiple probe locations, which were observed for instance for the complex phase separated model bilayers. Most of the common probes partition in both phases differing in TDFS traces. To separate the time courses could be possible by decomposing the multi-component time resolved emission spectra (TRES) into the respective contributions. However, this type of data processing seems to be ill-defined for the limited number of data points in recorded TRES (typically, TRES are recorded in 10 nm steps).

Even more entangled situation in comparison to the complex lipid membranes arises in proteins, which form an anisotropic entity with high chemical heterogeniety in all three dimensions. This results in an extremely complex TDFS response, which was illustrated for example for the dehalogenase enzymes (HLDs). The tunnel mouth region of the selected HLDs was labeled with a set of various fluorophores, based on Coumarin-120 and Prodan-like probes (denoted as Muc) (Amaro et al., 2013). In spite of the fact that the probes were positioned at the same well-defined location, the TDFS response was largely heterogenous. For the Coumarin-based probe, the TDFS kinetics in HLDs appeared to be significantly faster than those obtained for HLDs labeled with *Muc* probes. These experiments revealed that the specific contact sites between the probe and hydrated amino-acid residues (which naturally will be dependent on the chemical structure of the fluorophore) has to be regarded for the quantitative TDFS application. To identify these dye-specific effects the assistance of MD simulations is of high importance.

CHOICE OF THE SUITABLE DYES FOR MEMBRANE STUDIES

The proper choice of the fluorescent dye is essential for the successful TDFS implementation. The ideal probe should fulfill three basic requirements:

1. In order to introduce sufficient perturbation by the dye photoexcitation into the system, the probe must show a significant difference between the excited and ground state dipole moments in magnitude and/or direction. This difference is usually translated into the large Stokes shift observed for polar solvents.
2. The ideal TDFS dye is to possess a linear solvatochromic behavior, i.e., no specific interactions should interfere with the polarity dependence.
3. The knowledge of the location of the probe is clearly of utmost importance for the correct interpretation of data. A probe should have as defined location in the system of interest as possible, be it a lipid bilayer (e.g., depth of location) or a protein (e.g., specific labelling).

Coumarin-153 is one of the best examples of fluorescent dyes appropriate for TDFS studies, especially for the neat solvents (Horng et al., 1995) and micellar systems (Sonu and Saha, 2016). It shows large Stokes shift and linear solvatochromic behavior. Unfortunately, its derivatives tailored for the protein and membrane labelling are not commercially available which limits its applicability. Nevertheless, other coumarin derivatives, 6,7-dimethoxy-coumarin (Jesenska et al., 2009) and coumarin-120 (Amaro et al., 2013; Stepankova et al., 2013; Sykora et al., 2014), were used for TDFS studies of Dehalogenases. These dyes do not possess as superior characteristics as Coumarin-153, but they enable selective labelling of the biologically relevant region of dehalogenase enzymes. This illustrates that the choice of the dye is often a search for the optimal compromise among the basic requirements listed above. Please note, that not all coumarin derivatives are suitable for TDFS. For example the 7-hydroxy-4-methylcoumarin can adopt different forms resulting in a complex excited state kinetics (Choudhury et al., 2008; Choudhury and Pal, 2009; Amaro et al., 2015) that hinders interpretation of the TDFS data. Nonetheless, this coumarin is still sensitive to the extent of local hydration and can be used for qualitative studies of proteins in a site-specific fashion (Amaro et al., 2015). Similarly, the water-driven proton transfer of tryptophan analogues can be used for mapping hydration in a site-specific manner in biological systems via fluorescence techniques (Shen et al., 2013; Chen et al., 2016). Yet TDFS applicability of those Trp-based dyes is disqualified due to their complex photophysics.

Popular strategy for designing the TDFS probes is the insertion of an electron donating and electron withdrawing groups at a certain distance. This promotes intramolecular charge transfer upon excitation, thus inducing large changes in the dipole moment. The family of amino-substituted naphthalene probes designed in this way have been proven to be highly sensitive to polarity and have been common choices for TDFS studies in proteins and biomembranes. For the latter system, Prodan (Hutterer et al., 1998; Jurkiewicz et al., 2006; Först et al., 2014) and its derivatives Laurdan (Jurkiewicz et al., 2012b; Jurkiewicz et al., 2012c; Först et al., 2014; Macháň et al., 2014; Melcrová et al., 2016; Melcrová et al., 2019) and Patman (Hutterer et al., 1998; Olżyńska et al., 2007; Jurkiewicz et al., 2012c) are used to study the headgroup and carbonyl regions (Jurkiewicz et al., 2006; Jurkiewicz et al., 2012a). Furthermore, the list of the applicable TDFS dyes located in particular areas along the z-axis of a lipid bilayer can be expanded to provide detailed information on membrane hydration and polarity gradient (Hof, 1999; Sýkora et al., 2002a; Jurkiewicz et al., 2005). The examples are, from shallower to deepest, the probes Dauda (Sýkora et al.,

2002a), C17DiFU (Sýkora et al., 2002a), DTMAC (Jurkiewicz et al., 2012c; Först et al., 2014; Melcrová et al., 2019), ABA-C15 (Sýkora et al., 2002b), Prodan (Hutterer et al., 1998; Jurkiewicz et al., 2006; Jurkiewicz et al., 2012a; Först et al., 2014), Laurdan (Jurkiewicz et al., 2006; Jurkiewicz et al., 2012a; Jurkiewicz et al., 2012b; Jurkiewicz et al., 2012c; Först et al., 2014; Macháň et al., 2014; Melcrová et al., 2016; Melcrová et al., 2019), Patman (Hutterer et al., 1998; Jurkiewicz et al., 2006; Olżyńska et al., 2007; Jurkiewicz et al., 2012a; Jurkiewicz et al., 2012c), 2-AS (Hutterer et al., 1997; Sýkora et al., 2002a), 9-AS (Hutterer et al., 1997; Sýkora et al., 2002a; Jurkiewicz et al., 2012c), 16-AP (Hutterer et al., 1997; Jurkiewicz et al., 2012c). The use of identical fluorophores located at different positions allows for direct comparative studies to be performed (Jurkiewicz et al., 2012a; Jurkiewicz et al., 2012c). Chemical structures and fluorophore depth of location of these probes can be found in (Jurkiewicz et al., 2005). Since the fluorescent probes in lipid bilayer are relatively mobile, it is especially important to exclude the possibility of their relocation during the experiments. Considering the large gradient of the measured TDFS parameters across the membrane, even relatively small fluorophore instabilities can provide misleading output (Jurkiewicz et al., 2006). Therefore, probe location should be carefully checked by critical analysis of the TDFS results, but also by additional experiments, e.g., quenching experiments (Abrams and London, 1993).

Aminonaphtalene "Prodan-like" dyes have also been utilized for site-specific labelling of proteins for TDFS studies (Guha et al., 2005; Koehorst et al., 2010; Amaro et al., 2013; Cohen et al., 2016; Fischermeier et al., 2017). For example, Badan has been used to probe local protein hydration and dynamics at the active site of copper-transporting ATPase—LpCopA as a function of membrane lateral pressure (Fischermeier et al., 2017). Badan labelling was also applied for the membrane-embedded M13 coat protein to map TDFS at different depths of lipid bilayers (Koehorst et al., 2010). Another example is the use of TDFS of the Prodan-like dye MUC7 to study the hydration and mobility of the tunnel mouth of Dehalogenase proteins (Amaro et al., 2013).

The importance of the choice for the proper TDFS probe can be also strengthened by the inspection of the dyes which are unsuitable for TDFS. For example, NBD dyes display a small change of dipole moment upon electronic excitation of ~2 D (Amaro et al., 2016). Moreover its solvatochromic behaviour is far from being linear varying randomly with polarity and is sensitive to prominent specific solvent effects. Specifically, hydrogen bonding shifts the emission spectra to lower energies (Fery-Forgues et al., 1993). Therefore, NBD is not a good candidate for TDFS studies and its response in lipid bilayers (e.g., for the headgroup labelled NBD-PS) has been shown to correlate with dye position and water density along the bilayer normal, and not with the environment dynamics (Amaro et al., 2016). The lipophilic Di-4-ANEPPDHQ dye serves as an analogous example. Although it has been used as a reporter of membrane dynamics (i.e., phase state) (Jin et al., 2006; Amaro et al., 2017; Sezgin et al., 2017) it displays a complex TDFS behaviour. The evolution of the TRES FWHM displays multiple maxima recorded in cholesterol containing bilayers that suggest the existence of several underlying relaxation processes. These undesired effects may derive from different phenomena including interactions between the dye and membrane components, specifically cholesterol, or the multiple location of the dye in the membrane (Amaro et al., 2017).

TIME-DEPENDENT FLUORESCENCE SHIFT INSTRUMENTATION

As mentioned above, TDFS response can cover a huge time-span ranging from hundreds of femtoseconds up to microseconds. In addition to the fluorescence lifetime of the probe, which strictly sets the experimental time window, the choice of the instrumentation has to be also considered.

For mapping the ultrafast relaxation processes (i.e. shorter than ~20 ps), the techniques employing the ultrafast femtosecond lasers combined with the up conversion approach (Chosrowjan et al., 2015), Streak camera detection (Liu et al., 2014) or Kerr gating (Arzhantsev and Maroncelli, 2005) are of the most common choice. These techniques show an excellent time resolution (down to 200 fs for the upconversion and Kerr gating, ~1 ps for Streak camera set-ups), yet at the expense of the higher excitation powers, elevated instrumental complexity and cost, and certain limitations in the recording of the longer timescales.

Since the relaxation in biosystems are often dominated by the slow nanosecond components the ultrafast kinetics can be often neglected. The instrumentation of choice in such case would be time-correlated single photon counting (TCSPC) and multifrequency domain fluorometry (Boens et al., 2007; Lemmetyinen et al., 2014). Although based on different principles, both techniques yield fluorescence lifetimes with the comparable precision and time resolution (~10–20 ps) even for multi-component data (Lakowicz et al., 1984) which are typical for TDFS. Moreover, with the advances in semi-conductor laser sources covering substantially UV/VIS region and advances in timing electronics, the instrumentation is financially accessible and easily operable. The time-scale spanned by these techniques usually covers a substantial portion of the TDFS response in the headgroup and hydrocarbon regions of biomembranes and often also TDFS for dyes attached to proteins, which makes the TCSPC and phase-modulated fluorometry an ideal choice for monitoring TDFS in biological systems.

TIME-DEPENDENT FLUORESCENCE SHIFT IN MODEL LIPID MEMBRANES—APPLICATION HIGHLIGHTS

TDFS is nowadays a well-established method for studying model lipid membranes. As discussed before, it is sensitive to membrane hydration and to mobility of lipids. Since these two parameters

are easily affected by number of biologically relevant processes, the method can be successfully used to sense lipid packing, phase state of lipids, adsorption of peptides, specific effects of adsorbed salt ions, and oxidation of membrane components, to name just a few of them. Below we present applications that exemplify the sensitivity of TDFS to 1) model lipid membrane oxidation and 2) interaction with calcium ions.

Oxidized Model Lipid Membranes

Oxidation of membrane components can considerably change both their mobility and hydration (Jurkiewicz et al., 2012c). Phospholipids with polyunsaturated hydrocarbon chains easily oxidize to molecules with polar groups introduced at the end of the truncated hydrocarbon tails (see **Figure 2A**) and short-chain byproducts (e.g., hydroxynonenal (Fruhwirth et al., 2007; Vazdar et al., 2012). The shortened lipid tail of such an oxidized phospholipid (oxPL) not only changes the shape of the molecule from cylindrical to conical, but also, due to its hydrophilic character, loops back to the headgroup region (Sabatini et al., 2006). This behavior has number of consequences for the structure and dynamics of the lipid bilayer (Beranova et al., 2010; Khandelia and Mouritsen, 2009). First of all, it further increases the spontaneous curvature of the oxPL, which can lead to membrane destabilization, especially in the absence of cholesterol (Khandelia et al., 2014; Štefl et al., 2014). The newly introduced polar moiety can also serve as a carrier for other lipid headgroups lowering the energetic barrier of their flip-flop (Volinsky et al., 2011). TDFS studies, in which we used a series of polarity probes, showed that the introduction of truncated oxPLs changes the whole hydration profile of the lipid bilayer (**Figure 2A**). Interestingly, the augmented lipid mobility (shorter relaxation times) probed by Laurdan and Patman in oxPL-containing membranes match the faster lateral diffusion of phospholipids measured by fluorescence correlation spectroscopy (FCS) in those systems. This general rule of the correspondence between the time of TDFS relaxation and the time of lateral diffusion of lipids was frequently observed; see e.g., (Olšinová et al., 2018). There are however certain differences between the lateral diffusion of lipids and the local mobility probed by TDFS. For example, as depicted in **Figure 2**, the truncated oxPL tails with –(C=O)H terminus create voids in the headgroup region of the membrane. These voids allow for much faster relaxation probed by TDFS, but they do not influence the lateral lipid diffusion as much as oxPLs with terminated with –(C=O)O– group (please compare with the FCS results in Beranova et al. (2010). This example shows that probing locally, while having number of advantages, can also lead to misinterpretation. In general, one should avoid direct links between locally measured parameters (such as TDFS relaxation time) and macroscopic parameters (such as viscosity).

Not only phospholipids, but also cholesterol oxidizes. Many oxysterols are products of oxidative stress, but some of them are created by our organisms on purpose to be used in signaling and/or in cholesterol homeostasis (Kulig et al., 2016). Addition of as little as single OH group to cholesterol molecule can strongly influence the properties of a cholesterol-enriched model lipid membranes. It is substantial where this additional OH group is introduced. Based on TDFS measurements and computer simulations of we have distinguished two groups of oxysterols: ring- and tail-oxidized ones (Kulig et al., 2015b). **Figure 2B** depicts representatives of these two groups: 7β-OH-chol (ring-oxidized) and 27-OH-chol (tail-oxidized). Replacement of cholesterol in POPC lipid bilayer by 7β-OH-chol impairs cholesterol function as membrane stabilizer (cholesterol causes lipid ordering and condensation), which in TDFS is observed as increased mobility of lipids in the presence of 7β-OH-chol. On the other hand, 27-OH-chol does not influence TDFS parameters. But, due to the presence of hydrophilic moieties on both sides of the molecule, 27-OH-chol was found in simulations to oscillate fast between the two lipid leaflets. This movement results in increased membrane permeability to water and small polar solutes, even though, the average hydration probed by Laurdan is unchanged. This property of tail-oxidized sterols is utilized in our bodies. Since cholesterol do not pass through the blood-brain barrier, its excess is eliminated in the form of tail-oxidized sterol (mostly 24-OH-chol). It is advantageous that such oxysterol passes fast across the membranes without disturbing their properties.

Adsorption of Calcium Ions to Model Lipid Membranes

Various salt ions are omnipresent in cytoplasm and extracellular fluids. In our membranes there are receptors and channels specifically recognizing them, though, their adsorption to lipid bilayer itself is often overlooked. We proved that TDFS can be successfully used to study even subtle effects of the adsorption of salt ions to model lipid membranes (Jurkiewicz et al., 2012b; Vácha et al., 2010). This is because ions often interfere with the network of hydrogen bonds within the lipid headgroups altering mobility of lipids. Electrostatic interactions have an important role in the adsorption of ions, but the specificity of ionic effects is governed by other contributions, e.g., ion polarizability and its affinity to the hydrophilic/hydrophobic interface (Pokorna et al., 2013). In general, cations are attracted to negatively charged membranes as anions are attracted to positively charged ones, but the specific binding sites are determined by other factors. For example, adsorption of Ca^{2+} to the mixed lipid bilayer composed of 80 mol% zwitterionic POPC and 20 mol% anionic POPS is definitely enhanced by the presence of POPS, but the major Ca^{2+} binding sites are not the negatively charged carboxylic groups of POPS. TDFS results based on Laurdan and Dtmac probes, sensing lipid carbonyls and phosphate groups, respectively, together with sum frequency generation measurements, and molecular dynamics simulations revealed a complex picture of calcium adsorption to lipids (Melcrová et al., 2016). Multiple binding sites (lipid carbonyls and phosphates of both POPC and POPS molecules, as well as POPS carboxylic moieties) were occupied in proportions depending on lipid composition and calcium concentration. Ca^{2+} ions were also able to simultaneously bind multiple sites belonging to different lipid molecule bridging them together, which resulted in considerable lateral compression of the membrane and reduced lipid mobility. In TDFS, this was

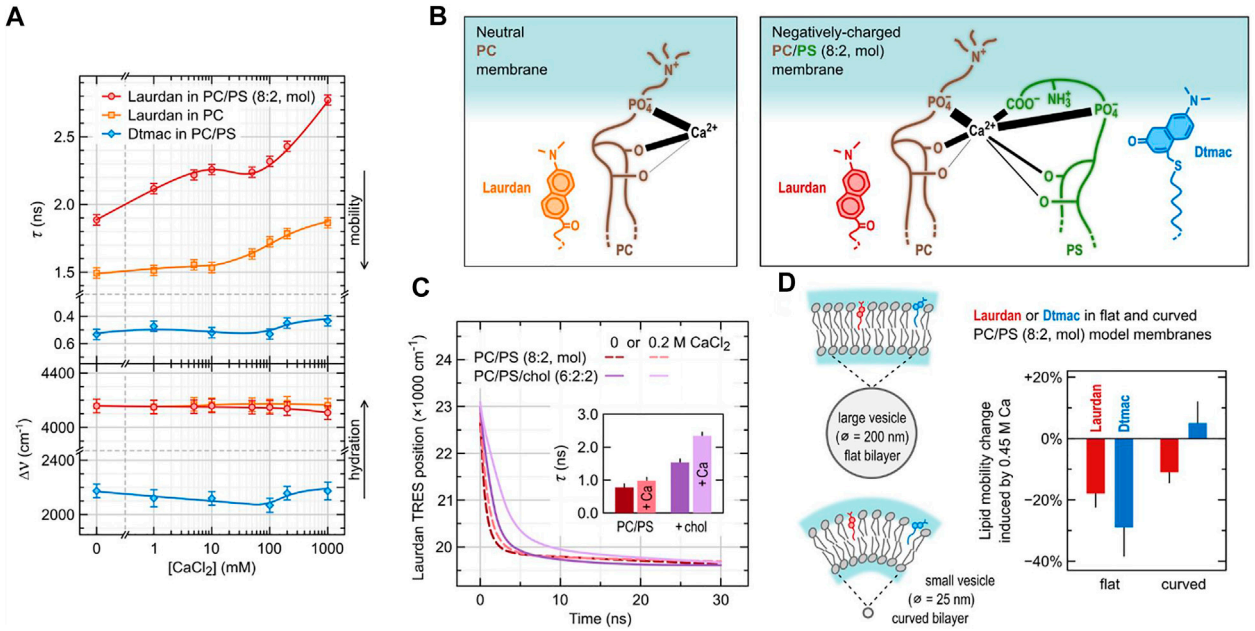

FIGURE 3 | Adsorption of calcium ions to model lipid membranes investigated using TDFS. **(A)** depicts TDFS parameters obtained for unilamellar liposomes composed of either pure phosphatidylcholine (PC) or its mixture with 20 mol% phosphatidylserine (PS) dispersed in $CaCl_2$ solutions. Laurdan and Dtmac were used to probe lipid carbonyl and phosphate regions, respectively. **(B)** summarizes the complex calcium interactions with phospholipids as obtained from the joined molecular dynamics and experimental study (Melcrová et al., 2016). Positions of the functional groups of lipids are taken from density profiles obtained in molecular dynamics simulations. The thickness of the black lines joining the functional groups with Ca^{2+} corresponds to the mean number of contacts between them. **(C)** shows the influence of cholesterol (chol) on the calcium adsorption to PC/PS model membranes. The results include the position of the maxima of Time-Resolved Emission Spectra (TRES) of Laurdan together with mean relaxation times (inside) obtained for PC/PS (8:2) and PC/PS/chol (6:2:2) lipid composition in the absence and in the presence of $CaCl_2$. **(D)** presents the effect of PC/PS membrane curvature on the adsorption of Ca^{2+}.

observed as an increase of the relaxation time. TDFS results together with the scheme of complex Ca^{2+}-lipid interactions are shown in **Figures 3A,B**. It is worth noting, that calcium induced only the changes in lipid mobility, but not hydration. Our experience shows that the relaxation time is the TDFS parameter that is the most sensitive to the adsorption of salt ions, while hydration changes are detected only rarely. When paired with computer simulations changes in TDFS relaxation time usually correlate with the changes in area per lipid. This is because mobility of lipids is usually more restricted in more condensed membranes. This relation, however, does not need to be true. One should be aware of the fact that it relates dynamic and structural properties of the lipid bilayer. The complex nature of calcium adsorption discussed above was not significantly affected by the presence of cholesterol in the membrane (**Figure 3C**, Melcrová et al., 2019). On the other hand, the change in membrane curvature resulted in qualitatively different binding pattern (**Figure 3D**). In highly curved membranes these are the lipid phosphates that attract the calcium ions more than carbonyls do, and these are the phosphates which mobility is hindered more than that of carbonyls. To measure these differences again the pair of Laurdan and Dtmac probes was used. Membrane curvature itself was also followed by TDFS in model zwitterionic bilayers labelled with Prodan and Patman, clearly indicating that the increased curvature elevates lipid mobility in the headgroup region (Sýkora et al., 2005). This conclusion is in full agreement with the timely results obtained by the modern label-free scattering techniques (vibrational sum frequency scattering (SFS), and second harmonic scattering (SHS)). Specifically, the combination of SFS and SHS proved the equal number of the lipid molecules in both bilayer leaflets even for the curved membranes which results in the elevated area per lipid and headgroup mobility in the outer leaflet of the bilayer (Okur et al., 2019). This effect gets more pronounced with increasing curvature. All these findings were anticipated by the TDFS approach, which further proves its potency to map the organization in the headgroup region.

CONCLUSION

Within the last decade the experimental advances in label free techniques together with computational methods allowed the development of a quantitative understanding of the hydration shell of biomembranes and proteins. While most of the methods described in chapter 2 are experimentally very demanding and expensive, the application of the TDFS technique on biomolecules requires a rather simple and inexpensive TCSPC equipment. The TDFS technique is a robust experimental technique with a remarkable reproducibility. The read-out parameters 1) overall dynamic Stokes shift Δν and 2)

characteristic relaxation time τ can report directly (i.e. without data modelling) on subtle changes in 1) the degree of hydration and 2) mobility, respectively, of the hydrated phospholipid or protein segment at the close vicinity of the fluorophore embedded in the bilayer. This implies that for a meaningful application of the TDFS technique the precise knowledge on the location of the dye is required. In protein science this pre-requisite is achieved by site-selected labelling, while the location of the chromophore of amphiphilic membrane probes can be determined by quenching experiments and molecular dynamic (MD) simulations. Together with MD simulations the TDFS approach identified how molecular parameters like membrane curvature (Sýkora et al., 2005; Magarkar et al., 2017), lipid composition (Jurkiewicz et al., 2005; Jurkiewicz et al., 2006; Olżyńska et al., 2007; Jurkiewicz et al., 2012b; Melcrová et al., 2019), presence of ions (Vácha et al., 2010; Jurkiewicz et al., 2012b; Pokorna et al., 2013; Melcrová et al., 2016; Melcrová et al., 2019), presence of pharmaceuticals (Först et al., 2014), membrane binding of peptides (Macháň et al., 2014; Olšinová et al., 2018), or lipid oxidation (Beranova et al., 2010; Volinsky et al., 2011; Jurkiewicz et al., 2012c; Vazdar et al., 2012; Štefl et al., 2014; Kulig et al., 2015b; Kulig et al., 2016) control the hydration and mobility in the headgroup region of bilayers. On the protein side the TDFS again combined with simulations demonstrated the significance of hydration and mobility in enzyme enantioselectivity (Jesenská et al., 2009; Stepankova et al., 2013; Sykora et al., 2014) as well as demonstrated how lateral membrane pressure changes the hydration profile in transmembrane channels (Fischermeier et al., 2017).

AUTHOR CONTRIBUTIONS

FS and HE elaborated the section devoted to the hydration shell of lipids and **Figure 1**, MA wrote the section on the choice of TDFS dyes, PJ prepared the sections focused on the TDFS in model lipid bilayers, its application highlights, and **Figures 2**, **3**, JS elaborated the introduction and instrumentation sections, MH suggested the overall concept of the article, prepared the conclusion section and performed a substantial part of the editing process.

ACKNOWLEDGMENTS

The authors acknowledge GAČR Grant 19-26854X.

REFERENCES

Abragam, A. (1961). *The Principles of Nuclear Magnetism*. New York: Oxford Science Publications.

Abrams, F. S., and London, E. (1993). Extension of the Parallax Analysis of Membrane Penetration Depth to the Polar Region of Model Membranes: Use of Fluorescence Quenching by a Spin-Label Attached to the Phospholipid Polar Headgroup. *Biochemistry* 32 (40), 10826–10831. doi:10.1021/bi00091a038

Amann-Winkel, K., Bellissent-Funel, M.-C., Bove, L. E., Loerting, T., Nilsson, A., Paciaroni, A., et al. (2016). X-ray and Neutron Scattering of Water. *Chem. Rev.* 116 (13), 7570–7589. doi:10.1021/acs.chemrev.5b00663

Amaro, M., Brezovský, J., Kováčová, S., Maier, L., Chaloupková, R., Sýkora, J., et al. (2013). Are Time-dependent Fluorescence Shifts at the Tunnel Mouth of Haloalkane Dehalogenase Enzymes Dependent on the Choice of the Chromophore? *J. Phys. Chem. B.* 117 (26), 7898–7906. doi:10.1021/jp403708c

Amaro, M., Brezovský, J., Kováčová, S., Sýkora, J., Bednář, D., Němec, V., et al. (2015). Site-Specific Analysis of Protein Hydration Based on Unnatural Amino Acid Fluorescence. *J. Am. Chem. Soc.* 137 (15), 4988–4992. doi:10.1021/jacs.5b01681

Amaro, M., Filipe, H. A. L., Prates Ramalho, J. P., Hof, M., and Loura, L. M. S. (2016). Fluorescence of Nitrobenzoxadiazole (NBD)-labeled Lipids in Model Membranes is Connected Not to Lipid Mobility but to Probe Location. *Phys. Chem. Chem. Phys.* 18 (10), 7042–7054. doi:10.1039/c5cp05238f

Amaro, M., Reina, F., Hof, M., Eggeling, C., and Sezgin, E. (2017). Laurdan and Di-4-ANEPPDHQ Probe Different Properties of the Membrane. *J. Phys. D: Appl. Phys.* 50 (13), 134004. doi:10.1088/1361-6463/aa5dbc

Amaro, M., Šachl, R., Jurkiewicz, P., Coutinho, A., Prieto, M., and Hof, M. (2014). Time-resolved Fluorescence in Lipid Bilayers: Selected Applications and Advantages over Steady State. *Biophys. J.* 107 (12), 2751–2760. doi:10.1016/j.bpj.2014.10.058

Arsov, Z. (2015). Long-range Lipid-Water Interaction as Observed by Atr-Ftir Spectroscopy. *Subcell. Biochem.* 71, 127–159. doi:10.1007/978-3-319-19060-0_6

Arzhantsev, S., and Maroncelli, M. (2005). Design and Characterization of a Femtosecond Fluorescence Spectrometer Based on Optical Kerr Gating. *Appl. Spectrosc.* 59 (2), 206–220. doi:10.1366/0003702053085007

Bagatolli, L. A. (2012). *LAURDAN Fluorescence Properties in Membranes: A Journey from the Fluorometer to the Microscope*. Berlin: Springer. 3–35. doi:10.1007/4243_2012_42

Bagchi, B. (2005). Water Dynamics in the Hydration Layer Around Proteins and Micelles. *Chem. Rev.* 105 (9), 3197–3219. doi:10.1021/cr020661+

Ball, P. (2008). Water as an Active Constituent in Cell Biology. *Chem. Rev.* 108 (1), 74–108. doi:10.1021/cr068037a

Beranova, L., Cwiklik, L., Jurkiewicz, P., Hof, M., and Jungwirth, P. (2010). Oxidation Changes Physical Properties of Phospholipid Bilayers: Fluorescence Spectroscopy and Molecular Simulations. *Langmuir* 26 (9), 6140–6144. doi:10.1021/la100657a

Beranová, L., Humpolíčková, J., Sýkora, J., Benda, A., Cwiklik, L., Jurkiewicz, P., et al. (2012). Effect of Heavy Water on Phospholipid Membranes: Experimental Confirmation of Molecular Dynamics Simulations. *Phys. Chem. Chem. Phys.* 14 (42), 14516–14522. doi:10.1039/c2cp41275f

Berkowitz, M. L., Bostick, D. L., and Pandit, S. (2006). Aqueous Solutions Next to Phospholipid Membrane Surfaces: Insights from Simulations. *Chem. Rev.* 106 (4), 1527–1539. doi:10.1021/cr0403638

Bhattacharyya, K. (2008). Nature of Biological Water: a Femtosecond Study. *Chem. Commun.* (25), 2848–2857. doi:10.1039/b800278a

Biedermannová, L., and Schneider, B. (2016). Hydration of Proteins and Nucleic Acids: Advances in experiment and Theory. A Review. *Biochim. Biophys. Acta (Bba) - Gen. Subjects.* 1860 (9), 1821–1835. doi:10.1016/j.bbagen.2016.05.036

Boens, N., Qin, W., Basarić, N., Hofkens, J., Ameloot, M., Pouget, J., et al. (2007). Fluorescence Lifetime Standards for Time and Frequency Domain Fluorescence Spectroscopy. *Anal. Chem.* 79 (5), 2137–2149. doi:10.1021/ac062160k

Borle, F., and Seelig, J. (1983). Hydration of *Escherichia coli* Lipids. *Biochim. Biophys. Acta Biomembr.* 735 (1), 131–136. doi:10.1016/0005-2736(83)90268-7

Calero, C., and Franzese, G. (2019). Membranes with Different Hydration Levels: The Interface between Bound and Unbound Hydration Water. *J. Mol. Liquids.* 273, 488–496. doi:10.1016/j.molliq.2018.10.074

Chang, C.-W., Guo, L., Kao, Y.-T., Li, J., Tan, C., Li, T., et al. (2010). Ultrafast Solvation Dynamics at Binding and Active Sites of Photolyases. *Proc. Natl. Acad. Sci.* 107 (7), 2914–2919. doi:10.1073/pnas.1000001107

Chen, Y.-T., Chao, W.-C., Kuo, H.-T., Shen, J.-Y., Chen, I.-H., Yang, H.-C., et al. (2016). Probing the Polarity and Water Environment at the Protein-Peptide Binding Interface Using Tryptophan Analogues. *Biochem. Biophys. Rep.* 7, 113–118. doi:10.1016/j.bbrep.2016.05.022

Chosrowjan, H., Taniguchi, S., and Tanaka, F. (2015). Ultrafast Fluorescence Upconversion Technique and its Applications to Proteins. *FEBS J.* 282 (16), 3003–3015. doi:10.1111/febs.13180

Choudhury, S. D., Nath, S., and Pal, H. (2008). Excited-state Proton Transfer Behavior of 7-Hydroxy-4-Methylcoumarin in AOT Reverse Micelles. *J. Phys. Chem. B.* 112 (26), 7748–7753. doi:10.1021/jp8004019

Choudhury, S. D., and Pal, H. (2009). Modulation of Excited-State Proton-Transfer Reactions of 7-Hydroxy-4-Methylcoumarin in Ionic and Nonionic Reverse Micelles. *J. Phys. Chem. B.* 113 (19), 6736–6744. doi:10.1021/jp8111759

Cohen, B. E., Mcananey, T. B., Park, E. S., Jan, Y. N., Boxer, S. G., Jan, L. Y., et al. (2016). Probing Protein Electrostatics with a Synthetic Fluorescent Amino Acid. *Science* 296 (5573), 1700–1703. doi:10.1126/science.1069346

Demchenko, A. P. (2002). The Red-Edge Effects: 30 Years of Exploration. *Luminescence* 17 (1), 19–42. doi:10.1002/bio.671

Disalvo, E. A., and Bakás, L. S. (1986). "Influence of the Surface Charge Distribution and Water Layers on the Permeability Properties of Lipid Bilayers," in *Electrical Double Layers in Biology*. Editor M. Blank (Boston, MA: Springer).

Disalvo, E. A. (2015). Membrane Hydration: A Hint to a New Model for Biomembranes. *Subcell. Biochem.* 71, 1–16. doi:10.1007/978-3-319-19060-0_1

Duboué-Dijon, E., and Laage, D. (2014). Comparative Study of Hydration Shell Dynamics Around a Hyperactive Antifreeze Protein and Around Ubiquitin. *J. Chem. Phys.* 141 (22), 22D529. doi:10.1063/1.4902822

Duboué-Dijon, E., Fogarty, A. C., Hynes, J. T., and Laage, D. (2016). Dynamical Disorder in the DNA Hydration Shell. *J. Am. Chem. Soc.* 138 (24), 7610–7620. doi:10.1021/jacs.6b02715

Fery-Forgues, S., Fayet, J.-P., and Lopez, A. (1993). Drastic Changes in the Fluorescence Properties of NBD Probes with the Polarity of the Medium: Involvement of a TICT State? *J. Photochem. Photobiol. A: Chem.* 70 (3), 229–243. doi:10.1016/1010-6030(93)85048-d

Fischermeier, E., Pospíšil, P., Sayed, A., Hof, M., Solioz, M., and Fahmy, K. (2017). Dipolar Relaxation Dynamics at the Active Site of an ATPase Regulated by Membrane Lateral Pressure. *Angew. Chem. Int. Ed.* 56 (5), 1269–1272. doi:10.1002/anie.201611582

Fogarty, A. C., and Laage, D. (2014). Water Dynamics in Protein Hydration Shells: The Molecular Origins of the Dynamical Perturbation. *J. Phys. Chem. B.* 118, 7715–7729. doi:10.1021/jp409805p

Foglia, F., Lawrence, M. J., Lorenz, C. D., and McLain, S. E. (2010). On the Hydration of the Phosphocholine Headgroup in Aqueous Solution. *J. Chem. Phys.* 133 (14), 145103. doi:10.1063/1.3488998

Först, G., Cwiklik, L., Jurkiewicz, P., Schubert, R., and Hof, M. (2014). Interactions of Beta-Blockers with Model Lipid Membranes: Molecular View of the Interaction of Acebutolol, Oxprenolol, and Propranolol with Phosphatidylcholine Vesicles by Time-dependent Fluorescence Shift and Molecular Dynamics Simulations. *Eur. J. Pharm. Biopharm.* 87 (3), 559–569. doi:10.1016/j.ejpb.2014.03.013

Fruhwirth, G. O., Loidl, A., and Hermetter, A. (2007). Oxidized Phospholipids: From Molecular Properties to Disease. *Biochim. Biophys. Acta.* 1772 (7), 718–736. doi:10.1016/j.bbadis.2007.04.009

Gawrisch, K., Parsegian, A. V., and Rand, P. R. (1990). *Membrane Hydration*. Berlin: Springer

Ge, M., and Freed, J. H. (2003). Hydration, Structure, and Molecular Interactions in the Headgroup Region of Dioleoylphosphatidylcholine Bilayers: An Electron Spin Resonance Study. *Biophys. J.* 85 (6), 4023–4040. doi:10.1016/s0006-3495(03)74816-4

Guha, S., Sahu, K., Roy, D., Mondal, S. K., Roy, S., and Bhattacharyya, K. (2005). Slow Solvation Dynamics at the Active Site of an Enzyme: Implications for Catalysis. *Biochemistry* 44 (25), 8940–8947. doi:10.1021/bi0473915

Hamley, I. W. (2000). *Introduction to Soft Matter: Polymers, Colloids, Amphiphiles and Liquid Crystals*. Chichester: Wiley

Hishida, M., and Tanaka, K. (2011). Long-range Hydration Effect of Lipid Membrane Studied by Terahertz Time-Domain Spectroscopy. *Phys. Rev. Lett.* 106 (15), 158102–158103. doi:10.1103/PhysRevLett.106.158102

Hof, M. (1999). Solvent Relaxation in Biomembranes, in *Applied Fluorescence in Chemistry, Biology and Medicine* Berlin: Springer, 439–456. doi:10.1007/978-3-642-59903-3_18

Horng, M. L., Gardecki, J. A., Papazyan, A., and Maroncelli, M. (1995). Subpicosecond Measurements of Polar Solvation Dynamics: Coumarin 153 Revisited. *J. Phys. Chem.* 99 (48), 17311–17337. doi:10.1021/j100048a004

Hutterer, R., Parusel, A. B. J., and Hof, M. (1998). Solvent Relaxation of Prodan and Patman: A Useful Tool for the Determination of Polarity and Rigidity Changes in Membranes. *J. Fluoresc.* 8, 389–393. doi:10.1023/a:1020532817530

Hutterer, R., Schneider, F. W., Lanig, H., and Hof, M. (1997). Solvent Relaxation Behaviour of N-Anthroyloxy Fatty Acids in PC-Vesicles and Paraffin Oil: A Time-Resolved Emission Spectra Study. *Biochim. Biophys. Acta.* 1323 (2), 195–207. doi:10.1016/s0005-2736(96)00186-1

Ito, N., Arzhantsev, S., Heitz, M., and Maroncelli, M. (2004). Solvation Dynamics and Rotation of Coumarin 153 in Alkylphosphonium Ionic Liquids. *J. Phys. Chem. B.* 108 (18), 5771–5777. doi:10.1021/jp0499575

Jesenská, A., Sýkora, J., Olžyńska, A., Brezovský, J., Zdráhal, Z., Damborský, J., et al. (2009). Nanosecond Time-dependent Stokes Shift at the Tunnel Mouth of Haloalkane Dehalogenases. *J. Am. Chem. Soc.* 131 (2), 494–501. doi:10.1021/ja804020q

Jin, L., Millard, A. C., Wuskell, J. P., Dong, X., Wu, D., Clark, H. A., et al. (2006). Characterization and Application of a New Optical Probe for Membrane Lipid Domains. *Biophys. J.* 90 (7), 2563–2575. doi:10.1529/biophysj.105.072884

Jurkiewicz, P., Sýkora, J., Olzyńska, A., Humpolíčková, J., and Hof, M. (2005). Solvent Relaxation in Phospholipid Bilayers: Principles and Recent Applications. *J. Fluoresc.* 15 (6), 883–894. doi:10.1007/s10895-005-0013-4

Jurkiewicz, P., Cwiklik, L., Jungwirth, P., and Hof, M. (2012a). Lipid Hydration and Mobility: An Interplay between Fluorescence Solvent Relaxation Experiments and Molecular Dynamics Simulations. *Biochimie* 94 (1), 26–32. doi:10.1016/j.biochi.2011.06.027

Jurkiewicz, P., Cwiklik, L., Vojtíšková, A., Jungwirth, P., and Hof, M. (2012b). Structure, Dynamics, and Hydration of POPC/POPS Bilayers Suspended in NaCl, KCl, and CsCl Solutions. *Biochim. Biophys. Acta.* 1818 (3), 609–616. doi:10.1016/j.bbamem.2011.11.033

Jurkiewicz, P., Olžyńska, A., Cwiklik, L., Conte, E., Jungwirth, P., Megli, F. M., et al. (2012c). Biophysics of Lipid Bilayers Containing Oxidatively Modified Phospholipids: Insights from Fluorescence and EPR Experiments and from MD Simulations. *Biochim. Biophys. Acta.* 1818 (10), 2388–2402. doi:10.1016/j.bbamem.2012.05.020

Jurkiewicz, P., Olžyńska, A., Langner, M., and Hof, M. (2006). Headgroup Hydration and Mobility of DOTAP/DOPC Bilayers: a Fluorescence Solvent Relaxation Study. *Langmuir* 22 (21), 8741–8749. doi:10.1021/la061597k

Khandelia, H., Loubet, B., Olžyńska, A., Jurkiewicz, P., and Hof, M. (2014). Pairing of Cholesterol with Oxidized Phospholipid Species in Lipid Bilayers. *Soft Matter* 10 (4), 639–647. doi:10.1039/c3sm52310a

Khandelia, H., and Mouritsen, O. G. (2009). Lipid Gymnastics: Evidence of Complete Acyl Chain Reversal in Oxidized Phospholipids from Molecular Simulations. *Biophys. J.* 96 (7), 2734–2743. doi:10.1016/j.bpj.2009.01.007

Koch, M. H. J., Vachette, P., and Svergun, D. I. (2003). Small-angle Scattering: A View on the Properties, Structures and Structural Changes of Biological Macromolecules in Solution. *Q. Rev. Biophys.* 36, 147–227. doi:10.1017/s0033583503003871

Koehorst, R. B. M., Laptenok, S., van Oort, B., van Hoek, A., Spruijt, R. B., van Stokkum, I. H. M., et al. (2010). Profiling of Dynamics in Protein-Lipid-Water Systems: a Time-Resolved Fluorescence Study of a Model Membrane Protein with the Label BADAN at Specific Membrane Depths. *Eur. Biophys. J.* 39 (4), 647–656. doi:10.1007/s00249-009-0538-6

König, S., Sackmann, E., Richter, D., Zorn, R., Carlile, C., and Bayerl, T. M. (1994). Molecular Dynamics of Water in Oriented DPPC Multilayers Studied by Quasielastic Neutron Scattering and Deuterium-nuclear Magnetic Resonance Relaxation. *J. Chem. Phys.* 100 (4), 3307–3316. doi:10.1063/1.466422

Kucerka, N., Nagle, J. F., Sachs, J. N., Feller, S. E., Pencer, J., Jackson, A., et al. (2008). Lipid Bilayer Structure Determined by the Simultaneous Analysis of Neutron and X-ray Scattering Data. *Biophys. J.* 95 (5), 2356–2367. doi:10.1529/biophysj.108.132662

Kühne, T. D., and Khaliullin, R. Z. (2013). Electronic Signature of the Instantaneous Asymmetry in the First Coordination Shell of Liquid Water. *Nat. Commun.* 4, 1450–1457. doi:10.1038/ncomms2459

Kulig, W., Cwiklik, L., Jurkiewicz, P., Rog, T., and Vattulainen, I. (2016). Cholesterol Oxidation Products and Their Biological Importance. *Chem. Phys. Lipids.* 199, 144–160. doi:10.1016/j.chemphyslip.2016.03.001

Kulig, W., Jurkiewicz, P., Olżyńska, A., Tynkkynen, J., Javanainen, M., Manna, M., et al. (2015a). Experimental Determination and Computational Interpretation of Biophysical Properties of Lipid Bilayers Enriched by Cholesteryl Hemisuccinate. *Biochim. Biophys. Acta.* 1848 (2), 422–432. doi:10.1016/j.bbamem.2014.10.032

Kulig, W., Olżyńska, A., Jurkiewicz, P., Kantola, A. M., Komulainen, S., Manna, M., et al. (2015b). Cholesterol under Oxidative Stress-How Lipid Membranes Sense Oxidation as Cholesterol Is Being Replaced by Oxysterols. *Free Radic. Biol. Med.* 84, 30–41. doi:10.1016/j.freeradbiomed.2015.03.006

Laage, D., Elsaesser, T., and Hynes, J. T. (2017). Water Dynamics in the Hydration Shells of Biomolecules. *Chem. Rev.* 117 (16), 10694–10725. doi:10.1021/acs.chemrev.6b00765

Ladbrooke, B. D., Williams, R. M., and Chapman, D. (1968). Studies on Lecithin-Cholesterol-Water Interactions by Differential Scanning Calorimetry and X-ray Diffraction. *Biochim. Biophys. Acta.* 150 (3), 333–340. doi:10.1016/0005-2736(68)90132-6

Lakowicz, J. R., and Keating-Nakamoto, S. (1984). Red-Edge Excitation of Fluorescence and Dynamic Properties of Proteins and Membranes. *Biochemistry* 23 (13), 3013–3021. doi:10.1021/bi00308a026

Lakowicz, J. R., Laczko, G., Cherek, H., Gratton, E., and Limkeman, M. (1984). Analysis of Fluorescence Decay Kinetics from Variable-Frequency Phase Shift and Modulation Data. *Biophys. J.* 46 (4), 463–477. doi:10.1016/s0006-3495(84)84043-6

Lemmetyinen, H., Tkachenko, N. V., Valeur, B., Hotta, J.-i., Ameloot, M., Ernsting, N. P., et al. (2014). Time-resolved Fluorescence Methods (IUPAC Technical Report). *Pure Appl. Chem.* 86 (12), 1969–1998. doi:10.1515/pac-2013-0912

Levy, Y., and Onuchic, J. N. (2006). Water Mediation in Protein Folding and Molecular Recognition. *Annu. Rev. Biophys. Biomol. Struct.* 35 (1), 389–415. doi:10.1146/annurev.biophys.35.040405.102134

Li, T., Hassanali, A. A., Kao, Y.-T., Zhong, D., and Singer, S. J. (2007). Hydration Dynamics and Time Scales of Coupled Water–Protein Fluctuations. *J. Am. Chem. Soc.* 129 (11), 3376–3382. doi:10.1021/ja0685957

Liu, L., Li, Y., Sun, L., Li, H., Peng, X., and Qu, J. (2014). Fluorescence Lifetime Imaging Microscopy Using a Streak Camera. *Multiphot. Microsc. Biomed. Sci. XIV* 8948, 89482L. doi:10.1117/12.2039056

Ma, Y., Benda, A., Kwiatek, J., Owen, D. M., and Gaus, K. (2018). Time-Resolved Laurdan Fluorescence Reveals Insights into Membrane Viscosity and Hydration Levels. *Biophys. J.* 115 (8), 1498–1508. doi:10.1016/j.bpj.2018.08.041

Macháň, R., Jurkiewicz, P., Olżyńska, A., Olsinova, M., Cebecauer, M., Marquette, A., et al. (2014). Peripheral and Integral Membrane Binding of Peptides Characterized by Time-dependent Fluorescence Shifts: Focus on Antimicrobial Peptide LAH4. *Langmuir* 30 (21), 6171–6179.

Magarkar, A., Jurkiewicz, P., Allolio, C., Hof, M., and Jungwirth, P. (2017). Increased Binding of Calcium Ions at Positively Curved Phospholipid Membranes. *J. Phys. Chem. Lett.* 8, 518–523. doi:10.1021/acs.jpclett.6b02818

Martelli, F., Crain, J., and Franzese, G. (2020). Network Topology in Water Nanoconfined between Phospholipid Membranes. *ACS Nano* 14 (7), 8616–8623. doi:10.1021/acsnano.0c02984

Melcrová, A., Pokorna, S., Pullanchery, S., Kohagen, M., Jurkiewicz, P., Hof, M., et al. (2016). The Complex Nature of Calcium Cation Interactions with Phospholipid Bilayers. *Sci. Rep.* 6. 38035. doi:10.1038/srep38035

Melcrová, A., Pokorna, S., Vošahlíková, M., Sýkora, J., Svoboda, P., Hof, M., et al. (2019). Concurrent Compression of Phospholipid Membranes by Calcium and Cholesterol. *Langmuir* 35 (35), 11358–11368. doi:10.1021/acs.langmuir.9b00477

Merzel, F., and Smith, J. C. (2002). Is the First Hydration Shell of Lysozyme of Higher Density Than Bulk Water? *Proc. Natl. Acad. Sci.* 99 (8), 5378–5383. doi:10.1073/pnas.082335099

Nagle, J. F., and Tristram-Nagle, S. (2000). Structure of Lipid Bilayers. *Biochim. Biophys. Acta.* 1469 (3), 159–195. doi:10.1016/s0304-4157(00)00016-2

Okur, H. I., Tarun, O. B., and Roke, S. (2019). Chemistry of Lipid Membranes from Models to Living Systems: A Perspective of Hydration, Surface Potential, Curvature, Confinement and Heterogeneity. *J. Am. Chem. Soc.* 141, 12168–12181. doi:10.1021/jacs.9b02820

Olšinová, M., Jurkiewicz, P., Kishko, I., Sýkora, J., Sabó, J., Hof, M., et al. (2018). Roughness of a Transmembrane Peptide Reduces Lipid Membrane Dynamics. *Iscience* 10, 87–97.

Olżyńska, A., Zań, A., Jurkiewicz, P., Sýkora, J., Gröbner, G., Langner, M., et al. (2007). Molecular Interpretation of Fluorescence Solvent Relaxation of Patman and 2H NMR Experiments in Phosphatidylcholine Bilayers. *Chem. Phys. Lipids* 147 (2), 69–77.

Pal, S. K., Peon, J., and Zewail, A. H. (2002). Biological Water at the Protein Surface: Dynamical Solvation Probed Directly with Femtosecond Resolution. *Proc. Natl. Acad. Sci.* 99 (4), 1763–1768. doi:10.1073/pnas.042697899

Pal, S. K., and Zewail, A. H. (2004). Dynamics of Water in Biological Recognition. *Chem. Rev.* 104 (4), 2099–2124. doi:10.1021/cr020689l

Parasassi, T., Conti, F., and Gratton, E. (1986). Time-resolved Fluorescence Emission Spectra of Laurdan in Phospholipid Vesicles by Multifrequency Phase and Modulation Fluorometry. *Cell. Mol. Biol.* 32 (1), 103–108.

Parasassi, T., De Stasio, G., d'Ubaldo, A., and Gratton, E. (1990). Phase Fluctuation in Phospholipid Membranes Revealed by Laurdan Fluorescence. *Biophys. J.* 57 (6), 1179–1186. doi:10.1016/s0006-3495(90)82637-0

Pokorna, S., Jurkiewicz, P., Cwiklik, L., Vazdar, M., and Hof, M. (2013). Interactions of Monovalent Salts with Cationic Lipid Bilayers. *Faraday Discuss.* 160, 341–358. doi:10.1039/c2fd20098h

Rhys, N. H., Duffy, I. B., Sowden, C. L., Lorenz, C. D., and McLain, S. E. (2019). On the Hydration of DOPE in Solution. *J. Chem. Phys.* 150 (11), 115104. doi:10.1063/1.5085736

Rønne, C., Åstrand, P. O., and Keiding, S. R. (1999). THz Spectroscopy of Liquid H2O and D2O. *Phys. Rev. Lett.* 82 (14), 2888–2891.

Russo, D., Hura, G., and Head-Gordon, T. (2004). Hydration Dynamics Near a Model Protein Surface. *Biophys. J.* 86 (3), 1852–1862. doi:10.1016/s0006-3495(04)74252-6

Sabatini, K., Mattila, J.-P., Megli, F. M., and Kinnunen, P. K. J. (2006). Characterization of Two Oxidatively Modified Phospholipids in Mixed Monolayers with DPPC. *Biophys. J.* 90 (12), 4488–4499. doi:10.1529/biophysj.105.080176

Sezgin, E., Schneider, F., Zilles, V., Urbančič, I., Garcia, E., Waithe, D., et al. (2017). Polarity-Sensitive Probes for Superresolution Stimulated Emission Depletion Microscopy. *Biophys. J.* 113 (6), 1321–1330. doi:10.1016/j.bpj.2017.06.050

Shen, J.-Y., Chao, W.-C., Liu, C., Pan, H.-A., Yang, H.-C., Chen, C.-L., et al. (2013). Probing Water Micro-Solvation in Proteins by Water Catalysed Proton-Transfer Tautomerism. *Nat. Commun.* 4 (1), 2611. doi:10.1038/ncomms3611

Sonu, S., Kumari, S., and Saha, S. K. (2016). Solvation Dynamics and Rotational Relaxation of Coumarin 153 in Mixed Micelles of Triton X-100 and Cationic Gemini Surfactants: Effect of Composition and Spacer Chain Length of Gemini Surfactants. *Phys. Chem. Chem. Phys.* 18 (3), 1551–1563. doi:10.1039/c5cp03835a

Sparr, E., and Wennerström, H. (2001). Responding Phospholipid Membranes-Interplay between Hydration and Permeability. *Biophysical J.* 81 (2), 1014–1028. doi:10.1016/s0006-3495(01)75759-1

Štefl, M., Šachl, R., Olzyńska, A., Amaro, M., Savchenko, D., Deyneka, A., et al. (2014). Comprehensive Portrait of Cholesterol Containing Oxidized Membrane. *Biochim. Biophys. Acta - Biomembr.* 1838 (7), 1769–1776.

Stepankova, V., Khabiri, M., Brezovsky, J., Pavelka, A., Sykora, J., Amaro, M., et al. (2013). Expansion of Access Tunnels and Active-Site Cavities Influence Activity of Haloalkane Dehalogenases in Organic Cosolvents. *ChemBioChem* 14 (7), 890–897. doi:10.1002/cbic.201200733

Stirnemann, G., Wernersson, E., Jungwirth, P., and Laage, D. (2013). Mechanisms of Acceleration and Retardation of Water Dynamics by Ions. *J. Am. Chem. Soc.* 135 (32), 11824–11831. doi:10.1021/ja405201s

Svergun, D. I., Richard, S., Koch, M. H. J., Sayers, Z., Kuprin, S., and Zaccai, G. (1998). Protein Hydration in Solution: Experimental Observation by X-ray and Neutron Scattering. *Proc. Natl. Acad. Sci.* 95 (5), 2267–2272. doi:10.1073/pnas.95.5.2267

Swenson, J., Kargl, F., Berntsen, P., and Svanberg, C. (2008). Solvent and Lipid Dynamics of Hydrated Lipid Bilayers by Incoherent Quasielastic Neutron Scattering. *J. Chem. Phys.* 129 (4), 045101. doi:10.1063/1.2955753

Sykora, J., Brezovsky, J., Koudelakova, T., Lahoda, M., Fortova, A., Chernovets, T., et al. (2014). Dynamics and Hydration Explain Failed Functional Transformation in Dehalogenase Design. *Nat. Chem. Biol.* 10 (6), 428–430. doi:10.1038/nchembio.1502

Sýkora, J., Jurkiewicz, P., Epand, R. M., Kraayenhof, R., Langner, M., and Hof, M. (2005). Influence of the Curvature on the Water Structure in the Headgroup Region of Phospholipid Bilayer Studied by the Solvent Relaxation Technique. *Chem. Phys. Lipids* 135 (2), 213–221. doi:10.1016/j.chemphyslip.2005.03.003

Sýkora, J., Kapusta, P., Fidler, V., and Hof, M. (2002a). On what Time Scale Does Solvent Relaxation in Phospholipid Bilayers Happen? *Langmuir* 18 (3), 571–574. doi:10.1021/la011337x

Sýkora, J., Mudogo, V., Hutterer, R., Nepras, M., Vaněrka, J., Kapusta, P., et al. (2002b). ABA-C15: A New Dye for Probing Solvent Relaxation in Phospholipid Bilayers. *Langmuir* 18 (24), 9276–9282. doi:10.1021/la026435c

Tielrooij, K. J., Paparo, D., Piatkowski, L., Bakker, H. J., and Bonn, M. (2009). Dielectric Relaxation Dynamics of Water in Model Membranes Probed by Terahertz Spectroscopy. *Biophys. J.* 97 (9), 2484–2492. doi:10.1016/j.bpj.2009.08.024

Tristram-Nagle, S., and Nagle, J. F. (2004). Lipid Bilayers: Thermodynamics, Structure, Fluctuations, and Interactions. *Chem. Phys. Lipids* 127 (1), 3–14. doi:10.1016/j.chemphyslip.2003.09.002

Tristram-Nagle, S. (2015). Use of X-Ray and Neutron Scattering Methods with Volume Measurements to Determine Lipid Bilayer Structure and Number of Water Molecules/Lipid. *Subcell Biochem.* 71, 17–43. doi:10.1007/978-3-319-19060-0_2

Ulrich, A. S., and Watts, A. (1994). Molecular Response of the Lipid Headgroup to Bilayer Hydration Monitored by 2H-NMR. *Biophys. J.* 66 (5), 1441–1449. doi:10.1016/s0006-3495(94)80934-8

Vácha, R., Jurkiewicz, P., Petrov, M., Berkowitz, M. L., Böckmann, R. A., Barucha-Kraszewska, J., et al. (2010). Mechanism of Interaction of Monovalent Ions with Phosphatidylcholine Lipid Membranes. *J. Phys. Chem. B* 114 (29), 9504–9509. doi:10.1021/jp102389k

Vazdar, M., Jurkiewicz, P., Hof, M., Jungwirth, P., and Cwiklik, L. (2012). Behavior of 4-hydroxynonenal in Phospholipid Membranes. *J. Phys. Chem. B* 116 (22), 6411–6415. doi:10.1021/jp3044219

Volinsky, R., Cwiklik, L., Jurkiewicz, P., Hof, M., Jungwirth, P., and Kinnunen, P. K. J. (2011). Oxidized Phosphatidylcholines Facilitate Phospholipid Flip-Flop in Liposomes. *Biophysical J.* 101 (6), 1376–1384. doi:10.1016/j.bpj.2011.07.051

Volke, F., Eisenblätter, S., Galle, J., and Klose, G. (1994). Dynamic Properties of Water at Phosphatidylcholine Lipid-Bilayer Surfaces as Seen by Deuterium and Pulsed Field Gradient Proton NMR. *Chem. Phys. Lipids* 70 (2), 121–131. doi:10.1016/0009-3084(94)90080-9

Wassall, S. R. (1996). Pulsed Field Gradient-Spin echo NMR Studies of Water Diffusion in a Phospholipid Model Membrane. *Biophys. J.* 71 (5), 2724–2732. doi:10.1016/s0006-3495(96)79463-8

Yada, H., Nagai, M., and Tanaka, K. (2008). Origin of the Fast Relaxation Component of Water and Heavy Water Revealed by Terahertz Time-Domain Attenuated Total Reflection Spectroscopy. *Chem. Phys. Lett.* 464 (4–6), 166–170. doi:10.1016/j.cplett.2008.09.015

Yamada, T., and Seto, H. (2020). Quasi-Elastic Neutron Scattering Studies on Hydration Water in Phospholipid Membranes. *Front. Chem.* 8, 8–5. doi:10.3389/fchem.2020.00008

Yamada, T., Takahashi, N., Tominaga, T., Takata, S.-i., and Seto, H. (2017). Dynamical Behavior of Hydration Water Molecules between Phospholipid Membranes. *J. Phys. Chem. B.* 121 (35), 8322–8329. doi:10.1021/acs.jpcb.7b01276

Zhong, D., Pal, S. K., and Zewail, A. H. (2011). Biological Water: A Critique. *Chem. Phys. Lett. Elsevier B.V.* 503 (1–3), 1–11. doi:10.1016/j.cplett.2010.12.077

Conflict of Interest: The authors declare that the research was conducted in the absence of any commercial or financial relationships that could be construed as a potential conflict of interest.

Publisher's Note: All claims expressed in this article are solely those of the authors and do not necessarily represent those of their affiliated organizations, or those of the publisher, the editors and the reviewers. Any product that may be evaluated in this article, or claim that may be made by its manufacturer, is not guaranteed or endorsed by the publisher.

GLOSSARY

2-AS 2-(9-anthroyloxy)stearic acid

9-AS 9-(9-anthroyloxy)stearic acid

16-AP (16-(9-anthroyloxy)palmitoic acid

ABA-C15 N-palmitoyl-3-aminobenzanthrone

ANS 8-Anilinonaphthalene-1-sulfonic acid

ATR-FTIR Attenuated Total Reflectance- Fourier Transform Infrared Spectroscopy

Badan 6-Bromoacetyl-2-Dimethylaminonaphthalene

C17DiFU 6,8-difluoro-4-heptadecyl-7-hydroxycoumarin

CaCl2 Calcium Chloride

Chol Cholesterol; - Coumarins: benzo-α-pyrones

Dauda 11-((5-dimethylaminonaphthalene-1-sulfonyl)amino) undecanoic acid

Di-4-ANEPPDHQ 1-[2-Hydroxy-3-(N,N-di-methyl-N-hydroxyethyl) ammoniopropyl]-4-[β-[2-(di-n-butylamino)-6-napthyl] vinyl]pyridinium dibromide

DMPC 1,2-dimyristoyl-sn-glycero-3-phoshatidylcholine

DOPC 1,2-dioleoyl-sn-glycero-3-phosphocholine

DOPE 1,2-dioleoyl-sn-glycero-3-phosphoethanolamine

DTMAC 4-[(n-dodecylthio)methyl]-7-(N,N-dimethylamino)-coumarin

FCS Fluorescence Correlation Spectroscopy

FWHM Full-Width at Half-Maxima (FWHM)

GP Generalized Polarization

GP-FLIM Generalized Polarization- Fluorescence Lifetime Imaging Microscopy

HLDs Haloalkane Dehalogenases; - Laurdan: 2-dimethylamino-6-lauroyl-naphthalene

LAXS Low Angle X-ray Scattering

MD Molecular Dynamics

NBD nitrobenzoxadiazole, 7-nitrobenz-2-oxa-l,3-diazol-4-y1

NMR: Nuclear Magnetic Resonance

OxPL Oxidized Phospholipid

Patman 6-palmitoyl-2- [[2-(triethylammonium)ethyl]methylamino] naphthalene chloride

PC Phosphotidylcholine

PE Phosphotidylethanolamine

PG Phosphatidylglycerol

POPC 1-palmitoyl-2-oleoyl-sn-glycero-3-phosphocholine

POPS 1-palmitoyl-2-oleoyl-sn-glycero-3-phospho-L-serine

Prodan 6-propionyl-2-(dimethylamino) naphthalene

PS Phosphatidylserine

QENS Quasi-Elastic Neutron Scattering

REES Red Edge Excitation Shift

SANS Small Angle Neutron Scattering

SAXS Small Angle X-ray Scattering

SFS Sum Frequency Scattering

SHS Second Harmonic Scattering

SR Solvent Relaxation

TCSPC Time-Correlated Single Photon Counting

TDFS Time-Dependent Fluorescence Shift

TDSS Time-Dependent Stokes Shift

THz TDS Terahertz Time-Domain Spectroscopy

TRES Time Resolved Emission Spectra

UV/VIS Ultraviolet–Visible Spectroscopy

frontiers in Chemistry

ORIGINAL RESEARCH
published: 29 October 2021
doi: 10.3389/fchem.2021.728738

Local Dynamics of the Hydration Water and Poly(Methyl Methacrylate) Chains in PMMA Networks

Yoshihisa Fujii[1], *Taiki Tominaga*[2], *Daiki Murakami*[3], *Masaru Tanaka*[3] *and Hideki Seto*[4]*

[1]*Department of Chemistry for Materials, Graduate School of Engineering, Mie University, Tsu, Japan,* [2]*Neutron Science and Technology Center, Comprehensive Research Organization for Science and Society, Tsuchiura, Japan,* [3]*Institute for Materials Chemistry and Engineering, Kyushu University, Fukuoka, Japan,* [4]*Institute of Materials Structure Science/J-PARC Center, High Energy Accelerator Research Organization, Tokai, Japan*

The dynamic behavior of water molecules and polymer chains in a hydrated poly(methyl methacrylate) (PMMA) matrix containing a small amount of water molecules was investigated. Water molecules have been widely recognized as plasticizers for activating the segmental motion of polymer chains owing to their ability to reduce the glass transition temperature. In this study, combined with judicious hydrogen/deuterium labeling, we conducted quasi-elastic neutron scattering (QENS) experiments on PMMA for its dry and hydrated states. Our results clearly indicate that the dynamics of hydrated polymer chains are accelerated, and that individual water molecules are slower than bulk water. It is therefore suggested that the hydration water affects the local motion of PMMA and activates the local relaxation process known as restricted rotation, which is widely accepted to be generally insensitive to changes in the microenvironment.

Keywords: poly(methyl methacrylate), water, quasi-elastic neutron scattering, dynamic behavior, swelling

OPEN ACCESS

Edited by:
Moyuan Cao,
Tianjin University, China

Reviewed by:
Raj Arya,
Dr. B. R. Ambedkar National Institute of Technology Jalandhar, India
Siddharth Surajbhan Gautam,
The Ohio State University, United States

***Correspondence:**
Hideki Seto
hideki.seto@kek.jp

Specialty section:
This article was submitted to Physical Chemistry and Chemical Physics, a section of the journal Frontiers in Chemistry

Received: *22 June 2021*
Accepted: *09 September 2021*
Published: *29 October 2021*

Citation:
Fujii Y, Tominaga T, Murakami D, Tanaka M and Seto H (2021) Local Dynamics of the Hydration Water and Poly(Methyl Methacrylate) Chains in PMMA Networks. Front. Chem. 9:728738. doi: 10.3389/fchem.2021.728738

INTRODUCTION

It is expected that the amount of polymer materials suitable for medical diagnosis and treatment will continue to increase in the coming years. To ensure such progress, the sorption and diffusion of water in polymers must be understood in detail, since they are important factors in drug delivery systems (Langer and Peppas, 1981; Arce et al., 2004), the desalination of water (Cath et al., 2006; Geise et al., 2010), fuel cells (Mauritz and Moore, 2004), coatings (van der Wel and Adan, 1999), and packaging (Auras et al., 2004). When a polymer is integrated as part of an organ, or as a diagnostic or *in situ* diagnostic or treatment equipment, the polymer surface is typically in contact with an aqueous phase, and so must be both biocompatible and able to adsorb water. Although poly(methyl methacrylate) (PMMA) is commonly used in many technological applications (Tetz and Jorgensen, 2015) due to its excellent cost performance in terms of its mechanical, optical, and interfacial properties, it does not exhibit a high biocompatibility or water content compared to other recently reported biocompatible materials. However, despite its low biocompatibility, PMMA has been employed as a medical material (Tetz and Jorgensen, 2015), although the accurate measurement of liquid water sorption in such vitreous polymers has been limited (Santos et al., 2017). Unlike transport experiments based on the use of polymers containing gases or vapors as diffusing agents, traditional weighing techniques that measure the diffusion of liquids in solid-state polymers (e.g., films) typically involve a tedious *ex situ* pat-and-weigh technique that can possess a low sensitivity and a high experimental error (Davis et al., 2011). In the case of PMMA/water mixtures, it was found that the polymer adsorbed only a small amount of water (~2 wt%), which had little effect on the polymer biocompatibility.

In terms of the mechanical relaxation behavior of PMMA, Tanaka et al. (2008) studied the thermal relaxation of this polymer at the water interface by scanning force microscopy (Fujii et al., 2010) and demonstrated that the segmental motion could be released at room temperature. In their experiment, the penetration depth of the probe tip, which should correlate with the analytical depth, was ~5 nm. Considering the existence of a PMMA density gradient close to the water interface, a faster molecular motion should appear closer to the interface. This phenomenon is primarily associated with the plasticization of the material, as extensively reported in the literature. Understanding how water molecules behave in a variety of restricted environments is therefore key to better understanding their roles in chemical and physical processes. In the context of biocompatibility, Tanaka and Mochizuki investigated the excellent blood compatibility of poly(2-methoxyethyl acrylate) (PMEA) in terms of its contact angle, equilibrium water content, and thermal analysis. Their differential scanning calorimetry (DSC) experiments showed that the water present in PMEA could be classified into three types, namely non-freezing water, freezing free water, and freezing intermediate water (Tanaka and Mochizuki, 2004). This categorization of water and its relationship with polymer biocompatibility have been verified using several experimental techniques (Miwa et al., 2009; Tanaka et al., 2021); however, the origin of intermediate water formation is not yet understood. As mentioned above, the majority of studies into the dynamics of hydrated polymer chains and the adsorbed water have been conducted on hydrophilic polymers that are easily swollen; few such studies have been carried out into hydrophobic polymer systems due to experimental difficulty.

Neutron scattering experiments on a protiated polymer sample can provide information regarding the self-correlation function of hydrogen atoms (H). Furthermore, since the difference between the incoherent cross-section of protium and the total cross-section of deuterium (D) is ~80 times larger, the intensity scattered by a subset of the protium hydrogens can be strongly enhanced if the selective deuteration of the other hydrogens is possible by means of chemical methods. Thus, quasi-elastic neutron scattering (QENS) via back-scattering spectroscopy, which covers both the temporal picosecond to nanosecond scale and the spatial scale from 0.3 to 8 nm, is an effective means to investigate the dynamics of both hydration water and bulk water (Telling, 2020). In addition, through the use of selective deuteration, the self-correlated dynamics of a specific component of a complex system can be observed. To date, several QENS measurements have been performed to examine the dynamic behavior of hydration water in the vicinity of biocompatible materials (Colmenero and Arbe, 2013). For example, the authors investigated the dynamic behavior of hydration water molecules between phospholipid membranes and demonstrated the existence of three types of water (Yamada et al., 2017; Seto and Yamada, 2020).

In this article, we report QENS results for mixtures of water and PMMA carried out from low to physiological temperature to estimate the activation energy of the local motion of PMMA. The hydration water in the vicinity of the PMMA chains can be categorized into three types: slow water with a relaxation time of more than sub-nanoseconds, medium-speed water whose relaxation time is slower than that of the bulk water, and fast water, whose characteristics are similar to that of bulk water. Although it is known that the dynamic behavior of medium-speed water is closely related to changes in the local motion of PMMA (Higgins and Benoit, 1994), the detailed dynamics of hydrated water and the local motion of PMMA, the latter of which is expected to change due to hydration, have not yet been clarified. Therefore, the correlation between the water and PMMA dynamics in the hydrated state are elucidated using the H/D contrast in both the water and PMMA components.

EXPERIMENTAL

The perdeuterated poly(methyl methacrylate) (dPMMA) was purchased from Polymer Source Inc., with a number-average molecular weight (M_n) of 15,500 g/mol, a weight average molecular weight (M_w) of 16,000 g/mol, and an M_w/M_n ratio of 1.02. Protiated PMMA (hPMMA) was also purchased from Polymer Source Inc., with an M_n value of 15,000 and an M_w/M_n ratio of 1.12. These polymers were used as received without any further purification. The dPMMA was dissolved in perdeuterated toluene to prevent the exchange of D and H during film preparation. Similarly, the hPMMA film was prepared in a protiated toluene solution. The film thicknesses were controlled to ~1 and 0.2 mm, respectively, to maintain a neutron transmittance of ~90% for each sample. The films were annealed under vacuum at 150°C for 24 h. Hydration films were prepared by immersing in Milli-Q water (H_2O) and deuterated water (D_2O, ≥99.96 atom% D) purchased from Sigma-Aldrich Co. LLC. The water content was calculated using the weight differences for the samples before and after water absorption. The water content of dPMMA/H_2O was 2.7 wt%, while that of dPMMA/D_2O was 2.4 wt%; these values are comparable to the saturated water content of PMMA. Since PMMA film is brittle even when it contains water, a flat specimen of the film was used since it cannot be bent into the cylindrical sample shape that is required for the QENS measurement cell. Thus, the sample sheets were installed on flat aluminum cells, as shown in **Figure 1**. The samples were wrapped with Nb foil with a thickness of 25 μm to avoid corrosion of the aluminum upon contact with water. Due to the fact that the scattering cross-sections of aluminum and the Nb foils are small in comparison to the incoherent cross-section of protons in the sample, their influence can be ignored by minimizing the thicknesses of the Nb and Al components.

The QENS measurements were performed using a time-of-flight near-backscattering spectrometer BL02 (DNA) (Shibata et al., 2015; Seto et al., 2017; Kajimoto et al., 2019) at the Materials and Life Science Experimental Facility (MLF) at the Japan Proton Accelerator Research Complex (J-PARC). The injected proton beam power incident on the neutron target was approximately 500 kW. The energy resolution was 12 μeV (high-flux mode), and was achieved using a Si 111 analyzer. The flat plate sample was placed at an angle of 30° with respect to the

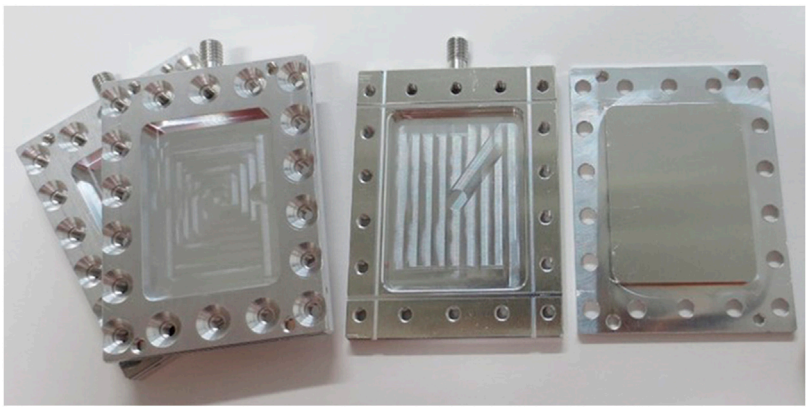

FIGURE 1 | Photographic image of the flat aluminum cell used in this study. The PMMA sheet wrapped in Nb foil was installed in the center of the sample space (30 mm × 40 mm) and sealed by an indium wire to prevent the evaporation of water during measurement.

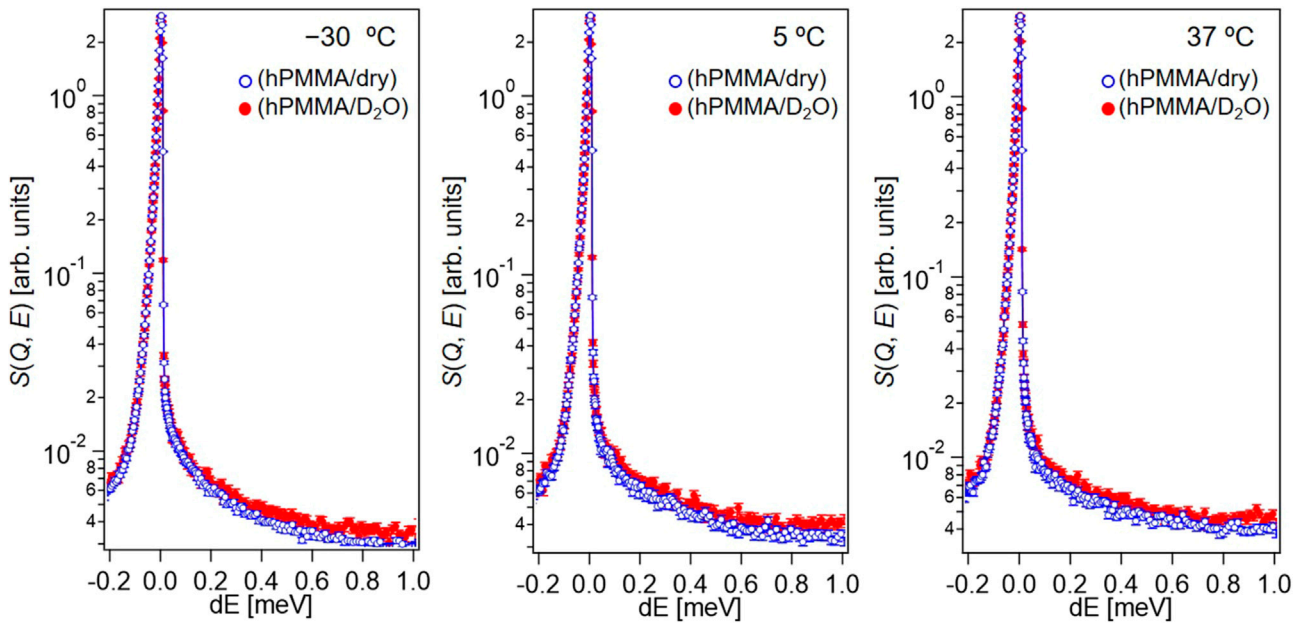

FIGURE 2 | QENS profiles of hPMMA/D_2O (red closed circles) and dry hPMMA (blue open circles) at Q ~1 $Å^{-1}$ of in the high-flux mode at −30, 5, and 37°C.

incident beam, and data were acquired in the Q range of 0.125–1.54 A^{-1}. The QENS measurements were performed at −30, 5, and 37°C, with energy transfer (E) ranges of $-0.2 < E$ [meV] < 1.0. Data analysis was performed without instrumental background or sample cell scattering. The detector efficiency and instrumental resolution function were obtained from the incoherent scattering of the vanadium standard. The dynamics of PMMA in the dry and hydrated states were measured using hPMMA and D_2O. When evaluating the dynamics of the water molecules present within the PMMA matrix, fitting was performed after subtracting the result of (dPMMA/D_2O) from (dPMMA/H_2O) at 37°C. This subtraction operation reduces the contribution of scattering from dPMMA to the maximum possible extent, and allows a detailed discussion of the water dynamics.

DSC measurements were carried out using an EXSTAR X-DSC7000 (Hitachi High-Tech Corp.) instrument. During scanning, the samples were cooled from 30 to −100°C at a rate of 5°C/min, held at −100°C for 5 min, and heated to 30°C at a rate of 5°C/min under a flow of nitrogen.

RESULTS AND DISCUSSION

To investigate the molecular dynamics of PMMA in the dry and hydrated states, dry hPMMA and hPMMA/D_2O were prepared.

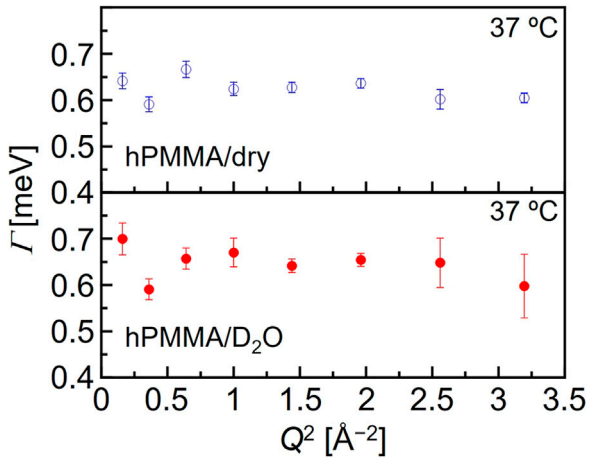

FIGURE 3 | Typical *Q*-dependence of the Lorentz function half width at half maximum (Γ) for the dry hPMMA and the hydrated hPMMA at 37°C.

During the QENS measurements of the dry hPMMA and hPMMA/D_2O samples, protons were only included in PMMA, so that the QENS signals mainly originated from the dynamics of the PMMA chains. **Figure 2** shows the QENS profiles of these two samples at Q ~1 $Å^{-1}$, which were recorded at −30, 5, and 37°C.

Upon examination of **Figure 2**, it is clear that the QENS profiles from the hydrated hPMMA sample (red closed circles) were broader than those from the dry hPMMA sample (blue open circles) at all temperatures measured. This indicates that the molecular mobility of PMMA was activated in the presence of water under these conditions, even when the temperature was lower than that required for the beta-relaxation process related to the side chain (i.e., -$COOCH_3$) of PMMA (McCrum et al., 1967). We then examined the assignment of the observed molecular motion by evaluating the temperature dependence of peak broadening (Γ). More specifically, we employed the sum of two terms, namely the delta function and the Lorentz function, to interpret the QENS profiles as follows:

$$S(Q,E) = R(Q,E) \otimes (\nu_1 \delta(Q,E) + \nu_2 L(\Gamma,E)) + B_g, \qquad (1)$$

where $R(Q, E)$, $\delta(Q, E)$, $L(\Gamma, E)$, and B_g represent the resolution function, the delta function, the Lorentz function, and the constant background, respectively. In addition, the ν_n (n = 1,2) is related to the number of hydrogen atoms in each motion. Here, Γ is the half-width at half-maximum (HWHM) of the Lorentz function. It is reasonable to interpret that $\delta(E)$ and $L(\Gamma, E)$ represent the immobile (frozen) chains and the mobile functional groups, respectively, which can be obtained by the resolution and the *Q-E* window of the DNA spectrometer in the high-flux mode. Fitting was performed using the least-squares method on Igor Pro (WaveMetrics). This interpretation is supported by the weak *Q*-dependence of Γ (shown in **Figure 3**), which could be evidence that the Lorentz function originates from a local motion of PMMA chains.

Figure 4 shows semilogarithmic plot for the dry and hydrated hPMMA samples. The horizontal axis represents the reciprocal of the measurement temperature ($1/T$), while the ordinate is the logarithm of the Γ of the Lorentz function. As can be seen from this figure, the HWHMs of the Lorentz function for both the dry and hydrated hPMMA samples increased with increasing temperature. Within the temperature range employed, the relationship between ln Γ and T^{-1} seems to be linear, thereby indicating that the plots can be represented using an Arrhenius type equation. This is a characteristic feature for relaxation processes in confined systems, such as in the case of side-chain rotation. Subsequently, using **Eq. 2**, the apparent activation energy (ΔH^*) was obtained for the local molecular motion:

$$\Gamma = \Gamma_\infty \exp(-\Delta H^*/k_B \cdot T) \qquad (2)$$

In this equation, ΔH^* is the activation energy barrier for rotation, k_B is the Boltzmann constant, and Γ_∞ is a temperature-independent pre-exponential factor. Based on previous literature (Mukhopadhyay et al., 1998), a value of 4.8 meV was adopted as Γ_∞ in the case of PMMA.

The activation energies of the dry and hydrated hPMMA samples were then estimated from the plots presented in **Figure 4**. More specifically, the ΔH^* value for the hydrated hPMMA was estimated to be 3.1 kJ/mol, which was significantly lower than the corresponding value for the dry hPMMA, i.e., 5.1 kJ/mol. It was therefore considered that the local motion observed in the QENS measurement originates from the CH_3 moieties bind to the polymer side-chain and backbone since the measurement temperature range was well below the glass transition temperature at which movement of the main chain was frozen. From the magnitude of these values of ΔH^*, the molecular dynamics observed during these QENS measurements were attributed to the local rotational motion of PMMA, which corresponds well with previous studies of QENS measurements (Arrighi et al., 1995; Sakai and Arbe, 2009). This difference could be attributed to the fact that the local

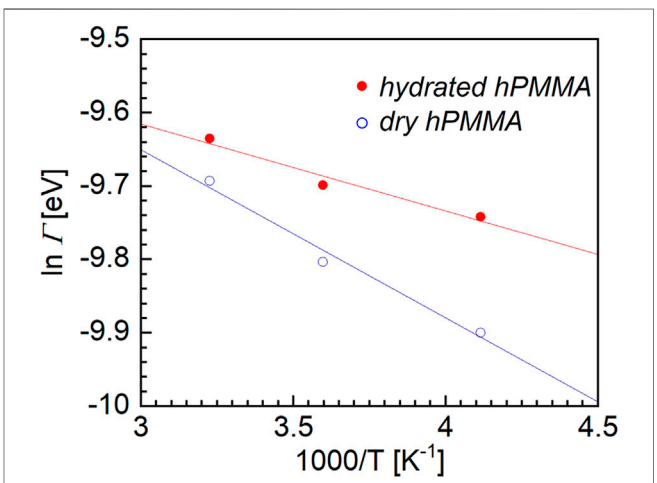

FIGURE 4 | Semilogarithmic plot between the half width at half maximum (Γ) of the Lorentz function, versus the reciprocal of the absolute temperature for the dry hPMMA and hydrated hPMMA samples.

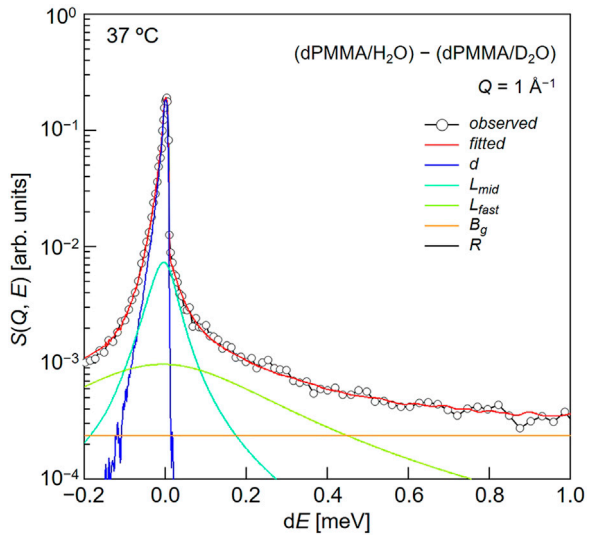

FIGURE 5 | Typical fitting result for a QENS profile obtained from the difference between dPMMA/H_2O and dPMMA/D_2O.

molecular motion in the hydrated sample is accelerated by water molecules. It should be noted here that early studies into the rotational motion of the ester methyl group in PMMA showed a peculiar temperature dependence for the width of the quasi-elastic component (Kunal et al., 2008), wherein the full width at half maximum (FWHM) versus the inverse of temperature did not follow a simple Arrhenius law. More specifically, the apparent activation energy was measured, and was found to vary from 1 kJ/mol at 150 K to 7 kJ/mol at room temperature. It should be emphasized that molecular motion on a relatively small scale is generally insensitive to changes in the microenvironment (McCrum et al., 1967). For polymers, these can arise from the motion of pendant groups and usually have no relation to structural relaxation or to the surroundings. On the other hand, a recent study using two-dimensional nuclear magnetic resonance spectroscopy revealed that β-relaxation is a complex process consisting of the hindered rotation of side chain groups in addition to local cooperative movement (Schmidt-Rohr et al., 1994). Furthermore, Fukao et al. (2001) used dielectric relaxation spectroscopy to examine the α_a- and β-relaxation processes in ultrathin films of PMMA. They claimed that once the thickness became smaller than a critical value of ~100 nm, the relaxation temperatures for the α_a- and β-processes decreased with a reduced thickness owing to the surface effects. This indicates that the β-process depends on the microenvironmental changes. Importantly, our findings do not contradict their results, and may suggest that extremely small-scale molecular motions, such as those of methyl groups, are also accelerated by water molecules.

It is known that characteristic relaxation times can vary significantly depending on the local configuration around the relaxing unit. For example, movement of the methyl group can be inhibited by direct connection to the main chain. However, if the methyl group exists as part of an ester or ether group attached to the main chain, as in the case of PMMA, these librational modes are hardly observable (Mukhopadhyay et al., 1998). Therefore, further QENS experiments using partially deuterated PMMA systems should be performed to clarify whether the local motion originates from directly linked methyl groups or from ester methyl groups.

Subsequently, we evaluated the dynamical behavior of water in the vicinity of the polymer chains in the hydrated PMMA. To evaluate the motion of the hydration water molecules present within the PMMA matrix, QENS experiments were carried out on the mixtures of dPMMA/H_2O and dPMMA/D_2O at 37°C, and the data corresponding to dPMMA/D_2O were subtracted from those of dPMMA/H_2O to estimate the contribution from H_2O. The QENS profiles were then obtained from the result of subtraction at Q ~1 Å^{-1}, as shown in **Figure 5**. For this purpose, we used the sum of three terms, namely one delta function and two Lorentz functions, to interpret the QENS profiles as follows:

$$S(Q,E) = R(Q,E) \otimes (\nu_1 \delta(Q,E) + \nu_2 L_{\mathrm{mid}}(\Gamma_{\mathrm{mid}}, E) + \nu_3 L_{\mathrm{fast}}(\Gamma_{\mathrm{fast}}, E)) + B_g \quad (3)$$

In this equation, the delta function represents the slow mode (i.e., narrower than the instrumental resolution) component, whereas the subscripts "mid" and "fast" indicate the middle-speed water and fast water components, respectively.

Figure 6 shows the Q-dependence of Γ_{mid} (black closed circles) and Γ_{fast} (red closed circles), and based on the observed trend, only Γ_{fast} could be explained by the jump diffusion model shown as the fitting line (blue). The fitting assuming the jump diffusion model (Bée, 1988) was performed based on the following equation:

$$\Gamma = Dq^2/(1 + Dq^2\tau) \quad (4)$$

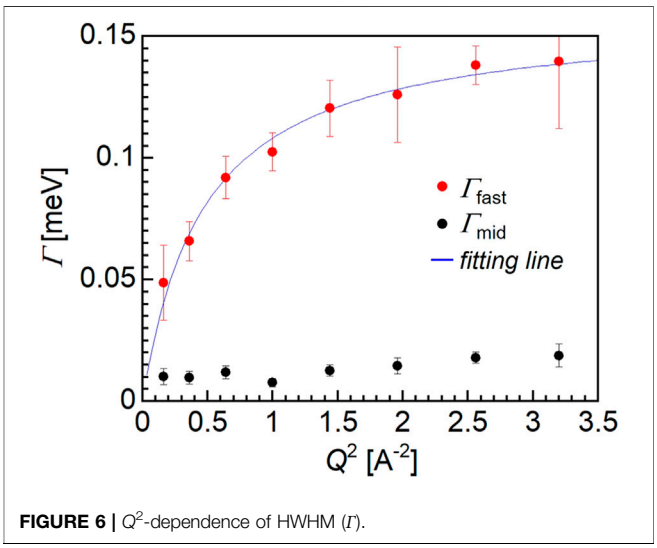

FIGURE 6 | Q^2-dependence of HWHM (Γ).

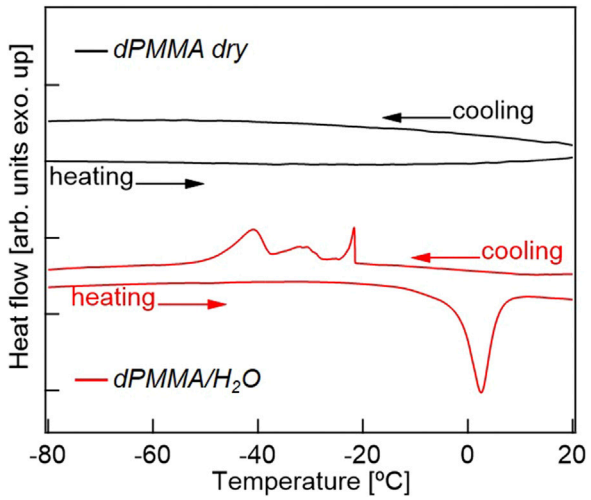

FIGURE 7 | DSC thermograms for dPMMA in its dry and hydrated states.

where τ and D are the mean residence time and the diffusion coefficient, respectively. Thus, from the fitting of the Q-dependence of Γ_{fast}, the τ and D values for the water molecules could be estimated. The diffusion coefficient of the fast mode was determined to be 1.3×10^{-9} m^2/s, which is approximately half of the value for bulk water, i.e., 2×10^{-9} m^2/s. Moreover, the mean residence time was 2.9×10^{-11} s for the fast mode water molecules, which is more than three times smaller than corresponding value for the bulk water molecules (i.e., 8×10^{-12} s). It should be noted that the motion of the hydration water molecules within the PMMA matrix is slower compared to that of the bulk water, despite PMMA being a hydrophobic polymer.

The relaxation time of the fast mode water ranges from approximately 10^{-12} to 10^{-11} s, which is one or two orders of magnitude faster than the NMR correlation time for intermediate water. It should be noted that the motion of water molecules observed by QENS was characterized by jump diffusion while NMR measurements mainly observe molecular rotations. Additionally, the diffusion coefficient of the fast mode water determined herein is comparable to that of the free water molecules in the case of a mixture of phospholipid (Seto and Yamada, 2020). This result therefore confirmed that water exists in the form of intermediate water in the hydrated PMMA, and this finding can be explained by considering the formation of hydrogen bonds between the water molecules and the carbonyl groups of PMMA (Lee et al., 2010).

Previously, the intermediate water present in biocompatible polymers has been mainly discussed based on DSC measurements, and was only found in polymers with relatively high water contents. Thus, **Figure 7** shows the DSC cooling and heating profiles of the dry dPMMA and hydrated dPMMA samples examined herein. As shown in the cooling profiles, a significant difference could be seen between the thermograms of the dry and hydrated PMMA specimens. More specifically, in the hydrated PMMA, exothermic peaks were observed in the range of −20 to −45°C; these peaks were not observed in the case of the dry PMMA. Based on previous results (Tanaka and Mochizuki, 2004), it can be considered that these exothermic peaks are caused by the freezing of hydration water. In addition, compared with previously reported results for biocompatible materials with high water contents, the peak at approximately −20°C originates from the freezing of free water, while the peak at approximately −40°C may be derived from the intermediate water. The wide range of exothermic peaks in the cooling scan may reflect the difference in the hydration state due to the heterogeneity of the hydration water in PMMA. The proportion of intermediate water to the total amount of water was calculated from the enthalpy of water crystallization obtained from the DSC thermograms with reference to the literature (Toyokawa et al., 2021). Assuming that the peak at approximately −45°C was derived from intermediate water, 28% of the 2.6 wt% water content of PMMA is present as intermediate water, which is an extremely small value compared to those determined for biocompatible materials, such as PMEA (Tanaka and Mochizuki, 2004). In a previous review by Tsuruta, it was mentioned that the shape change of the time-resolved IR spectrum (in the OH stretching vibrational region) for the sorbed water of PMMA was surprisingly similar to that of PMEA despite the small amount of sorbed water (Tsuruta, 2010). However, considering the supportive research carried out to date and the results obtained in the current study, our findings represent the first observation of intermediate water in a hydrophobic polymer with a low water content. In addition, the discovery that local restricted motions are affected by extremely small amounts of hydrated water molecules also adds new knowledge to this area.

CONCLUSION

In this work, we focused on the dynamic behavior of water in the vicinity of poly(methyl methacrylate) (PMMA), which is a typical glassy polymer with a low water solubility. For this purpose, quasi-elastic neutron scattering (QENS) experiments were carried out on the dry and hydrated states of PMMA in combination with judicious hydrogen/deuterium labeling to independently investigate the dynamic behaviors of the polymer chains and the hydration water. We found that the motion of the hydration water molecules in PMMA was slower than that in the bulk water, despite PMMA being a hydrophobic polymer. Based on the obtained results, the cause of the weak biocompatibility of PMMA, a hydrophobic polymer with a low water content, was clarified. These results are also of interest since the majority of studies carried out into the dynamics of hydrated polymer chains and the adsorbed water have been conducted on hydrophilic polymers that are easily swollen, with very few reports being published into hydrophobic polymers.

DATA AVAILABILITY STATEMENT

The original contributions presented in the study are included in the article/Supplementary Material, further inquiries can be directed to the corresponding authors.

AUTHOR CONTRIBUTIONS

The experiments were performed by all the authors, and data analysis was carried out by YF and TT. The draft of the manuscript was prepared by YF, HS, and TT. The DSC measurements and analysis were performed by DM and MT. All the authors listed have discussed this research, made a substantial, direct, and intellectual contribution to the work, and approved it for publication.

FUNDING

The neutron experiments at the Materials and Life Science Experimental Facility at J-PARC were performed under user programs (Proposal Nos. 2018B0235 and 2020A0247). This work was supported by the JSPS KAKENHI Grant Numbers JP19H05717 and JP19H05720 (Aquatic Functional Materials).

ACKNOWLEDGMENTS

The authors thank Dr. Takeshi Yamada for experimental support and helpful discussions.

REFERENCES

Arce, A., Fornasiero, F., Rodríguez, O., Radke, C. J., and Prausnitz, J. M. (2004). Sorption and Transport of Water Vapor in Thin Polymer Films at 35 °C. *Phys. Chem. Chem. Phys.* 6, 103–108. doi:10.1039/B307996A

Arrighi, V., Higgins, J. S., Burgess, A. N., and Howells, W. S. (1995). Rotation of Methyl Side Groups in Polymers: A Fourier Transform Approach to Quasielastic Neutron Scattering. 1. Homopolymers. *Macromolecules* 28, 2745–2753. doi:10.1021/ma00112a021

Auras, R., Harte, B., and Selke, S. (2004). An Overview of Polylactides as Packaging Materials. *Macromol. Biosci.* 4, 835–864. doi:10.1002/mabi.200400043

Bée, M. (1988). *Quasielastic Neutron Scattering: Principles and Applications in Solid State Chemistry, Biology and Materials Science*. Bistol, England: AdamHilger. ISBN 0-85274-371-8.

Cath, T., Childress, A., and Elimelech, M. (2006). Forward Osmosis: Principles, Applications, and Recent Developments. *J. Membr. Sci.* 281, 70–87. doi:10.1016/j.memsci.2006.05.048

Colmenero, J., and Arbe, A. (2013). Recent Progress on Polymer Dynamics by Neutron Scattering: From Simple Polymers to Complex Materials. *J. Polym. Sci. B Polym. Phys.* 51, 87–113. doi:10.1002/polb.23178

Davis, E. M., Benetatos, N. M., Regnault, W. F., Winey, K. I., and Elabd, Y. A. (2011). The Influence of thermal History on Structure and Water Transport in Parylene C Coatings. *Polymer* 52, 5378–5386. doi:10.1016/j.polymer.2011.08.010

Fujii, Y., Nagamura, T., and Tanaka, K. (2010). Relaxation Behavior of Poly(methyl Methacrylate) at a Water Interface. *J. Phys. Chem. B* 114, 3457–3460. doi:10.1021/jp909373g

Fukao, K., Uno, S., Miyamoto, Y., Hoshino, A., and Miyaji, H. (2001). Dynamics Ofαandβprocesses in Thin Polymer Films: Poly(vinyl Acetate) and Poly(methyl Methacrylate). *Phys. Rev. E* 64, 051807. doi:10.1103/PhysRevE.64.051807

Geise, G. M., Lee, H.-S., Miller, D. J., Freeman, B. D., McGrath, J. E., and Paul, D. R. (2010). Water Purification by Membranes: The Role of Polymer Science. *J. Polym. Sci. B Polym. Phys.* 48, 1685–1718. doi:10.1002/polb.22037

Higgins, J. S., and Benoit, H. C. (1994). *Polymers and Neutron Scattering*. Oxford: Oxford University Press.

Kajimoto, R., Yokoo, T., Nakamura, M., Kawakita, Y., Matsuura, M., Endo, H., et al. (2019). Status of Neutron Spectrometers at J-PARC. *Physica B: Condensed Matter* 562, 148–154. doi:10.1016/j.physb.2018.11.061

Kunal, K., Robertson, C. G., Pawlus, S., Hahn, S. F., and Sokolov, A. P. (2008). Role of Chemical Structure in Fragility of Polymers: A Qualitative Picture. *Macromolecules* 41, 7232–7238. doi:10.1021/ma801155c

Langer, R., and Peppas, N. (1981). Present and Future Applications of Biomaterials in Controlled Drug Delivery Systems. *Biomaterials* 2, 201–214. doi:10.1016/0142-9612(81)90059-4

Lee, W.-J., Chang, J.-G., and Ju, S.-P. (2010). Hydrogen-bond Structure at the Interfaces between Water/poly(methyl Methacrylate), Water/Poly(Methacrylic Acid), and Water/poly(2-Aminoethylmethacrylamide). *Langmuir* 26, 12640–12647. doi:10.1021/la904898v

Mauritz, K. A., and Moore, R. B. (2004). State of Understanding of Nafion. *Chem. Rev.* 104, 4535–4586. doi:10.1021/cr0207123

McCrum, N. G., Read, B. E., and Williams, G. (1967). *Anelastic and Dielectric Effects in Polymeric Solids*. New York: Dover.

Miwa, Y., Ishida, H., Saitô, H., Tanaka, M., and Mochizuki, A. (2009). Network Structures and Dynamics of Dry and Swollen Poly(acrylate)s. Characterization of High- and Low-Frequency Motions as Revealed by Suppressed or Recovered Intensities (SRI) Analysis of 13C NMR. *Polymer* 50, 6091–6099. doi:10.1016/j.polymer.2009.10.037

Mukhopadhyay, R., Alegría, A., Colmenero, J., and Frick, B. (1998). Methyl Group Dynamics in Poly(vinyl Acetate): A Neutron Scattering Study. *Macromolecules* 31, 3985–3993. doi:10.1021/ma970575p

Sakai, V. G., and Arbe, A. (2009). Quasielastic Neutron Scattering in Soft Matter. *Curr. Opin. Colloid Interf. Sci.* 14, 381–390. doi:10.1016/j.cocis.2009.04.002

Santos, M. C., Bendiksen, B., and Elabd, Y. A. (2017). Diffusion of Liquid Water in Free-Standing Polymer Films Using Pressure-Contact Time-Resolved Fourier Transform Infrared Attenuated Total Reflectance Spectroscopy. *Ind. Eng. Chem. Res.* 56, 3464–3476. doi:10.1021/acs.iecr.7b00114

Schmidt-Rohr, K., Kulik, A. S., Beckham, H. W., Ohlemacher, A., Pawelzik, U., Boeffel, C., et al. (1994). Molecular Nature of the .Beta. Relaxation in Poly(methyl Methacrylate) Investigated by Multidimensional NMR. *Macromolecules* 27, 4733–4745. doi:10.1021/ma00095a014

Seto, H., Itoh, S., Yokoo, T., Endo, H., Nakajima, K., Shibata, K., et al. (2017). Inelastic and Quasi-Elastic Neutron Scattering Spectrometers in J-PARC. *Biochim. Biophys. Acta (Bba) - Gen. Subjects* 1861, 3651–3660. doi:10.1016/j.bbagen.2016.04.025

Seto, H., and Yamada, T. (2020). Quasi-Elastic Neutron Scattering Study of the Effects of Metal Cations on the Hydration Water between Phospholipid Bilayers. *Appl. Phys. Lett.* 116, 133701. doi:10.1063/1.5144012

Shibata, K., Takahashi, N., Kawakita, Y., Matsuura, M., Yamada, T., Tominaga, T., et al. (2015). The Performance of TOF Near Backscattering Spectrometer DNA in MLF, J-PARC. *JPS Conf. Proc.* 8, 036022. doi:10.7566/JPSCP.8.036022

Tanaka, K., Fujii, Y., Atarashi, H., Akabori, K.-i., Hino, M., and Nagamura, T. (2008). Nonsolvents Cause Swelling at the Interface with Poly(Methyl Methacrylate) Films. *Langmuir* 24, 296–301. doi:10.1021/la702132t

Tanaka, M., and Mochizuki, A. (2004). Effect of Water Structure on Blood Compatibility? Thermal Analysis of Water in Poly(meth)acrylate. *J. Biomed. Mater. Res.* 68A, 684–695. doi:10.1002/jbm.a.20088

Tanaka, M., Morita, S., and Hayashi, T. (2021). Role of Interfacial Water in Determining the Interactions of Proteins and Cells with Hydrated Materials. *Colloids Surf. B: Biointerfaces* 198, 111449. doi:10.1016/j.colsurfb.2020.111449

Telling, M. T. F. (2020). *A Practical Guide to Quasi-Elastic Neutron Scattering*. UK: Royal Society of Chemistry.

Tetz, M., and Jorgensen, M. R. (2015). New Hydrophobic IOL Materials and Understanding the Science of Glistenings. *Curr. Eye Res.* 40, 969–981. doi:10.3109/02713683.2014.978476

Toyokawa, Y., Kobayashi, S., Tsuchiya, H., Shibuya, T., Aoki, M., Sumiya, J., et al. (2021). A Fully Covered Self-Expandable Metallic Stent Coated with Poly (2-methoxyethyl

Acrylate) and its Derivative: *In Vitro* Evaluation of Early-Stage Biliary Sludge Formation Inhibition. *Mater. Sci. Eng. C* 120, 111386. doi:10.1016/j.msec.2020.111386

Tsuruta, T. (2010). On the Role of Water Molecules in the Interface between Biological Systems and Polymers. *J. Biomater. Sci. Polym. Edition* 21, 1831–1848. doi:10.1163/092050610X488269

van der Wel, G. K., and Adan, O. C. G. (1999). Moisture in Organic Coatings - a Review. *Prog. Org. Coat.* 37, 1–14. doi:10.1016/S0300-9440(99)00058-2

Yamada, T., Takahashi, N., Tominaga, T., Takata, S.-i., and Seto, H. (2017). Dynamical Behavior of Hydration Water Molecules between Phospholipid Membranes. *J. Phys. Chem. B* 121, 8322–8329. doi:10.1021/acs.jpcb.7b01276

Conflict of Interest: The authors declare that the research was conducted in the absence of any commercial or financial relationships that could be construed as a potential conflict of interest.

Publisher's Note: All claims expressed in this article are solely those of the authors and do not necessarily represent those of their affiliated organizations, or those of the publisher, the editors and the reviewers. Any product that may be evaluated in this article, or claim that may be made by its manufacturer, is not guaranteed or endorsed by the publisher.

frontiers in Chemistry

ORIGINAL RESEARCH
published: 17 December 2021
doi: 10.3389/fchem.2021.753958

Dynamics of Water and Other Molecular Liquids Confined Within Voids and on Surface of Lignin Aggregates in Aging Bio Crude Oils

Massimo Bonini[1], *Emiliano Fratini*[1]* *and Antonio Faraone*[2]*

[1]Department of Chemistry "Ugo Schiff" and CSGI, University of Florence, Sesto Fiorentino, Italy, [2]Center for Neutron Research, National Institute of Standards and Technology, Gaithersburg, MD, United States

Neutron scattering methods were employed to study the microscopic structure and dynamics of Bio Crude Oils (BCOs) and their lignin fractions. The structure of the carbonaceous aggregates was investigated using Small Angle Neutron Scattering to reveal a fractal hierarchy as well as a growth of the aggregates as the aging of the BCO proceeds. Elastic Neutron Scattering measurements indicate that BCO liquid phase, comprised of water and other hydrogenated molecular liquids, is in a state of extreme confinement. Quasi-Elastic Neutron Scattering yields information on the molecular motions, indicating that long range translational diffusion is suppressed and only localized dynamics take place on the tens of picosecond time range. The obtained results provide quantitative information on the molecular activity, as aging proceed, in these reactive materials of relevance as potential renewable energy sources.

Keywords: pyrolysis oil, lignin aggregation, neutron scattering, water dynamics, confined water, lignin dynamics

OPEN ACCESS

Edited by:
Hideki Seto,
High Energy Accelerator Research Organization, Japan

Reviewed by:
Yangyang Wang,
Oak Ridge National Laboratory (DOE), United States
Alejandro Gil-Villegas,
University of Guanajuato, Mexico

***Correspondence:**
Emiliano Fratini
emiliano.fratini@unifi.it
Antonio Faraone
afaraone@nist.gov

Specialty section:
This article was submitted to Physical Chemistry and Chemical Physics, a section of the journal Frontiers in Chemistry

Received: *05 August 2021*
Accepted: *26 October 2021*
Published: *17 December 2021*

Citation:
Bonini M, Fratini E and Faraone A (2021) Dynamics of Water and Other Molecular Liquids Confined Within Voids and on Surface of Lignin Aggregates in Aging Bio Crude Oils. Front. Chem. 9:753958. doi: 10.3389/fchem.2021.753958

1 INTRODUCTION

The energetic scenario depicted by most analysts and Kyoto agreement on CO_2 emissions control require the development of new fuels based on renewable sources. In the last couple of decades, Bio Crude Oils (BCOs) have attracted a considerable attention as possible renewable energy from biomass (Ringer et al., 2006). These oils are obtained from the pyrolysis of biomass: i.e., by heating a feed-stock such as wood, agricultural wastes, paper, algae, animal wastes, etc., at high temperature, and rapidly quenching the obtained liquid products. Unfortunately, BCOs are poorly stable since numerous reactions take place after their production, making them very reactive and leading to several problems in their handling and final use. In particular, compared to conventional mineral fuels, pyrolysis oils show long-term instability with a strong dependency on the storage temperature (Oasmaa and Kuoppala, 2003). Therefore, the characterization of the BCOs and the way they are affected by aging represents a crucial step in order to employ these oils in practical applications and in particular as substitutes of mineral oils. In general, BCOs are formed by a large number of organic compounds, mainly carboxylic acids, carbohydrates and lignin derivatives, together with a variable amount of water. Unfortunately, some of these organic compounds are very reactive and seem to be the main responsible for the aging process (Bridgwater, 2008). During storage these components chemically react to produce larger molecules leading to changes in the physical properties, such as viscosity and density. Previous studies proposed that etherification and esterification occurring between hydroxyl, carbonyl, and carboxyl groups (Czernik et al., 1994) are the main chemical reactions taking place in pyrolysis oils and producing water as a byproduct of the condensation

TABLE 1 | Physico-chemical parameters of the BCO from BTG (Chiaramonti et al., 2011). Here mass% indicates the percentage mass fraction.

Parameter	Value
Carbon (mass%)	42.79
Hydrogen (mass%)	7.57
Nitrogen (mass%)	<0.01
Oxygen (balance) (mass%)	49.57
Water content (mass%)	21.7
Ash content (mass%)	0.047
Solids content (mass%)	0.27
Density (kg/m^3)	1207
Kinematic viscosity (10^{-6} m^2/s)	65.1
pH	2.85

reactions. Lignin's derived compounds are indicated as pyrolytic lignin and are obtained as the water-insoluble fraction of BCOs (SipiläSipila et al., 1998). Gel Permeation Chromatography and ^{13}C-NMR measurements (Scholze et al., 2001) demonstrated that pyrolytic lignin mainly consist of trimers and tetramers, even though larger structural units remain intact during the pyrolysis. These results are in agreement with the thermal ejection theory formulated by Piskorz (Overend and Chornet, 1999), where lignin oligomers are considered to be directly expelled from wood particles as a result of a partial cracking of lignin molecules during the pyrolysis. In a previous SANS investigation, some of the Authors have verified the validity of this theory and elucidated the role of pyrolytic lignin in the aging of BCOs (Fratini et al., 2006). In particular, the possibility to correlate the aggregation between pyrolytic lignin into clusters with the evolution of the BCOs chemical and physical properties was disclosed. This is of great importance in the formulation of pyrolysis fuels with long-term stability. The investigation reported an increase of both the volume fraction of the scattering objects and the number of spherical sub-units per cluster (i.e., the aggregation number) as time passes after BCO production. The obtained fractal dimensions values range between 1.4 and 1.5, i.e., values typical of branched structures that are generated by the aggregation of small lignin units as a consequence of the chemical reactivity of this peculiar fluid (Fratini et al., 2006).

The microscopic dynamics of the liquid phases in the BCO plays a crucial role in determining the reactions taking place during aging. Dynamic neutron scattering techniques offer the unique capability to measure the single particle dynamics of the hydrogen atoms in the system over length scales of the order of the Ångstrom and time scales ranging from few picoseconds to nanoseconds. This microscopic mobility of the liquid species is indicative of the activity in the system.

Among the liquid species present in BCO, water accounts for more than 20% (see **Table 1**). However, the environment the water molecules experience is vastly different from the bulk: in fact, water is most reasonably confined on the surface and within the nanoscopic voids of the carbonaceous aggregates generated by the lignin units as well as intermixed and hydrogen bonded with other molecular liquids (carboxylic acids, aldehydes/ketones, ethers, esters, etc.) (Oasmaa et al., 2003). As such, water in BCO should be considered interfacial water and an exemplary case of how, in many instances of relevance, water molecules are found confined on surfaces, in microcavity, or dispersed within a different liquid phase.

The present work reports the results of an investigation, performed using mainly Quasi-Elastic Neutron Scattering (QENS) (Bée, 1988; Gardner et al., 2020), of the microscopic mobility of the hydrogen atoms in BCO as a function of aging. In parallel, Small Angle Neutron Scattering (SANS) is employed to determine the micro-structure of the aggregates in BCO and its evolution during aging. The analysis of the temperature dependence of the mean squared displacement of the hydrogen atoms provides information on the confinement experienced by the liquid phases. The analysis of QENS data provides information on the nanoscale dynamics in terms of both time scale and length scale of the mobility. A comparison with the dynamics of the diverse lignin fractions is carried out as well.

2 METHODS

2.1 Samples

Bio-crude oil was supplied by Biomass Technology Group (BTG, Netherlands) and was produced in their fast pyrolysis plant in Enschede from a batch of pine chips. Main physico-chemical properties of the investigated BCO are reported in **Table 1**. Additional details on this batch can be found elsewhere (Chiaramonti et al., 2011). Samples corresponding to four aging stages have been investigated and are labelled, hereinafter, as "fresh," "12 months," "12 months at 40°C" and "15 months." All of the samples were stored at room temperature during the first month after their production. After the first month, "fresh" sample was frozen and taken back to the liquid state before carrying out the measurements. Similarly, "12 months" sample was stored at room temperature and frozen 13 months after production (12 months after "fresh"). Sample labeled as "15 months" was never frozen and always stored at room temperature, as the measurements were carried out exactly 16 months after production. Sample labeled as "12 months at 40°C" was stored, after the first month at room temperature, at 40°C during the next year and then frozen until measurements. Samples containing low and high molecular weight lignin fractions have been investigated as well, with the same aging times and storage conditions. The extraction procedure was conducted as reported in (Oasmaa et al., 2003). In brief, 400 g of water were added to 5 g of BCO in a Erlenmeyer flask so to separate the water insoluble fraction rich in lignin. The water-insoluble fraction was removed by filtration and further extracted with dichloromethane (i.e., CH_2Cl_2) so to obtain Low Molecular Mass (LMM, CH_2Cl_2-soluble part, about 400 Da) and High Molecular Mass (HMM, CH_2Cl_2-insoluble part, 1050 Da) lignin fractions. Both fractions were evaporated at 40°C overnight to remove any residue of CH_2Cl_2.

2.2 Neutron Scattering

In a neutron scattering measurement the experimentally determined quantity is the double differential scattering cross-

section, $\frac{\partial^2\sigma}{\partial\Omega\partial E}$, the probability that a neutron is scattered within the solid angle Ω+dΩ exchanging an energy E < E_i-E_f < E + dE with the sample, E_f and E_i being the neutron final and initial energy, respectively.

Because of the way the neutrons are scattered by the nuclei in the sample, the scattering can be decomposed in the sum of two contributions: the coherent component, $[\frac{\partial^2\sigma}{\partial\Omega\partial E}]_{coh}$, which yields information on the relative positions and motions of the atoms in the sample, and an incoherent contribution, $[\frac{\partial^2\sigma}{\partial\Omega\partial E}]_{inc}$, which does not contain any structural information and only depends by total amount of the scatterers, yielding information on the single-particle dynamics:

$$\frac{\partial^2\sigma}{\partial\Omega\partial E} = \left[\frac{\partial^2\sigma}{\partial\Omega\partial E}\right]_{coh} + \left[\frac{\partial^2\sigma}{\partial\Omega\partial E}\right]_{inc} \tag{1}$$

Neutron scattering probes the structure and dynamics at the nanoscale. The distances probed are determined by the inverse of the exchanged wavevector, $\mathbf{Q} = \mathbf{k}_i - \mathbf{k}_f$, where $\mathbf{k}_i$ and $\mathbf{k}_f$ are the initial and final wavevector of the scattered neutron. For isotropic samples the differential scattering cross section only depends on the modulus of $Q = |\mathbf{Q}|$. In general, Q is a function of the scattering angle, θ, and the energies, E_i and E, $Q(\theta, E_i, E)$; however, for small values of E, it is a function of the scattering angle and the wavelength of the incoming neutrons, λ, only:

$$Q = \frac{4\pi}{\lambda}\sin\left(\frac{\theta}{2}\right) \tag{2}$$

The microstructure of the BCO was investigated using SANS, for Q values in the range from 3×10^{-3} Å^{-1} to ≈0.6 Å^{-1}, corresponding to length-scales approximately from 1 to 500 nm. In this range, the overwhelming contribution to the scattering is coherent and the incoherent component is just a Q-independent background.

The dynamics of the bio-oils was studied using QENS measurements for Q values 0.5 Å^{-1} ≤ Q ≤ 2.0 Å^{-1}. In this Q range, to a first approximation, the scattering signal originates from the incoherent dynamics of the hydrogen atoms.

2.2.1 SANS

SANS is a static scattering technique which measures the scattered intensity without any analysis of the exchanged energy. Thus, it gives access to the differential scattering cross section:

$$\frac{\partial\sigma}{\partial\Omega} \approx \int_{-\infty}^{\infty}\left[\frac{\partial^2\sigma}{\partial\Omega\partial E}\right]dE \tag{3}$$

where the integration over the whole energy range is always approximated because of experimental constraints. Since in SANS the probed length-scales contain a relative large number of atoms, the scattering power can be expressed in terms of an average scattering length density:

$$\rho_p = \frac{\sum_i b_i^{coh}}{V_p} \tag{4}$$

where b_i^{coh} is the coherent scattering length density of the i-th atom contained in the scattering object of volume V_p.

Within certain approximations, the SANS intensity produced by a collection of uniform scatterers dispersed in a continuous medium (i.e., usually the dispersing medium or "solvent") can be expressed as:

$$I(Q) = n_p\left(\rho_p - \rho_s\right)^2 V_p^2 P(Q) S^{SANS}(Q) + bkg \tag{5}$$

where $I(Q)$ is the scattering intensity (i.e., the differential scattering cross section normalized by the scattering volume), n_p is the number density of the particles, $(\rho_p - \rho_s)$ represents the contrast between the scattering length density of the scattering object ρ_p and the one of the continuous medium ρ_s, V_p is the volume of the scattering object, $P(Q)$ is the form factor describing the shape of the scattering particles, $S^{SANS}(Q)$ is the structure factor representing the Fourier transform of the relative position of the scatterers and bkg is the incoherent background.

The BCO samples investigated in this article can be considered as lignin dispersions in a mixture of water and organic molecules (that we have referred to as "solvent" in the previous section). Several structural models have been already screened for BCOs showing that the structure of the system in the liquid state can be better described by polydisperse clusters with a certain fractal nature originated by the aggregation of smaller lignin spherical units (Fratini et al., 2006). This approach is based on the work of Liu et al. (1995) where they followed the agglomeration of asphaltene primary units in liquid dispersions as a function of the asphaltene volume fraction and temperature. In the present case, considering aggregates consisting of S elementary spherical particles with radius, R_1, fractal dimension, D_f, degree of polydispersity on the average cluster size, ν, and assuming a continuous distribution of cluster size or small enough unit particle, the integral form of the scattering **Eq. 5** reduces to:

$$I(Q) = \frac{\left(\rho_p - \rho_s\right)^2 \phi V_u S}{\Gamma(2-\pi)}\Bigg[F(3-\nu, Q\xi)[1+Q^2\xi^2]^{-D_f(3-\nu)/2} + G(2-\nu, Q\xi)\left[\frac{Q\xi}{h}\right]^{D_f}\Bigg] + \frac{C_P}{Q^4} + bkg \tag{6}$$

where ϕ and V_u are, respectively the volume fraction and molecular volume of the base units; ξ is the correlation length of the fractal object defined as $\xi = hR_1S^{1/D_f}$ with $h = \sqrt{\frac{D_f(D_f+1)}{6}}$. The functions $F(a, x)$ and $G(a, x)$ have the form:

$$F(a, x) = \Gamma(a) - \Gamma(a, u) \tag{7}$$

and:

$$G(a, x) = \sin\left[\frac{(D_f-1)\pi}{2}\right]\frac{\Gamma\left(a, \left(\frac{Q\xi}{h}\right)^{D_f}\right)}{D_f - 1} \tag{8}$$

with:

$$u = \left[\frac{h^2(1+Q^2\xi^2)}{Q^2\xi^2}\right]^{D_f/2} \tag{9}$$

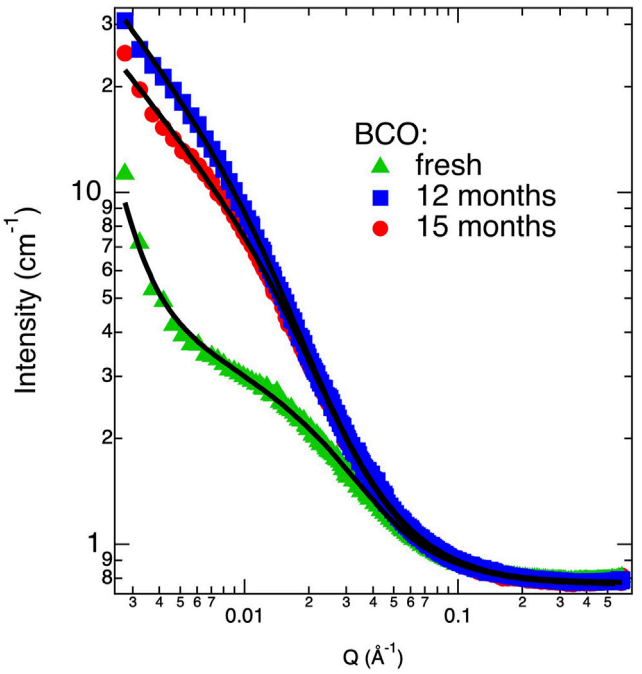

FIGURE 1 | Scattering intensity profiles (markers) and correspondent best fits (lines) according to **Eq. 6** for some of investigated BCO samples.

$x = Q\xi$ and $\Gamma(a)$ and $\Gamma(a, b)$ are the Gamma and incomplete Gamma function, respectively.

An additional Porod's term with amplitude C_P and Q^{-4} dependence is also included to take into account the low Q intensity increase present in the "fresh" sample (see **Figure 1**) and indicating the presence of aggregates at the upper limit of the dimensional range spanned by the SANS experiment (i.e., $2\pi/Q_{min}$).

Eq. 6 has been used in this work with ϕ, S, D_f and ν as adjustable parameters while R_1 was kept fixed at 2.7 Å (Fratini et al., 2006). This model assumes the unit particles as monodisperse, a condition typical of the chemical nature of BCOs. The contrast between the lignin aggregates and continuous medium, $(\rho_p - \rho_s)$ can be calculated by the mass fraction of the scattering objects and the elemental analysis of the bio-oil and lignin as already described in (Fratini et al., 2006) using the composition and density values reported in **Table 1**.

2.2.2 QENS

Within the approximation that the overwhelming contribution to the neutron scattering originates from the incoherent scattering of the hydrogen atoms, the double differential scattering cross section for the QENS measurement is:

$$\frac{\partial^2\sigma}{\partial\Omega\partial E}(\theta, E) = \hbar\frac{k_f}{k_i}N_H\frac{\sigma_H^{inc}}{4\pi}S_H^{self}(Q, E)\otimes R(Q, E) \qquad (10)$$

where N_H is the number of hydrogen atoms in the system, $\sigma_H^{inc} = 80.27$ b is the incoherent scattering cross section of the hydrogen atoms, and $R(Q, E)$ is the instrumental resolution function. $S_H^{self}(Q, E)$ is the single particle, i.e., self-dynamic structure factor of hydrogen atoms in the system:

$$\hbar S_H^{self}(Q, E) = \int_0^\infty \langle\exp\{-i\mathbf{Q}\cdot[\mathbf{r}_H(t) - \mathbf{r}_H(0)]\}\rangle \exp\left\{-i\frac{E}{\hbar}t\right\}dt = \int_0^\infty F_H^{self}(Q, t)\exp\{-iEt_h\}dt \qquad (11)$$

where $F_H^{self}(Q, t)$ is the intermediate scattering function, ISF, and $\langle\ldots\rangle$ indicates an ensemble average.

In particular, Elastic Neutron Scattering (ENS) measurements determine the value of the differential scattering cross-section for $E = 0$, within the instrumental resolution:

$$\frac{\partial^2\sigma}{\partial\Omega\partial E}(\theta, E\approx 0) = \hbar\frac{k_f}{k_i}N_H\frac{\sigma_H^{inc}}{4\pi}\int_{-\infty}^{\infty}S_H^{self}(Q, E)\times R(Q, E)dE = \hbar\frac{k_f}{k_i}N_H\frac{\sigma_H^{inc}}{4\pi}\int_0^\infty F_H^{self}(Q, t)\times R^t(Q, t)dt \qquad (12)$$

$R^t(Q, t)$ being the time Fourier transform of the instrumental resolution function (Fratini et al., 2013).

The position of the H atoms can be decomposed as the sum of the position of a reference point, $\mathbf{r}_R$, such as the center of mass of the molecule, the relative position with respect to the reference point, $\mathbf{b}$, and the vector defining the vibrational displacement from the bond equilibrium position, $\mathbf{u}$:

$$\mathbf{r}_H = \mathbf{r}_R + \mathbf{b} + \mathbf{u} \qquad (13)$$

Within the decoupling approximation, the motions described by these three vectors, namely translational, reorientational and conformational, and vibrational, are statistically independent, hence:

$$\langle\exp\{-i\mathbf{Q}\cdot[\mathbf{r}_H(t) - \mathbf{r}_H(0)]\}\rangle \approx \langle\exp\{-i\mathbf{Q}\cdot[\mathbf{r}_R(t) - \mathbf{r}_R(0)]\}\rangle\times \langle\exp\{-i\mathbf{Q}\cdot[\mathbf{b}(t) - \mathbf{b}(0)]\}\rangle\times\langle\exp\{-i\mathbf{Q}\cdot[\mathbf{u}(t) - \mathbf{u}(0)]\}\rangle \qquad (14)$$

Bond vibrational motions are too fast to fall within the instrumental energy window and only cause a reduction of the total scattering intensity in the QENS window. In terms of its ISF, $F_{rc}^{self}(Q, t)$, or its dynamic structure factor, $S_{rc}^{self}(Q, E)$, the reorientational and conformational dynamics can be expressed as the sum of products of Q dependent and time dependent factors:

$$F_{rc}^{self}(Q, t) = A_0(Q) + \sum_l A_l(Q)\exp\{-\Gamma_l t\} \qquad (15)$$

$$S_{rc}^{self}(Q, E) = A_0(Q)\delta(E) + \sum_l A_l(Q)\mathrm{Lor}(\Gamma_l) \qquad (16)$$

where $\mathrm{Lor}(\Gamma_l)$ represents a Lorentzian function with a full width half maximum equal to Γ_l. The reorientational and conformational dynamics is characterized by a time independent term, which in the energy domain results in the presence of a delta function, i.e., a resolution limited feature centered at $E = 0$. The Q dependence of this contribution, $A_0(Q)$, is referred to as the Elastic Incoherent Structure Factor (EISF) and represents the spatial Fourier transform of the volume explored

by the hydrogen atoms during their motion, with respect to the reference point.

Finally, as far as the dynamics of $\mathbf{r}_R$ is concerned, when the point of reference represents the center of mass of a molecule in the liquid phase (a common choice to model the data in liquids), the corresponding dynamics represents the translational motion of the molecule. Models corresponding for example to Fickian, jump, or confined diffusion have been developed, generally characterized by a Q dependence of the characteristic relaxation time.

In water and other liquids, the accuracy of the decoupling approximation between the translational and reorientational and conformational motions is limited to several percent and it is hard to determine *a priori*, therefore, even if employed very commonly, it represents a major limitation to the accurate interpretation of QENS results (Faraone et al., 2003).

2.3 Instrumentation

SANS measurements were performed on D22 at the Institute Laue Langevin (ILL), Grenoble, France. The incoming neutron wavelengths was set to 6 Å with a $\Delta\lambda/\lambda \approx 10\%$. Three sample to detector distances were employed to cover a Q range from 3×10^{-3} Å^{-1} to about 0.6 Å^{-1}. Data were corrected for the dark counts intensity and the contribution from the empty containers and converted to 1D absolute intensity using standard routines at ILL. All the SANS measurements were carried out using Hellma quartz cells of 1 mm path length at 20.0°C ± 0.1°C.

Elastic scan measurements were performed on the High Flux Backscattering Spectrometer (HFBS) at National Institute of Standards and Technology (NIST) Center for Neutron Research (NCNR), in Gaithersburg, MD, United States. In this operation mode both the initial and final energy of the neutrons detected is determined by Bragg reflection of the neutrons by the Si(111) crystals of both the monochromator and the analyzers. To ensure minimal wavelength (i.e., energy) spread of the detected neutrons, the analyzers are arranged in such a way that only backscattered neutrons of the required energy satisfy the Bragg condition and reach the detectors. The corresponding instrumental resolution is of ≈0.8 μeV. A set of detectors records the intensity of neutrons for 16 Q values. The elastic scattered intensity is recorded as the sample temperature is changed using a cold cycle refrigerator with a temperature accuracy of ≈0.1 K. The temperature scan rate was 1/60 K/s. Samples were spread in thin annular sheets of ≈0.5 mm thickness, to minimize multiple scattering, and contained in aluminum cans sealed with indium.

QENS Time-of-Flight measurements were performed on the cold disk chopper IN5 at ILL. An incoming wavelength of 5 Å was selected. The instrumental resolution function could be well reproduced by a Gaussian function with a Full Width at Half Maximum varying from ≈82 μeV to ≈88 μeV depending on the scattering angle. Data were converted to sets of 16 constant Q spectra in the range from 0.5 Å^{-1} to 2.0 Å^{-1} using standard routines available in LAMPS.

Both ENS and QENS data were analyzed using DAVE (Azuah et al., 2009).

TABLE 2 | Best fitting parameters obtained from SANS analysis by using **Eq. 6** with R_1 = 2.7 Å.

	Fresh	12 months	15 months
S	189 ± 2	886 ± 14	626 ± 8
D_f	1.87 ± 0.01	1.92 ± 0.03	1.94 ± 0.01
ν	1.19 ± 0.01	1.27 ± 0.01	1.39 ± 0.01
C_P ($\cdot 10^{-10}$)	2.77 ± 0.15	—	—
bkg	0.773 ± 0.001	0.778 ± 0.002	0.769 ± 0.002

3 RESULTS AND DISCUSSION

3.1 SANS Results

Figure 1 shows the SANS curves of some of the BCO samples investigated in this study. As it can be clearly depicted, the scattering signal increases passing from the "fresh" to the "12 months" sample. The "15 months" sample shows a small decrease in the scattered intensity with respect of the "12 months" sample, most reasonably due to a partial sedimentation of larger aggregates. Fitting these curves with **Eq. 6** allows for a quantitative picture of the evolution of BCO structure at the nanoscale. **Table 2** lists the results of the best fits done according to **Eq. 6**. In particular, all the samples can be modeled using the structure factor associated to a fractal assembly of spherical lignin units of about 2.7 Å. In the case of the "fresh" sample an extra term accounting for the Porod's contribution from larger aggregates is also included (i.e., the scattering coming from the surface of the aggregate). This contribution does not provide any benefit to the final fits in all other samples probably because this fraction of larger objects precipitates out of the sample at longer times or it is covered by the scattering of the growing fractal assembly. The aggregation parameter, S, (i.e., the average number of units present in the fractal assembly) increases from 189 for the fresh sample to 886 after 12 months of aging. This value decreases to 626 after 15 months of aging, consistently with the hypothesis of sedimentation of part of the larger aggregates. The fractal dimension associated to the clusters are slightly increasing with the aging time, but they are in all cases around 1.9. More important, the polydispersity parameter ν shows a significant increase as a function of aging time from 1.2 to 1.4. Values of S and D_f are greater than the ones reported in the literature on a batch of BCO produced by VTT starting from different biomass and production plant (Fratini et al., 2006) thus indicating that the lignin aggregates formed in the present case are more clustered and have a denser structure. The index ν gives information on the degree of polydispersity associated to the cluster size and more important reveals the mechanisms behind cluster formation. Smaller ν are found in the case of broader cluster size distribution with values around 1.4 typical for reaction limited aggregation (RLA) and around 1.9 in the case of diffusion limited mechanism (DLA) (Chen et al., 1992). Value of ν obtained in the present investigation are slightly lower than 1.4 showing that the clustering mechanisms is dominated by a RLA process. The high value of the incoherent background are in line with the high hydrogen content evidenced by the CHNO analysis.

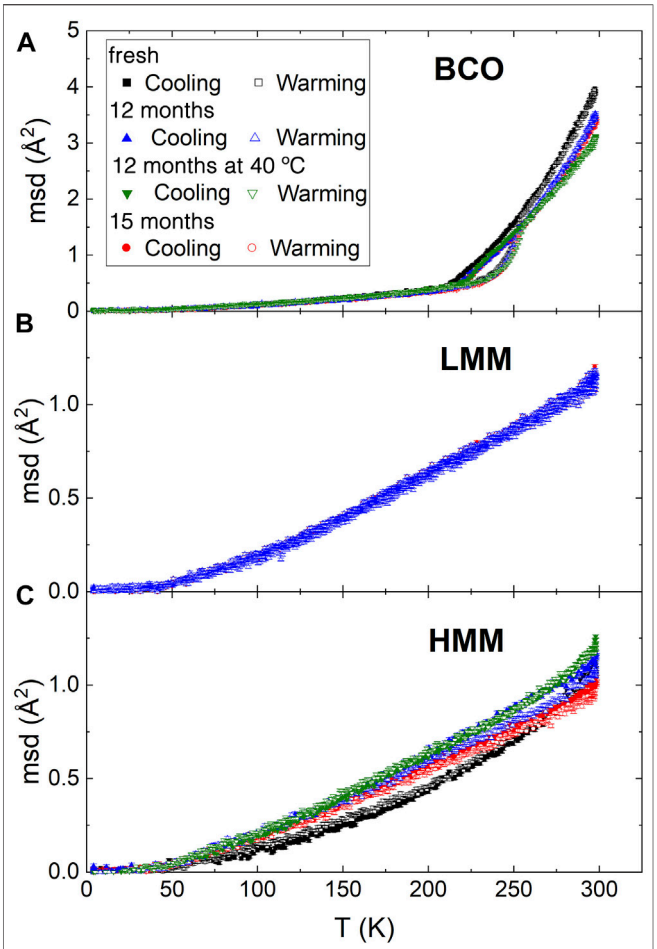

FIGURE 2 | Temperature dependence of the mean squared displacement over a timescale of ≈1 ns, obtained from the elastic neutron scattering measurements on HFBS. Samples at four aging stages were tested as indicated in the legend of plot **(A)** [The legend applies to plot **(B,C)** as well]. Measurements for each sample were performed first cooling and then heating it back again to 300 K. Plot **(A,B,C)** report the results for BCO, low and high molecular mass lignin fractions, respectively.

3.2 ENS Results

Within the Guassian approximation the single particle ISF is related to the mean squared displacement (*msd*) of the hydrogen atoms.

$$S_H^{self}(Q,E) = \mathcal{F}\left\{\exp\left\{-\frac{1}{6}Q^2\langle[\mathbf{r}(t)-\mathbf{r}(0)]^2\rangle\right\}\right\} \qquad (17)$$

where $\mathcal{F}\{\}$ represents a Fourier transform operation.

Within some approximations, from **Eqs 12**, **17**, the *msd* over the timescale determined by the energy resolution of the spectrometer, ≈ 1 ns in the HFBS case, can be derived as a linear fit to the data:

$$-3\ln\left(\frac{\frac{\partial^2\sigma}{\partial\Omega\partial E}(Q,E\approx 0,T)}{\frac{\partial^2\sigma}{\partial\Omega\partial E}(Q,E\approx 0,T_0)}\right) = I_0 + \mathrm{msd}(T)\times Q^2 \qquad (18)$$

where T_0 is the lowest temperature measured, for which it is assumed that no significant dynamics is observable. I_0 is the intercept of the linear fit in Q^2, accounting for experimental errors as well as for the presence of non Gaussian contributions.

Figure 2 reports the temperature dependence of the *msd* of the hydrogen atoms for the present investigation. Although for BCO it is much less pronounced, all the samples display an upturn of the curves at ≈ 50 K which is associated to the activation of methyl groups rotation (Senses et al., 2018). The *msd* of the BCO samples is characterized by a hysteresis loop in the range from 200 to 250 K. Interestingly, BCO can be cooled without displaying a sudden drop in the *msd* which is the hallmark of freezing. A rather sharp change in the slope of the curve is observed at ≈ 220 K, which can be associated to a liquid to glass transition. This temperature is not far from the much discussed dynamic transition temperature in proteins (Doster et al., 1989) and other water hydrated systems (Tavagnacco et al., 2019), which is believed to be intimately related to the dynamics of interfacial water (Chen et al., 2006). This result suggests that lowering the storing temperature below this transition threshold might be a way to suppress the reactivity of the BCO. On the other hand in the hysteresis loop, on warming, a fast increase of the *msd* just above 225 K is followed by a drastic change of slope at 250 K, overlapping with the cooling data. This unusual pattern of the *msd* curves indicates the frustration of crystallization of the liquids because of confinement and interfacial interactions. As a comparison, water confined within nanoporous matrices with pores of ≈28 Å and ≈24 Å display a depression of the freezing point of more than 50°C and 70°C, respectively; whereas for pores of ≈20 Å diameter, no freezing signature can be observed even with differential scanning calorimetry (Yoshida et al., 2008).

Above 250 K, in the liquid phase, the *msd* of BCO decreases with aging. However, this reduction in mobility is not monotonic as indicated by the fact that the "12 months" and "15 months" samples show similar values of the *msd*. Remarkably, the "12 months at 40°C" sample displays slightly smaller *msd* values which could be a consequence of the greater reactivity of the sample stored at 40°C leading to an increased amount of water, as well as other liquids, in the confined and interfacial state. The increase in size of the carbonaceous aggregates supports this picture.

As a comparison, the behavior of the pyrolytic lignin fractions is quite different. The absolute value of the *msd*, even at the highest temperature investigated of 300 K, is of about 1 Å^2; much lower than the one encountered for BCO. This is not surprising considering that lignin is a solid phase and therefore no long distance dynamics is expected. Moreover, beyond the already discussed upturn of the *msd* at 50 K, no other significant feature is present in the whole temperature range. The warming and cooling scans do not show any hysteresis consistently with the absence of phase changes in these matrices. Although the low molecular weight lignin display no dependence on aging, slight changes are observed in the high molecular weight case. In these samples, the mobility of the hydrogen atoms increases with aging. The chemical reactions taking place induce a rearrangement of the molecular and chemical structure of the lignin which allows for a slightly increased molecular mobility. It could be speculated, although no direct evidence can be provided, that the same changes take place in the lignin components of the BCO

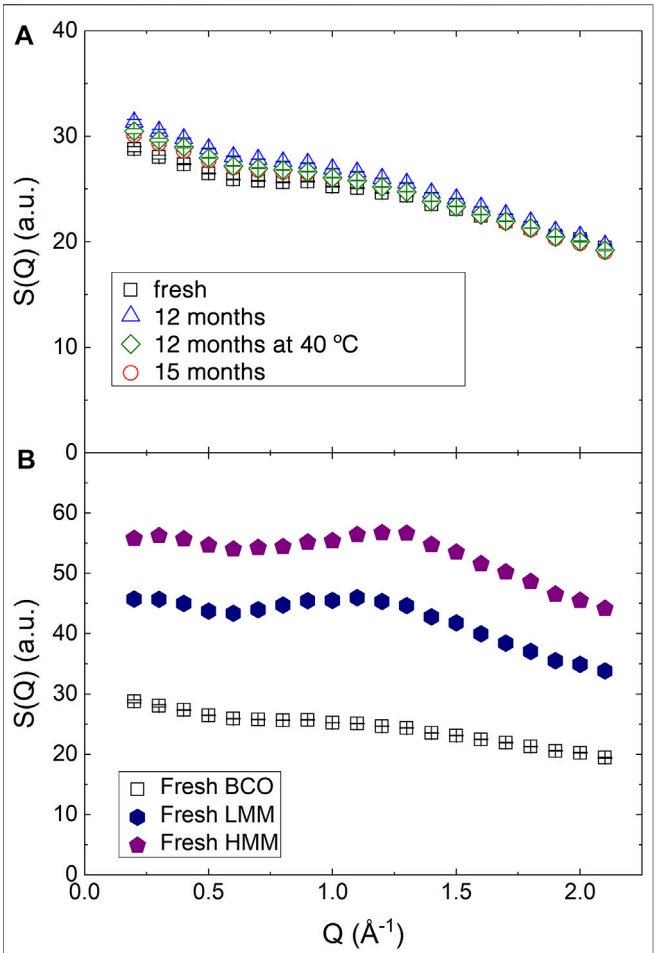

FIGURE 3 | Structure factor as obtained integrating the QENS spectra collected on IN5 over *E* (see **Eq. 3**). **(A)** BCO at four aging stages. **(B)** The structure factor of fresh BCO is compared to the structure factor of the fresh low and high molecular mass lignin fractions.

during aging, as a result of similar chemical reactions and structural rearrangements. The increase in size of the aggregates observed by SANS is consistent with this scenario. Interestingly, around room temperature, which is the most relevant range for the applications of these products, the increase of the *msd* is much larger for the sample aged at 40°C with respect to the others, confirming the higher reactivity of this sample.

3.3 QENS Results

The structure of the samples at molecular length scales was investigated by integrating the QENS spectra over the available energy range to obtain an approximation of the structure factor, as indicated in **Eq. 3**. The obtained results are reported in **Figure 3**. For BCO, as shown in panel (a) the slight decrease of $S(Q)$ up to ≈0.70 $Å^{-1}$ is likely due to the high Q tail of the SANS pattern and indicates the presence of not negligible coherent neutron scattering contributions. The further decrease at higher Q values is instead related to the limited energy range covered in the integration. Small differences can be observed among the samples differing for their aging even if the trends are not monotonic and difficult to be interpreted.

Figure 3B reports the structure factor for the fresh lignin fractions. The broad peak observed in the middle of the reported Q range is similar to the one observed in amorphous cellulose using X-ray diffraction (Park et al., 2010) and Kraft lignin (Goudarzi et al., 2014). The slight increase of the peak position in the HMM sample indicates a more compact structure of the low molecular weight lignin.

The presence of structural features in the samples indicates that the interpretation of the QENS results cannot neglect the presence of residual coherent signal beside the single particle dynamics of the hydrogen atoms. Moreover, the inherent inhomogeneity of the sample and the complexity introduced by confinement prevent from developing a detailed model of the microscopic motion of the hydrogen atoms. Therefore, an empirical approach is employed to gain information on the general geometry and timescales of the motions.

Figures 4, **5** display the QENS spectra at two Q values (0.7 and 1.4 Å) for fresh BCO and for the aging stages of BCO investigated

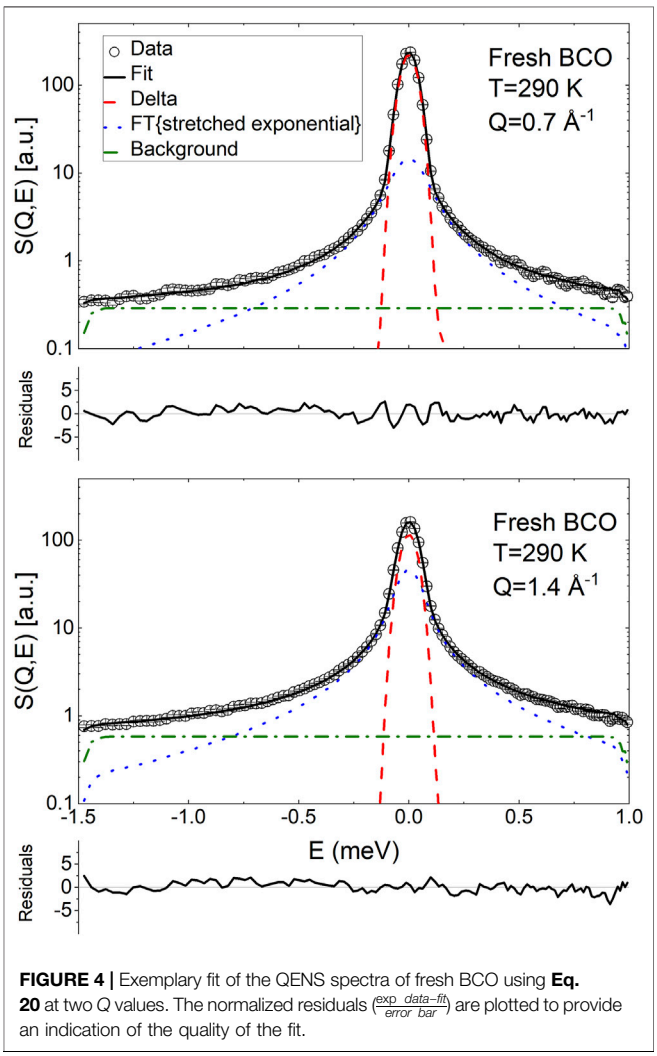

FIGURE 4 | Exemplary fit of the QENS spectra of fresh BCO using **Eq. 20** at two Q values. The normalized residuals ($\frac{exp\ \ data-fit}{error\ \ bar}$) are plotted to provide an indication of the quality of the fit.

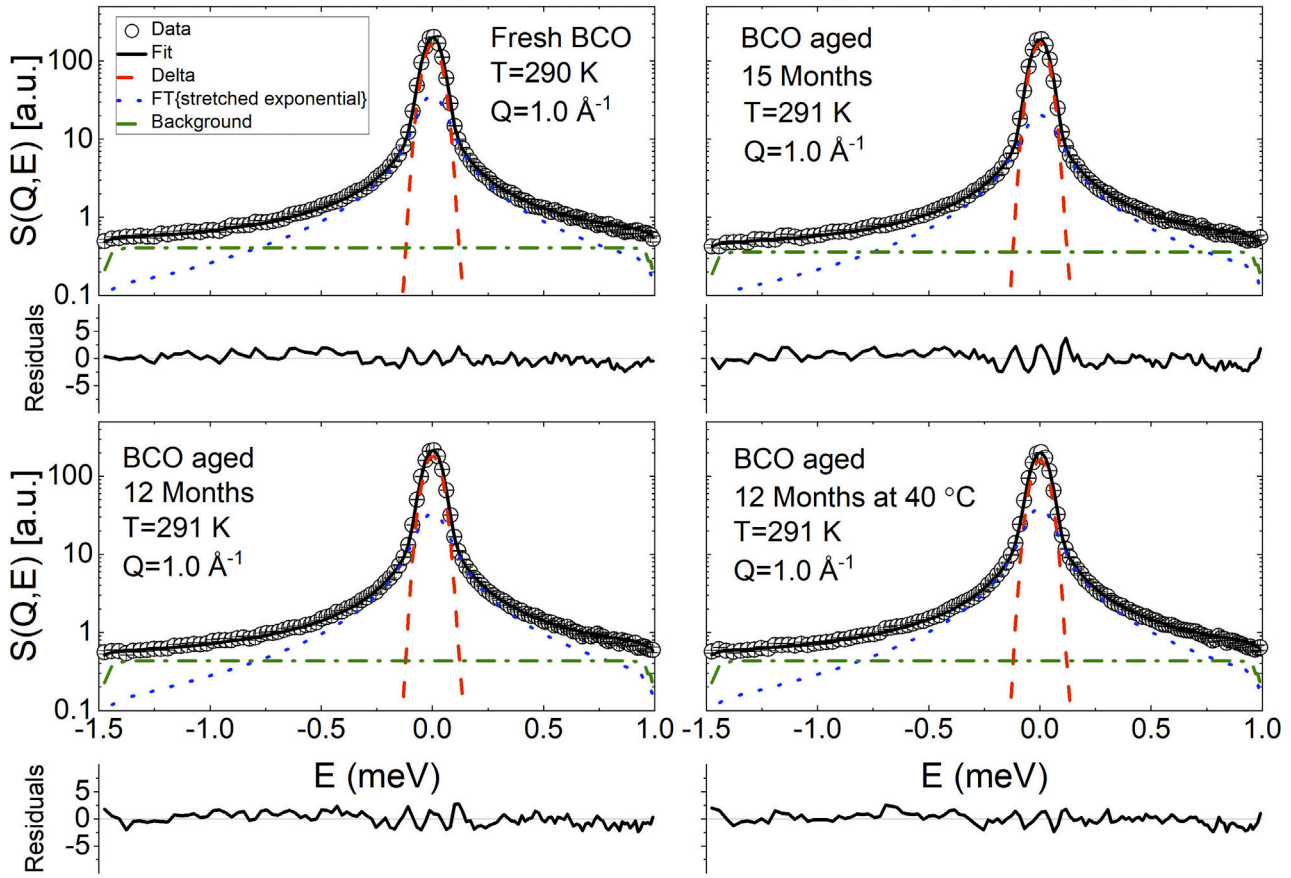

FIGURE 5 | Exemplary fit of the QENS spectra of BCO at four aging stages using **Eq. 20**. The normalized residuals ($\frac{exp\ \ data-fit}{error\ \ bar}$) are plotted to provide an indication of the quality of the fit.

at $Q = 1$ Å^{-1}, respectively. The spectra are characterized by the presence of a resolution limited component, from now on referred as delta. Therefore, the ISF of the single particle dynamics of the hydrogen atoms has been modeled as the sum of stretched exponential decay and a constant background:

$$S_H^{self}(Q,E) = A^{\delta}(Q) + \left[1 - A^{\delta}(Q)\right]\mathcal{F}\left\{\exp\left\{-\left[\frac{t}{\tau(Q)}\right]^{\beta(Q)}\right\}\right\} \tag{19}$$

The time independent term, $A^{\delta}(Q)$, accounts for the presence of immobile[1] hydrogen atoms in the aggregates. Moreover, the presence of this time independent term can be originated by a rotational and reorientational dynamics of the hydrogen atoms in a molecule, when diffusion of the point of reference, i.e., the center of mass, is too slow to be appreciated by the spectrometer employed because of its limited resolution. The stretched exponential function is commonly employed as an empirical way to describe relaxation data that do not follow a simple Debye behavior. The case $\beta = 1$ coincides with an exponential relaxation, whereas values of β increasingly smaller than one indicate higher degrees of non-exponential behaviour. A stretched behavior of the ISF can originate either from a distribution of exponential relaxations with different characteristic times or from intrinsically non exponential relaxation processes (Colmenero et al., 1999).

Therefore, considering the molecular heterogeneity of the BCOs giving rise to a distribution of exponential relaxation times, the data have been analyzed using the following fitting function:

$$S(Q,E) = A(Q)\left\{A^{\delta}(Q)\delta(E) + \left[1 - A^{\delta}(Q)\right]\right.$$
$$\left.\mathcal{F}\left\{\exp\left[-\left[\frac{t}{\tau(Q)}\right]^{\beta(Q)}\right]\right\}\otimes R(Q,E)\right\} + \text{bkg} \tag{20}$$

where A(Q) represents the total spectral intensity, δ(E) is a Dirac delta function, and *bkg* is a background which accounts for fast dynamical processes outside the instrumental window as well as instrumental background contributions.

[1]In QENS, the term immobile is commonly used to refer to atoms whose dynamics is much slower than the instrumental time window of the instrument, in this case extending to ≈20 ps.

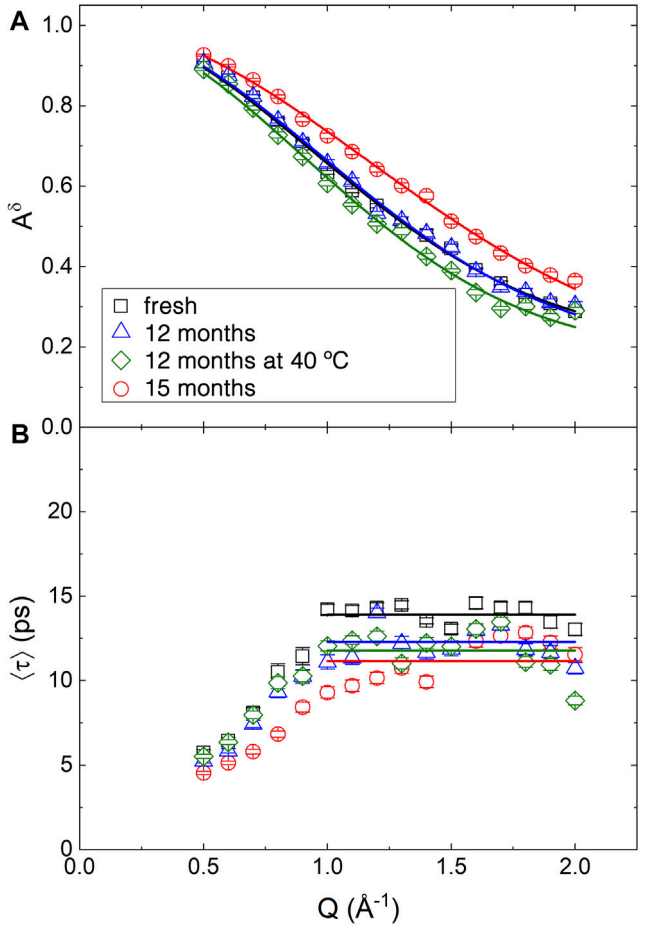

FIGURE 6 | *Q* dependence of the best fitting parameters obtained from the QENS spectra of BCO at four aging stages using **Eq. 20**. **(A)** Continuous lines are the fitting according to **Eq. 21**. **(B)** Straight lines indicate the expected plateau value of $\langle\tau\rangle$ for $Q \geq 1$ Å^{-1}.

Besides **Eq. 20**, several other fitting equations have been employed. None of the models which did not contain an immobile contribution was able to describe the spectra satisfactorily or would yield nonphysical results. Using the sum of a delta function and a Lorentzian, i.e., forcing $\beta(Q) = 1$ in **Eq. 20**, also yielded unsatisfactory fits. Using the sum of a delta and two Lorentzian functions allowed to obtain good fitting; however, since the model of **Eq. 20** has one less fitting parameter and the overall results of the models were the same, only the results of the fitting from **Eq. 20** are presented. The reader is cautioned, however, to keep in mind that, given the complexity of the samples and the limited *Q*/*E* probed, the present results should be considered preliminary in the sense that, as more information on the samples are gathered from other measurements and investigations, a more refined and insightful fitting model might be developed.

Figure 6 reports the main results on the microscopic dynamics of the hydrogen atoms. Plot (a) shows the *Q* dependence of A^δ. As discussed before, the delta contribution to the spectra arises both from immobile hydrogen atoms (over all length scales) and from the reorientational and conformational dynamics of the hydrogen atoms with respect to a reference point immobile on the instrumental time scale. Therefore, $A^\delta(Q)$ results have been analyzed using the equation:

$$A^\delta(Q) = \left(1 - A^{\text{imm}}\right) * \exp\left[-\frac{\left(QR_g^{rc}\right)^2}{3}\right] + A^{\text{imm}} \qquad (21)$$

A^{imm} represents the fraction of immobile atoms. The Gaussian term is analogue to the Guinier expression used to model the low-*Q* region of the SANS curves. Here it is used to extract a characteristic size of the region explored by the hydrogen atoms in their reorientational and conformational motion.

The stretched exponential function, often also referred to as the Kolrausch-Williams-Watts (KWW) function (Williams and Watts, 1970), can be considered as the results of the presence of a distribution of exponential relaxation. The first moment of the distribution defines the average relaxation time of the distribution, $\langle\tau\rangle$ (Johnston, 2006):

$$\langle\tau\rangle = \frac{\tau}{\beta}\Gamma\left(\frac{1}{\beta}\right) \qquad (22)$$

The *Q* dependence of $\langle\tau\rangle$ is reported in **Figure 6B**. The increase of $\langle\tau\rangle$ with *Q* for $Q < 1.0$ Å^{-1} is not physical. It is probably related to the strong correlation in the fitting between the various fitting parameters. Moreover, the presence of a coherent contribution at low *Q*, as observed in **Figure 3** might introduce some artifacts. Above $Q = 1$ Å^{-1} the data fluctuate around an average value indicated by the horizontal lines in the figure. In fact, as indicated by **Eq. 15**, for a reorientational and conformational (*rc*) type of dynamics, the timescale of the motion should be time independent. In a liquid, because of the diffusive motion, a Q^2 dependence of the broadening should be observed. The absence of an appreciable diffusive contribution in the sample indicates that the long distance translational motion of the molecules in the liquid phase is too slow to be appreciated. Fresh BCO appears as a sticky substance and has a macroscopic viscosity 65 times larger than water (Chiaramonti et al., 2011); although the mobility at the atomic level might not scale with the viscosity, this occurrence explains the absence of a diffusive component in the spectra.

Table 3 reports the results of the fitting of $A^\delta(Q)$. The average value of $\langle\tau\rangle$ as well as of the stretching exponent β, are also reported as $\overline{\langle\tau\rangle}$ and $\bar{\beta}$. The behavior of the parameters with aging is not monotonic. The volume explored by the hydrogen atoms in fresh BCO has a characteristic size of ≈1.3 Å. This can be compared to the distance between the hydrogen atom and the center of mass in water, 0.98 Å, or the typical radius of methyl groups rotation. Hence, the motion is highly restricted to local rearrangements of the chemical bonds or roto-translational motion of water and the other hydrogenated liquids on the surface of the carbonaceous aggregates. Interestingly, the R_g obtained in the 15 months aged BCO is significantly while both the 12 months aged samples retain R_g values similar to the one of fresh BCO. The value of A^{imm}, of the order of 20%, is comparable to the volume fraction of the fractal aggregates

TABLE 3 | Fitting results of the Q dependence of the parameters extracted from the QENS spectra.

	Rg (Å)	A^{imm}	$\langle\tau\rangle$ (ps)	$\bar{\beta}$
BCO				
Fresh	1.31 ± 0.02	0.21 ± 0.02	13.9 ± 0.2	0.603 ± 0.003
12 months	1.26 ± 0.04	0.18 ± 0.02	12.3 ± 0.3	0.622 ± 0.004
12 months at 40°C	1.37 ± 0.03	0.18 ± 0.02	11.8 ± 0.4	0.638 ± 0.003
15 months	1.06 ± 0.02	0.16 ± 0.02	11.2 ± 0.4	0.625 ± 0.004
Lignin				
LMM	1.52 ± 0.05	0.869 ± 0.003	4.02 ± 0.06	1 ± 0
HMM	1.21 ± 0.06	0.833 ± 0.008	4.80 ± 0.13	1 ± 0

observed in SANS. On the other hand, A^{imm}, displays with aging the opposite trend as the one observed in R_g, with the smallest immobile fraction observed in the 15 months sample, and similar values recorded for the fresh and 12 months aged samples. However, these results points to the fact that as the chemical reactions take place in the BCO matrix with aging, an increasing number of molecules is comprising the carbonaceous aggregates or is bound and trapped within them; the remaining fractions of molecules being the ones with increased mobility.

The time scale of the motion is of the order of 10 ps. This can be compared with the timescale of the microscopic mobility of water: in fact, water molecules are believed to diffuse in the liquid through a sequence of random jumps. The time spent by the water molecules in between jumps, the residence time, has been measured using QENS (Teixeira et al., 1985). Even if the QENS spectra of BCO do not demonstrate a diffusive like Q^2 dependence of the quasielastic broadening, the residence time is akin to the timescale measured in the present experiment, because it is related to the broadening of the QENS spectra at high Q, in a Q independent region. The values found for BCO are comparable to the ones observed in bulk water at ≈ 250 K. This confirm the extreme confinement experienced by the liquid phases in BCO: in fact, it was proposed that interfacial water displays the same dynamics of bulk water at a temperature ≈20 K lower (Chen et al., 1995). Cured cement, also provides an interesting point of comparison, since it is characterized by a significant fraction of interfacial water which plays a major role in its continuous curing. Also in QENS data from cement, the Q dependence of interfacial water dynamics is observed to increasingly deviate from the expected diffusive behavior as curing goes on (Fratini et al., 2001). Moreover, as a comparison, in cement timescales of the order of 10 ps were observed in the dynamics of the interfacial water after few days of curing (Fratini et al., 2002). Once again we observe that the 15 months sample mobile hydrogen atoms display the slower dynamics with the 12 months aged samples approaching again the values of fresh BCO. The stretching exponent $\bar{\beta}$ indicates the presence of a broad distribution of relaxation time with a slight decrease of the non-exponential behaviour from the fresh to the BCO sample aged at 40°C.

QENS measurements were also performed on samples of fresh LMM and HMM lignin fractions. The data were analyzed according to **Eq. 20**; however, the obtained values of β were close to unity and therefore the parameter was fixed to 1. Hence, the QENS data were essentially fitted using the sum of a delta function and a Lorentzian broadening. Examples of the fitting are shown in **Figure 7**.

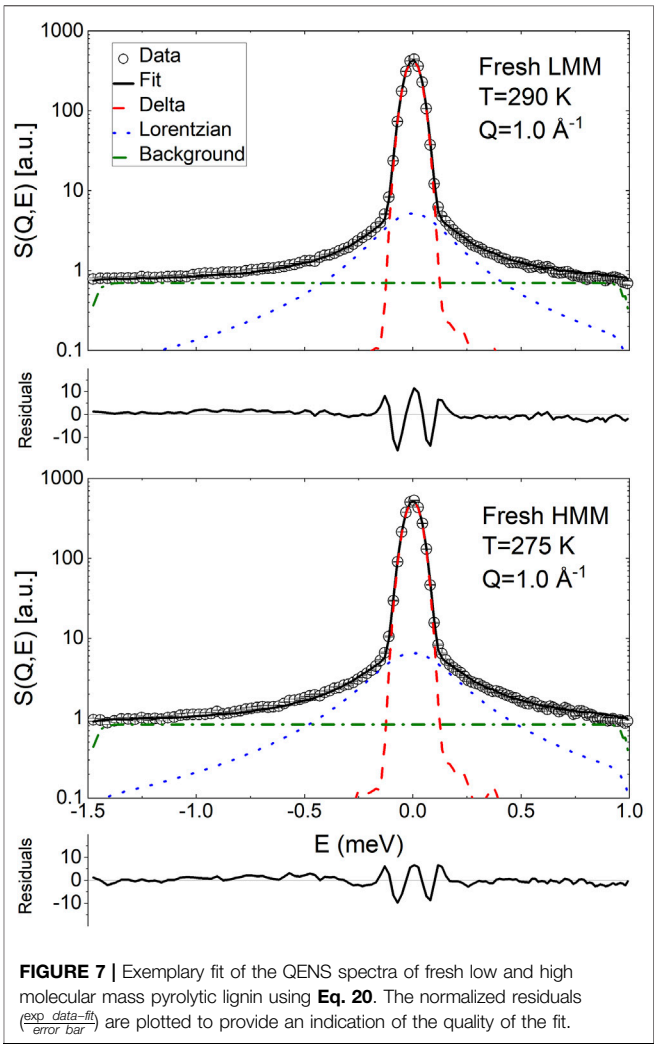

FIGURE 7 | Exemplary fit of the QENS spectra of fresh low and high molecular mass pyrolytic lignin using **Eq. 20**. The normalized residuals $\left(\frac{exp\ data-fit}{error\ bar}\right)$ are plotted to provide an indication of the quality of the fit.

Figure 8 reports the Q dependence of the fitting parameters. The A^{δ} data were analyzed as the ones for BCO using **Eq. 21**; a mean relaxation time, $\bar{\tau}$, was extracted as well. The obtained results are reported in **Table 3**. The main difference with respect to the BCO is the much larger immobile fraction, A^{imm}. The time

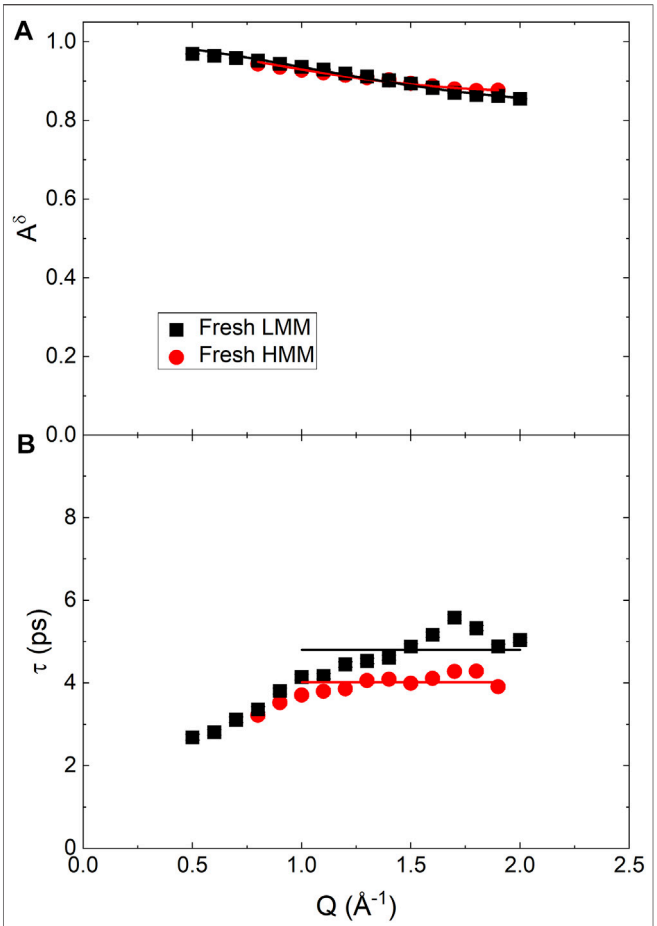

FIGURE 8 | *Q* dependence of the best fitting parameters obtained from the QENS spectra of fresh low and high molecular mass pyrolytic lignin fraction using **Eq. 20**, with $\beta = 1$. **(A)** Continuous lines are the fitting according to **Eq. 21**. **(B)** Straight lines indicate the expected plateau value of τ for $Q \geq 1$ Å^{-1}.

scale of the motions are faster than the ones found in BCO which indicates that the dynamics observed originates mostly from local rearrangements of the chain conformation. The results are consistent with what reported in hydrated polymer systems (Noferini et al., 2019). Please, note that the fact that no significant stretching of the ISF was observed is attributed to the small fraction of mobile hydrogen atoms and the consequent difficulty in obtaining an accurate modeling.

4 CONCLUSION

BCOs hold tremendous potential as a novel renewable energy source. However, their reactivity partially limits the possibilities of their practical use. Gaining molecular insights on the properties of these systems might be the key to improve their applicability. However, from a physical chemical point of view, BCOs are extremely complex materials for their heterogeneity in molecular composition and large interface area of the diverse constituents. In this regard, they represent a practical example of widespread presence of interfacial water in nature. This paper reports the results of an investigation of the microscopic structure and dynamics of BCOs and their lignin components. The solid fraction, composed of mesoscopic carbonaceous aggregates, grows significantly with aging as evidenced by SANS. However, the changes in the microscopic dynamics of the interfacial liquid phases are more subtle. The dynamics of the hydrogen atoms, both in the solid and liquid phase, is limited to local re-orientation and conformation changes of the order of 1 to 2 Å. The timescales of the motion, around room temperature, are comparable to the ones of deeply supercooled bulk water or interfacial water in curing cement. This mobility is however required for the aging of BCO and elastic neutron scattering measurements suggest that storing the samples at ≈ 220 K might suppress its intrinsic reactivity.

NOTE

Throughout the paper, error bars and uncertanties of the raw data represent one standard deviation, and error bars of the fitted parameters represent one standard deviation.

DATA AVAILABILITY STATEMENT

The datasets presented in this study can be found in online repositories. The names of the repository/repositories and accession number(s) can be found below: https://www.ncbi.nlm.nih.gov/, JAGFBX000000000 https://www.ncbi.nlm.nih.gov/, JAGFBW000000000. Raw data were generated at ILL and NCNR. The derived data that support the findings of this study are available from the corresponding authors.

AUTHOR CONTRIBUTIONS

MB and EF: Prepared the samples, performed the QENS experiment, and analyzed the SANS data. AF: Performed the elastic scan measurements, and analyzed the QENS data. All authors contributed equally to the design of the experiments and overall study as well as to the writing of the manuscript.

ACKNOWLEDGMENTS

Authors acknowledge Prof. Y. Liu (NCNR), Dr. L. Porcar (ILL) for their help in setting up and performing the SANS experiment. Dr. J. Olivier (ILL) and Dr. M. Tyagi (NCNR) are also acknowledged for their help in setting up QENS and elastic scan measurements, respectively. MB and EF kindly acknowledge partial financial support from Consorzio per lo Sviluppo dei Sistemi a Grande Interfase (CSGI). Access to HFBS was provided by the Center for High Resolution Neutron Scattering, a partnership between the National Institute of Standards and Technology and the National Science Foundation under Agreement No. DMR-2010792.

REFERENCES

Azuah, R. T., Kneller, L. R., Qiu, Y., Tregenna-Piggott, P. L. W., Brown, C. M., Copley, J. R. D., et al. (2009). Dave: A Comprehensive Software Suite for the Reduction, Visualization, and Analysis of Low Energy Neutron Spectroscopic Data. *J. Res. Natl. Inst. Stand. Technol.* 114, 341–358. doi:10.6028/jres.114.025

Bée, M. (1988). *Quasielastic Neutron Scattering : Principles and Applications in Solid State Chemistry, Biology and Materials Science*. Bristol: Philadelphia: A. Hilger.

A. Bridgwater (Editor) (2008). *Fast Pyrolysis of Biomass*. repr edn (Newbury: CPL Press), 2.

Chen, S. H., Rouch, J., and Tartaglia, P. (1992). Light Scattering from Polydispersed Fractal Clusters in Solution. *Croatica Chemica Acta* 65, 353–366.

Chen, S.-H., Gallo, P., and Bellissent-FunelBellissentFunel, M.-C. (1995). Slow Dynamics of Interfacial Water. *Can. J. Phys.* 73, 703–709. doi:10.1139/p95-104

Chen, S.-H., Liu, L., Fratini, E., Baglioni, P., Faraone, A., and Mamontov, E. (2006). Observation of Fragile-To-strong Dynamic Crossover in Protein Hydration Water. *Proc. Natl. Acad. Sci.* 103, 9012–9016. doi:10.1073/pnas.0602474103

Chiaramonti, D., Rizzo, A., Peruzzi, N., Bonini, M., Fratini, E., and Baglioni, P. (2011). Preliminary Investigation of Pyrolysis Oil Upgrading via Emulsification with Biodiesel. In Proceedings of the 19th European Biomass Conference and Exhibition 6-10 June 2011. ISBN: 9788889407554, Publisher: ETA-Florence Renewable Energies. doi:10.5071/19THEUBCE2011-VP2.5.16

Colmenero, J., Arbe, A., Alegría, A., Monkenbusch, M., and Richter, D. (1999). On the Origin of the Non-exponential Behaviour of the -relaxation in Glass-Forming Polymers: Incoherent Neutron Scattering and Dielectric Relaxation Results. *J. Phys. Condens. Matter* 11, A363–A370. doi:10.1088/0953-8984/11/10a/033

Czernik, S., Johnson, D. K., and Black, S. (1994). Stability of wood Fast Pyrolysis Oil. *Biomass and Bioenergy* 7, 187–192. doi:10.1016/0961-9534(94)00058-2

Doster, W., Cusack, S., and Petry, W. (1989). Dynamical Transition of Myoglobin Revealed by Inelastic Neutron Scattering. *Nature* 337, 754–756. doi:10.1038/337754a0

Faraone, A., Liu, L., and Chen, S.-H. (2003). Model for the Translation-Rotation Coupling of Molecular Motion in Water. *J. Chem. Phys.* 119, 6302–6313. doi:10.1063/1.1601599

Fratini, E., Chen, S.-H., Baglioni, P., and Bellissent-Funel, M.-C. (2001). Age-dependent Dynamics of Water in Hydrated Cement Paste. *Phys. Rev. E* 64. doi:10.1103/PhysRevE.64.020201

Fratini, E., Chen, S.-H., Baglioni, P., Cook, J. C., and Copley, J. R. D. (2002). Dynamic Scaling of Quasielastic Neutron Scattering Spectra from Interfacial Water. *Phys. Rev. E* 65. doi:10.1103/PhysRevE.65.010201

Fratini, E., Bonini, M., Oasmaa, A., Solantausta, Y., Teixeira, J., and Baglioni, P. (2006). Sans Analysis of the Microstructural Evolution during the Aging of Pyrolysis Oils from Biomass. *Langmuir* 22, 306–312. doi:10.1021/la051990a

Fratini, E., Faraone, A., Ridi, F., Chen, S.-H., and Baglioni, P. (2013). Hydration Water Dynamics in Tricalcium Silicate Pastes by Time-Resolved Incoherent Elastic Neutron Scattering. *J. Phys. Chem. C* 117, 7358–7364. doi:10.1021/jp312684p

Gardner, J. S., Ehlers, G., Faraone, A., and García SakaiSakai, V. (2020). High-resolution Neutron Spectroscopy Using Backscattering and Neutron Spin-echo Spectrometers in Soft and Hard Condensed Matter. *Nat. Rev. Phys.* 2, 103–116. doi:10.1038/s42254-019-0128-1

Goudarzi, A., Lin, L.-T., and Ko, F. K. (2014). X-ray Diffraction Analysis of Kraft Lignins and Lignin-Derived Carbon Nanofibers. *J. Nanotechnol. Eng. Med.* 5, 021006. doi:10.1115/1.4028300

Johnston, D. C. (2006). Stretched Exponential Relaxation Arising from a Continuous Sum of Exponential Decays. *Phys. Rev. B* 74. doi:10.1103/PhysRevB.74.184430

Liu, Y. C., Sheu, E. Y., Chen, S. H., and Storm, D. A. (1995). Fractal Structure of Asphaltenes in Toluene. *Fuel* 74, 1352–1356. doi:10.1016/0016-2361(95)00098-P

Noferini, D., Faraone, A., Rossi, M., Mamontov, E., Fratini, E., and Baglioni, P. (2019). Disentangling Polymer Network and Hydration Water Dynamics in Polyhydroxyethyl Methacrylate Physical and Chemical Hydrogels. *J. Phys. Chem. C* 123, 19183–19194. doi:10.1021/acs.jpcc.9b04212

Oasmaa, A., and Kuoppala, E. (2003). Fast Pyrolysis of Forestry Residue. 3. Storage Stability of Liquid Fuel. *Energy Fuels* 17, 1075–1084. doi:10.1021/ef030011o

Oasmaa, A., Kuoppala, E., and Solantausta, Y. (2003). Fast Pyrolysis of Forestry Residue. 2. Physicochemical Composition of Product Liquid. *Energy Fuels* 17, 433–443. doi:10.1021/ef020206g

R. P. Overend and E. Chornet (Editors) (1999). *Biomass, a Growth Opportunity in green Energy and Value-Added Products: Proceedings of the 4th Biomass Conference of the Americas: Oakland Marriott City Center*. 1st ed edn. (Oakland, California, USAKidlington, Oxford, UK: Pergamon). Meeting Name: Biomass Conference of the Americas OCLC: ocm42458275.

Park, S., Baker, J. O., Himmel, M. E., Parilla, P. A., and Johnson, D. K. (2010). Cellulose Crystallinity index: Measurement Techniques and Their Impact on Interpreting Cellulase Performance. *Biotechnol. Biofuels* 3. doi:10.1186/1754-6834-3-10

Ringer, M., Putsche, V., and Scahill, J. (2006). *Large-scale Pyrolysis Oil Production: A Technology Assessment and Economic Analysis*. U.S. Department of Energy Office of Scientific and Technical Information. doi:10.2172/894989 Large-Scale Pyrolysis Oil Production: A Technology Assessment and Economic Analysis.

Scholze, B., Hanser, C., and Meier, D. (2001). Characterization of the Water-Insoluble Fraction from Fast Pyrolysis Liquids (Pyrolytic Lignin). *J. Anal. Appl. Pyrolysis* 58-59, 387–400. doi:10.1016/S0165-2370(00)00173-X

Senses, E., Tyagi, M., Pasco, M., and Faraone, A. (2018). Dynamics of Architecturally Engineered All-Polymer Nanocomposites. *Acs Nano* 12, 10807–10816. doi:10.1021/acsnano.8b02514

SipiläSipila, K., Kuoppala, E., FagernäsFagernas, L., and Oasmaa, A. (1998). Characterization of Biomass-Based Flash Pyrolysis Oils. *Biomass and Bioenergy* 14, 103–113. doi:10.1016/S0961-9534(97)10024-1

Tavagnacco, L., Chiessi, E., Zanatta, M., Orecchini, A., and Zaccarelli, E. (2019). Water-polymer Coupling Induces a Dynamical Transition in Microgels. *J. Phys. Chem. Lett.* 10, 870–876. doi:10.1021/acs.jpclett.9b00190

Teixeira, J., Bellissent-Funel, M.-C., Chen, S. H., and Dianoux, A. J. (1985). Experimental Determination of the Nature of Diffusive Motions of Water Molecules at Low Temperatures. *Phys. Rev. A.* 31, 1913–1917. doi:10.1103/PhysRevA.31.191310.1103/physreva.31.1913

Williams, G., and Watts, D. C. (1970). Non-symmetrical Dielectric Relaxation Behaviour Arising from a Simple Empirical Decay Function. *Trans. Faraday Soc.* 66, 80. doi:10.1039/tf9706600080

Yoshida, K., Yamaguchi, T., Kittaka, S., Bellissent-Funel, M.-C., and Fouquet, P. (2008). Thermodynamic, Structural, and Dynamic Properties of Supercooled Water Confined in Mesoporous Mcm-41 Studied with Calorimetric, Neutron Diffraction, and Neutron Spin echo Measurements. *J. Chem. Phys.* 129, 054702. doi:10.1063/1.2961029

Author Disclaimer: Certain trade names and company products are identified in order to specify adequately the experimental procedure. In no case does such identification imply recommendation or endorsement by the National Institute of Standards and Technology, nor does it imply that the products are necessarily the best for the purpose.

Conflict of Interest: The authors declare that the research was conducted in the absence of any commercial or financial relationships that could be construed as a potential conflict of interest.

Publisher's Note: All claims expressed in this article are solely those of the authors and do not necessarily represent those of their affiliated organizations, or those of the publisher, the editors and the reviewers. Any product that may be evaluated in this article, or claim that may be made by its manufacturer, is not guaranteed or endorsed by the publisher.

Advantages of publishing in Frontiers

OPEN ACCESS
Articles are free to read for greatest visibility and readership

FAST PUBLICATION
Around 90 days from submission to decision

HIGH QUALITY PEER-REVIEW
Rigorous, collaborative, and constructive peer-review

TRANSPARENT PEER-REVIEW
Editors and reviewers acknowledged by name on published articles

Frontiers
Avenue du Tribunal-Fédéral 34
1005 Lausanne | Switzerland

Visit us: www.frontiersin.org
Contact us: frontiersin.org/about/contact

REPRODUCIBILITY OF RESEARCH
Support open data and methods to enhance research reproducibility

DIGITAL PUBLISHING
Articles designed for optimal readership across devices

FOLLOW US
@frontiersin

IMPACT METRICS
Advanced article metrics track visibility across digital media

EXTENSIVE PROMOTION
Marketing and promotion of impactful research

LOOP RESEARCH NETWORK
Our network increases your article's readership